TRAJECTORIES OF CHARGED PARTICLES IN ELECTROSTATIC POWDER COATING SYSTEMS

by

MING LEANG ANG

A Doctoral Thesis

Submitted in partial fulfilment of the requirements
for the award of

Doctor of Philosophy
of the Loughborough University of Technology

January 1981

Supervisor : P.J. LLOYD
Chemical Engineering Department

To my

Father and Mother

Acknowledgements

First and foremost my supervisor John Lloyd deserves many thanks for his encouragement and guidance. Equal thanks are also due to Geoff Boyden for his expert advice on the use of photography for particle tracking and I deeply appreciate the number of painstaking hours he spent helping with the experimentation and processing of results.

A debt of gratitude to the following is acknowledged with pleasure: -

Mr. Leo Moore and his workshop team for the construction of the rig.

Mr. Ian Sinclair for his advice on the electrical aspect of the experiment.

Mr. F.G. MacCabee and the Transport Technology Department for the loan of the hot wire anemometry system, smoke visualisation equipment and the use of the wind tunnel.

Co-ordinated Powder Research Programme for the financial support of the project and the frequent exchange of ideas with the representatives of the sponsoring companies, including -

Ault and Wiborg Paints Limited
Aerostyle Limited
Berger Paints Limited
Binks-Bullows Limited
Carrs Paints Limited
Blundell Permoglaze Limited
DeVilbiss Company Limited
Donald Macpherson Powder Limited
Drynamels Limited
GEMA, SA
I C I Limited Paints Division
International Paint Company Limited
The Nordson Corporation
TAM-SAMES, et Cie
Volstatic Limited

Mr. Peter Thompson, NRDC, Chairman - Steering Committee.

Late Professor A.W. Bright, Dr. S. Singh and Dr. J.F. Hughes (Elec. Eng. Dept., University of Southampton) for their helpful discussions.

Professor D.C. Freshwater for the use of the Chemical Engineering research facilities.

Various members of staff of the Chemical Engineering Department for their useful suggestions.

Mrs. Irene Newton and Mrs. Rita Mathews for the typing of the manuscript.

Summary

In an electrostatic powder coating process, charged plastic particles of high resistivity are transported in an air jet to be deposited on an earthed object. The trajectory of a particle is determined by the interaction of various aerodynamic and electrostatic forces. The objective of this study is to identify the forces involved and to obtain a complete understanding of these forces affecting the particle trajectories in a spray booth. It is vitally important to understand the fundamental mechanisms of the process as the first step towards improving the deposition efficiency.

Particle trajectories were calculated by solving numerically the equation of motion which was formulated by performing a force balance. A computer program was developed to,

(i) predict the particle trajectories and particle velocities.

(ii) demonstrate the effects of the various parameters at every stage of the particle flight.

Initially, various mathematical models were developed to describe these forces. The air flow from the spraying device was found to be the most important particle transporting mechanism and could be suitably described by an axisymmetric turbulent submerged jet solution. To verify the accuracy of the theory measurement of the air velocity distribution in the test section using a hot wire anemometry system was compared with calculated data. The electrical forces considered were due to the external applied field, image force field and the space charge field. Poisson's equation was solved for a simple conical geometry and the theory compared favourably with published experimental data of field intensity distribution. The importance of another phenomenon - 'corona wind' was also examined. It was shown that the field enhancement near the object was due to the space charge effect and this led to the establishment of a criterion to assess the space charge contribution.

Experimentally, the motion of particle with size ranging from 45 to 120 µm was recorded using a photographic technique. The calculated trajectories were found to compare reasonably well with the experimental data. With reduction in particle size the discrepancy became more severe as the particle turbulent diffusion mechanism became increasingly significant.

CHAPTER 4 THE ELECTRICAL FORCES

CHAPTER 5 CORONA WIND EFFECT

CHAPTER 6 EXPERIMENTAL INVESTIGATION OF PARTICLE TRAJECTORIES

CHAPTER 7 COMPARISON OF EXPERIMENTAL AND THEORETICAL TRAJECTORIES - RESULTS AND DISCUSSION

CHAPTER 8 GENERAL DISCUSSION AND SUMMARY

List of Photographs

CHAPTER I

INTRODUCTION

1.1 ELECTROSTATIC POWDER COATING IN INDUSTRY

Electrostatic powder coating (EPC), a process very similar to electrostatic precipitation, has been used since early 1960 in the metal finishing industry. The basic feature of the process is that polymer particles are given a net charge and are deposited on a grounded, conducting substrate. The coating is then fused and cured to form the protective film.

There are basically two EPC systems, namely the electrostatic fluidised bed (EFB) and electrostatic powder spraying (EPS) (2,3,29,61). The fluidised bed system, invented by Irwin Gemmer in 1950 uses polymer powders of particle size, ranging from 30 - 300μm to produce coating thickness of about 100 - 200μm. It is a hot dip process in which heated objects to be coated are dipped in a fluidised bed of powder. This process however suffers from marked disadvantages. The main one is the thicknesses produced are much greater than the 30 - 150μm films to which the paint industry is accustomed. The process did prove however the practicality of powder coating and led the way towards a newer and more versatile process - the electrostatic powder spraying technique.

In 1962, as an extension to the idea of electrostatic paint spraying, the French spray equipment manufacturers S.A.M.E.S. developed the electrostatic powder gun. Since that time, the powder process has made a great impact upon the traditional paint markets mainly because thin coatings ($<$ 100μm) of good quality finishing are easily obtained. The advantages of this process are listed in Table 1.1

The process has been successfully employed in many areas of the metal working industries, notably hardware, tools, domestic appliances, outdoor furniture and automobile components. In 1975 it was estimated that powder coating held a 2% share of the industrial painting market. It was estimated that by 1980 the share wouldincrease to 20%(4). The figure will improve if the automotive industry decides to produce powder coated car bodies. At present, several components for underbody, underbonnet and interior fitments are powder coated. In the United States and Japan great progress has been made in using acrylic powder top coats, whereas elsewhere development is proceeding on the lines of powder coating as a primer coat. The industry is, nevertheless, actively pursuing the eventual idea of complete powder coated car body.

TABLE 1.1 THE ADVANTAGES OF EPC

Application Qualities	Film Qualities
no solvents and reduce hazards risk	very good adhesion
suitable for automation because of the natural self limiting mechanism of the process	high scratch resistance
	high abrasive resistance
	uniform thickness
low material wastage because overspray can be re-used. Powder utility can be 98-99% efficiency (with recirculation)	good impact resistance
fast application	good flexibility
	very good electrical insulation
uniform powder distribution	good chemical corrosion resistance
application by semi-skilled operators	high heat resistance

1.2 Basic Arrangement of the Process

The typical electrostatic powder spraying process is as shown in Figure 1.1. General descriptions of the process have been reported by Levinson(1),Korf(29),Stribley(77),Miller(7) and Bright(31). Basically the EPC method comprises of four stages and they are:

(i) Powder charging
(ii) Powder transport from the charging region to the substrate
(iii) Powder adhesion
(iv) Fusion of Powder

Powders are pneumatically fed from a fluidised hopper to a spray gun. Located at the nozzle of the gun is a pointed electrode producing a corona discharge generated by a high voltage supply (60-100 Kv). Usually a negative voltage is applied to produce a negative corona. The particles passing through the region are therefore charged by bombardment with ions produced by the corona discharge. The charged particles are directed towards the object to be coated by the combined action of the carrier air jet and the electrostatic field developed between the gun and the earthed substrate. As in conventional spray gun, although the transfer of powder is due largely to the air flow, the field reduces the over-spray by concentrating the powder towards the object. Also distribution of the field lines will allow a uniform coating to be produced.

The deposited powder particles form a multi-layer until a limiting thickness is reached. Further particles arriving will be rejected by the layer due to the back ionisation phenomena. The next stage is the stoving stage where the deposited layer is fused and cured by baking in an oven at about $180^{\circ}C$ to form a coating.

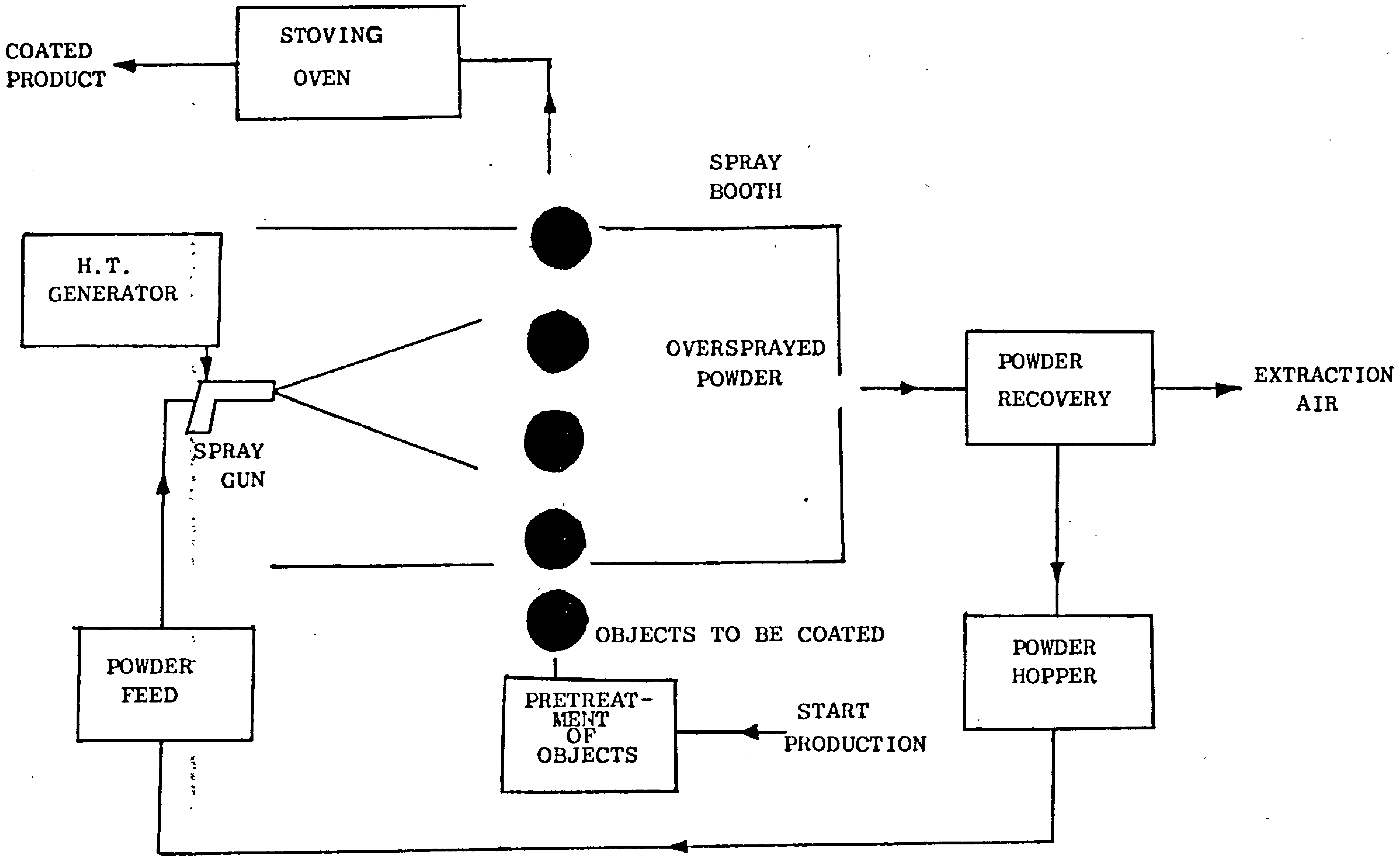

Figure 1.1 Arrangement for a Powder Coating System

Oversprayed powder is collected by the recovery system and may be recycled.

The first two stages of the EPC process are most important in determining the efficiency of the process. The next two stages will determine the quality of the coatings.

1.3 Deposition Efficiency

One of the main attractions of powder coating process is the possible efficient utilisation of materials. Accomplished by the recycling of oversprayed powder, powder utilisation can be greater than 95% efficient with good design (78). Without the recycling process, the powder utilisation efficiency known as deposition efficiency or transfer efficiency is defined as follows,

$$\text{Deposition Efficiency} = \frac{\text{weight of powder deposited on object}}{\text{weight of powder sprayed}}$$

Generally, the deposition efficiency is restricted to a comparatively low figure of about 60% (106). Despite the high utilisation efficiency that is achievable, Cowley (79), Lever (106) and Winter (78) believed that low transfer efficiency is hindering further progress in the use of powder coating.

There are various obvious reasons why the transfer efficiency needs to be improved considerably especially when multi colour operations are involved.

(1) In single colour operation, the deposition efficiency will determine the number of recycles necessary to obtain high utilisation of powders. Depending on the efficiency of reclamation equipment, the recovery and transport of oversprayed powder can pose severe operational problems.

(2) With multi colour operation, there are generally three methods of colour changes.

(i) If powder is to be recovered for recycling in its original colour, avoidance of cross contamination is vital, and therefore each colour must be reclaimed separately. The use of separate booths, spray guns and recovery systems for each colour is one solution(107) but for big installation involving a few colour changes, the capital equipment cost can be very high.

(ii) Alternatively, after each colour application, the booth and the recovery system are cleaned. This is only feasible if the equipment can be cleaned with relative ease. With conventional equipment, the time required can vary from 1.5 to 8 hours (78) although equipment is now available which reduces this time from between 10 - 30 mins.

(iii) The simplest solution is to achieve higher transfer efficiency and to reclaim oversprayed powder as a mixture of colours. The small amount of mixed material can either be discarded or used for non-decorative functional coatings. This method is reckoned to be practical if transfer efficiency of 80% can be achieved (107). In some automotive top coat applications, this method is adopted even with a transfer efficiency of 60% (108).

Therefore, if powder coating is to develop at an increasing rate, it is essential to maximise the transfer efficiency of the process. Of the four stages of EPC listed, the first two, i.e. powder charging and powder transport are most relevant to the transfer efficiency and are subjects of investigation in this study.

1.4 Assessment of Problems and How to Evaluate Them

There are generally two methods of studying the deposition efficiency, one is a direct method and the other is indirect.

1.4.1 Direct Measurement of Overall Deposition Efficiency

Whether a charged particle will be deposited will depend on the resultant of the interaction of aerodynamic and electrostatic forces. The powder coating process is thus controlled by both electrostatic and aerodynamic factors such as particle size, electrode voltage, resistivity and others. The influence of some of these parameters on the deposition efficiency has been studied experimentally by various people and are listed in Table 1.2. In most of these experiments the overall deposition efficiency is measured by the amount of powder deposited on the substrate to produce a certain thickness. The results summarised in Table 1.2 indicate the significance of the variable with respect to the deposition efficiency.

Most of the experimental results were obtained (109) by moving the spray gun over the substrate to achieve uniform coating thickness. Since deposition efficiency depends on the gun position, and also the way the gun is moved relative to the surface, the results therefore show only the general trend of the effects of various parameters on deposition efficiency.

In order to examine the influence of one variable, experimental conditions have to be standardised and strictly controlled. Its realisation with respect to the numerous parameters therefore can be quite doubtful. An exercise of examining a few variables can

TABLE 1.2

SUMMARY OF RESULTS OF INVESTIGATIONS OF DEPOSITION EFFICIENCY y

Variable	General Conclusions	References
Gun voltage	For a certain coating thickness an increase in charging voltage results in increasing y. As coating film thickness increases, the effect becomes less pronounced. The smaller the feed rate, the higher the y with increasing voltage.	8,54,109,110
Powder Feed Rate	Increase in powder flow rate lowers y.	54
Substrate Size	y is dependent on the ratio of substrate size to the spray diameter but there is a limiting value.	109,110
Booth air Velocity	Both absolute booth air velocity and its direction relative to spraying direction affect y.	109
Film thickness	Generally, y decreases with increase in film thickness at a fixed charging voltage.	8,109
Spraying distance	Generally, y decreases with an increase in spraying distance	109,110
Particle Size	Spherical particles deposit more efficienty than irregularly shaped particles. y in general increases with increasing particle size.	109
Surface Resistivity.	For optimum y, surface resistivity should be in the range of $10^8 - 10^{14}$ ohm -meter.	109
Gun air velocity	y depends on the ratio between carrying air velocity at gun exit and spraying distance.	110
Electrode types	Configuration of the field determined by the shape of electrode has remarkable influence.	111

lead to difficult statistical analysis and also many experiments are required. The direct measurement of deposition efficiency although indicates the significance of various operating variables, the results may be difficult to interpret and have to be treated as just correlations.

1.4.2 Study of Particle Trajectories

This is a more fundamental approach and it involves studying the pathlines of particles. Unlike the first method which tends to be mainly experimental, the study of trajectories can be both experimental and theoretical. The trajectory of a particle into any precisely defined flow can be calculated if the entry conditions are known and the forces encountered during its flight are taken into account. The equation of motion can then be formulated. The method suffers from two drawbacks. Firstly calculation is only possible under certain conditions and assumptions have to be made. Secondly, the precision of the calculation will depend on how precisely the various forces can be described mathematically.

For the study of powder coating process, the choice of this method seems most logical for a few reasons.

(i) Instead of looking at the influence of individual variable, a package incorporating most of the variables is required for the calculation of particle trajectories. With the aid of present computer resources, it is possible to study the effect of the variables theoretically instead of performing many experiments.

(ii) A survey of the literature shows the scarcity of theoretical studies in powder coating process. The users of powder coatings are still largely restricted to rules of thumb when attempting to control the process. This also invariably involves many trial and error experiments. For example there is no powder coating literature available to estimate the effects of gun nozzle diameter, spraying distance and other operating variables. Therefore any theoretical development for the trajectory study can be used for prediction of influence of a variable.

(iii) The design of spray booth is of great importance since the transfer of charged particles to the object takes place in it. A properly designed spray enclosure aids the deposition process and collects oversprayed powder for recycling back into the feed system. There are various methods of providing a controlled air flow which serves both functions (30,113). Other innovations to improve the deposition include the use of an electric curtain of electrodes (112,114), use of 'booster' electrodes (106) and the use of 'cloud' chamber (30). All these design features serve the same purpose of attempting to 'focus' the powder onto the object either electrostatically or aerodynamically. Provided the regions of the forces and boundary conditions are defined, the trajectory method will enable theoretical study of introducing various focussing forces possible. Results derived from trajectory study can therefore be applied in the design of spray booth.

1.5 Resumé

The following steps summarise the approach in this thesis to investigate particle trajectories in electrostatic powder coating.

(1) Analysis of forces involved.

(2) Force balance to produce equation of motion

(3) Mathematical models to describe the flow and electrostatic fields and comparison with experimental data

(4) Computer program to solve the equation of motion

(5) Comparison of experimental and theoretically predicted trajectories.

To formulate the equation of motion for the calculation of particle trajectories, it is essential first to identify the forces involved in the powder coating process. Once the charged particles leave the gun nozzle, they move towards the object along the resultant of the aerodynamic and electrostatic forces and are also subjected to the gravitational force.

The air flow pattern is comparatively simple and are due to two components,

(i) the transport air used for transferring particles from the gun to the object and

(ii) the secondary air (extraction air) drawn by the dust filtration unit.

The electrostatic forces are more complex. The main deposition force is due to the applied field due to the presence of the electrode and the earthed object. As will be discussed in Chapter 4, this inter-electrode field distribution is time dependent which makes an analysis of field distribution very difficult indeed. The growth of the deposited layer creates a field of opposing strength which varies with the thickness of the layer. The presence of a cloud of ions and charged particles will also greatly influence the field distribution. The arrival of free ions causes an increase in the field strength of the deposited layer. When this field reaches the breakdown strength of the layer, a phenomenon known as 'back-ionisation' occurs (48). Emission of positive ions (for system employing negative electrode) will neutralise the charges of the oncoming powder. Hence decreasing the deposition rate.

Another important velocity component is that due to the corona or ionic wind. This is a phenomenon of air motion induced by the movement of ions. Little literature has been published on this topic mainly because of the experimental difficulties of measurements.

Clearly, with the presence of so many inter-relating forces, a complete description of the field distribution incorporating all these forces is almost impossible. Also primarily due to experimental difficulties, there is a scarcity of available literature on the study of individual force. Therefore in this study many simplifying assumptions have to be made before mathematical models can be proposed.

The equation of motion of a particle is obtained by doing a force balance. The equation is solved numerically to calculate the particle trajectories in two dimensions. The general requirements of the program include,

(i) calculation of the particle trajectories with and without the influence of electrostatic fields and

(ii) the facility to introduce the appropriate forces with the defined boundary conditions when required.

A photographic technique known as chronophotography was chosen for the experimental study of particle trajectories. Against the drawback that this method is only capable of studying dilute suspensions its two major assets are:

(i) the complete trajectory of a particle can be recorded giving rise to the particle velocity components.

(ii) the method is suitable to study time dependent process by taking photographs at regular intervals.

The experimental and theoretical results were then compared.

A further investigation was conducted to measure the air velocity profile in the experimental region. Although it is common knowledge that transport air is the predominant force in powder transfer, its study has always been overlooked in the literature but its importance acknowledged. This exercise is to verify the accuracy of the air flow field model.

The main objective of this study is to set the precedence for investigation of particle trajectories in electrostatic powder coating. Although the study has been centred mainly on the onset of the process which seems a very unsatisfactory approach, the theoretical consideration, experimental technique, and computer program have been designed to be used to describe the full industrial process.

CHAPTER 2.

TRAJECTORY CALCULATION

2.1 GENERAL

The trajectory of a particle can be calculated by solving the equation of particle motion. This method has been adopted in numerous recent studies in flow of gas - solid suspensions in topics such as designs in classifier (11) , spray dryer (12) and in aerosol filtration (13,14).

Study of charged particles trajectories in electrostatic fields has attracted attention mainly in electrostatic precipitation (18,19), aerosol collection (20, 21, 22, 23) and electrostatic powder coating (24). The fundamentals of electrohydrodynamic flow are considered by Boothroyd (17) and Soo (25). Most of these studies are only possible under ideal conditions where often potential flow and viscous flow models are used and particle inertia is neglected. Also very simple electrostatic force models are used because of difficulties in defining the boundary conditions and field configuration. Abuaf(24) has studied theoretically and experimentally the behaviour of a jet of charged polyethylene particles of 250 - 350μm in an EPC process. There was less disengagement of particles from the air stream and the presence of electric field confined the particles within the jet.

2.2 Trajectory Calculation

2.2.1 Equation of Motion

Consider flow of a suspension of particles in a fluid, under the influence of an electric field and gravity, the equation of motion is obtained by doing a force balance. The general Lagrangian vector equation is as follows:

$$\underbrace{m_p \frac{d\vec{V}_p}{dt}}_{\text{inertial force}} = \underbrace{C_D \, \pi \, \frac{d_p^2}{4} \, \frac{\rho_f}{2} \left| \vec{V}_{rel} \right| \vec{V}_{rel}}_{\text{drag force}}$$

$$+ \underbrace{\pi \frac{d_p^3}{6} \left(\rho_s - \rho_f \right) \vec{g}}_{\text{gravitational force}} + \underbrace{\Sigma F_e}_{\text{electrical field forces}} \qquad (2.1)$$

where $\vec{V}_p$ = absolute particle velocity

ρ_s = density of solid particle

ρ_f = density of fluid

$\vec{g}$ = vector of gravity constant g

C_D = drag coefficient

m_p = mass of a single particle

d_p = particle diameter

$\vec{V}_{rel}$ = relative velocity of particle

F_e = electric field force

Consider a particle at point P (x,y) in two dimensional flow field as shown in Figure 2.1,

$$\vec{V}_p = \vec{V} - \vec{V}_{rel} \qquad (2.2)$$

$$\dot{x} = \frac{dx}{dt} = U - V_{rel\ x} \qquad (2.3)$$

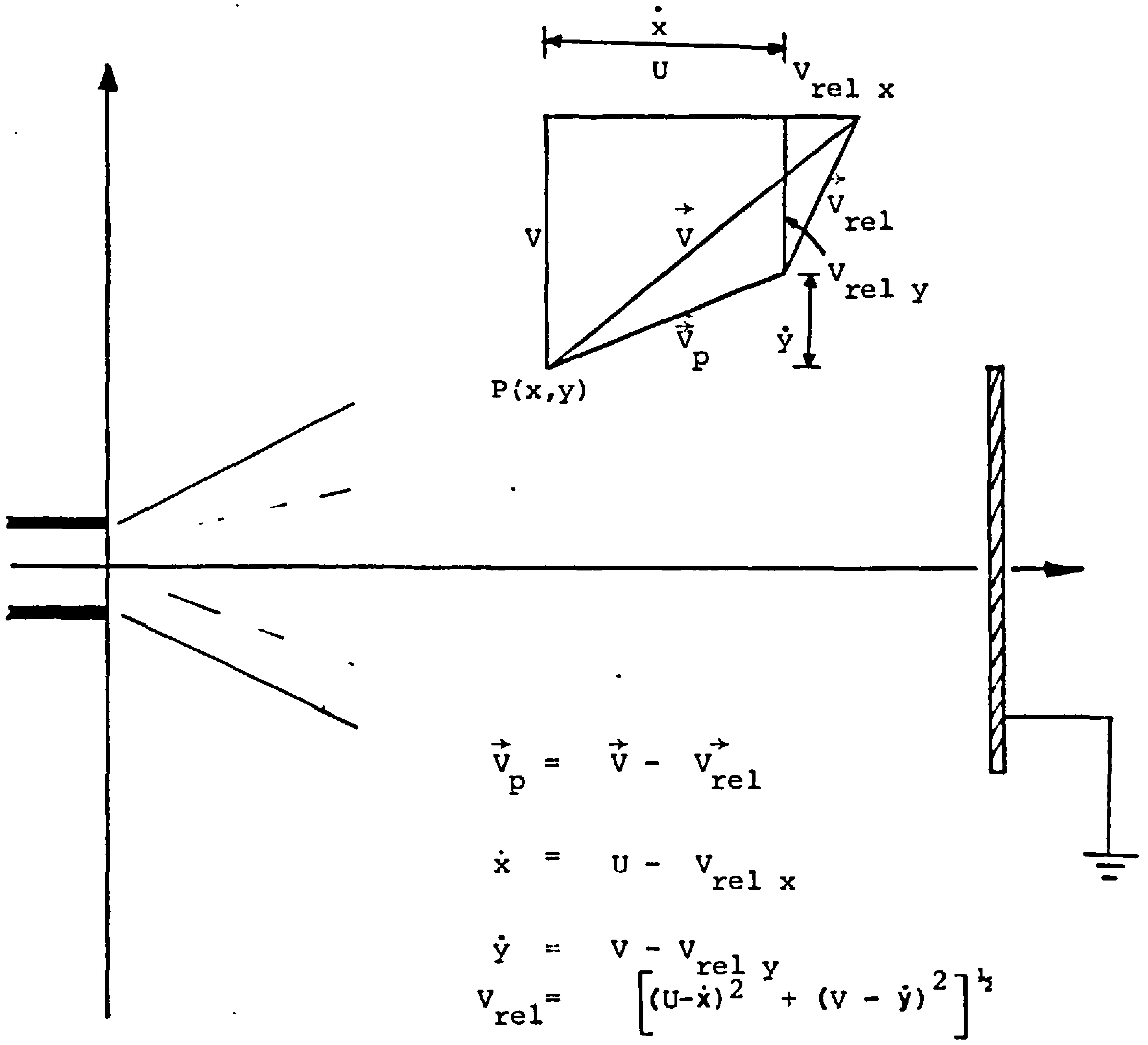

Figure 2.1 Schematic Representation of the Flow Field

$$\dot{y} = \frac{dy}{dt} = V - V_{rel\ y} \tag{2.4}$$

$$V_{rel} = \left[(U - \dot{x})^2 + (V - \dot{y})^2\right]^{\frac{1}{2}} \tag{2.5}$$

where $\vec{V}$ = fluid velocity

U = x component of fluid velocity

V = y component of fluid velocity

$V_{rel\,x} = V_{rel}$ in x direction

$V_{rel\,y} = V_{rel}$ in y direction

In order to solve equation (2.1), the following assumptions are made,

(i) particles are spherical and monosized,

(ii) the suspension is dilute and particle/particle interaction can be ignored,

(iii) each particle is considered a point mass and does not affect the flow pattern of the stream and the electric field.

2.2.2. Drag Coefficient

The drag coefficient C_D for a particle depends primarily on the Reynolds number based on the fluid particle relative velocity,

$$Re_p = \frac{\rho_s \left|\overrightarrow{V_{rel}}\right| d_p}{\mu} \qquad (2.5)$$

where μ is the fluid viscosity. Stokes determined the drag on a spherical particle by solving the Navier - Stokes equation and neglecting the inertial term. The drag coefficient for Stokes range ($Re_p < 1$) is given by,

$$C_D = 24/Re_p \qquad (2.6)$$

The drag coefficient is influenced by shape, roughness and orientation of the particle, together with the rotation and traverse motion. Torobin (15) summarised these effects by a series of correlations. Generally most of these effects are too complex to be considered and therefore drag coefficient for spherical particle is used. A series of empirical formulae of drag coefficients for spheres expressed as a function of Reynolds number is listed in References 11, 12, and 17. The formulae are for stationary flow conditions and the drag on an accelerating particle is not necessarily the same. Therefore for an irregularly shaped particle the experimental drag values and the calculated ones may vary considerably. Some of the formulae with their maximum relative errors are summarised by Kurten et al (11). One possible method of achieving high degree of accuracy is to feed the computer with the experimental drag values for the entire range of Reynolds number during the integration.

For the Reynolds number under consideration, the drag coefficient is expressed by equation (2.7) (16),

$$C_D = \left(\frac{Re_p}{24} \right) (1.0 + 0.15\, Re_p^{0.687})$$

$$\text{for } Re_p < 1000 \qquad (2.7)$$

2.2.3. Trajectory equations for $Re_p > 1$ and $Re_p < 1$

Resolving equation (2.1) in the x and y directions, for $Re_p > 1$,

$$m_p \frac{d^2x}{dt^2} = C_D \, \pi \frac{d_p^2}{4} \frac{\rho_f}{2} V_{rel} \left(U - \frac{dx}{dt}\right) + \sum F_{ex} \qquad (2.8)$$

$$m_p \frac{d^2y}{dt^2} = C_D \pi \frac{d_p^2}{4} \frac{\rho_f}{2} V_{rel} \left(V - \frac{dy}{dt} \right) + \Sigma F_{ey} - (m_p - m_f) g \qquad (2.9)$$

and for $Re_p < 1$,

$$m_p \frac{d^2x}{dt^2} = 3 \pi \mu d_p \left(U - \frac{dx}{dt} \right) + \Sigma F_{ex} \qquad (2.10)$$

$$m_p \frac{d^2y}{dt^2} = 3 \pi \mu d_p \left(V - \frac{dy}{dt} \right) + \Sigma F_{ey} - (m_p - m_f) g \qquad (2.11)$$

Equations (2.10) and (2.11) can be reduced to dimensionless form by using the following substitutions of dimensionless parameters to give equations (2.12) and (2.13).

$$\left. \begin{aligned} x^* &= \frac{x}{d} \\ y^* &= \frac{y}{d} \end{aligned} \right\} \quad \text{dimensionless co-ordinates}$$

$$\left. \begin{aligned} U^* &= \frac{U}{U_o} \\ V^* &= \frac{V}{U_o} \end{aligned} \right\} \quad \text{dimensionless velocities}$$

$$\tau = \frac{tU_o}{d} \quad \text{dimensionless time}$$

$$\left. \begin{aligned} F^*_{ex} &= \frac{\Sigma F_{ex}}{3\pi\mu d_p U_o} \\ F^*_{ey} &= \frac{\Sigma F_{ey}}{3\pi\mu d_p U_o} \\ G^* &= \frac{(m_p - m_f) g}{3\pi\mu d_p U_o} \end{aligned} \right\} \quad \text{dimensionless forces}$$

$$N_{st} = \frac{U_o \rho_s d_p^2}{18 \mu d} \quad \text{Stokes number}$$

where d = characteristic dimension of substrate
U_o = exit fluid velocity

$$N_{st} \frac{d^2 x^*}{d\tau^2} = U^* - \frac{dx^*}{d\tau} + \Sigma F_{ex}^* \tag{2.12}$$

$$N_{st} \frac{d^2 y^*}{d\tau^2} = V^* - \frac{dy^*}{d\tau} + \Sigma F_{ey}^* - G^* \tag{2.13}$$

N_{st} is an inertial parameter which accounts for mass inertia of the particles.

The range of Reynolds number considered is approximately between $Re_p = 21$ (for $d_p = 50\mu m$ and $U_o = 6.0$ m/s) and $Re_p = 80$ (for $d_p = 115\ \mu m$ and $U_o = 10.0$ m/s). Although equations (2.12) and (2.13) are strictly applicable for creeping flow (i.e. $Re_p < 0.1$) as revealed widely in literature for low Reynolds number consideration they often produce good agreement with experimental results. This is probably due to the fact that the drag coefficient of a particle is dependent on its own motion and structure. It may actually attain a drag value of similar magnitude as that of a sphere in similar flow conditions. As a first approximation, equations (2.12) and (2.13) were solved with a potential source flow solution. They were considered for two other reasons,

(i) In most powder coating processes, Stokes law is assumed valid in estimation of velocities. Solving equations (2.12) and (2.13) will show the deviation of an ideal flow condition to that representing practical spraying conditions.

(ii) Equations (2.12) and (2.13) are shown later (Chapter 4) to include a dimensionless electrostatic parameter N_{app}. Like the Stokes number N_{st} which considers the inertia, N_{app} considers the influence of electrical forces. Under ideal condition, the importance of both parameters can be compared and assessed.

Equations (2.8) and (2.9) were solved using turbulent jet theory.

2.3 Prediction Procedure

2.3.1 Method of Solution

The numerical integration is performed using a fourth-order Runge - Kutta technique (26, 27) for the set of equations for $\frac{dx}{dt}$, $\frac{dV_{ix}}{dt}$, $\frac{dy}{dt}$ and $\frac{dV_{iy}}{dt}$. V_{ix} and V_{iy} are particle velocities in the x and y directions respectively. Equations (2.8) and (2.9) can be reduced to a set of four first order differential equations:

$$\frac{dx}{dt} = V_{ix} \quad , \quad \frac{dy}{dt} = V_{iy}$$

$$\frac{d^2x}{dt^2} = \frac{dV_{ix}}{dt} = f_1 \ (x, y, V_{ix})$$

$$\frac{d^2y}{dt^2} = \frac{dV_{iy}}{dt} = f_2 \ (x,y, V_{iy}) \qquad (2.14)$$

Similarly a set of dimensionless equations can be deduced for equations (2.12) and (2.13).

To initiate the calculation, the boundary conditions required are:

$$\text{at } t = 0 \ , \quad x = x_o, \ y = y_o \ ,$$

$$V_{ix} = V_{ixo}, \quad V_{iy} = V_{iyo}$$

Equations (2.14) are solved numerically on an ICL 1904A digital computer with small constant interval of time Δt. Constant time interval is preferred as opposed to an increment in distance to allow for more trajectory points as the particle approaches the substrate. The particle generally deccelerates away from the gun nozzle mainly because of the diminishing velocity component due to the transport air. At the same time, the build up of charged particles deposited will considerably modify the velocity component due to the electrical forces. Therefore, the choice of constant time increment will increase the accuracy of the calculation and will also allow better interpretation of the influence of electrostatic forces in the viscinity of the target.

2.3.2. Description of the Computer Program

In general, the method for determining the particle trajectory is as follows;

(i) A particle is assigned specific starting position (x_o,y_o) and with some given particle velocities V_{ixo} and V_{iyo}. The values of x_o,y_o, V_{ixo} and V_{iyo} are obtained from experimental data.

(ii) The physical boundaries of the aerodynamic flow field and the electrical force fields must be defined (Section 2.4), i.e. determining the zones of influence. At a particular point in space, a series of YES/NO decisions are made to determine the nature of forces encountered. A positive response will result in the magnitude of the appropriate forces to be calculated.

(iii) The equations are then integrated simultaneously with a time interval of Δt (0.0017 sec < Δt < 0.0025 sec). The Δt value for such a numerical integration procedure must be chosen within the framework of two conflicting requirements. It must be small enough to preserve accuracy and to prevent the occurrence of numerical instability yet not too small to incur large solution times. Although rules are available to indicate the stability limits, a trial and error approach was chosen. The Δt value chosen was of the same magnitude as the flashing rate of the stroboscope used during experiments. A check of different time intervals ($\Delta t \pm 0.25 \Delta t$) showed that the maximum differences of result were within 5%. As the solution time was reasonable and the results differed slightly, it was decided that the step size was acceptable.

(iv) The new position (x_1, y_1) of the particle is checked and successive steps are calculated until the target is reached or the particle arrives at a similar target x co-ordinate.

Figure 2.2 is a simplified flow chart of the program. Several programs were produced to solve equations (2.8) - (2.9) and (2.12) - (2.13). Listing of a program is given as an example in Appendix 1 which will also include samples of computer results.

A GINO graph plotting routine (28) is incorporated to plot the predicted trajectories. The computer result print-out will include:

(i) Calculation of particle trajectories with and without the presence of electrostatic forces with subsequent plotting of two predicted trajectories on the same set of axes.

Figure 2.2 Simplified Flow Chart for Computational Scheme.

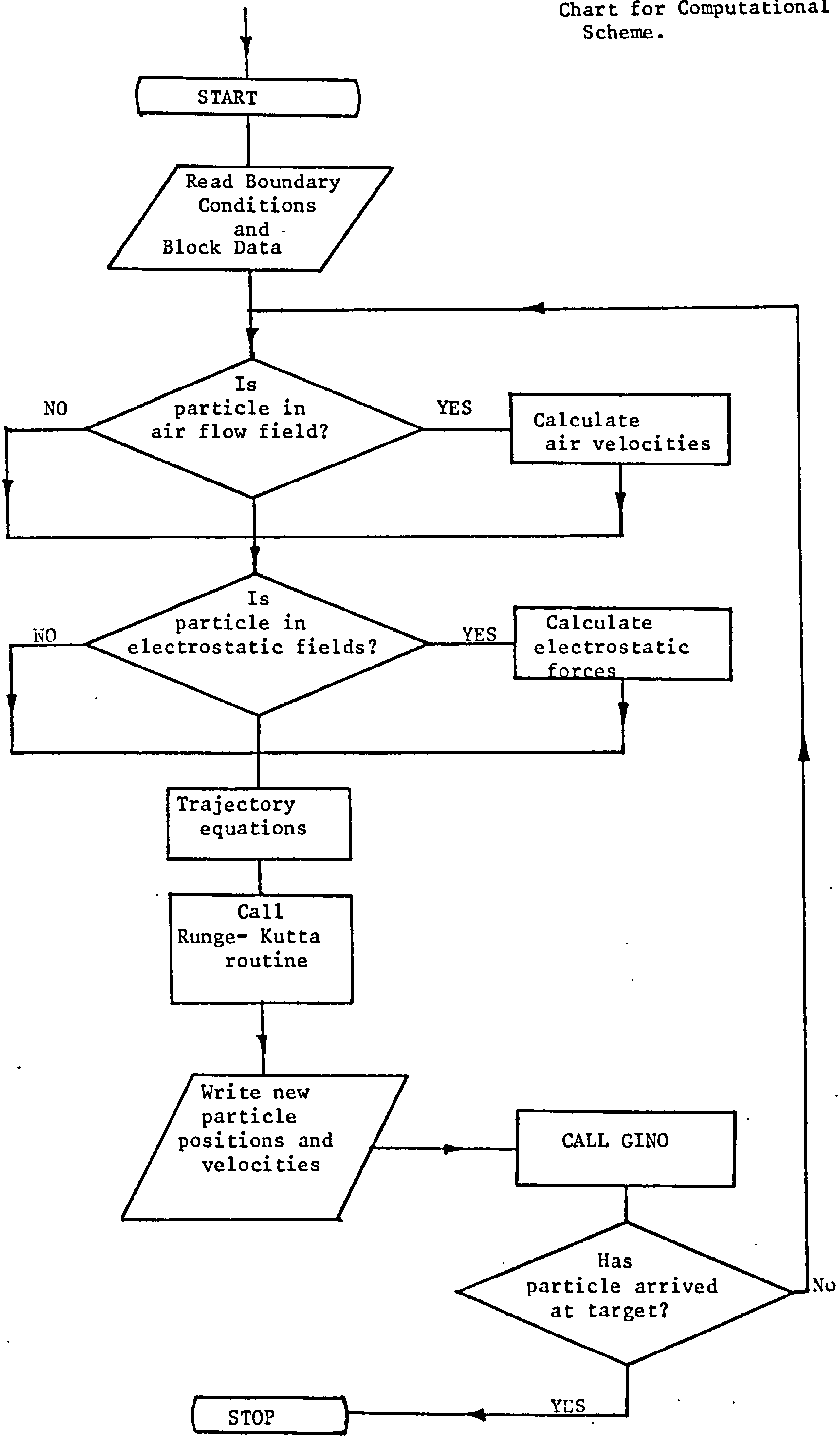

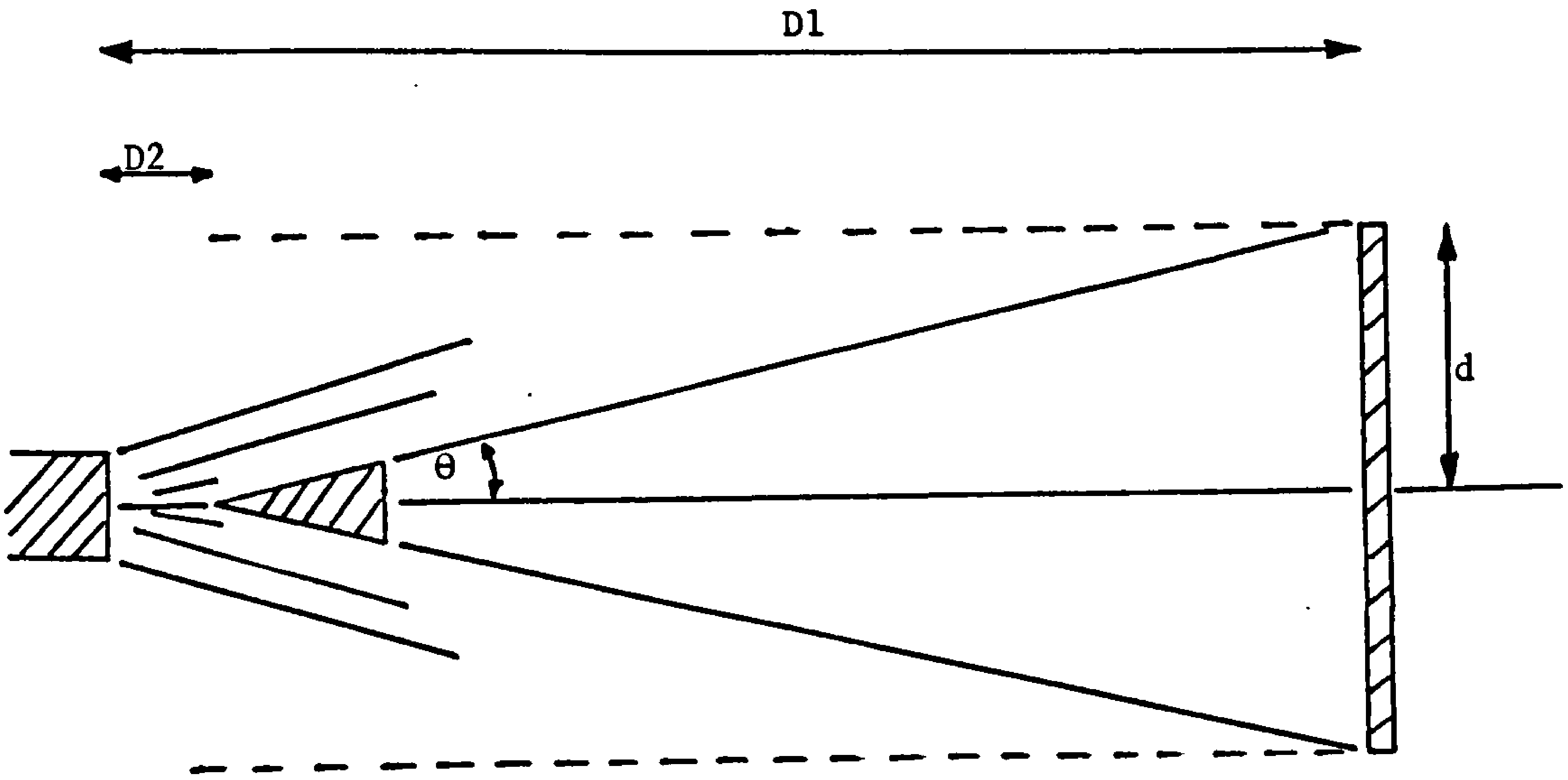

(i) image force $y = \pm d$

$$D2 \leq x \leq D1$$

(ii) Conical zone where other electrical forces are considered

$$y = \pm \tan \theta \, (x - D2)$$

$$D2 \leq x \leq D1$$

Figure 2.3 Schematic Representation of Process

(ii) the values of the various components of the trajectory equations during each step of calculation.

2.4 Aerodynamic and Electrostatic Forces Analysis

Figure 2.3 is a schematic representation with defined boundaries for the various regions of operation of the forces. The air flow field is the resultant of essentially three flows:

(1) The air jet from the spray nozzle for transporting particles to the substrate, typically of the order of 8 - 15 m/s.

(2) Flow around the object

(3) The secondary air flow due to the suction of the filtration system, normally about 0.3 m/s (30).

Figure 2.4 shows the secondary air flow round a flat plate at main stream velocity of 0.3 m/s. The flow visualisation photograph shows that ignoring the region behind the object the flow can be considered uniform laminar flow. There was no significant change in the air flow pattern for velocities from 0.3 (Re = 1140) to 0.7 (Re = 3010) m/s in the visualisation experiments. In this study, this flow is neglected due to its low magnitude. However, a uniform flow solution can be easily superimposed on the other air flows if required.

A cloud of charged particles when they emerge from the source are subjected to a number of forces analysed by Bright (31) as shown in Figure 2.5. In calculating the electric field one must consider,

(i) the applied field E_{app} produced by the electrode system (point/plane or cone/plane electrode system),

(ii) the space charge field E_{sp} due to the charged particles and the ions,

(iii) the image field of the charged particle E_i and

(iv) the field E_n due to the deposited layer.

In addition, the 'ionic' wind is generated due to interaction of (i) and (ii).

The scheme shown in Figure 2.3 using a conical geometry assumes that the earthed electrode acts as a perfect sink. It is within this conical space that the forces apart from the particle image force are experienced. The choice of geometry seems logical as the use of point/plane electrode (or cone/plane electrode) system primarily determines the shape of the applied field which

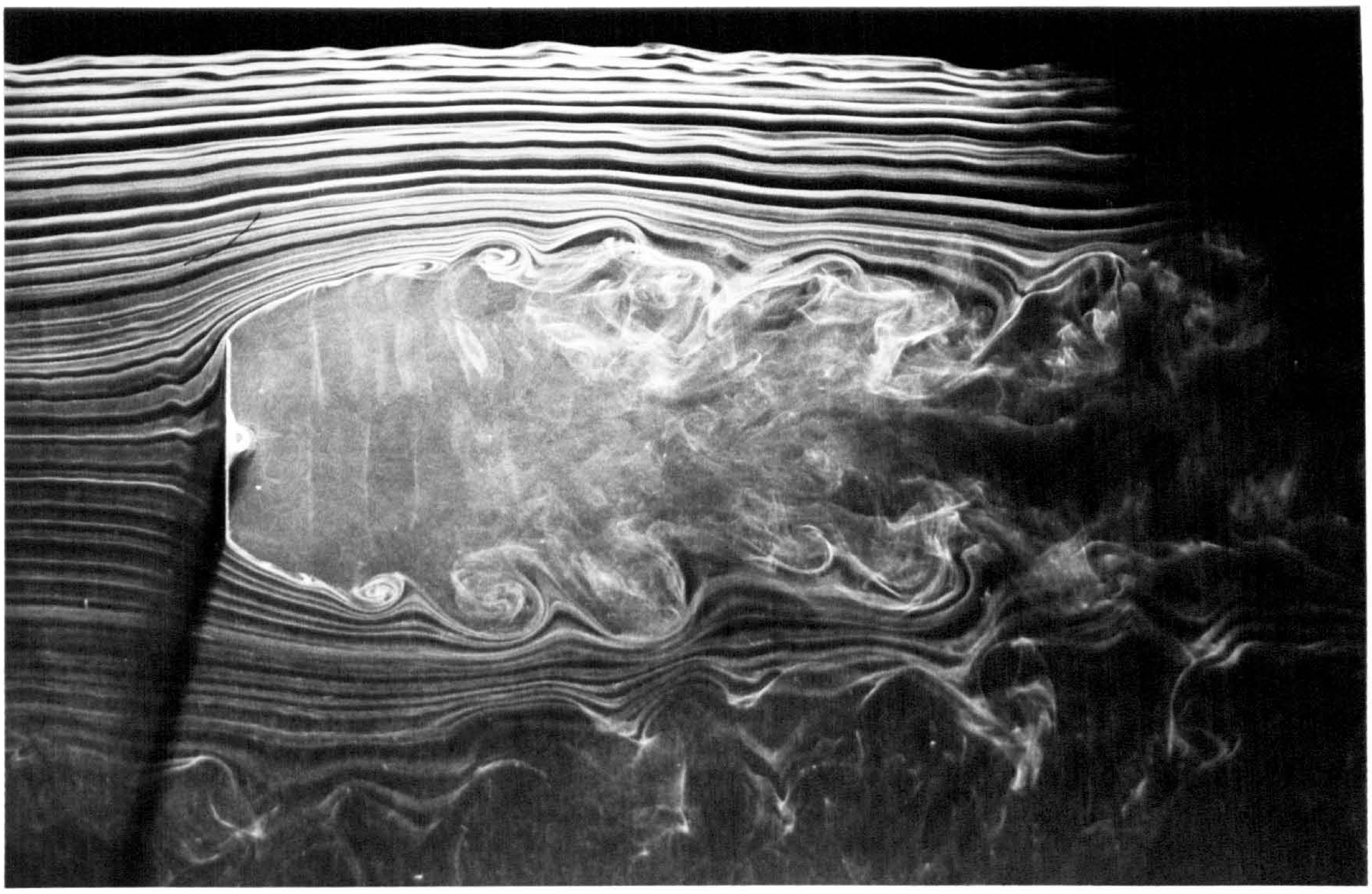

Figure 2.4 Flow Visualisation of Secondary Air Flow Due to Filtration System (Air Velcoity = 0.3 m/sec)

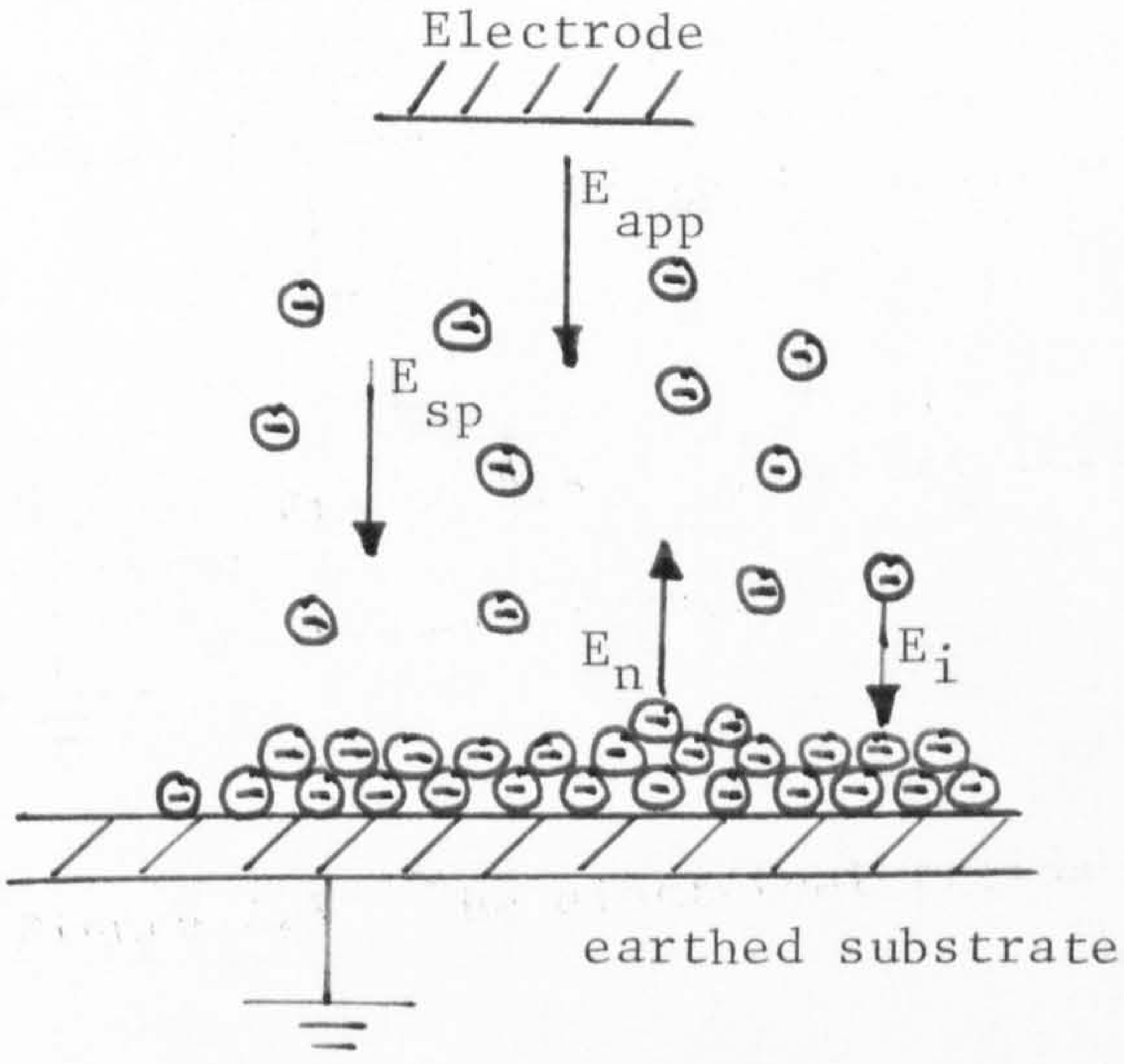

E_{app} = applied field

E_i = image field of charged particle

E_n = field due to deposited layer

E_{sp} = space charge field of charged particles and ions

Figure 2.5 The electrical fields of EPC Process is conical. The total space charge consists of the particulate space charge and the ionic space charge. Although experimentally particles emerge outside the conical region, this will not significantly modify the space charge effect because very few particles are used. Therefore the space charge essentially is only due to the ionic component. Without particles microammeter reading was 12 x 10^{-6} amp and showed a change of 1.0-1.5 x 10^{-6} amp with the introduction of charged particles. Ions generated by the electrode are assumed to stream towards the 'perfect sink' and therefore confined within the cone. Consequently the ionic wind is only felt in the cone. The field E_n due to deposited layer is neglected when using a very dilute suspension.

The image field is assumed to extend within the width of the plate electrode for simplicity since most particle trajectories examined are within this space. The magnitude of the image force only becomes important when the particle is in the vicinity of the object since the image force is inversely proportional to the square of the distance from the object. All these forces are examined in greater detail in Chapter 4. If other forces (e.g. introduction of further air flows and electrostatic fields) are to be considered similar procedure of defining the boundaries is required. The choice of using a flat plate as the coating object is for ease of experimental manipulation.

2.5 Summary

For the prediction of particle trajectories, a computational procedure is described. The method aims to combine simplicity and speed with the inclusion of the dominant influences affecting these trajectories. The complexity of the interaction of forces particularly regarding the electrical components results in requiring many simplifying assumptions. Before solving the equations the 'spheres' of influence for the forces must be defined.

CHAPTER 3

Air Flow Distribution Study on an EPS System.

3.1. Introduction

For the common EPS system, the air flow field in the spray booth is the resultant of two separate air flows, one due to the powder recovery system and one due to the powder feed system via the powder spray gun. The success of the prediction of the particle trajectories depends very much on the knowledge of the flow patterns in the different regions of the spray booth and also the accuracy of the value of drag coefficient to be used in the equations of motion. The air flow contribution due to the powder recovery unit can be neglected for reasons discussed in Chapter 2 and this chapter. Figure 3.1 shows a typical industrial hand spraying device (7) and there is great variation in design and configuration from manufacturer to manufacturer (29, 61). The spray gun used in conjunction with the powder feed system performs three basic functions,

(i) activation of the powder feed pump

(ii) activation of the high voltage power supply and

(iii) control of spray size and pattern.

The gun illustrated in figure 3.1 includes a distribution disc (also known as deflector or diffuser) which 'spreads' out the emerging powder suspension, i.e. conversion of the axial velocities to radial velocities.

Spray patterns are generally cone shaped or rod shaped and there are three common methods used industrially to adjust the size and shape of the powder spray pattern. The deflector can be either

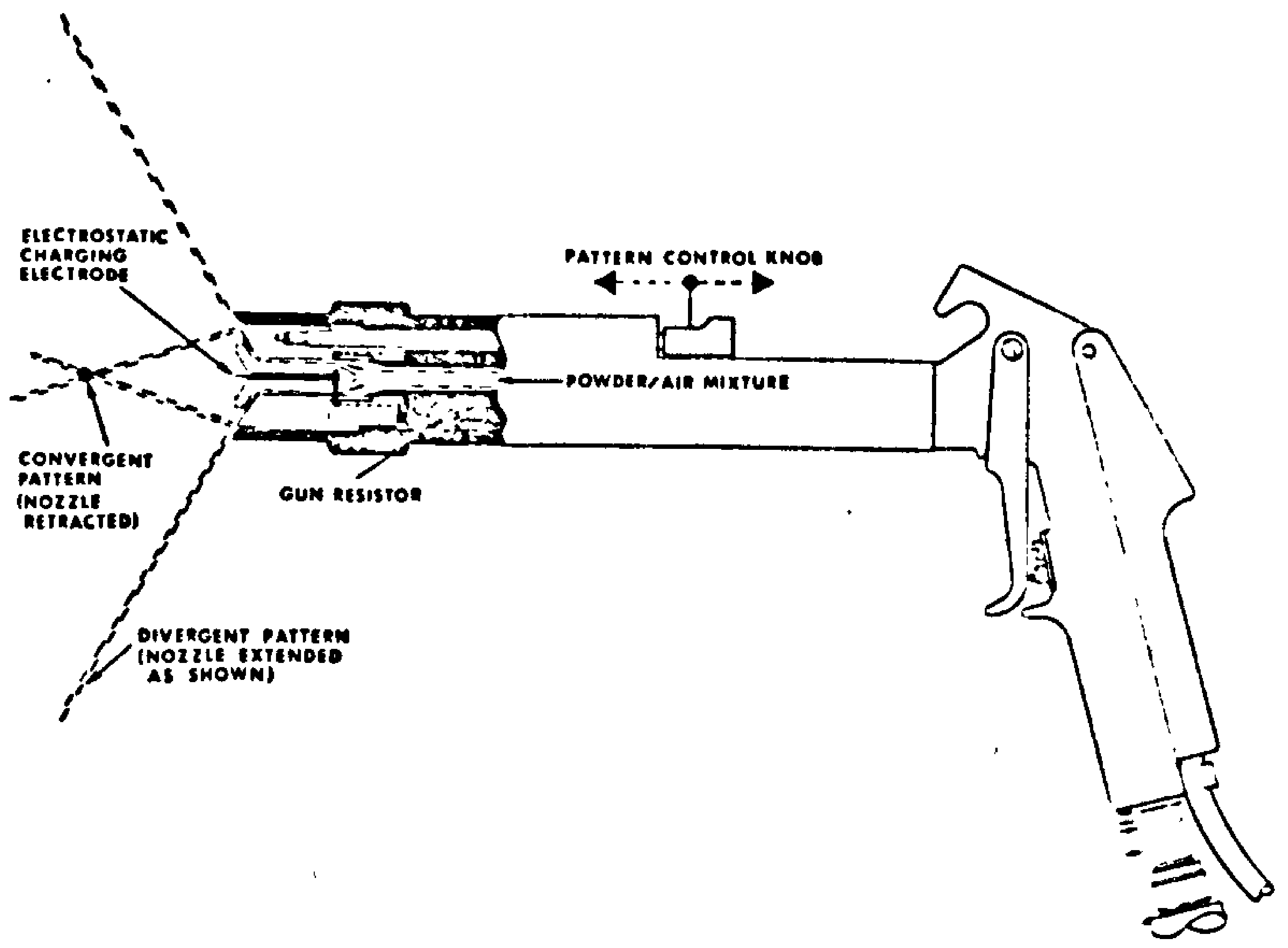

Figure 3.1 Industrial Electrostatic Powder Spray Gun

stationary or rotating type. Another method is the use of secondary air blowing tangentially or radially into the powder suspension. Complete control of the spray pattern can therefore be obtained at the gun trigger assembly using these devices.

The emerging air velocity from the spray gun ranges normally of the order of 8 - 15 m/s and is controlled by the powder delivery assembly. The powder feed system is responsible for a constant delivery of powder and the flow must not be subjected to great fluctuation during the stopping and starting of operation. There are numerous designs of powder feed system and most of them can be classified as hopper - venturi-feeder or fluidised-bed venturi - system.

The air flow pattern is not just a simple emerging jet flow from the spraying nozzle. A complete description of the resultant air flow field of an EPS process will involve the study of the following flows:

(i) an air jet impinging on the object

(ii) wake formation due to the presence of deflector at the nozzle

(iii) the co - flowing external secondary stream giving rise to a compound jet

(iv) wake development behind the object and

(v) the presence of particles creating a two phase jet.

Depending on the magnitude of the initial air jet and the secondary stream the flows listed above can make significant contribution in the deposition process. With the great variation in the design of the spraying device, theoretical and experimental studies to simulate this much varied resultant air flow would present a daunting task. Furthermore the simulation would also be hampered by a lack of theoretical development in most of the areas listed.

The approach adopted in this study therefore is where possible the literature appertaining to the study of these flows is briefly reviewed and the importance of the individual contribution is assessed accordingly with experimental or theoretical justification. The two phase jet flow despite its importance is only described briefly for two reasons. Firstly the experimental scheme for tracking of particle trajectories has the prerequisite of using a dilute suspension and secondly as shown widely in the literature, there is a scarcity of two phase turbulent jet studies.

A simplified and generalised system involving the use of an air jet issued from a nozzle with inclusion of simple electrodes is used. From the flow visualisation experiment, the theoretical model of the source type seems most appropriate. Initially air flow from a nozzle was studied theoretically and experimentally and later with the inclusion of electrodes near the nozzle. Two types of electrodes were used, a point electrode and a conical electrode. The use of a point electrode primarily is to allow assessment of contribution of particle velocity due to the aerodynamic forces and the electrical forces whilst the use of conical electrode is to simulate to some extent the action of a deflector. The shape and positioning of the electrodes are consistent with the theoretical model described in Chapter 4.

Initially there were two solutions available for velocity calculation, one of the turbulent round jet and the other a potential source flow. The theoretical calculation for velocity distribution was compared with experimental results obtained using a hot wire anemometer. The turbulent round jet solution was found to be adequate but the potential flow model led to an overestimation of air velocities.

3.2 Theory of Turbulent jet Flow.

3.2.1. The Turbulent jet Model.

The literature on single phase axially symmetrical submerged turbulent jet is voluminous and as in most studies of turbulent flows, the analytical solutions are not complete and are generally based on phenomenological theories supplemented by experimental observations. Extensive reviews of most of the studies are presented by Abramovich (6), Hinze (62) and Rajaratnam (63). For the present trajectory calculation, only the time average velocities are required and solutions pertaining to estimate these quantities are discussed. The other important quantities associated with the turbulent transport, e.g. the fluctuating velocity components and the Lagranian integral time scale are neglected. The main difficulty in solving turbulent flows invariably is to model the Reynolds stresses. The current state of art for modelling turbulent jet flows is to seek a general transport model capable of predicting accurately the full range of flows from discharge to the fully established flow region. The model must also take into account a wide range of effects like buoyancy, crossflow and surface interaction. Various models have been reported (64, 65, 66) achieving varying degree of success. Better agreement was obtained for plane jet than for round jet. These models are complex and not easily applied. The first theoretical treatment of a circular jet was given by Tollmien (67) who based his study on Prandtl's mixing length hypothesis and his solution is used for velocity calculation.

The jet model as shown in Figure 3.2 is divided into three parts : the initial region (or flow development region), the transitional region and the main region (or fully developed flow region). In the initial region as the turbulence penetrates inwards towards the jet axis there is a region of undiminished mean velocity known as the potential core. The core is surrounded by a mixing layer. Further downstream the core vanishes as the turbulence penetrates to the axis and the jet is considered fully developed. The dimensionless velocity profiles in different cross sections are self similar and this property is exhibited in a large number of turbulent jet flows. The transitional region (6) is assumed to exist for a short length and is normally neglected.

3.2.2. The Impingement of a Circular Jet.

In EPC spraying, the jet of suspended particles is directed at the object to be coated. The presence of the object will introduce further complication in the velocity calculation.

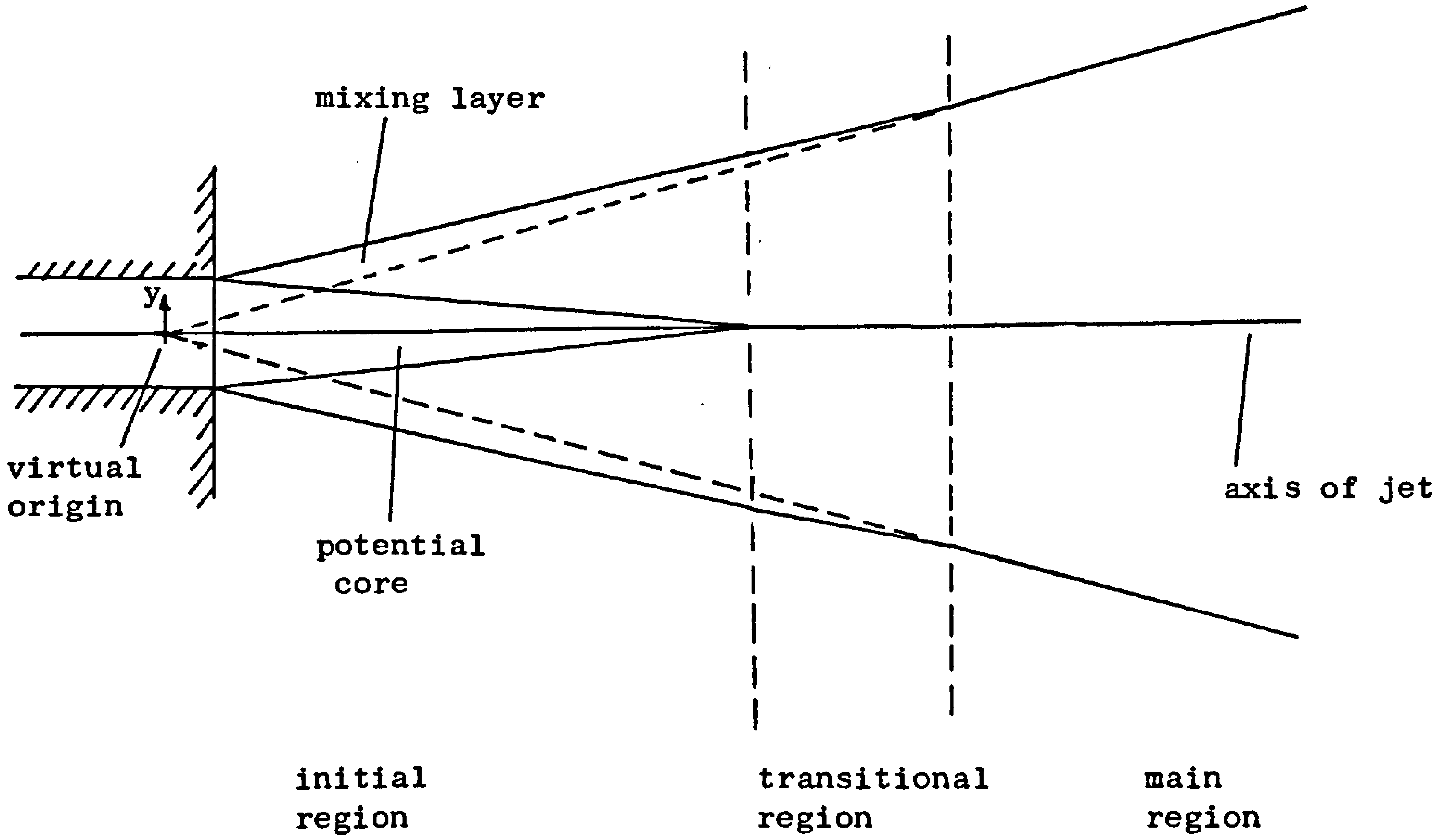

Figure 3.2 Diagram of turbulent free jet.

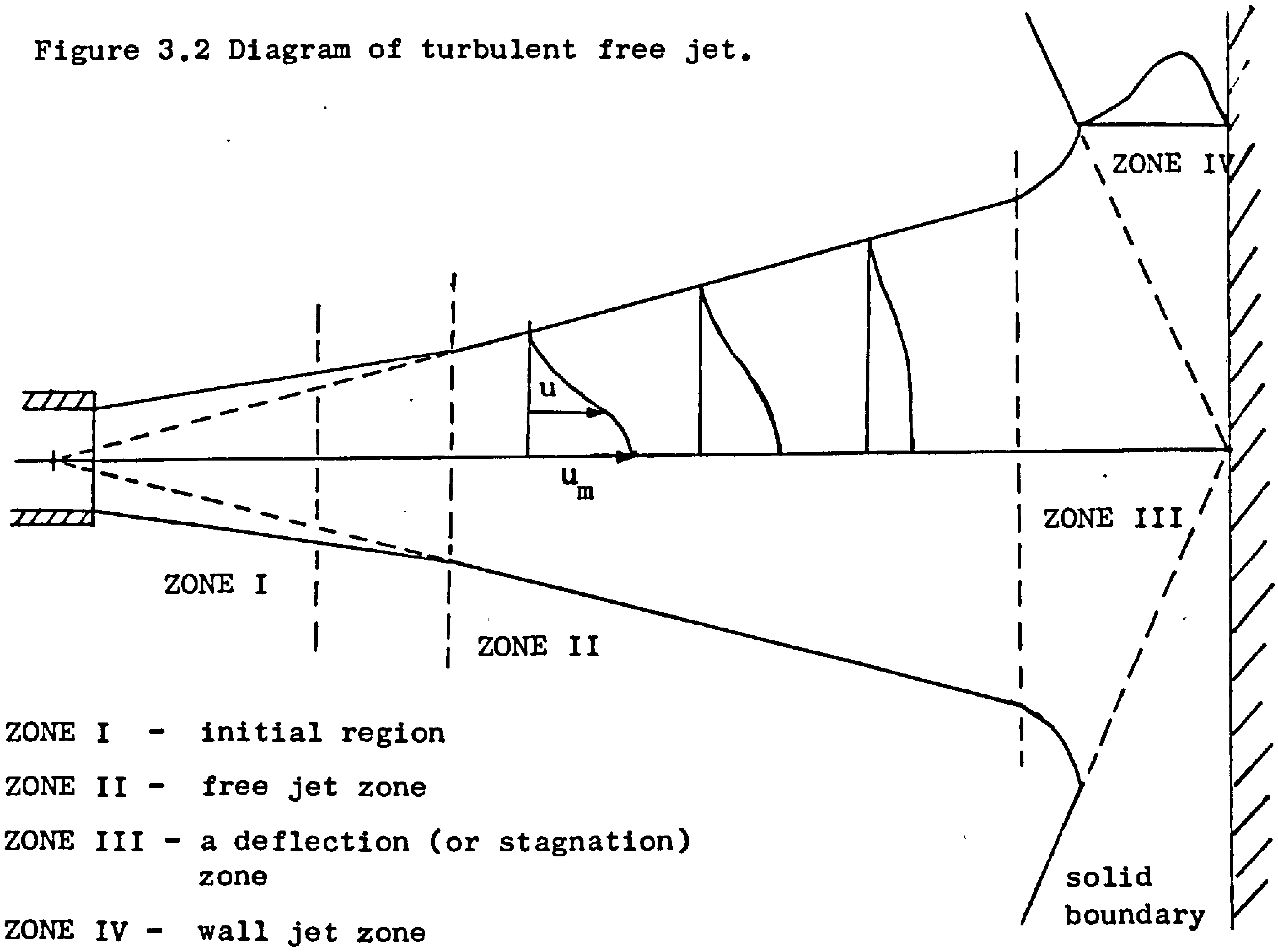

Figure 3.3 Schematic diagram of jet impinging on a flat boundary

Depending on the velocity of spraying, the size of spray and the nature of the object, this influence may be significant. Poreh (68) defined the following zones of a circular submerged jet impinging normally on a smooth boundary as shown in Figure 3.3,

ZONE I - initial region
ZONE II - free jet region
ZONE III - a deflection zone (or stagnation zone)
ZONE IV - a wall jet zone

To estimate the upstream influence of the stagnation plate on the mean flow, the free jet and impinging jet velocity distributions were compared in several experimental studies (68, 69, 70, 71). The general conclusion is that the effect of the presence of a plate is felt by a free jet when the distance from the nozzle is greater than 70 - 90% of the nozzle - plate distance for a wide range of velocities. Figure 3.4 illustrates the radial wall jet profile produced by a circular impinging jet and Figure 3.5. shows the variation of centreline velocity.

Various theoretical relationships (63, 68) are available for velocity calculation and they invariably involve evaluating some virtual quantities (e.g. virtual origin or velocity) by experimentation. However for this study and spraying under general EPS operating conditions, the wall jet development can be ignored for two reasons,

(i) Figure 3.27 shows that variation of velocity profiles of an impinging jet and air jet is negligible.

(ii) The trajectory experiments showed a dominance of electrical forces in the vicinity of the object, overcoming the effect of the jet.

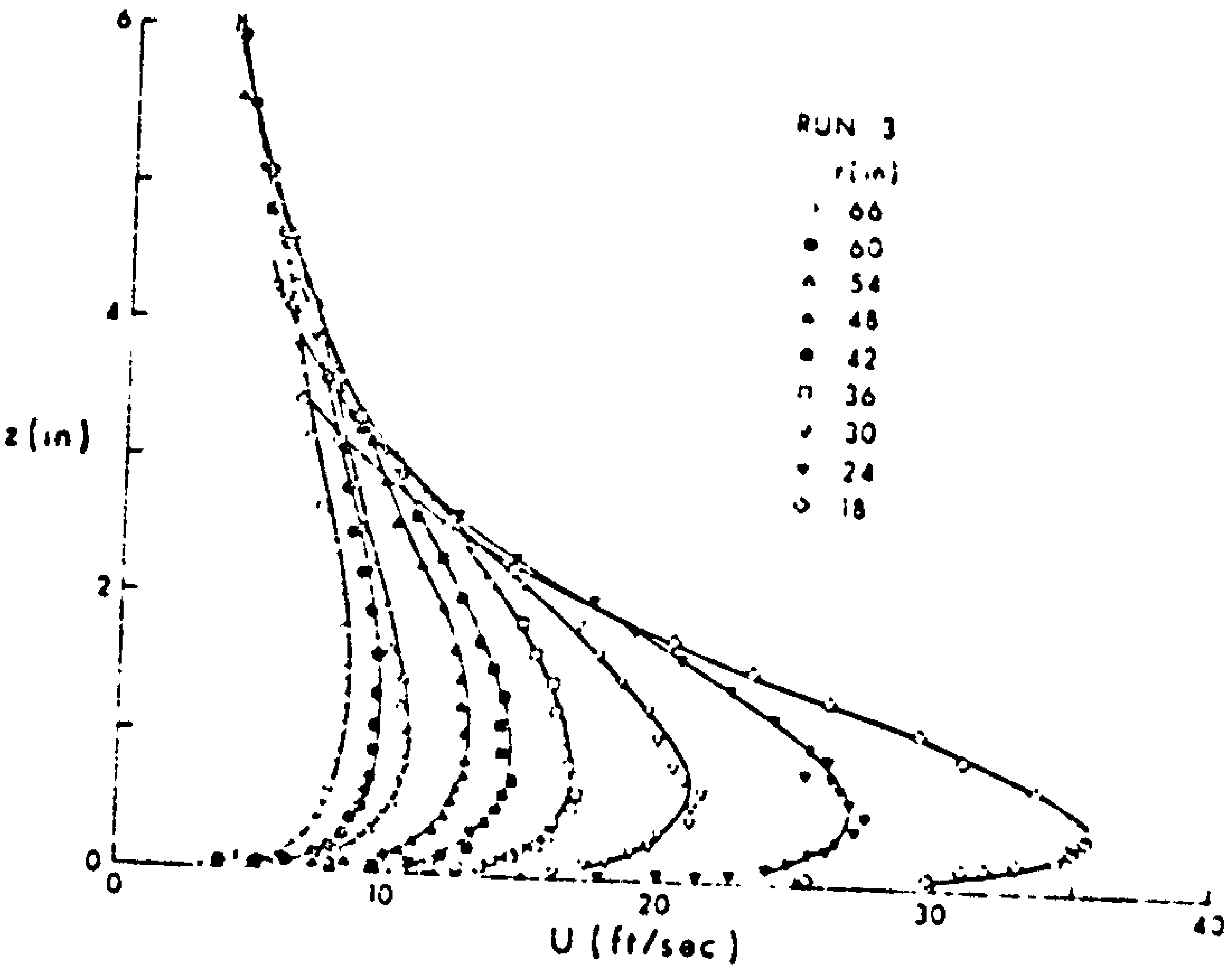

Figure 3.4 Velocity distribution in the radial wall jet produced by the impinging circular jet (reproduced from Reference 63)

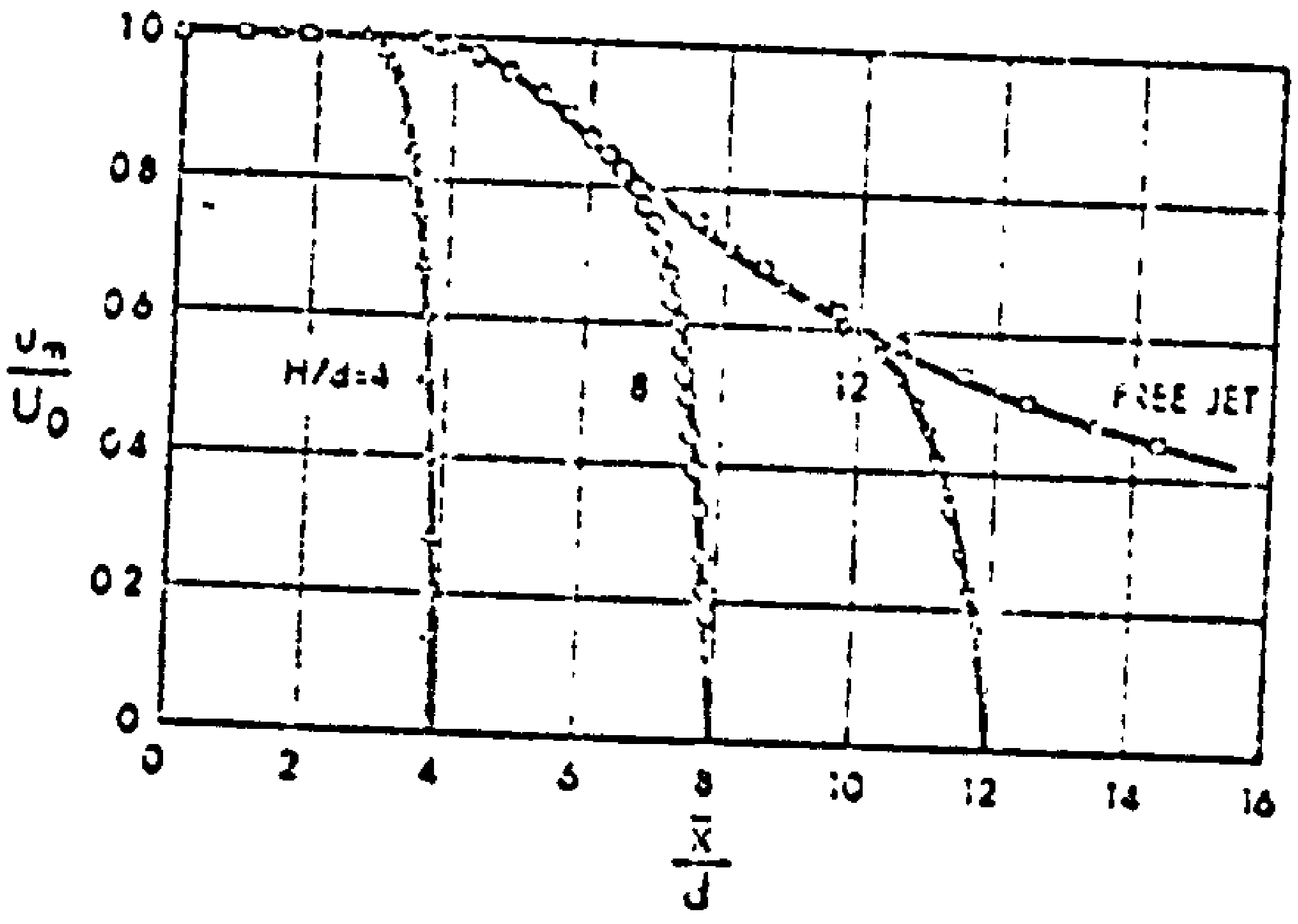

Figure 3.5 Variation of centreline velocity for circular impinging jet (reproduced from Reference 63)

3.2.3. Theory of jet for the fully developed region.

The flow can be modelled as a growing incompressible, turbulent, axisymmetric shear layer, the growth being attributed to surrounding fluid entraining into the jet. Also the flow is of boundary layer nature, i.e. the region of space in which a solution is being sought does not extend far in a transverse direction, as compared with the main flow direction and that the traverse gradients are large. Consequently it is permissible to study such problems using time mean boundary layer equations.

The continuity equation is,

$$\frac{\partial}{\partial x}(uy) + \frac{\partial}{\partial y}(vy) = 0 \tag{3.1}$$

where u, v are the velocity components of the axial and radial (x, y) components. Neglecting the axial pressure gradients results in the following simplified axial mementum equation (63),

$$u\frac{\partial u}{\partial x} + v\frac{\partial u}{\partial y} = \frac{1}{\rho y}\frac{\partial y\tau}{\partial y} \tag{3.2}$$

where τ is the shear stress. Equations (3.1) and (3.2) are the simplified equations of motion for circular jet.

To integrate the two equations involving three unknowns (u, v, τ) ,a third equation must therefore be constructed to express the turbulent shear stress in terms of the main flow parameters. There are several theories of free turbulence modelling this quantity τ and are well documented in several books (e.g. 6, 62, 72). The main ones are briefly described in this section.

Boussinesq's concept that a turbulent fluid could be treated as obeying the Newtonian viscosity law defines the effective viscosity by,

$$\mu_{eff} = \tau / \left(\frac{du}{dy}\right) \tag{3.3}$$

The first evaluation of μ_{eff} was due to Prandtl guided by the kinetic theory of gases proposed the well known 'Mixing-length' hypothesis expressed as,

$$\mu_{eff} = \rho\, l^2 \left|\frac{du}{dy}\right| \qquad (3.4)$$

Therefore,

$$\tau = \rho\, l^2 \left|\frac{du}{dy}\right| \frac{du}{dy} \qquad (3.5)$$

where l is the mixing length. Using this original concept, Tollmien proceeded to obtain the solution for an axisymmetric jet.

Other proposals imply that μ_{eff} aresubstantially uniform across sections through the boundary layer.Prandtl later proposed for at any section across a free jet,

$$\mu_{eff} = \text{const}\ \rho\ d\ (U_{max} - U_{min}) \qquad (3.6)$$

where d is some measure of the width of the jet and U_{max} and U_{min} are the maximum and minimum velocities in the cross section. Gortler solved the problem of a submerged jet using Prandtl's new theory. Taylor's physical model assumes that tangential stresses are caused by vorticity transfer and not momentum, resulting in,

$$\tau = \frac{1}{2}\, \rho\, l_w^2 \left|\frac{du}{dy}\right| \frac{du}{dy} \qquad (3.7)$$

$$\text{where } l_w = \sqrt{2}\ l$$

In addition, there is Von Karman's similarity hypothesis stating,

$$\tau = \rho \lambda^2 \left(du/_{dy}\right)^4 \Big/ \left(d^2u/_{dy^2}\right)^2 \qquad (3.8)$$

, λ being an empirical constant.

The theories of Boussinesq, Prandtl, Von Karman and Taylor are 'deductive', i.e. a hypothesis is made concerning the turbulent shear stress and with the equations of continuity and motion, velocity distributions are deduced. As against this deductive concept Reichardt proposed an inductive theory of turbulence. The theory (6, 62) although very widely used has been severely criticised for the purely phenomenological approach. For free turbulent flows, experiments have shown that the velocity distributions across the mixing zones follow closely Gaussian error or related functions. Therefore assuming that a turbulent process is a statistical process and using the 'momentum - transfer' law, Reichardt transformed the equation of motion to a form of which its solution would be a Gaussian error function. Although the theory does not give a true picture of the turbulence-flow mechanism, its wide acceptance is due to its good agreement with experimental results. But this is not really surprising since the equation of motion has been transformed artificially to agree with experimental evidence. The velocity distribution of a free jet according to Reichardt's theory is given by,

$$\frac{u}{u_m} = \exp\left[-\left(\frac{y}{\sqrt{2}\,Cm\,x}\right)^2\right] \qquad (3.9)$$

where Cm is an experimental coefficient known as the spreading coefficient.

The three most widely used turbulent jet theories are those due to Prandtl - Tollmien, Prandtl - Gortler and Reichardt and comparison with experimental results (6, 72) all three have shown good agreement. The slight discrepancy generally occurs near the jet axis and the outer region of the jet. Tollmien's solution is adopted in this study because it has been well tested and also it is physically a more realistic model as compared to Reichardt's.

3.2.4. Tollmien's solution (6, 67).

For a fully developed jet, the velocity profile at any cross section is similar and contours of equal dimensionless velocity are straight lines. If these straight lines are extended downstream the jet will have the appearance of a flow from a source — the point of intersection of the straight lines.

Let,

$$\frac{u}{u_m} = f\left(\frac{y}{x}\right) = f(\eta) \qquad (3.10)$$

where u_m is the centre line velocity in the corresponding cross section as the local velocity u. The axial velocity variation can be shown to be,

$$u_m = \frac{m}{x} \qquad (3.11).$$

where m is a dimensionless factor independent of x. The Stokes stream function ψ for an axisymmetric flow is defined as,

$$\begin{aligned} u &= \frac{1}{y}\frac{\partial\psi}{\partial y} \\ v &= -\frac{1}{y}\frac{\partial\psi}{\partial x} \end{aligned} \qquad (3.12)$$

Therefore,

$$\begin{aligned}\psi &= \int u\ y\ dy \\ &= m\ x \int f(\eta)\ \eta d\eta \\ &= m\ x\ F\ (\eta)\end{aligned} \qquad (3.13)$$

where $F\ (\eta) = \int_o^{\eta} f\ (\eta)\ \eta\, d\eta$

With equation (3.13), equation (3.12) can be rewritten as,

$$u = \frac{m}{x}\ \frac{F\ '(\eta)}{\eta} \qquad (3.14)$$

$$v = \frac{m}{x}\left(F\ '(\eta) - \frac{F\ (\eta)}{\cdot\eta}\right) \qquad (3.15)$$

By doing a momentum balance for a control surface of area 2πydx symmetrical about the axis gives,

$$2\pi\ \rho\ \ uvydx\ +\ 2\pi\ \rho\ \ d\int_{\alpha}^{y} u^2\ y\ \ dy\ = \tau\ 2\pi ydx \qquad (3.16)$$

Equation (3.16) reduces to,

$$uv\ +\ \frac{d}{dx}\int_{\alpha}^{y} u^2\ \ dy\ = \frac{\tau}{\rho} \qquad (3.17)$$

Using Prandtl mixing length hypothesis for τ with $l = Cx$ from equation (3.5),

$$uv\ +\ \frac{d}{dx}\int_{\alpha}^{y} u^2\ \ dy\ + C^2x^2\left(\frac{du}{dy}\right)^2 = 0 \qquad (3.18)$$

where C is a constant.

Combining with equations (3.14) and (3.15), equation (3.18) is transformed to,

$$C^2 \left[F''(\eta) - \frac{F'(\eta)}{\eta} \right]^2 = F(\eta)\, F'(\eta) \qquad (3.19)$$

Equation (3.19) can also be obtained by substituting the various expressions into equation (3.2).

To eliminate the constant C, a quantity φ is defined as,

$$\varphi = \frac{y}{ax} \qquad (3.20)$$

where $a = C^{2/3}$

Consequently,

$$u = \frac{m}{x} \frac{F'(\varphi)}{\varphi} \qquad (3.21)$$

$$v = \frac{am}{x} \left[F'(\varphi) - \frac{1}{\varphi} F'(\varphi) \right] \qquad (3.22)$$

$$\left[F''(\varphi) - \frac{F'(\varphi)}{\varphi} \right]^2 = F(\varphi)\, F'(\varphi) \qquad (3.23)$$

To solve the differential equation, Tollmien defined

$$F(\varphi) = e^{z} \quad , \quad z' = Z \qquad (3.24)$$

Substitution of the above definitions, equation (3.23) is reduced to a first order equation,

$$Z' = \frac{Z}{\varphi} - Z^2 - Z^{0.5} \qquad (3.25)$$

The equation was solved by Tollmien using a series expansion and the solution is of the form,

$$Z = z' = \frac{2}{\varphi} - \frac{2\sqrt{2}}{7}\varphi^{\frac{1}{2}} - \frac{1}{245}\varphi^{2} + \frac{\sqrt{2}}{1715}\varphi^{7/2} + \frac{37}{240100}\varphi^{5}$$

$$+ 0.000014\,\varphi^{13/2} \qquad (3.26)$$

Integrating equation (3.26)

$$z = \ln\frac{\varphi^2}{2} - 0.27\,\varphi^{1.5} - 0.001\,\varphi^{3} + 0.00018\,\varphi^{4.5}$$

$$+ 0.000025\,\varphi^{6} + 0.000002\,\varphi^{7.5} \qquad (3.27)$$

From equation (3.24)

$$F'(\varphi) = z' e^{z} \qquad (3.28)$$

The dimensionless velocity equations from equations (3.21) and (3.22) become,

$$\frac{u}{u_m} = \frac{F'(\varphi)}{\varphi} \qquad (3.29)$$

$$\frac{1}{a}\frac{v}{u_m} = F'(\varphi) - \frac{F(\varphi)}{\varphi} \qquad (3.30)$$

For a circular jet issuing into a stagnant environment and expanding under zero pressure gradient, since there is no external force involved, the momentum of the jet in the axial direction is preserved. The conservation of the momentum flux is expressed by,

$$\frac{d}{dx}\int_{0}^{\alpha} 2\pi y \; dy \; \rho u^{2} = 0$$

Hence,

$$2\pi\rho \int_0^{\alpha} u^2 \; y \; dy = \pi R_o^2 \; \rho \; U_o^2 = M_o \qquad (3.31)$$

where R_o is the nozzle radius and U_o is the initial velocity. Rewriting equation (3.31) with the inclusion of equation (3.20),

$$2 \int a^2 \; x^2 \varphi \; d\varphi \; u_m^2 \; \frac{F\,'(\varphi)^2}{\varphi^2} = R_o^2 \; U_o^2$$

$$\frac{u_m}{U_o} = \frac{1}{\sqrt{2} \; \frac{ax}{R_o}} \; \frac{1}{\sqrt{\int_0^{\alpha} \frac{[F\,'(\varphi)]^2}{\varphi} \, d\varphi}} \qquad (3.32)$$

The integral of equation (3.32) was evaluated to be,

$$\int_0^{\alpha} \frac{[F\,'(\varphi)]^2}{\varphi} \, d\varphi = 0.536$$

Hence,

$$\frac{u_m}{U_o} = \frac{0.96}{\frac{ax}{R_o}} \qquad (3.33)$$

Equation (3.33) is used to calculate the axial velocity distribution of a circular jet.

At the initial section of the fully developed jet, where $u_m/U_o = 1$,

$$\frac{ax}{R_o} = 0.96$$

x is the axial position from the source and to locate this virtual origin,

$$x = S_o + S$$

where S is the distance from the nozzle and S_o is the separation of the nozzle and the source pole.

Comparison of the theory and experimental data was very good (6). The value of the coefficient a from various experimental studies ranges from 0.066 to 0.27 and is found to be dependent on the ratio of the average to the maximum velocity at the nozzle, i.e. the shape of the initial velocity profile.

3.2.5. The initial region

When a jet is issued into a stagnant mass of fluid, at the nozzle the generation of shear stresses due to velocity discontinuity leads to the development of shear layer. This turbulent layer penetrates inwards into the potential core and outwards into the ambient fluid. The end of the potential core is situated where the inner boundary of the annular shear layer meets the axis of the jet. To date there are few experimental and theoretical studies concerning the developing region mainly due to the lack of application and also the flow structure is very complex. The early studies on this transition zone of flow are summarised by Albertson et al (115). Recent experimental examination of the flow structure of the initial region led to several suggestions of flow mechanisms (73, 74, 75). Crow (74) reported that within the first four diameters the core is surrounded by a wedge-shaped mixing subregion with short interfacial waves and up to ten diameters the flow is oscillatory. Other theory (75) suggested that the mixing layer consisted of an axial array of toroidal vortices. Not surprisingly therefore few theoretical studies emerged during the last few years. There is no analytical expression of time average velocities in which the mixing layer and the jet main region are smoothly joined together.

The effort is now centred on modelling of the complete jet flow instead of describing each region. For the time being, velocity calculation is restricted to using various empirical formulae. A summary of some theoretical expressions and experimental results from various investigations is presented by Abramovich (6) and Rajaratnam (63).

This zone extends for a limited distance from the jet origin. The length of the initial region L can be estimated by a number of empirical relationships, normally expressed as a function of the ratio of the velocity of surrounding fluid to the initial jet velocity ($\bar{\gamma} = U_s/U_o$), e.g.

$$\frac{L}{2R_o} = 4 + 12\bar{\gamma} \qquad (62) \qquad\qquad (3.34)$$

$$\frac{L}{R_o} = \frac{1 + \bar{\gamma}}{c(1 - \bar{\gamma})\sqrt{0.214 + 0.144\bar{\gamma}}} \qquad (6) \qquad (3.35)$$

$$\frac{R_1}{R_o} = 0.95 - 0.097\,\frac{\bar{x}}{R_o} \qquad (63) \qquad (3.36)$$

For a submerged jet ($\bar{\gamma} = 0$) L is calculated to be about four or five jet diameter long according to the above equations but experiments have disclosed much greater values. The experimental data indicated that generally the zone extends to a distance of about nine jet diameters.

The presence of a diffuser in the initial region of the jet flow from a gun therefore creates an even more complex flow picture. A survey of the literature to date shows that there is no investigation of flow past an object in the initial region of a jet flow from a nozzle. Therefore with the lack of theoretical and experimental data for this configuration, the following simplifications are made for the trajectory calculation in the initial flow development region,

(i) The velocity distribution between the nozzle and the diffuser/electrode is neglected since in the particle tracking experiments there was a temporary loss of particle trajectory in this region. The first trajectory point recorded after passing the electrode was used to initiate the calculation. This temporary loss results from either,

(a) For the rate of flashing of the stroboscope used, a particle with high initial velocity traversing a short distance would not produce sufficient number of images.

or (b) This initial region is overexposed because of the shiny appearance of the electrode and therefore the images tend to be masked.

(ii) For the region between the fully developed jet and the electrode, linear velocity relationships derived from measurements are used.

3.2.6. Compound jet

When the surrounding fluid is also in motion in the direction of the jet, the jet is known as a compound jet (6, 63). Therefore the secondary air flow and the main jet air flow in EPC can be treated as one flow entity and analysed using the compound jet theory. Alternatively as suggested previously, due to its low magnitude the secondary flow can be treated as a uniform flow to be superimposed onto the main jet flow. However if the velocity is increased further, the main jet flow undoubtedly will be affected.

Similar to the other jet flow problems various correlations are available for velocity distribution calculation. Examples are,

(i) Squire and Trouncer's expression for $U_o/U_s > 1$

$$\frac{u}{u_m} = \frac{1}{2}\left(1 + \cos\frac{\pi}{2}\,\frac{y}{b}\right) \qquad (3.37)$$

where $b = y$ for $u = \frac{u_m}{2}$

U_s = secondary air stream velocity

(ii) Forstall and Shapiro's expression for u_m,

$$\frac{u_m}{U_o - U_s} = \frac{4 + 12\ U_s/U_o}{x/2R_o} \qquad (3.38)$$

(iii) Bradbury's expression for u_m,

$$\frac{u_m}{\sqrt{U_o(U_o - U_s)}} = \frac{12.6}{\left(\frac{x}{R_o}\right)} \qquad (3.39)$$

For when $\bar{\gamma}\,(U_s/U_o) < 1$, Abramovich (6) derived the following relationships to calculate the axial velocity u_m and radius of any cross section of an axially symmetric jet.

$$c\,(\bar{x} - \bar{x}_o) = \bar{r} + \frac{0.69}{p^2}\left[\left(\bar{r}^2 + p^2\right)^{1.5} + \bar{r}^3 - p^2\right] \qquad (3.40)$$

and

$$\frac{u_m}{U_o} = \Delta\bar{U}_m = \frac{\Phi_2(\xi)}{c(\bar{x} - \bar{x}_o)}\sqrt{\frac{n_{2u} - \bar{\gamma}\,n_{1u}}{A_1\,(1 - \bar{\gamma})^2}} \qquad (3.41)$$

where $c = 0.22$ for axisymmetric jet

$\bar{x}_o = \frac{x_o}{r_o}$, $x = \frac{x}{r_o}$

$\bar{r} = \frac{r}{r_o}$

x_o and r_o are axial and radial distances for the initial cross section

$$p^2 = 8.1 \frac{(n_{2u} - \bar{\gamma} n_{1u})}{\bar{\gamma}^2}$$

$$n_{1u} = \int_0^1 \frac{\rho_o u_o}{\rho_{om} U_{om}} \frac{dF_o}{F_o}$$

$$n_{2u} = \int_o^1 \frac{\rho_o U_o^2}{\rho_{om} U_{om}^2} \frac{dF_o}{F_o}$$

$A_1 = 0.258$

U_{om} is the axial velocity at the initial cross section of area F_o

$$\Phi_2(\xi) = \frac{(9.76 + 2\xi)(1 + \sqrt{1 + \xi}) - 8}{4.16\sqrt{1 + \xi}(1 + \sqrt{1 + \xi})}$$

$$\xi = 1.92 \frac{\mu}{\Delta \bar{U}_m} \quad , \quad \mu = \frac{\bar{\gamma}}{1 - \bar{\gamma}}$$

For calculation, a graphical plot of the auxiliary function $\Phi_2(\xi)$ is available. Curves for various values of $\bar{\gamma}$ calculated from the above relationships are given in Figure 3.6. In the present trajectory investigation because of the low magnitude of $\bar{\gamma}$ ($\bar{\gamma} = 0.03$ for U_s = 0.3 m/s and U_o = 8.0 m/s), as shown in Figure 3.6 the compound jet can be treated as a simple submerged jet ($\bar{\gamma} = 0$). In a typical powder coating process (U_o of 8 - 15 m/s) the velocity of the secondary stream must be greater than about 1.5 - 3.0 m/s to significantly modify the air flow from the spray gun.

3.3 The two phase turbulent jet.

When a second phase is introduced into a fluid changes in flow characteristics occur. The theoretical prediction of the changes are

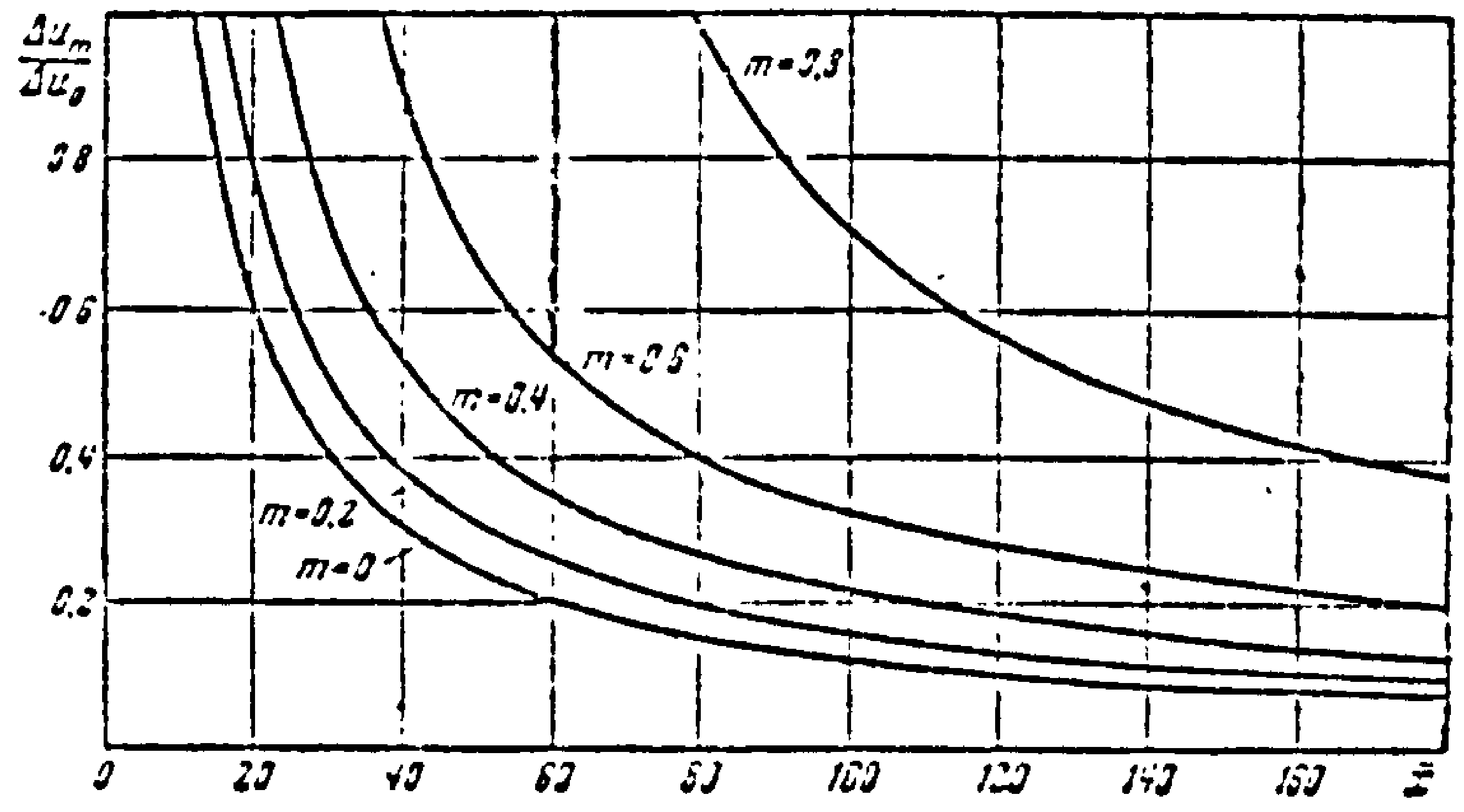

Figure 3.6 Variation of the dimensionless axial velocity in an axisymmetric jet for $m < 1$ ($\bar{\gamma} = m$).

hindered since for the simpler case of one phase flow there are no complete solutions and the interaction between the turbulence of the mainstream and the dispersed phases presents a problem of great complexity. Also until the recent availability of laser Doppler anemometry system there is a lack of suitable measurement technique leading to a scarcity of experimental data. Although the applications of two phase jet are numerous, as reflected in the literature there is a lack of basic understanding of the underlying phenomena. Soo (25) and Boothroyd (17) summarised various early experimental and theoretical studies in multiphase flow systems. However there is no general theory that can be applied directly to solve the flow characteristics of a two phase turbulent jet. In EPS system which involve the use of 'heavily-loaded' jets, the effect of particle concentration on flow is critical. Although in the current analysis, the solids loading is sufficiently low that particle fluid interaction can be discounted, a survey of the current state of art in two phase turbulent round jet is included, with emphasis on the experimental studies. Table 3.1 lists the very few experimental investigations of two phase axisymmetric jet. The indication is that further extensive investigations are required to assess the loading effects on turbulent jet flow .

3.3.1 Experimental studies

(a) Lightly loaded jets

Most of the published literature on two phase turbulent jet studies centre on lightly loaded jets. Popper et al (80) presented an extensive experimental study of the effect of oil droplets ($d_p < 50$ μm) dispersed in an axially symmetric jet. The particle velocity was measured for volume concentration of oil in air of 10^{-6}, using a laser Doppler anemometer. The experimental results are in good agreement with other studies with the following main conclusions:

(i) Two phase jets are narrower that single phase jet under similar conditions.

(ii) The velocity distributions of the droplets are self similar with a lower spreading coefficient C_m of equation (3.9) of 0.050 - 0.058. For a single phase jet C_m normally is of the range $0.071 < C_m < 0.080$.

(iii) Near the nozzle the particle velocities are lower than the free jet velocity whilst in the fully developed jet region ($x/2R_o > 8$) the rate of decay of the axial particle velocity is lower than the corresponding air jet.

Goldschmidt et al (81) and Hestroni et al (82) studied lightly loaded jets using the hot wire anemometry. The particle loading ratio λ_o is the ratio of the mass density of the particle cloud at the

Table 3.1 Experimental studies of two phase turbulent round jet

Author	Suspension	Particle Loading λ_o	Particle Size (μm)	Experimental Technique
Popper et al (80)	oil/air	10^{-3}	<50	laser Doppler anemometer
Hetsroni, Sokolov (82)	oil/air	$2 - 8 \times 10^{-3}$	13	hot wire anemometer
Abuaf, Gutfinger (83)	polyethylene particles/air	very low	250 - 417	photography
Shinichi Yuu et al (76)	fly ash/air	$0.7 - 2 \times 10^{-3}$	15 - 20	isokinetic sampling
McComb, Salih (84)	tungsten particles /air		6	laser Doppler anemometer
Laats (86)	shale/air	0 - 1	20 - 60	isokinetic sampling
Laats, Frishman, (87, 88)	corundum/air	0 - 1.4	17 - 80	isokinetic sampling
Singh, S (116)	epoxy particles /air		15 - 70	laser Doppler anemometry

nozzle to the density of the suspending fluid. For lightly loaded jets, $\lambda_o \ll 1.0$. Their results have been treated with caution as the impingement of droplets on the hot wire probe could lead to erroneous data. Hetsroni and Sokolov (82) measured the velocity distributions for the time average and fluctuating components, and the probability density functions (volumetric concentration of $3.08 \times 10^{-6} - 7.79 \times 10^{-6}$). They found that the droplets ($d_p \sim 13\mu m$) flux distribution can be described by a Gaussian curve with a spreading coefficient of 0.05. Similarly a Gaussian curve can also represent the time average velocity profile of the two phase jet with spreading coefficients of 0.05 - 0.06. The magnitude of the coefficients is similar to results obtained by Popper and his colleagues (80). Also in the range of investigation the coefficient is different from that for a single phase jet and is inversely proportional to the droplet flux. They further concluded that the droplets cause suppression of turbulence in the dissipation range. In the two phase round jet the centre line velocity decreases as $\left(\frac{x}{2R_o}\right)^{-1.2}$ to $\left(\frac{x}{2R_o}\right)^{-1.3}$ instead of $\left(\frac{x}{2R_o}\right)^{-1}$ for single phase jet. For lightly loaded jet, the fluid mean velocity field is sensibly unchanged from that of a clean jet. Also the measured particle mean mass flux profiles generally attain a self similar form.

Abuaf et al (83) examined large particles of 250 - 400 μm in air jet using photographic technique and found that their motion was almost unaffected by the main fluid. The experimental results are essentially in agreement with other studies.

For small particle, the main concern is the study of turbulent diffusion mechanism of particle in the jet. Shinichi et al (76) studied the diffusion experimentally and theoretically using a very dilute suspension of 15 - 20 μm diameter particles (volumetric concentration of 4.0×10^{-7} to 2.0×10^{-6}). The fluid properties of a single phase jet would apply to the two phase jet. The particle inertia and the fluid large eddies, which are expressed by the Stokes number and the Lagrangian integral time scale respectively, play an important role in the diffusion transport mechanism. The results indicate that the particle diffusivity decreases with the increase of particle inertia.

Mc Comb et al (84, 85) presented a theory which describes the diffusion of tracer particles in a turbulent jet. The motion is characterised by a dimensionless perturbation parameter $\varepsilon = \frac{A U_o \tau}{d} \left(\frac{d}{x}\right)^2$. τ is the particle momentum relaxation time, d is the diameter of the jet nozzle with U_o the nozzle velocity and A is a constant with a value of 7.02 for a round free jet. The relaxation time is a function of density and size of the particle and the viscosity of the medium. The mean particle concentration and particle velocity profile can be described using power series in ε. The limit $\varepsilon \rightarrow 0$ represents the case of infinitesimal particles which move as part of the fluid. The study was extended to $\varepsilon = 0.3$ using the laser Doppler anemometer ($d_p \sim 6$ μm) and there was good agreement of theoretical and experimental results.

(b) <u>The heavily loaded jets.</u>

Laats and Frishman (86, 87, 88) presented most of the very few studies of heavily loaded jets for loading ratio of up to 1.4 with 20 - 80 μm diameter particles. The experimental results show that the axial velocity decay is smaller and the velocity profiles are narrower than for a single phase jet at the corresponding point. The main findings are confirmed by the results of Popper et al (80). Also the decays are proportional to the loading ratio.

Melville and Bray (89) using the experimental results of Laats and Frishman obtained good correlations of the mean fluid velocity and particle mass flux fields in terms of initial particle loading by using dimensional analysis and physical arguments. The two phase jet is divided into two regions : a near field region in which essentially there is no net momentum transfer between the phases and a far field region in which all the momentum has been transferred to the suspending fluid. For the near field region exponential functions of initial particle loading is used to correlate with the experimental data of the corresponding single phase jet. A power law function is used for the far field region. The dynamics of the fluid phase of the far field region are equivalent to that of a single phase jet with a virtual origin, the position of which is dependent on the particle size and the initial particle loading. The dependence of the virtual origin on loading ratio is well predicted whilst the dependence on particle size is less certain.

3.3.2 Models of two phase jet.

To date there are only a few attempts to model the two phase turbulent jets - to study the effects of the particles on fluid turbulence and the reciprocal response of the particles to turbulence. Danon et al (90) solved the mean flow equations with first order closure scheme using a turbulence energy model to calculate the eddy viscosity. Additional dissipation was hypothesised as caused by the relative velocity between the particle and the fluid. The predicted reduction in the turbulence energy level was low when compared with experimental results. They concluded that the particles bring about a change in the structure of turbulence affecting the production and dissipation of turbulent energy. By relating and adjusting the length scale which represented the turbulence structure to the particle concentration, good agreement was obtained.

Melville and Bray (91) presented the most comprehensive study so far with a review of the previous modelling attempts. Instead of considering the suspension as a single inhomogeneous continuum, the concept used is to treat the suspension as two interpenetrating continua maintaining their own identities. A set of differential equations with a first order closure scheme was used with various models to describe the transport coefficients, i.e. the eddy viscosity and eddy diffusivity of both fluids. There were good agreement for the mean velocity and the mean flux of particles data.

3.3.3 Two phase jet in EPS

For EPS, the general requirement for a good spray gun design is smooth powder delivery of 0.002 kg/s. However most commercially available hand guns are generally capable of a delivery rate of 0 - 0.01 kg/s (29). A survey of the powder delivery rate and air volumetric flow rate of various makes of commercial guns (29) shows maximum loading ratio of 2 - 4.4. The powder spraying is furthermore complicated by the presence of diffusers of differing shapes and sizes with the diffusers either stationary or rotating. Several immediate problems are encountered when applying two phase jet knowledge to EPS.

(i) The two phase jet results obtained by the various investigators to date are quite inconclusive. With the loading ratio shown to be the critical factor, its effect on the main flow is not yet fully realised.

(ii) The loading ratio for EPC is considerably more than what has been investigated so far.

(iii) The results so far are for simple jet geometry without the presence of diffuser of any kind in the jet stream.

Therefore further extensive investigations with emphasis on collecting experimental data are required before assessment can be made about the loading effect on the flow characteristics in EPC spraying.

The only known experimental study of particle velocity distribution of powder spraying in EPC process is that of Singh (116). Using epoxy powder of 15 - 70 μm and a powder feed rate of 2 gm/s he produced velocity profiles very similar to those of Popper et al (80). This suggests that despite the high loading ratio, the approach of Popper may be adopted, i.e. the particle velocity distribution can be described by the single phase jet equation with modification of the spreading coefficient and location of different virtual origin. Therefore if the self similar property can be established for two phase flow from a spray gun, this approach for the time being may be adequate for prediction of particle velocity distribution.

3.4 Potential flow solution

Another solution which seems appropriate to describe the flow from a spray gun is to use an ideal potential flow of some source type. To solve equations (2.12) and (2.13), the potential flow model adopted is as shown in Figure 3.7, consisting of

(a) a potential source flow and

(b) potential flow past a vertical flat plate

Near the object, the source flow velocity profile is assumed to approach that of streaming flow. This solution was the first to be used in the trajectory calculation because of its simplicity.

3.4.1. Flow past a vertical plate

The solution for potential flow normal to a vertical plate (92)

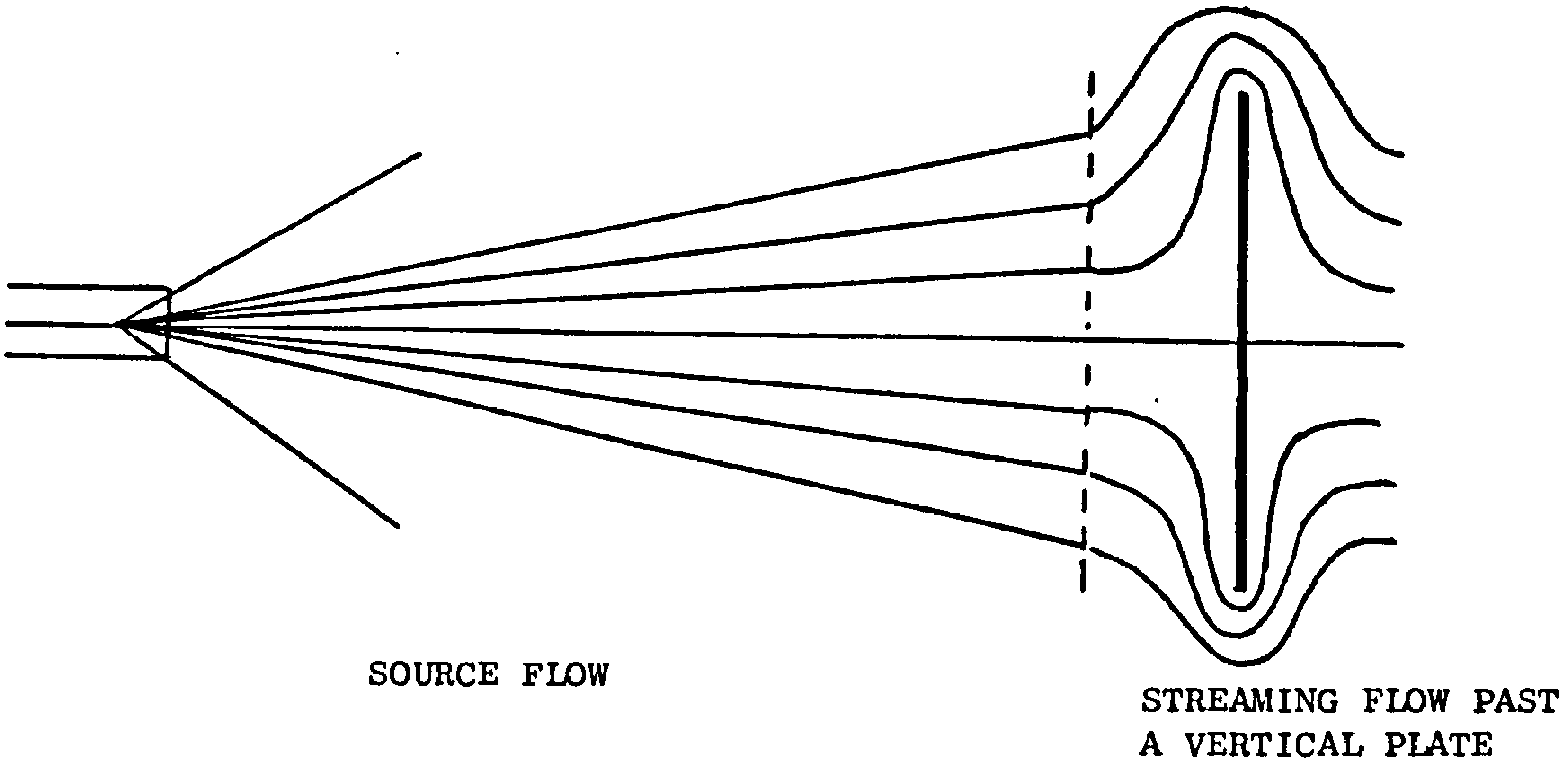

Figure 3.7 Potential flow model

is derived using conformal transformation technique - an analytical method of determining patterns of irrotational flow. The succesive transformations leading to the final solution are shown in Figure 3.9.

First a set of elliptic coordinates (ξ , η , z) as shown in Figure 3.8 are defined as follows. Using the transformation,

$$Z = C \cosh \zeta \qquad (3.42)$$

where Z and ζ are complex variables given by,

$$Z = x + iy \qquad \zeta = \xi + i\eta$$

the following relationships are defined,

$$x = C \cdot \cosh \xi \cos \eta \qquad (3.43)$$

$$y = C \sinh \xi \sin \eta \qquad (3.44)$$

$$\frac{x^2}{C^2 \cosh^2 \xi} + \frac{y^2}{C^2 \sinh^2 \xi} = 1 \qquad (3.45)$$

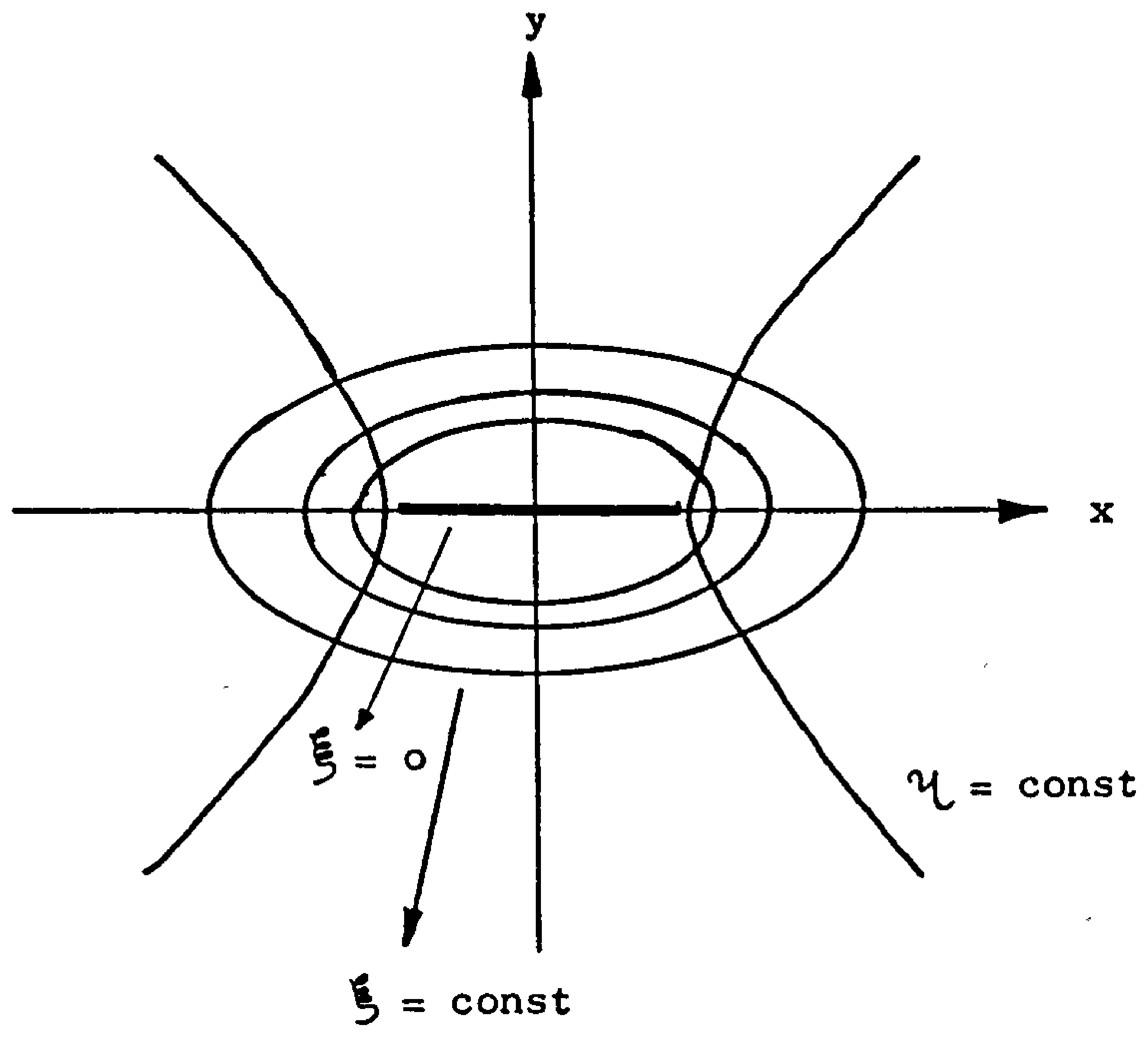

Figure 3.8 Elliptic co-ordinates ξ, η, z

$$\frac{x^2}{C^2\cos^2\eta} - \frac{y^2}{C^2\sin^2\eta} = 1 \qquad (3.46)$$

$$a = C\cosh\xi_o \qquad (3.47)$$

$$b = C\sinh\xi_o \qquad (3.48)$$

$$a^2 - b^2 = C^2 \qquad (3.49)$$

The curves of constant values of ξ are ellipses and are confocal with a distance of 2C between the foci. For constant values of η, the curves are hyperbolas confocal with one another and with the ellipses. $\xi = \xi_o$ corresponds to an ellipse in the Z plane with semi major axis C cosh ξ_o and semi minor axis C sinh ξ_o.

For streaming flow past a cylinder, the complex potential W is,

$$W = U\left(Z_1 + \frac{a^2}{Z_1}\right) \qquad (3.50)$$

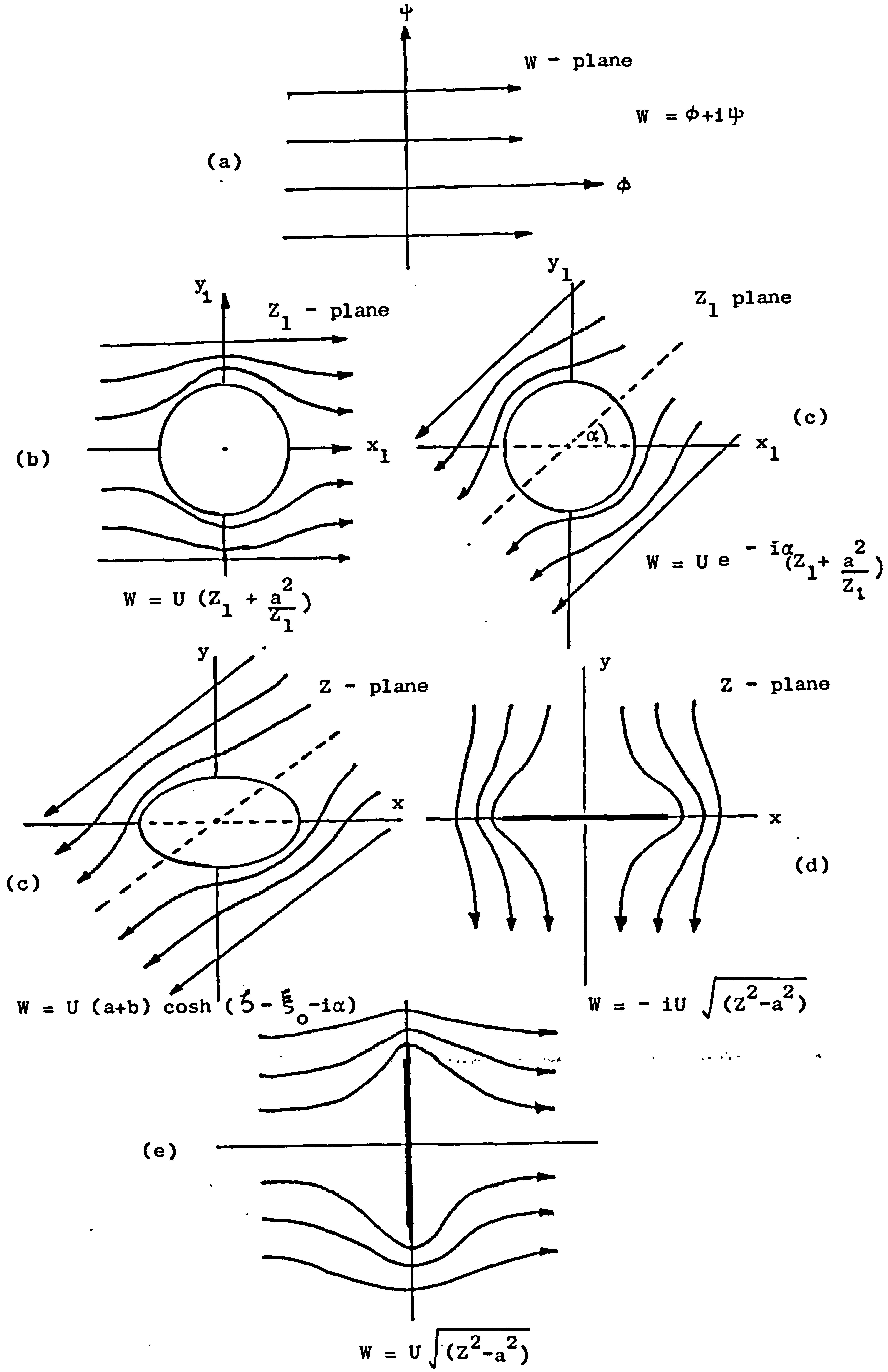

Figure 3.9 Flow normal to a vertical wall

with U the main stream velocity and $W = \Phi + i\Psi$, where ϕ is the velocity potential and Ψ is the stream function. If the stream makes an angle α with the real axis the complex potential in the Z_1 plane is,

$$W = U\left(Z_1 e^{-i\alpha} + \frac{(a+b)^2 e^{i\alpha}}{4Z_1} \right) \qquad (3.51)$$

With the Joukowski transformation,

$$Z = Z_1 + \frac{C^2}{4Z_1} \qquad (3.52)$$

concentric circles in the Z_1 plane map into confocal ellipses in the Z plane.

The inverse of the transformation,

$$Z_1 = \frac{1}{2}\left(Z + \sqrt{Z^2 - C^2}\right) \qquad (3.53)$$

with $C^2 = a^2 - b^2$ therefore maps the region outside the ellipse of semi-axes a, b in the Z plane on the region outside the circle of radius $\frac{1}{2}(a+b)$ in the Z_1 plane. Substituting equation (3.53) into equation (3.51), results in,

$$W = \frac{1}{2} U (a+b)\left[\frac{e^{-i\alpha}\left(Z + \sqrt{(Z^2 - C^2)}\right)}{a+b} + \frac{e^{i\alpha}\left(Z - \sqrt{(Z^2 - C^2)}\right)}{a-b} \right]$$

$$(3.54)$$

Further substitution with expressions for elliptic coordinates gives,

$$W = U(a+b)\cosh(\zeta - \xi_o - i\alpha) \qquad (3.55)$$

Equation (3.55) is the complex potential for flow past an ellipse in elliptical coordinates. If b→0, the ellipse becomes a plate with

$\xi_0 = 0$. Therefore equation (3.55) becomes

$$W = U\, a \cosh (\zeta - i\alpha)$$

$$= U\,(Z \cos\alpha - i\sqrt{(Z^2 - a^2)}\,\sin\alpha) \qquad (3.56)$$

When the stream is normal to the plate ($\alpha = 90^\circ$) and therefore,

$$W = -\,i\,U\sqrt{(Z^2 - a^2)} \qquad (3.57)$$

To obtain horizontal flow normal to a vertical plate the Z plane is rotated through 90° by using the transformation,

$$Z' = i\,Z \qquad (3.58)$$

Using the definitions

$$V = \frac{-d\psi}{dx} \quad , \quad u = \frac{d\psi}{dy}$$

and by expanding the right side and equating the real and imaginary parts, the following equations for calculation of the velocity components u and v are obtained,

$$U^4\, x^2 y^2 - \psi^4 = \psi^2\, U^2\,(x^2 - y^2 + a^2) \qquad (3.59)$$

$$u = \frac{y\,U^2\,(\psi^2 - U^2\,y^2)}{\psi\,(2\,\psi^2 - U^2\,y^2 + U^2\,x^2 + U^2 a^2)} \qquad (3.60)$$

$$v = \frac{y\,U^2\,(\psi^2 + U^2 x^2)}{\psi\,(2\psi^2 - U^2 y^2 + U^2 x^2 + U^2 a^2)} \qquad (3.61)$$

where
$$\psi = \left(\frac{-B + \sqrt{B^2 - 4\,C^1}}{2}\right)^{\frac{1}{2}}$$

$$B = U^2\,(x^2 - y^2 + a^2)$$

$$C^1 = -U^4 x^2 y^2$$

This is an ideal solution but it does not represent the complete motion past an actual plate since the speed becomes infinite at the edges of the plate. For the trajectory calculation the flow after the plate is not considered and therefore this potential solution is used in the present calculation.

3.4.2 Potential source flow

The stream function of an axisymmetric potential source flow (93, 94) is given by,

$$\psi = \frac{m}{2}\left(1 - \frac{x}{(x^2+y^2)^{\frac{1}{2}}}\right) \qquad (3.62)$$

where m is the strength. The velocity components u and v are expressed as,

$$u = \frac{1}{2\pi y} \quad \frac{d\psi}{dy}$$

$$= \frac{m}{4\pi}\left(\frac{x}{(x^2 + y^2)^{1.5}}\right) \qquad (3.63)$$

$$v = - \frac{1}{2\pi y} \quad \frac{d\psi}{dx}$$

$$= \frac{m}{4\pi}\left(\frac{y}{(x^2 + y^2)^{1.5}}\right) \qquad (3.64)$$

Two solutions are therefore available to describe the flow from a nozzle. A series of experiments using the hot wire anemometer was conducted to measure the air velocity distribution and to assess the validity of both the theories.

3.5 Experimental investigation of air velocity distribution

3.5.1. Experimental set up and technique

The experimental set up for the velocity profile measurement is as described in Chapter 6 with the measurement instrumentation as shown in Figure 3.10. The measurements were made for two reasons,

(i) To test the validity of both the theories discussed earlier and to compare the experimental results with the documented results of free jet measurements.

(ii) To examine whether the theory would still apply with the presence of small electrodes in the jet.

The time average velocities were measured by means of a constant temperature hot wire anemometer (DISA type 55A01) employing a sensing element of 1.25 mm long. Prior to measurement, the anemometer was calibrated in a low speed wind tunnel using Furness micromanometer. During the measurement, the calibration was constantly checked at the nozzle exit with a pitot tube connected to the micromanometer. The micromanometer with a range of 0.002 mm - 10 mm wg had an accuracy of 2% of the scale chosen. The fluid velocity could be determined to within 0.1 m/s.

Axial velocity distributions were recorded at $x/2R_o = 12$, 17 and 24. The plate was located at $x/2R_o = 26.3$. The axial velocity distribution along the centreline was also measured up to a distance of 24 jet diameters. Similar measurements were made using a pitot tube connected to the Furness micromanometer and the results were consistent with the hot wire measurement. The pitot tube measurements enabled quick check of the correctness of the positioning and calibration of the hot wire anemometer. The jet emerged from a nozzle of 0.6 cm diameter with exit velocities ranging from 7 - 11 m/s. The experiments were conducted for a round free jet and round jets with the presence of point and conical electrodes, impinging on a square flat plate of 5.3 cm. The plane of measurement was located using similar laser arrangement described in Chapter 6 for the location of the focussing plane for the photographic system. The measurement points were located using a grid mounted on an optical bench. As shown in Figure 3.10 fine vertical movement was possible using a micrometer

Figure 3.10. Apparatus for measurement of air velocity distribution

arrangement to which a perspex holder which firmly held the hot wire anemometer was attached.

3.5.2 Results and discussion

Figures 3.11 - 3.14 show the decay of the jet centreline velocity as a function of axial distance from the exit. For a free jet, the result of Figure 3.11 shows the existence of a potential core of length of nine jet diameters downstream from the nozzle and thereafter, the decay rapidly assumes the x^{-1} type of behaviour characteristic of a self preserving axi-symmetric jet. With the presence of electrodes, Figures 3.12 and 3.13 show a region of reduced velocity extending for about five jet diameters after the electrodes and thereafter, the x^{-1} response is evident.

Equation (3.33) can be written as,

$$\frac{u_m}{U_o} = \frac{C}{(x - S_o)/R_o} \qquad (3.65)$$

where C = 0.96/a, S_o is the distance of the source pole from the nozzle and x is the axial distance from the source. A summary of the various calculated values of the terms of equation (3.65) obtained from curves best fitting the experimental data is given in Table 3.2.

Note: For the trajectory calculation, the origin of the co-ordinate system is at the nozzle and not from the source pole.

Figure 3.11 Variation of the centre-line velocity of a round jet

Figure 3.12 Variation of the centre-line velocity of a round jet.

Figure 3.13 Variations of the centre-line velocity of a round jet.

Figure 3.14 Variation of the centre-line velocity of a round jet.

Figure 3.15 Comparison of theoretical velocity profile and mean velocity distribution across the downstream part of an axially symmetric jet

Figure 3.16 Comparison of theoretical velocity profile and mean velocity distribution across the downstream part of an axially symmetric jet.

Figure 3.17 Comparison of theoretical velocity profile and mean velocity distribution across the downstream part of an axially symmetric jet.

Figure 3.18 Experimental velocity profiles at different sections of an axially symmetric jet.

Figure 3.19 Comparison of theoretical velocity profile and mean velocity distribution across the downstream part of an axially symmetric jet.

Figure 3.20 Comparison of theoretical velocity profile and mean velocity distribution across the downstream part of an axially symmetric jet.

Vertical distance from jet centre-line y (mm)

Figure 3.21 Comparison of theoretical velocity profile and mean velocity distribution across the downstream part of an axially symmetric jet.

Figure 3.22 Experimental velocity profiles at different sections of an axially symmetric jet.

Figure 3.23 Comparison of theoretical velocity profile and mean velocity distribution across the downstream part of an axially symmetric jet

Figure 3.24 Comparison of theoretical velocity profile and mean velocity distribution across the downstream part of an axially symmetric jet.

Figure 3.25 Comparison of theoretical velocity profile and mean velocity distribution across the downstream part of an axially symmetric jet.

Figure 3.26 Experimental velocity profiles at different sections of an axially symmetric jet

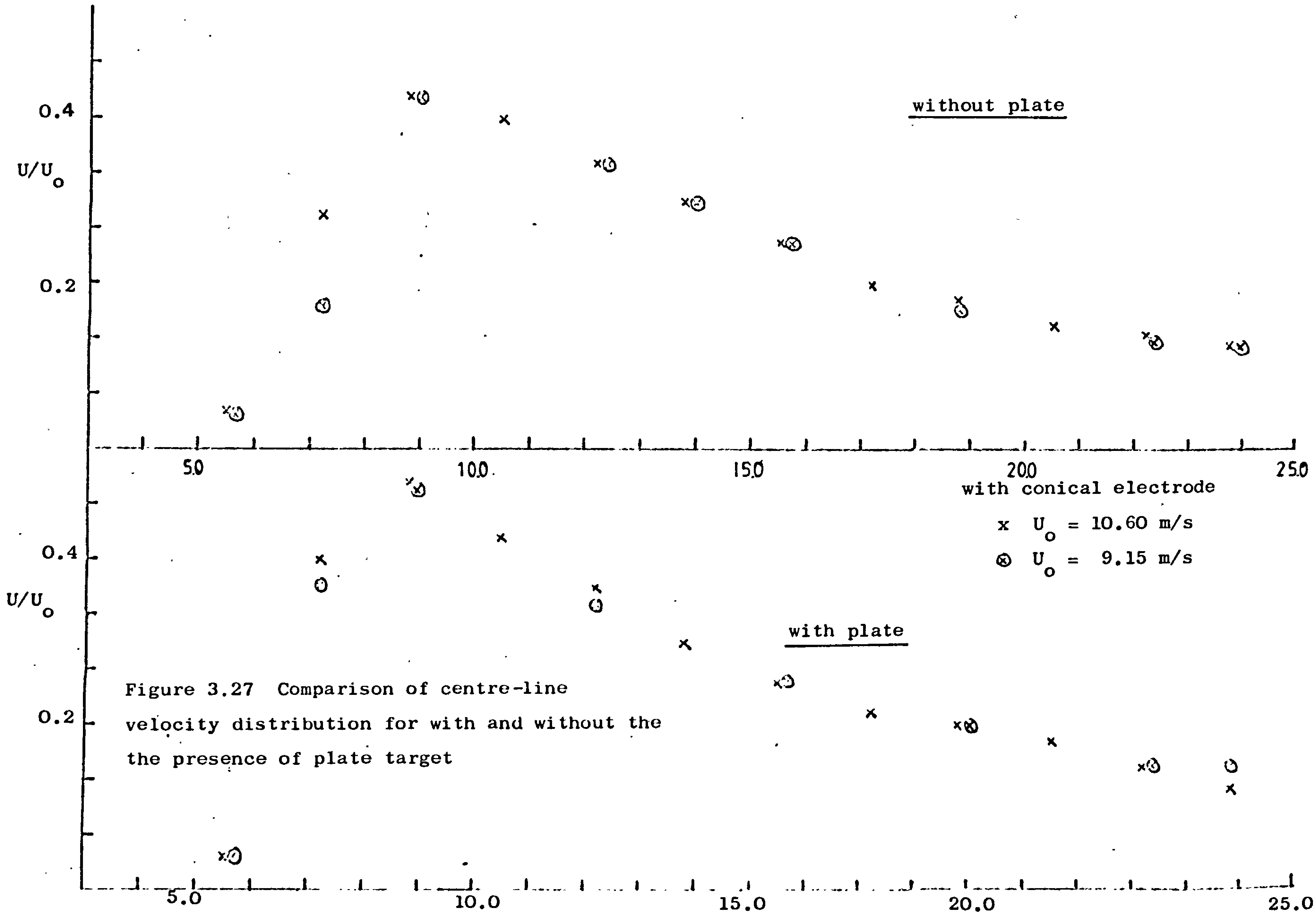

Figure 3.27 Comparison of centre-line velocity distribution for with and without the the presence of plate target

Table 3.2 Calculated values of various terms of the jet centreline velocity equation

	C	a	S_o(m)
Free jet	9.40	0.10	0.025
Jet with point electrode	5.81	0.165	0.016
Jet with conical electrode	6.47	0.148	0.015

Figure 3.14 shows that the presence of electrodes reduces the jet centreline velocity considerably but the comparison of results of the experiments with electrodes shows insignificant variation. The region behind the electrode presents difficulty in both measurement and theoretical analysis for the flow of thin jet with the presence of small object in the initial region of the jet. No known study of this configuration could be found in the literature. The measurement would require more sophisticated instrument with small spatial resolution. For the present analysis, for the region betweem the electrodes and the fully developed jet zone the velocity profiles are found to be adequately described by the following expressions derived from curve fitting. For point electrode,

$$\frac{u}{U_o} = 0.11 \frac{x}{2R_o} - 0.108 \qquad (3.66)$$

and for conical electrode,

$$\frac{u}{U_o} = 0.12 \frac{x}{2R_o} - 0.597 \qquad (3.67)$$

For an axisymmetric jet, the values of a obtained by various investigators (6) ranged from 0.06 - 0.27 with the values typically of 0.06 - 0.08 for naturally turbulent jets. The higher coefficients were obtained with artificial free jet generated by using turbulence producing grids and guide vanes. The slightly higher value of a = 0.1 obtained may be due to,

(i) All the studies employed wide jets as compared with the present jet of initial diameter of 0.6 cm. The difficulty of measurement with a hot wire anemometer in thin jet would introduce higher experimental error.

(ii) In all jet studies the jet nozzle was designed specially to produce homogenous turbulence and smooth velocity profile at the outlet. No special design was made in this study to ensure the production of jet of homogenous turbulence. Furthermore, the intake of air through the powder feeder as described in Chapter 6 would possibly disrupt the homogeneity of the pipe flow and consequently would enhance the turbulence. There is no available experimental data for comparing the values of a obtained with the presence of electrodes. The smaller values of S_o compared with the free jet value is consistent with the idea of the electrode also functioning as a diffuser.

Figures3.15 - 3.26 present the axial velocity distributions recorded at $x/2R_o$ of 12,17 and 24. The theoretical curves were obtained using calculated values obtained from the measurement of the centreline velocity. All the results show that the dimensionless velocity distributions in different cross sections are self similar and self preservation commences at $x/2R_o$ of 10. The agreement of the free jet results of Figures 3.15 - 3.17 with Tollmien's solution is good with a maximum deviation of 6% of the jet exit velocity. The predicted jet is slightly wider.

With the introduction of electrodes the prediction is surprisingly consistent. The decay of the predicted curves is not as rapid as the experimental values and as the jet spreads radially the disagreement becomes more pronounced. With the conical electrode, Figures 3.23 - 3.26 show a maximum deviation of about 13% of the jet exit velocity. Also the width of the jet is considerably overestimated. The consistent overestimation of the width of the jet for all cases is probably due to the poor convergence of equations (3.26)-(3;27) when approaching the jet boundary. Therefore for the boundary of the jet an alternative solution (6) is available by setting the function Z with the requirement that it vanishes at the boundary resulting in,

$$Z = z' = \frac{1}{4}(\varphi_{rp} - \varphi)^2 - \frac{1}{8\varphi_{rp}}(\varphi_{rp} - \varphi)^3 - \frac{3}{64\varphi^2_{rp}}(\varphi_{rp} - \varphi)^4$$

$$+ \frac{1}{64} - \frac{3}{128\varphi^3_{rp}}(\varphi_{rp} - \varphi)^5 - \left(\frac{19}{1280\varphi_{rp}} + \frac{133}{10240\varphi^4_{rp}}\right)$$

$$(\varphi_{rp} - \varphi)^6 \qquad (3.68)$$

Equation (3.68) converges well near the boundary where equation (3.26) is useless. In the trajectory calculation this complication was avoided by imposing a suitable physical limit of velocity after which the jet was assumed to be no longer felt.

This use of thin jet presented considerable difficulty in measurement and location of position to be measured. With the initial jet diameter of 0.6 cm and maximum jet width of about 5 cms, a reading was taken at 3 mm interval with a hot wire of length 1.25mm to provide the number of data points. Using a micrometer for position adjustment for the anemometer every precaution was made to ascertain of the location of velocity to be measured. As shown in the experimental results, the decay of velocity with respect to the radial distance from the centreline is rapid and errors incurred from position measurement will undoubtedly mean imparting errors to the velocity magnitude. The error due to location of measurement point was estimated to be ± 1mm and a probable maximum error in the velocity measurement due to this was about 10% of the jet outlet velocity.

Figure 3.27 shows that with the presence of a plate the centreline velocity profile does not depart from the values for when the plate is absent. Compared with the results of other investigations of impinging jet flow the maximum jet exit velocity of 10.6 m/s is considerably lower and therefore the development of wall jet is possibly insignificant. As for the region behind the plate the velocity was found to be negligible.

Finally, as shown in all figures, the use of potential source solution will lead to gross overestimation as expected since it represents an ideal flow and the solution lacks the ability to 'damp' rapidly.

3.5.3 Conclusions

The velocity distributions for a free round jet with and without the presence of electrodes were measured using a hot wire anemometer and the following conclusions could be derived:

(i) Using the Tollmien solution for an axisymmetric jet, the agreement between the experimental and theoretical results is good. The results also agree qualitatively with results of other investigators. The main difficulty involved in the experiment was to extract sufficient data points from a thin jet.

(ii) With the presence of electrodes the use of the solution with different virtual sources surprisingly gave reasonable agreement. The calculated velocity values and the widths of jets were overestimated.

In view of the lack of studies on the effect of the presence of simple objects in the jet initial region as in the case of a spray gun, using Tollemien solution with a different virtual source to describe the jet flow seems a satisfactory approach.

(iii) For the range of velocities considered in this study, the effect on velocity due to presence of object to be coated can be discounted. Also there is no apparent flow behind the object.

(iv) The use of potential flow solution led to overestimation of the velocity distribution and thickness of the jet.

3.5.4 Implication of the experimental results

In most commercial powder spray guns the one common feature is the positioning of the charging electrode. As shown in Figure 3.1 the electrode is situated at the end of the diffuser. From the experimental results, by using simple and small electrodes, it is shown that there exists a region of several jet diameters in length where the velocity is very much less than that for a free jet. Depending on the exit velocity and the shape and size of the diffuser this region may be considerably extended. During the spraying process there is the unlikelihood of particles emerging from the jet with certain inertia to enter this vortex zone. This has two important implications as regards to particle charging. Firstly at the immediate neighbourhood of the electrode where the field intensity is highest the particles can be most efficiently charged. Secondly if the efficient mixing of the particles and ions occurs further downstream the residence time in this high field region is significantly reduced. As will be discussed in the next chapter both the residence time and the magnitude of field intensity are of great importance in achieving maximum particle charging. This electrode - deflector design in the industrial spray gun is perhaps a contributor of the reported poor charging of particles in EPS process. To overcome this problem, for the particle trajectory experiments the electrode design is modified bearing in mind the prime functions required of the electrode — to provide the deposition field and to charge the particles efficiently. The modification is discussed in Chapter 6.

3.6 Resume

Due to the much varied design of industrial spray guns, the air flow study was conducted using a simplified spray gun consisting of just the spray nozzle and attached electrode. The air jet flow was studied both theoretically and experimentally. Other possible jet flow problems associated with the actual spraying process, e.g. two phase jet flow and the effect of secondary air stream, were examined and the literature reviewed. Comparing with experimental results obtained from hot wire anemometer measurement, the Tollmien solution was found to give satisfactory agreement.

CHAPTER 4

THE ELECTRICAL FORCES

4.1 INTRODUCTION

A preliminary analysis of the electrostatic forces involved in the powder coating process was included in Chapter 1. The role of the corona electrode is dual purpose. It produces the ions required for the particle charging and it also determines the deposition field between the target and the electrode. The electric field is the result of two major components:

(i) The applied field due to the applied voltage and the particular geometry of the electrode arrangement.

(ii) The space charge field due to the presence of ions and charged particles.

There is an existing difference of opinion as to the relative importance of these two fields. An attempt is therefore made to investigate this and to establish a criterion to determine whether the space charge influence can be neglected.

A model is proposed to describe the electric field and to test its validity, theoretical predictions are compared with Corbett's experimental data (10). The agreement is found to be good.

4.2 The Electric Field E

Industrial powder spray guns generally employ three main categories of charging devices. They are:

(i) Annular charging zone,

(ii) Internal charging system and

(iii) Point charging zone (needle electrode)

Figure 3.1 shows the most commonly used type, one of the third category using an electrode with a sharp profile. The geometry system chosen in this study is confined therefore to a point electrode - plane collecting electrode (i.e. one with a large radius of curvature) system. Also the bulk of Corbett's (10) field measurement data which would provide comparison for the theoretical study is that of point-plane system.

A survey of the literature revealed a scarcity of information on studies of electric field distribution in point-plane system. There is a distinct lack of experimental data mainly because of lack of suitable measuring device. Corbett's thesis presented the major experimental study.

With a given space charge density ρ, the differential equation of the field is,

$$\nabla^2 V = -\frac{\rho}{\varepsilon_o} \qquad (4.1)$$

where V = voltage

ε_o = permittivity of free space

Equation (4.1) is the Poisson's equation which governs all electrostatic phenomena. The potential field E is related to the voltage by:

$$E = -\nabla V \qquad (4.2)$$

When the space charge effect can be neglected, equation (4.1) reduces to the Laplace equation:

$$\nabla^2 V = 0 \qquad (4.3)$$

The general techniques of solving these equations with reference to the appropriate boundary conditions are given in most electromagnetic texts (e.g. 32, 33) and good examples can be found in electrostatic precipitation studies (19). The problem is essentially a three dimensional case and seeking a solution is quite difficult. Thus in most studies, various assumptions are invariably made to simplify the problem.

Adachi et al (34) in the study of ionic wind generation between a needle and plane electrodes solved equations (4.1) and (4.2) using a computational relaxation method. The Laplace field as a solution of equation (4.3) was used as a crude approximation of the field to initiate the numerical calculation. Wu (35) presented the most comprehensive and up to date survey of various aspects of EPC process. His solutions for a one dimensional Poisson's equation describe the field distribution by:

$$E = \left\{ \frac{(V_a - V_p) \quad - \quad \frac{\rho}{4\varepsilon_o} (R^2 - C^2)}{r \ln \left(\frac{R}{C}\right)} \right\} + \frac{\rho r}{2\varepsilon_o} \qquad (4.4)$$

and the potential variation by:

$$V = \left\{ V_a - \frac{\rho}{4\varepsilon_o} (R^2 - C^2) \right\} \frac{\ln(^r/R)}{\ln(^C/R)} + \frac{V_p \ln(^C/r)}{\ln (^C/R)} + \frac{\rho}{4\varepsilon_o} (R^2 - r^2) \qquad (4.5)$$

where V_a = electrode potential

V_p = potential of deposited layer on collecting electrode

C = radius of curvature of point electrode

R = point/plane electrode separation

r = radial co-ordinate

The choice of cylindrical co-ordinate system by Adachi and Wu however gave a physical representation of describing a line-plane system rather than that of a point-plane geometry. Abuaf (24) in his study of trajectories of charged particles ignored the effect of the charge density assuming the use of dilute suspension. By an image analysis method, the equations obtained in Cartesian co-ordinates are,

$$V = k_1 \left[\frac{1}{(x^2 + y^2)^{\frac{1}{2}}} \right] \tag{4.6}$$

and

$$E_x = -\frac{dV}{dx} = k_2 \left[\frac{x}{(x^2 + y^2)^{3/2}} \right] \tag{4.7}$$

where k_1 and k_2 are experimental constants. The constants were determined by the electrode geometry and applied voltage. As shown later, the neglection of charge density is valid only if certain criterion is complied.

The main obstacle to most field studies has been the difficulty of electrical measurement in ionic clouds. The introduction of any measurement probe must be avoided as undoubtedly it will disturb the electric field. A ballistic probe technique was developed by Pauthenier (38) in his classical study of field charging theory. Corbett extended the technique and presented a series of experimental data of electric field distribution in the inter-electrode gap for a point/plane system. The space charge density could be determined independently by the variable speed probe system.

The method involved firing ball bearings through the air space to be investigated from a specially designed air gun and were caught in a Faraday cage. Along the same line of firing several charge measurements were made at different measured velocities. From a plot of charge against velocity, values of field and ion current density could be calculated. The probe technique was found unsuitable for field measurement in a mixed ionic and charged particulate system. The serious limitation was due to complex powder - probe interaction. The charged powder interacted with the probe to reduce the charge measurement by an amount which was independent of probe velocity.

His main experimental finding in ionic cloud measurement was that of a rise in the field intensity near the earthed surface as shown in Figures 4.2 - 4.4. Although it was shown that the ionic space charge density considerably modified the applied field, the idea that it was entirely due to the space charge was dismissed. Using a simple one dimensional model, the following equations were derived from Poisson's equation,

$$E^2 = E_o^2 + \frac{2\,J\,x}{\varepsilon\,\varepsilon_o\,k} \tag{4.7}$$

$$\frac{d^2E}{dx^2} = -\left(\frac{J}{\varepsilon\,\varepsilon_o k}\right)^2 \frac{1}{E^3} \tag{4.8}$$

where J = current density

k = ionic mobility

E_o = field intensity at $x = x_o$

Equation (4.8) shows a negative d^2E/dx^2 contrary to experimental evidence of a positive d^2E/dx^2, i.e. there is a rise of field gradient as the plane electrode is approached. He postulated that the discrepancy was due to the formation of insulating film on the electrode. Using different electrodes it was found that the electrode effects could alter appreciably the field distribution particularly near the collecting surface. The model suggested however seems unrealistic since equation (4.7) suggests an increasing value of E with x whereas Figures 4.2 - 4.4 show trough shaped curves.

Wu's theoretical analysis attributed the field enhancement of the collecting surface as due entirely to space charge effect. The space charge also played a vital role of suppressing the corona electrode field. His theoretical result was consistent with various studies of electric field distribution in electrostatic precipitation process (19, 36). The theoretical model adopted in this study is similar to Wu's approach and one of the main objectives is to apply the theoretical predictions to Corbett's experimental data to assess the validity of the model.

4.3 Theory of a Simplified Model of the Electric Field

Figure 4.1 shows the basic arrangement of the model in spherical co-ordinates. The earthed substrate is positioned at a distance R away from the point (or conical) electrode at the origin. Both the target and the electrode surfaces are approximated by spherical shells with the appropriate spherical radii. The model assumes that potential is experienced only within the confinement of a cone determined by the electrode arrangement.

Corbett's off axis field measurements showed only a slight change of values (except in the viscinity of the corona point) and therefore a one dimensional analysis is logical. Also all quantities within the cone are symmetrical with respect to the polar and cone angles (ϕ, θ) and a narrow angle cone (20°) is used in the study.

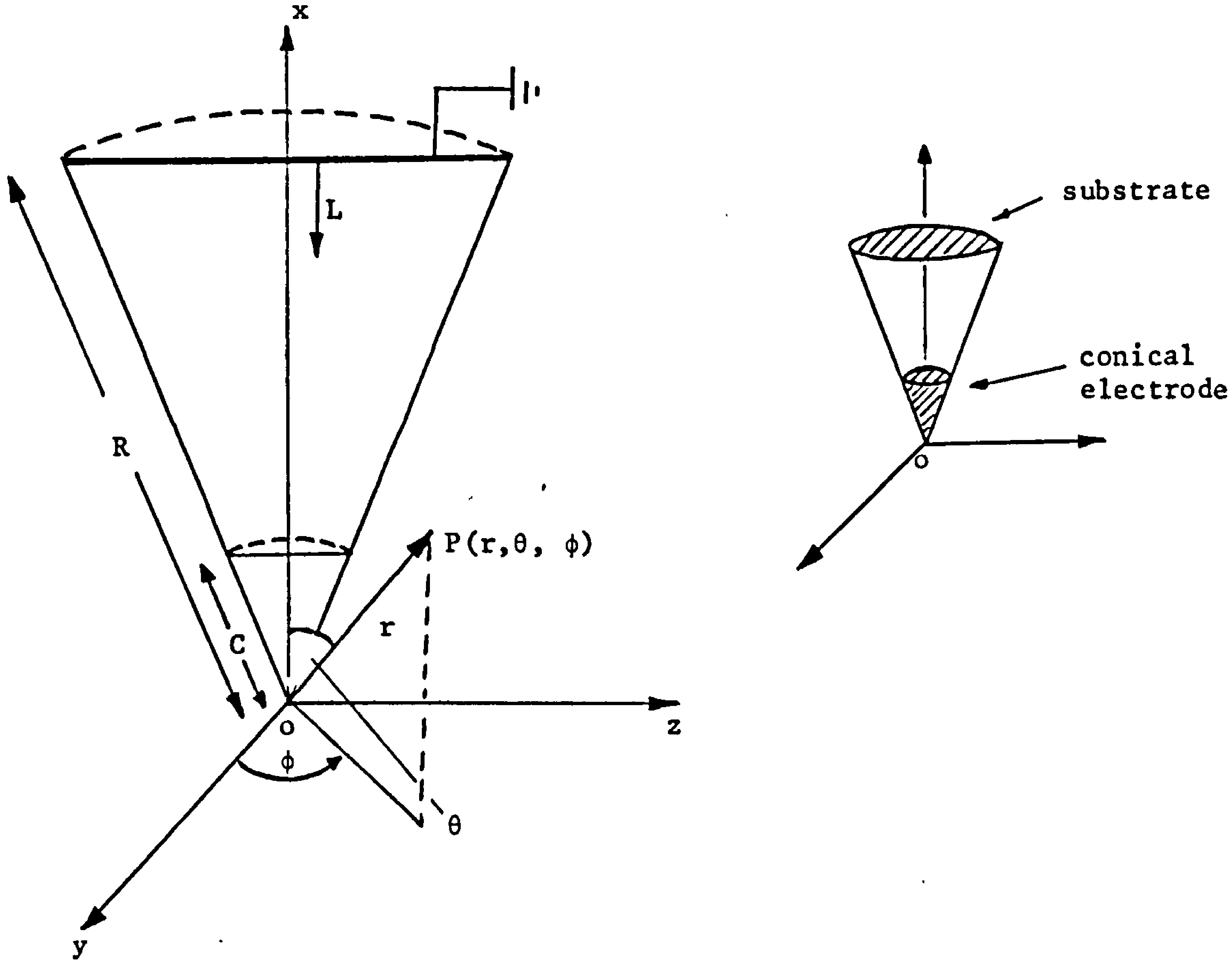

Figure 4.1 Schematic Representation of Electrostatic Field Model

The variation with ϕ and θ is assumed minimal.

The Poisson's equation is given by:

$$\frac{1}{r^2}\frac{\partial}{\partial r}\left(r^2\frac{\partial V}{\partial r}\right) = -\frac{\rho}{\varepsilon_o} \tag{4.9}$$

The field intensity is related to the potential by:

$$E(r) = -\frac{\partial V}{\partial r} \tag{4.10}$$

The assumption of an uniform space charge density ρ is again consistent with Corbett's experimental evidence. The off axis ionic number density data showed that except near the point electrode, the assumption is reasonable. Equation (4.9) is integrated to,

$$r^2 \frac{\partial V}{\partial r} = -\frac{\rho}{3\varepsilon_o} r^3 + \beta \tag{4.11}$$

and

$$V = -\frac{\rho}{6\varepsilon_o} r^2 - \frac{\beta}{r} + \gamma \tag{4.12}$$

Two special cases are considered in the evaluation of equations (4.11) and (4.12).

4.3.1 Electric Field with Space Charge

If there is charged particulate layer deposition on the object, the layer exerts a potential of V_p with field strength of E_n. The boundary conditions are:

$$\begin{aligned} V(R) &= V_p \\ V(C) &= V_a \\ \rho &= \rho \end{aligned} \tag{4.13}$$

Substitutions of quantities in equations (4.13) into equation (4.12) give,

$$V = V_a + \frac{\rho}{6\varepsilon_o} (C^2 - r^2) + \beta \left(\frac{1}{C} - \frac{1}{r} \right) \tag{4.14}$$

where

$$\begin{aligned} \beta &= -\left\{ \frac{(V_a - V_p) - \frac{\rho}{6\varepsilon_o} (R^2 - C^2)}{\left(\frac{1}{C} - \frac{1}{R}\right)} \right\} \\ \gamma &= V_a + \frac{\rho}{6\varepsilon_o} C^2 + \frac{\beta}{C} \end{aligned} \tag{4.15}$$

Combining equations (4.10) and (4.11), the field strength distribution is,

$$\begin{aligned} E(r) &= \frac{\rho}{3\varepsilon_o} r - \frac{\beta}{r^2} \\ &= \frac{\rho}{3\varepsilon_o} r + \left\{ \frac{(V_a - V_p) - \frac{\rho}{6\varepsilon_o} (R^2 - C^2)}{\left(\frac{1}{C} - \frac{1}{R}\right)} \right\} \frac{1}{r^2} \end{aligned} \tag{4.16}$$

The field on the electrode surface E_o is derived from equation (4.16) when r = C,

$$E_o = \frac{\rho}{3\varepsilon_o} C - \frac{\beta}{C^2} \qquad (4.17)$$

The radial field intensity is therefore related to the corona electrode by combining equations (4.16) and (4.17) to give,

$$E = \left[E_o C^2 + \alpha (r^3 - C^3) \right] \frac{1}{r^2} \qquad (4.18)$$

where

$$\alpha = \frac{\rho}{3\varepsilon_o}$$

When $V_p = 0$, the grounded substrate becomes a perfect sink.

4.3.2 Electric Field without Space Charge

In the absence of space charge, i.e. when there is no corona, the boundary conditions for equations (4.9) and (4.10) are,

$$\begin{aligned} \rho &= 0 \\ V(R) &= V_p \\ V(C) &= V_a \\ E(C) &= E_o \end{aligned} \qquad (4.19)$$

Using similar procedure as in the preceding section, the following equations are obtained,

$$V = \frac{V_a C (r - R) + V_p R (C - r)}{r (C - R)} \qquad (4.20)$$

$$E = \frac{RC (V_a - V_p)}{r^2 (R - C)} \qquad (4.21)$$

$$E = E_o \frac{C^2}{r^2} \qquad (4.22)$$

Table 4.1 is a summary of the equations derived. Before comparing the equations with Corbett's experimental data, the importance of space charge effect in EPC process is first examined.

TABLE 4.1 EQUATIONS FOR ELECTRIC FIELD AND POTENTIAL DISTRIBUTIONS

With space charge ρ	$V = V_a + \frac{\alpha}{2}(C^2 - r^2) + \beta\left(\frac{1}{C} - \frac{1}{r}\right)$	(4.14)
	$E = \alpha r - \frac{\beta}{r^2}$	(4.16)
	$E = \left[E_o C^2 + \alpha(r^3 - C^3)\right]\frac{1}{r^2}$	(4.18)
	$\alpha = \frac{\rho}{3\varepsilon_o}$	
	$\beta = -\left\{\frac{(V_a - V_p) - \frac{\rho}{6\varepsilon_o}(R^2 - C^2)}{\left(\frac{1}{C} - \frac{1}{R}\right)}\right\}$	
Without space charge	$V = \frac{V_a C(r - R) + V_p R(C - r)}{r(C - R)}$	(4.20)
	$E = \frac{RC(V_a - V_p)}{r^2(R - C)}$	(4.21)
	$E = E_o \frac{C^2}{r^2}$	(4.22)

4.4 Space Charge Phenomena

The space charge field can be of great significance in determining powder coating performance. Yu (39) and Faith et al (40) investigated both theoretically and experimentally precipitation of charged particles by their own space charge. In EPC process, inside surfaces of objects, which are electrostatically screened areas, the space charge field E_{sp} is the principal electrostatic force responsible for deposition. To get good penetration it is important to project a dense cloud of charged particles into the screened areas by air transport. For a spherical cloud of radius R, E_{sp} is estimated by a radial field description (9),

$$E_{sp} = \frac{\rho R}{3\varepsilon_o} \qquad (4.23)$$

The expression is similar to the space charge density part of equation (4.16)

4.4.1 Ionic and Particulate Space Charge

The current flow between the corona electrode and the object is carried by three different species of charge carriers: electrons, ions and charged particles. The space charge for a single species is related to the current density and electric field by equation (4.24),

$$j = N e \bar{\mu} E = \rho \bar{\mu} E \qquad (4.24)$$

where j = current density
N = number density
e = electrical charge
$\bar{\mu}$ = carrier electrical mobility
(ratio of field and particle velocity)

The total current density is the summation for the three species:

$$j_t = j_e + j_i + j_p$$
$$= N_e e \bar{\mu}_e E + N_i e \bar{\mu}_i E + N_p e \bar{\mu}_p E \qquad (4.25)$$

where e, i, p denote electrons, ions and particles respectively. In powder coating, sufficient quantity of electronegative gas molecules are present to strip essentially of all the free electrons.

Therefore,

$$\rho \, \bar{\mu}_{eq} E = \rho_i \, \bar{\mu}_i E + \rho_p \bar{\mu}_p E \qquad (4.26)$$

$$\rho = \rho_i + \rho_p \qquad (4.27)$$

$\bar{\mu}_{eq}$ is the equivalent mobility for the total space charge ρ .

By manipulation of the various equations listed above and supplemented with experimental data, Oglesby (36,37) indicated the techniques of estimating the various ratios of charge densities. The expressions (4.26) and (4.27) also enable one to derive current - voltage - electric field relationships as compared with charge density - voltage - field expressions listed in Table 4.1

4.4.2. Space Charge Effect in Powder Coating

Corbett experienced great difficulty in determining directly charge density and field intensity distribution in particulate clouds. Hence an alternative indirect method is required to estimate the particulate charge density. Wu (35) estimated (calculation based on 10μm particles) that in EPC the effect of ion space charge can be neglected. The calculation procedure is similar to Oglesby's (36,37) approach.

The ratio of particle charge density to ion charge density is expressed by:

$$\frac{\rho_p}{\rho_i} = \frac{j_p}{j_i} \cdot \frac{\bar{\mu}_i}{\bar{\mu}_p} \qquad (4.28)$$

The ratio j_p/j_i can be determined experimentally. This ratio, under typical spraying conditions was found to be about 0.1(35).

In Cheever's (41) study of charge acceptance and decay of powder coating particles, a ratio of similar magnitude was obtained.

The mobility of a particle is defined as the ratio of the particle velocity V_p to the electric field E.

$$\bar{\mu}_p = \frac{V_p}{E} \qquad (4.29)$$

The mobility of ions $\bar{\mu}_i$, typified by negative oxygen ions in air is generally of the order of 2.2 cm^2/V sec. For a charged particle, $\bar{\mu}_p$, can be estimated from the value of the migration velocity w, given by Stoke's Law as,

$$V_p = w = \frac{qE}{3\pi\mu\, d_p} \qquad (4.30)$$

In an electric field of 3 Kv/cm, for a 10μm particle w is calculated to be 44 cm/sec. Equation (4.29) becomes

$$\bar{\mu}_p = \frac{44}{3x10^3} = 1.46 \times 10^{-2}\ cm^2/V\ sec$$

and

$$\frac{\bar{\mu}_i}{\bar{\mu}_p} = \frac{2.2}{1.46 \times 10^{-2}} = 1.5 \times 10^2$$

and

$$\frac{\rho_p}{\rho_i} = 0.1 \times 1.5 \times 10^2 = 15$$

For the example cited above the ionic charge density can therefore be neglected. However, a 50μm particle will result in a five fold increase in w with a consequent reduction in the value of ρ_p/ρ_i . Thus, the size distribution is important in determining the ratio. With a knowledge of the ratio and ρ_i, the magnitude of ρ_p can be estimated. In this study, using a dilute suspension, the quantity ρ_p is ignored.

4.5 Comparison of theory with Extracted Experimental Data

Corbett using the high speed ballistic probe studied the electric field distribution for different type of collecting electrodes. Typical measured field value was between 10^5-10^6 v/m. Figures (4.2) - (4.4) show experimental results using copper, aluminium and gold plated electrodes. The main observation was the enhancement of the field intensity near the earthed electrode. For the different plane electrodes under similar experimental conditions, i.e. same electrode spacing, point current and applied voltage there was appreciable variation in the rise of various electric fields. This discrepancy was found to be caused by the formation of insulation layers of different chemical composition (e.g. alumina layer on the aluminium electrode, oxide layer on the copper electrode) resulting in inefficiency of ion discharging. The concept of the electrode acting as a perfect sink is questionable since there was a build up in the ionic charge density in its neighbourhood. The electrode effect can therefore influence considerably the electric field distribution.

Figures 4.2 - 4.4 show comparisons of experimental data with theoretical curves predicted by equation (4.16). For a particular set of experimental data the first experimental point was used to obtain the space charge density to initiate the calculation. A perfect sink situation is assumed, i.e. $V_p = 0$.

4.5.1 Results and Discussion

(i) The theoretical curves are found to be generally in good agreement with the experimental data results considering the

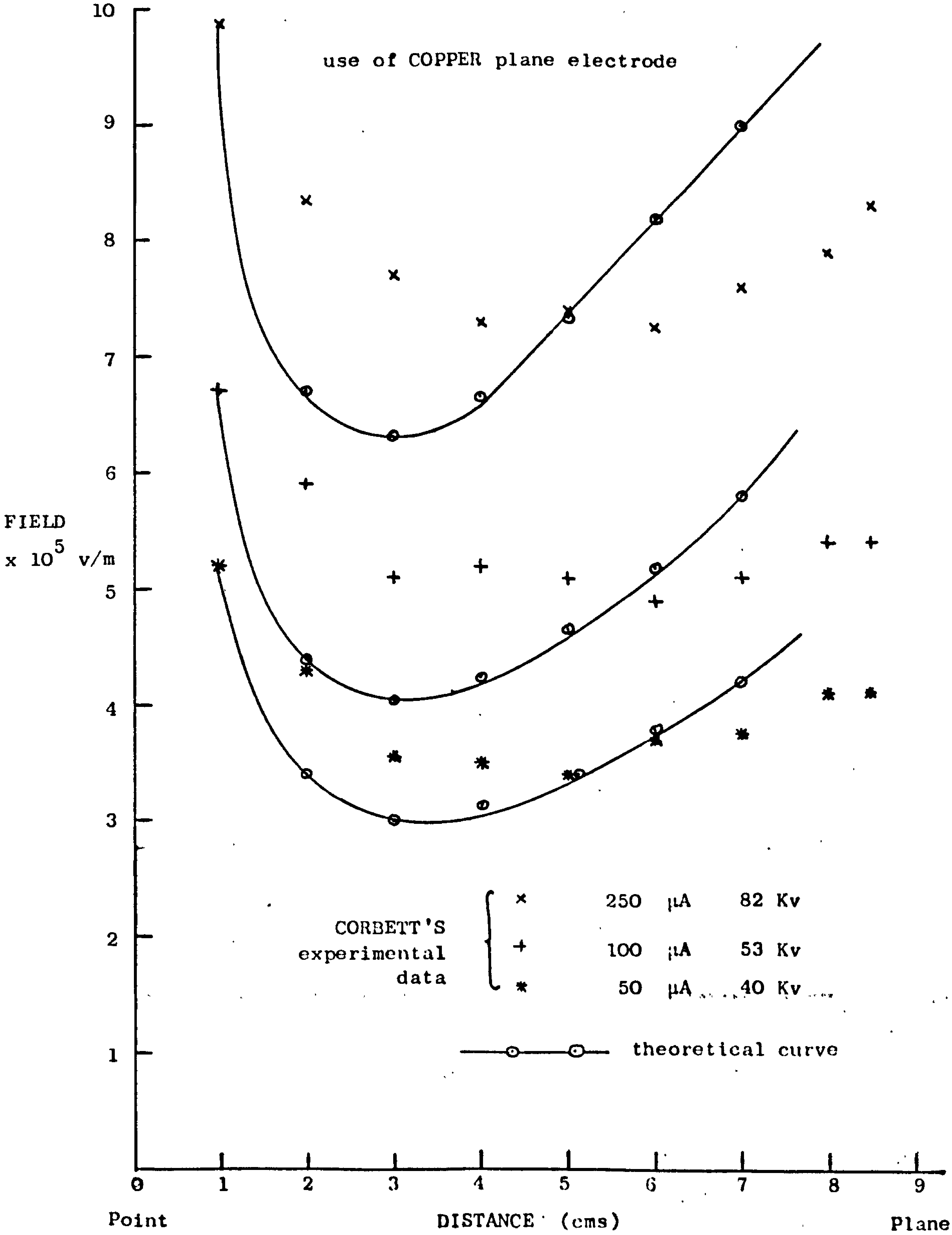

Figure 4.2 Comparison of experimental and theoretical data

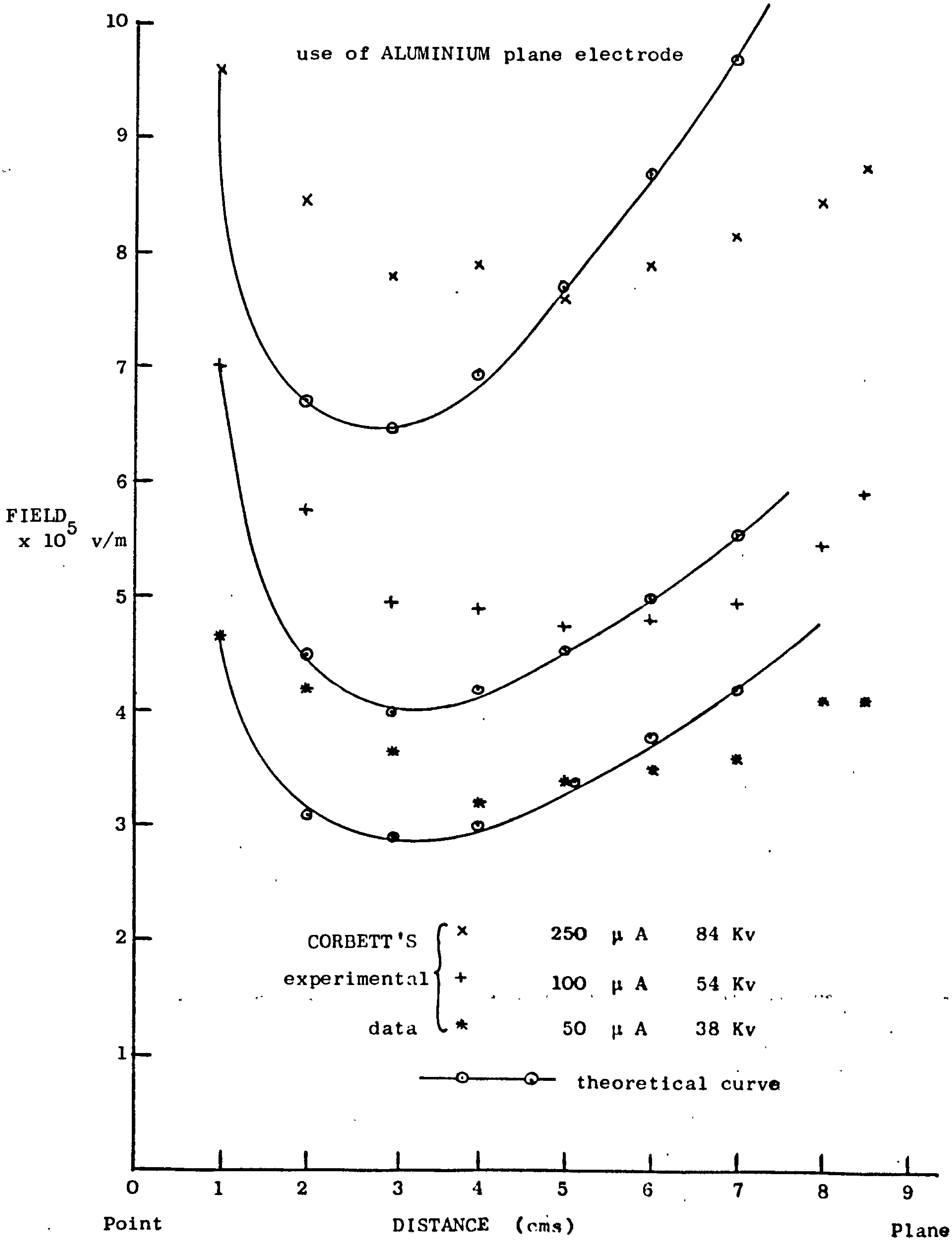

Figure 4.3 Comparison of Experimental and Theoretical data

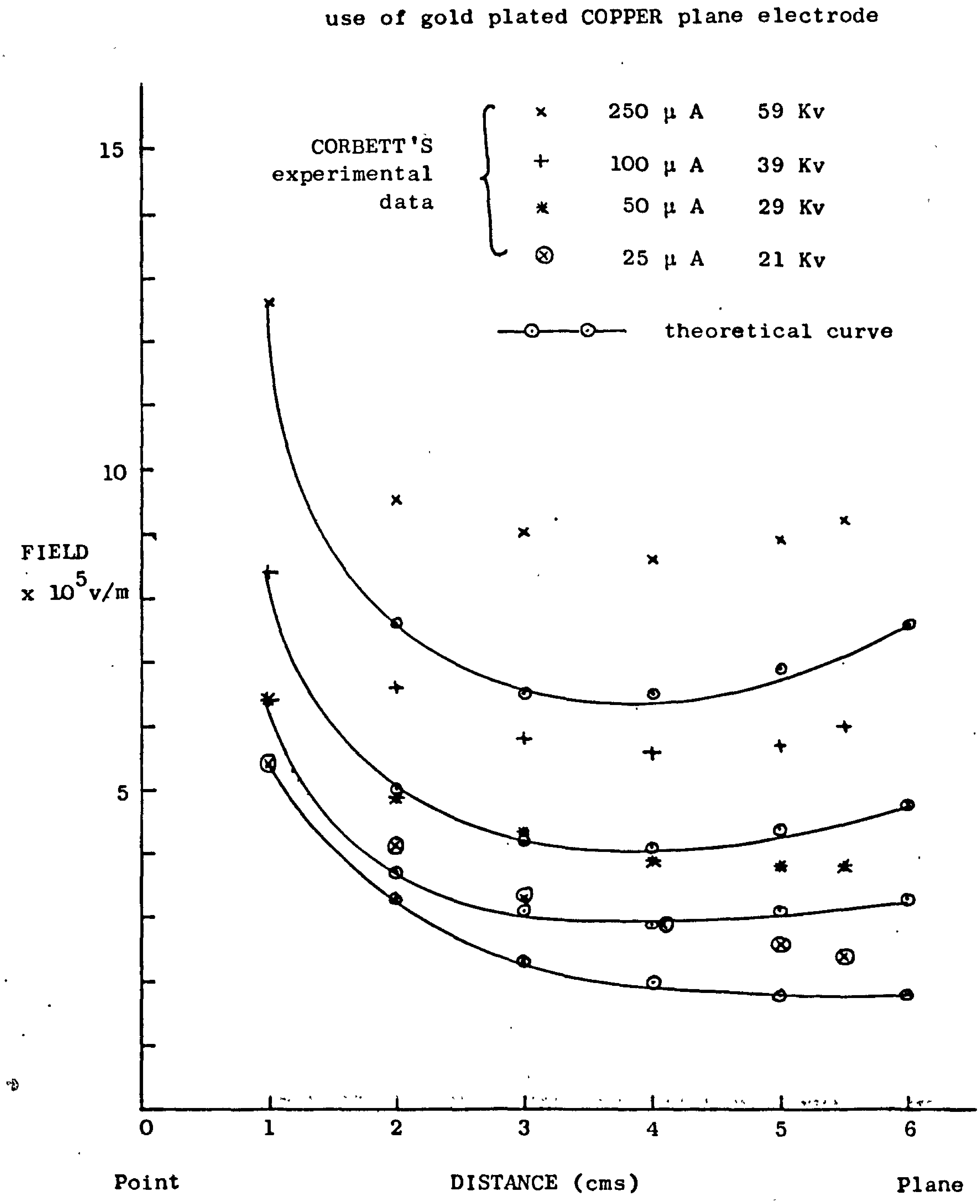

Figure 4.4 Comparison of experimental and theoretical data

simplicity of the theoretical model. The maximum variation between experimental and calculated points is about 20%.

(ii) Comparison is more favourable for the lower applied voltages i.e. lower point currents. The prediction for experiments of 250μA point current is a bit exaggerated especially near the plane.

(iii) This discrepancy in experimental and theoretical results may be due to several factors. Besides the many assumptions used in the theoretical derivation, it may also be due to the electrode experimental set up. A centimeter long electrode was mounted on a hemispherical end of a polished brass rod of diameter 1.27 cm. The brass rod would undoubtedly contribute to the field distribution of a strictly point - plane system.

(iv) Equation (4.16) consists of two parts. The first part αr is responsible for the ascent in field after the minima and β/r^2 describes the decay before the minima. From the experimental curves the decay would be more aptly described by β/r. Wu's solution represented by equation (4.4) has a decay proportional to $1/r$ and a linear rise in field. Equation (4.4) therefore seems to offer a more accurate prediction. However the calculated charge density values are considerably lower than experimental data.

If instead, V_p has a finite value, i.e. an imperfect sink situation, the value of β/r^2 decreases since $(V_a - V_p)$ decreases. This will lead to better agreement with Corbett's data. The existence of an imperfect sink was proved using different electrodes. A better agreement could be obtained if a value of V_p can be estimated.

(v) Only limited information of charge density values could be extracted from Corbett's data. From this data, the calculated values are in good agreement. For the gold plated electrode data except in the close viscinity of the electrode the mean measured value was 2.5×10^{-4} c/m^3 as compared with a calculated value of 1.6×10^{-4} c/m^3. Wu's solution yielded a figure of 1.1×10^{-4} c/m^3.

(vi) The field rise exhibits a positive gradient (i.e. $d^2E/dx^2 > o$) but the theoretical curve is linear. This is not surprising since a deposited layer is found to modify the field considerably and it is not possible to take this effect into account without using a more sophisticated model. The small scatter of the experimental points of Figures 4.2 - 4.4 show that a linear curve fitting will indeed give good prediction.

(vii) Figure 4.4 shows that with decreasing value of applied voltage the experimental curves begin to level off. The prediction exhibits the same trend.

The theoretical model therefore despite its simplicity seems to describe the field intensity distribution for a point-plane system adequately. The value of the ionic charge density is responsible for the enhancement of the field near the electrode surface. As shown in Figure 4.4 as the density value decreases, the enhancement diminishes accordingly. The next questions to be resolved are the importance of the magnitude of the charge density and also whether it is possible to dismiss the charge density effect in the powder coating operation.

4.6 The Enhancement and Suppression of Electric Field

By denoting the field intensity without and with space charge by E_p and E_{sp} respectively, equations (4.16) and (4.21) are combined to produce,

$$E_{sp} = \left[\frac{(V_a - V_p) - \frac{\rho}{6\varepsilon_o}(R^2 - C^2)}{(R - C)}\right] \frac{CR}{r^2} + \frac{\rho r}{3\varepsilon_o}$$

$$= E_p - \frac{\rho\, C\, R\, (R^2 - C^2)}{6\varepsilon_o\, r^2\, (R - C)} + \frac{\rho r}{3\varepsilon_o}$$

$$= E_p + \delta$$

where $\delta = \delta_1 + \delta_2$

$$\delta_1 = -\frac{\rho\, C\, R\, (R^2 - C^2)}{6\varepsilon_o\, r^2\, (R - C)}$$

$$\delta_2 = \frac{\rho r}{3\varepsilon_o}$$

δ describes the contribution of the space charge effect to the field distribution and its importance can now be examined. When r is small, i.e. near the corona point, δ is negative since δ_1 is much greater than δ_2. Near the substrate, δ is positive since δ_2 is predominant. Therefore,

$\delta < o$ when $r \rightarrow c$; $\delta_1 >> \delta_2$

$\delta > 0$ when $r \rightarrow R$; $\delta_1 << \delta_2$

In the viscinity of the corona electrode, the electric field suffers a suppression by a value of δ_1. Near the earthed electrode E_{sp} is increased by δ_2. Figure 4.5 illustrates the augmentation and suppression effects of the space charge. Theoretical curves for varying magnitudes of space charge density are plotted. By reducing the magnitude by an order ($\rho = 0.18 \times 10^{-4}$ c/m^3) the field distribution is effectively that of field devoid of space charge as shown by curves 2 and 4. Curve 3 shows that halving the value

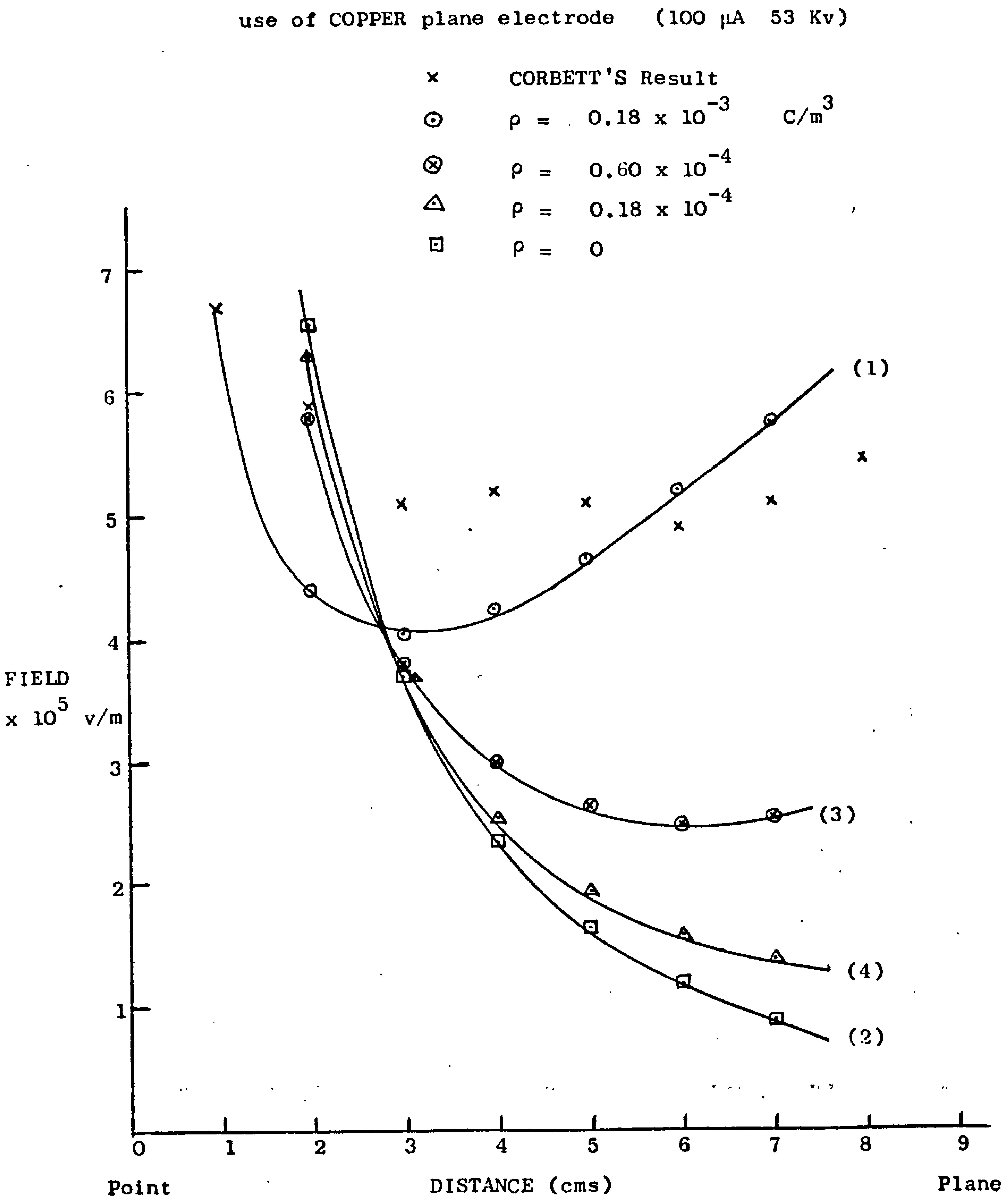

Figure 4.5 Comparison of field distribution for varying charge densities

($\rho = 0.60 \times 10^{-4}$ c/m^3), the rise in field is minimal. This calculation is consistent with Corbett's experimental result shown in Figure 4.4. Therefore space charge influence can be insignificant if its value is less than a critical value.

4.6.1. Criterion for Assessing the Importance of Space Charge Effect

From equation (4.16) if,

$$\left[\frac{(V_a - V_p) - \frac{\rho}{6\varepsilon_o}(R^2 - C^2)}{(\frac{1}{C} - \frac{1}{R})}\right]\frac{1}{r^2} \gg \frac{\rho r}{3\varepsilon_o}$$

it follows that the relationship,

$$(V_a - V_p) \gg \frac{\rho}{6\varepsilon_o}(R^2 - C^2)$$

is true. When the relationship is satisfied, the effect of space charge density can be neglected. The magnitude of $\left[(V_a - V_p) - \frac{\rho}{6\varepsilon_o}(R^2 - C^2)\right]$ can be used as a criterion to gauge the significance of ρ.

For the various graphs of Figure 4.5, the values of $\frac{\rho}{6\varepsilon_o}(R^2 - C^2)$ are tabulated in Table 4.2 to illustrate this point. For curve 4 the criterion is satisfied and it is identical with curve 2. Curve 3 shows that the criterion is partially true and the field is modified.

For the present work (V_a = 60 Kv, R = 0.15 m) for $\frac{\rho}{6\varepsilon_o}(R^2 - C^2)$ to equal $(V_a - V_p)$, $\rho = 1.4 \times 10^{-4}$ c/m^3. From the experimental data, ρ is estimated to be 10^{-5} c/m^3 which will effectively yield a curve of the nature of curve 3 of Figure 4.5. In the trajectory prediction, calculations are performed for the applied electrostatic field and the space charge influence is considered as a correction for the applied field strength.

TABLE 4.2 COMPARISON OF $(V_a - V_p)$ and $\frac{\rho}{6\varepsilon_o}(R^2 - C^2)$

Graph	$V_a - V_p$ (V)	ρ (c/m^3)	$\frac{\rho}{6\varepsilon_o}(R^2 - C^2)$
1	53×10^3	0.18×10^3	33.9×10^3
2		0	0
3		0.60×10^{-4}	11.30×10^3
4		0.18×10^{-4}	3.4×10^3

4.7 Particle Charging

There are two main charging mechanisms relevant to powder coating technology, viz, corona charging and triboelectric charging (9, 35). Corona charging is by far the most popular method. With the presence of strong applied electric field, ion bombardment charging (field charging) is the dominant corona charging mechanism. Ion diffusion charging is neglected since it is important only for particles smaller than 0.2 μm diameter.

The charge q for a spherical particle of diameter d_p, acquired after t seconds in a constant electric E_o is given by the classical Pauthenier's equation (38),

$$q = 3\pi \left(\frac{\varepsilon}{\varepsilon + 2}\right) \varepsilon_o \, d_p^2 \, E_o \, \frac{t}{t + \tau} \qquad (4.32)$$

where ε = relative permittivity of powder

τ = particle charging time constant

τ is the time in which half the limiting charge is attained and is given by,

$$\tau = \frac{4\varepsilon_o}{\rho_i \, \bar{\mu}_i} \qquad (4.33)$$

where ρ_i is the ionic charge density and $\bar{\mu}_i$ the ionic mobility. Equation (4.32) can also be expressed as,

$$q = 3\pi \left(\frac{\varepsilon}{\varepsilon+2} \right) \varepsilon_o \, d_p^2 \, E_o \left(1 + \frac{4\varepsilon_o E_o}{Jt} \right)^{-1} \qquad (4.34)$$

The saturation charge for when $t = \alpha$ is,

$$q = 3\pi \left(\frac{\varepsilon}{\varepsilon+2} \right) \varepsilon_o \, d_p^2 \, E_o \qquad (4.35)$$

For polymer particle ε is of the order of 2.0

Equation (4.35) is for spherical particles. Powder coating particles are normally irregularly shaped and will thus theoretically acquire higher charges than equivalent spheres because of the larger surface area. Smith (42) studying non-spherical particle charging in a corona discharge concluded that the increase in saturation charge was unlikely to be of any practical significance. If the charge was expressed as per unit surface area the shape factor could be neglected. Pech (43) also stated that any charge deviation could be ignored if the particle did not differ too much in the three dimensions, a condition largely satisfied by plastic powders.

The value of τ is of the order of 10^{-3}- 10^{-4} sec (19). Therefore for saturation charge, a particle must stay in a charge zone of field E_o for 10^{-3} -10^{-4} sec. Equation (4.34) shows that to obtain maximum charge Jt must be large. Bright (9) suggested that

$J \approx 10^{-2}$ A/m^2 and $t \approx 10^{-3}$ sec for well designed spray guns. In the current study of particle trajectories, particles emerged with maximum velocity of about 5 m/s. A calculated residence time of 1.0 x 10^{-3} sec was required to traverse a 1 cm long electrode charging zone (for conical electrode, residence time is 5 x 10^{-3} sec) with longer flight time for smaller particle velocity. Also an internal electrode was employed to effectively increase this time. As the particles streamed towards the target, further charging would result. Therefore every effort was taken to attain the saturation charge.

Measurement of corona charging of particles has been the subject of various investigators (35,41, 44,45,46,47). Most of the data reported however were obtained from conditions quite different from the real coating process. Zabel (44) using single polymer particle of diameter 0.1 mm to 0.2 mm concluded that the limiting charge was proportional to d_p instead of d_p^2. Lacchia's measurement of net charge to mass ratio showed that generally the magnitude was 10 to 20 times lower than the predicted value (45) and particles were not uniformly charged. For a 40μm diameter particle, a measured value of approximately 3 x 10^{-15} c/particle as compared with a calculated value of 6 x 10^{-14} c/particle was obtained. Cheever (41) using a commercial powder of 21μm mean particle diameter obtained a value of 10^{-13} - 7 x 10^{-14} c/particle. Wu (35) examined primary and secondary charging using two experimental techniques. Primary charging is defined as the charging during flight and secondary charging after deposition. The study was conducted for various operational variables (e.g. heat, humidity, powder feed rates, spray distance, etc.) and a series of governing relationships were defined.

Despite the much varied experimental conditions and techniques, several general conclusions can be derived from the various studies.

(i) Though equation (4.35) tends to overestimate the charge acceptance, it remains the best available solution for estimation.

(ii) It is difficult to simulate the practical charging conditions in EPS especially with a decreasing charging field towards the target and varying particle velocity.

(iii) The charge per particle data is normally derived from measurement of charge per unit mass of powder using a known value of powder density. This therefore would invariably introduce error in estimating the charge per particle. The error may be considerable when considering using a mean size to represent a size distribution.

(iv) The rate of charge decay can be ignored during the first few minutes of coating operation.

4.8 The Deposited Layer

The growth of the powder layer with its related properties has been an area of early intensive research with a concerted effort of finding a mechanism to explain the 'self-limiting layer' phenomenon. The mechanism is back ionisation (48). Due to the high resistivity (10^{14}-10^{16} ohm-m) of coating powder, the deposited particles do not discharge quickly. With the growth of layer, the voltage and the electric field increase until the onset of back corona with the attainment of a limiting coating thickness. The value of the surface potential V_p in equation (4.18) therefore is time dependent and its magnitude considerable.

Makin et al (49), Hardy (8), Wu (35) and Golovoy (50) have all investigated the surface potential of a chargedpowder layer and the implication of critical coating thickness. The first three studies adopted a similar model by solving a one dimensional Poisson's equation for the deposited layer prior to occurrence of back ionisation. The surface potential V_p expression for a layer of thickness ℓ according to Wu and Hardy in various forms is given by,

$$\begin{aligned} V_p &= \frac{\rho_\ell \, \ell^2}{2K\varepsilon_o} \\ &= \frac{3 \, E_{ps} m^2}{KB\rho_s \, d_p} \\ &= \frac{BQ \, \ell^2}{2 \, \varepsilon} \end{aligned} \tag{4.36}$$

where ρ_ℓ = volume charge density

K = effective diaelectric constant of layer

E_{ps} = field at particle surface

m = mass/unit area of substrate

B = bulk density

ρ_s = particle density

Q = charge/unit mass of powder

Equation (4.36) shows that the voltage increases with the square of layer thickness and this was substantiated by experimental evidence.

In addition, Makin et al (49) derived an expression describing the time dependence of the growth of powder layer and the saturated coating thickness ℓ_o. The expression is,

$$\ell = \ell_o \tanh\left(\frac{\alpha t}{\ell_o}\right) \tag{4.37}$$

with

$$\alpha = \frac{n \, \bar{\mu}_p U \, V_a}{RP} \tag{4.38}$$

$$\ell_o = \left(\frac{2}{9} \; \frac{\varepsilon \, V_a d_p}{E_o \, P \, \gamma}\right)^{\frac{1}{2}} \tag{4.39}$$

$$\gamma = 1 + \frac{j_i}{E_n n \bar{\mu}_p q} \tag{4.40}$$

where U = particle volume

p = porosity

$\bar{\mu}_p$ = particle mobility

V_a = applied voltage

R = electrode separation

E_o = electrode field

n = particle number density

j_i = ion current density

E_n = field immediately outside layer

q = particle charge

t = time

The theoretical treatment showed quantitative agreement with experimental results. The theory also suggested non-dependence of limiting coating thickness on cloud density, exposure time and gun to substrate distance as shown by equation (4.39). The model adopted by all studies assumed a simple packing of layer after layer of spherical particles. This indeed is oversimplification and particle packing in electrostatic deposition is an area which has been overlooked. However, the simple derivation does include a particle packing parameter, viz, the bulk density B.

In the current study with the use of dilute suspension and also experimentally particle build up was not permitted, the value of V_p was neglected. If required, the estimation of V_p using the above expressions could be incorporated in the electric field calculation.

4.9 The Image Force Field

If a charged particle is at a distance L from the earthed object its image force is expressed as,

$$F_{ix} = \frac{q^2}{4\pi\varepsilon_o L^2} \qquad (4.41)$$

In EPS this is one of the major forces responsible for powder adhesion (31). In the trajectory calculation the magnitude of this force is however insignificant when compared with the applied field force as illustrated by a simple calculation. At a corona field of 1×10^6 V/m, the saturation charge q for a 40μm diameter particle is 6×10^{-14}C/particle. At a distance of 1 cm from the target, the particle image force F_{ix} according to equation (4.41) is 3×10^{-13} N whilst the force due to the applied field (assuming $E = 1 \times 10^5$ V/m) is 6×10^{-9} N. For agglomerates F_{ix} can become important for q is proportional to d_p^2 (31).

For completeness of the forces analysis, this force is included in the computer program and the boundaries defined as shown in Figure 2.3.

4.10 The Dimensionless Trajectory Equations with Inclusion of Electrical Number

Equation (4.20) which is the applied field potential equation without space charge, when with $V_p = 0$ reduces to,

$$V = \frac{V_a\, C\, (r - R)}{r\, (C - R)} \qquad (4.42)$$

Therefore the electric field components are,

$$E_x = \frac{R\, C\, V_a\, x}{(x^2+y^2)^{3/2}\, (R-C)} \qquad (4.43)$$

$$E_y = \frac{R\,C\,V_a\,y}{(x^2+y^2)^{3/2}(R-C)} \qquad (4.44)$$

From the dimensionless trajectory equations given by equations (2.12) and (2.13) the dimensionless applied field forces components F^*_{appx}, F^*_{appy} are defined as,

$$F^*_{appx} = \frac{F_{appx}}{B_1} = \frac{q\,E_x}{3\pi\mu d_p U_o} \qquad (4.45)$$

$$F^*_{appy} = \frac{F_{appy}}{B_1} = \frac{q\,E_y}{3\pi\mu d_p U_o} \qquad (4.46)$$

Combining equations (4.43) and (4.45) and with the dimensionless distance quantities x^* and y^*,

$$F^*_{appx} = \frac{q\,R\,C\,V_a}{B_1 d^2(R-C)} \cdot \frac{x^*}{\left((x^*)^2+(y^*)^2\right)^{3/2}} \qquad (4.47)$$

$$F^*_{appx} = N_{app} \cdot I_{appx} \qquad (4.48)$$

where

$$N_{app} = \frac{q\,R\,C\,V_a}{B_1 d^2(R-C)}, \qquad I_{appx} = \frac{x^*}{\left((x^*)^2+(y^*)^2\right)^{3/2}}$$

Similarly,

$$F^*_{appy} = N_{app} \cdot I_{appy} \qquad (4.49)$$

where

$$I_{appy} = \frac{y^*}{\left((x^*)^2+(y^*)^2\right)^{3/2}}$$

The term $\frac{q\,R\,C\,V_a}{d^2(R-C)}$ is equivalent to an electric force whereas B_1 is representative of inertial force. N_{app} generally known as the electrical number (21) therefore is a parameter to assess the importance of electrical forces. I_{app} is the positional parameter.

For the image force, equation (4.41) can be written as,

$$F^*_{ix} = \frac{q^2}{B_1 4\pi\epsilon_o d^2} \cdot \frac{1}{(L^*)^2} \qquad (4.50)$$

$$= N_I \cdot I_{IX}$$

where $L^* = \frac{L}{d}$, the dimensionless distance from the object.

The final dimensionless trajectory equations look like,

$$N_{st}\frac{d^2x^*}{d\tau^2} = U^* - \frac{dx^*}{d\tau} + \underbrace{N_{app}I_{appx} + N_I I_{Ix}}_{\sum F^*_{ex}} \qquad (4.51)$$

$$N_{st}\frac{d^2y^*}{d\tau^2} = V^* - \frac{dy^*}{d\tau} + \underbrace{N_{app}\, I_{appy}}_{F^*_{ey}} - G^* \qquad (4.52)$$

Similarly, the other electrical forces equations can be manipulated to yield dimensionless quantities. Equations(4.51) and(4.52) were used in the trajectory calculation. The calculation of the Stokes number N_{st} and the electrical number enablesone to consider the influence of electrical forces in an electrodynamic flow.

4.11 Summary

For the trajectory calculation, at a specific point under consideration, the evaluation of the field strength is required for calculation of the electrostatic forces. Using a simple model for a point-plane electrode geometry equations for field intensity and potential with and without space charge effect were derived. Three of the electrical force fields analysed in Chapter 1 were considered. To test the validity of the model, theoretical predictions were compared with experimental result for ionic clouds obtained by

Corbett (10). The prediction agreed reasonably whilst the shape and behaviour of the experimental curves were well predicted.

Also the space charge effect was shown to be responsible for the suppression of field strength at the corona region and enhancement near the object. The value of the space charge density calculated was of similar magnitude as the measured value.

It was demonstrated that with decreasing space charge density, its effect on the applied field distribution correspondingly became less pronounced. This led to the establishment of a criterion which would assess the importance of the space charge effect. If it is satisfied the charge density influence can be ignored.

There was no experimental data available for the comparison of charged particulate clouds. However, if the total charge density due to the contribution of the ionic and the charge particulate components can be evaluated, the model should adequately describe the modified field distribution.

CHAPTER 5

CORONA WIND EFFECT

5.1 INTRODUCTION

When ions in a partially ionised medium (gases and insulating liquids) move under the influence of an electric field, there is momentum transfer to the carrier medium due to friction. The resulting air movement is variously known as the electric wind, corona wind or electric aura. This mechanical force produced is appreciable if ions of only one sign are present.

The corona wind was one of the earliest manifestations of gaseous discharge. Although it attracted the attention of a host of eminent scientists including Faraday, Maxwell and Newton, the literature on this topic is scarce indeed. In 1962 Robinson (51) gave the most complete historical account of applying this ion drag phenomenon to fluid pumps, high voltage generators, loudspeakers, thermoelectric convertors and other devices. Then there was a lull in this research until recently when this mechanical wind was found to be of significant influence in electrostatic precipitation and electrostatic powder coating processes. The published experimental data showed a great variation in magnitude depending on the experimental conditions.

The literature is reviewed in this section and a model based on Robinson's study is adopted to estimate the effect of corona wind in EPS.

5.2. PREVIOUS STUDIES OF CORONA WIND

Stuetzer (52, 53) gave one of the earliest complete accounts of theoretical and experimental investigation of an ion drag pump for insulating fluids. The first investigation (52) of static pressure generation showed that pressure of the order of 10 mm of water in gases under atmospheric pressure and of 1000 mm of water in insulating liquids could be obtained in a single stage device. The experiments were conducted with short corona point - earthed electrode distance with a maximum value of 4 cms.

In EPS, Singh (54) using the energy conservation principle, obtained an expression by equating the kinetic energy and energy stored in unit volume of material in an electric field. The corona wind velocity V_c is approximated by,

$$V_c = \left(\frac{\epsilon_o}{\rho_a}\right)^{\frac{1}{2}} E \qquad (5.1)$$

where ρ_a = air density

For $E = 2.4 \times 10^5$ v/m, V_c is of the order of 0.67 m/s.

Experimental measurements (55) showed that generally in powder coating process, V_c assumed a value of about 1 m/s . Near the corona point, where the field strength was highest, V_c could attain a maximum value of about 5 m/s . Experiments were conducted using both hot wire anemometer and laser Doppler anemometer and Figure 5.1 shows schematically the experimental set up. The introduction of a wire screen for removal of ions generated by the corona point might however lead to a generation of a secondary stream of corona wind due to the interaction of the corona point and the screen. The experimental value obtained therefore could be an overestimation of the true electric wind velocity. The magnitude of the wind velocity was found to be consistent between the corona point and the collecting electrode.

Recently various studies were conducted to examine the ionic wind effect in electrostatic precipitation. Adachi (56) first

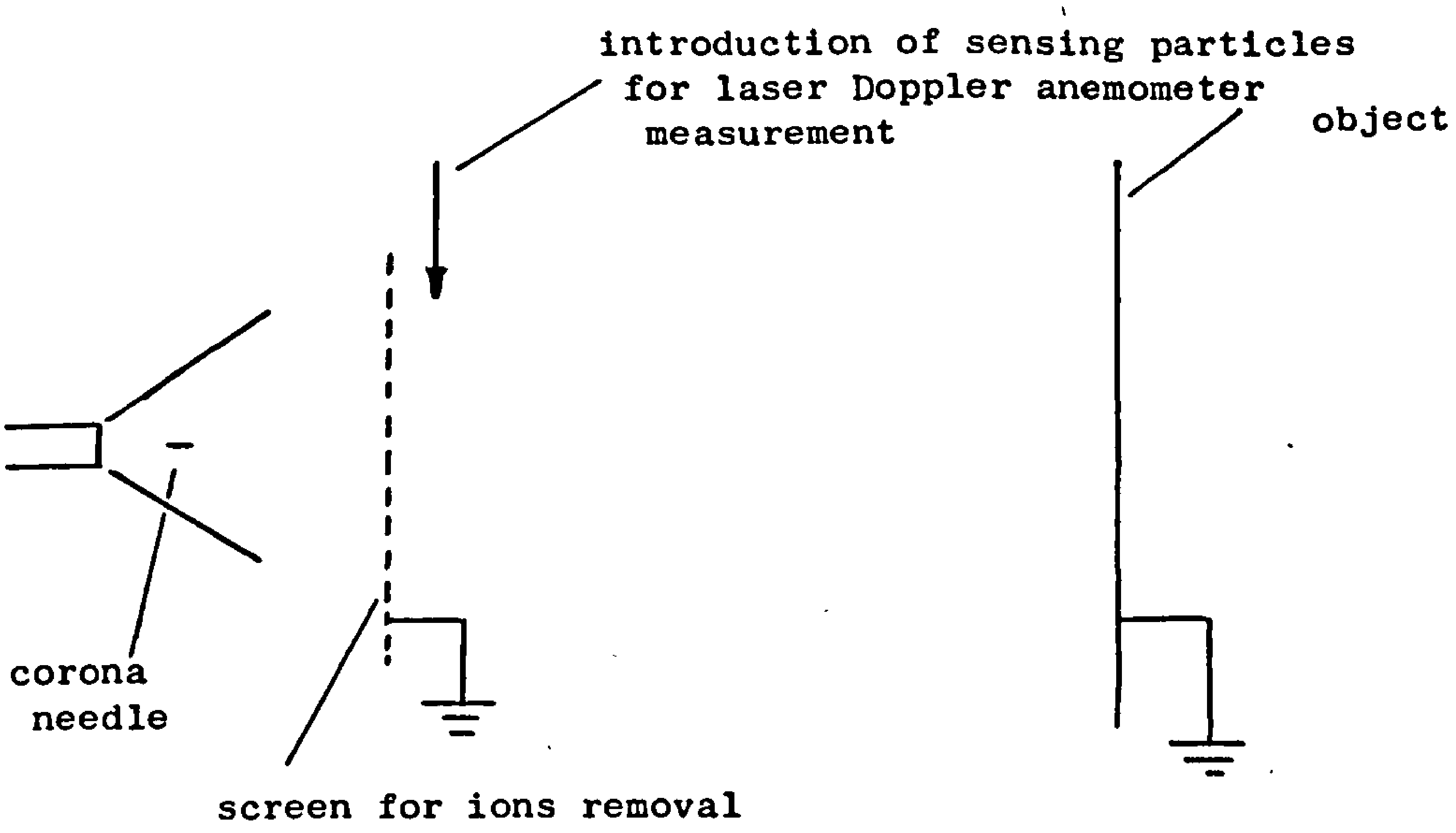

Figure 5.1. Schematic representation of ionic wind velocity measurement experiment (55)

introduced the use of Schlieren photography as an effective method of measuring ionic wind. Schlieren photography is an optical technique for showing up in visible form any local variation in refractive index in a transparent field of view, usually invisible to the naked eye. The objective was to establish the usefulness of the technique by obtaining Schlieren photographs for needle-plate, wire-plate and wire-net electrode geometries. Using a wire-net electrode arrangement with a 2.0 cm separation, a value of about 2 m/s was obtained for an applied voltage of 18 KV. Various types of ionic wind, viz positive, negative, secondary, alternating current and reverse ionisation ionic winds were identified (57). The distributions of positive and negative winds were studied for a needle/plate electrode geometry and Figure 5.2 illustrates some of the experimental results.

Masuda et al (58) using the laser Doppler anemometer showed that

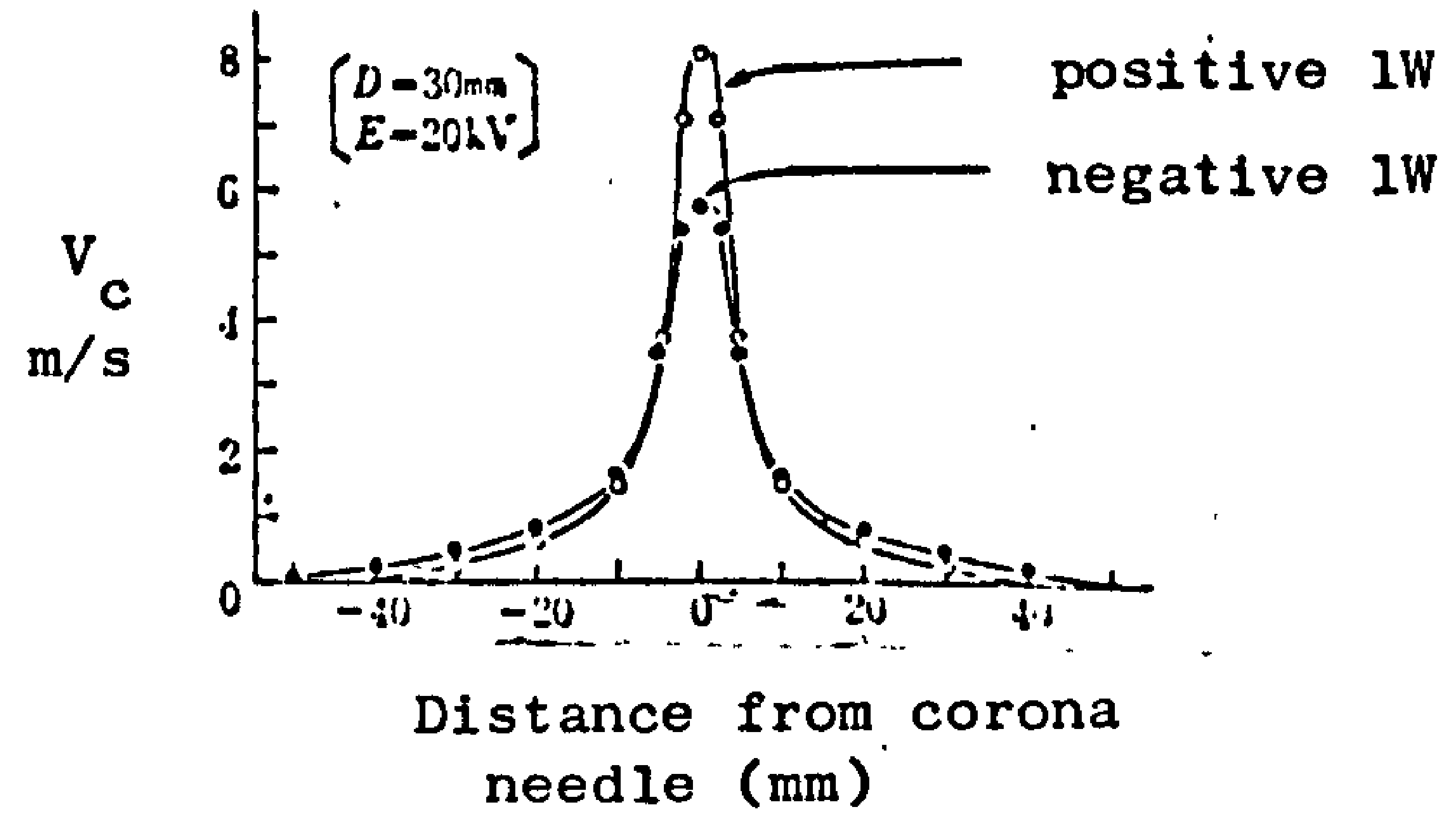

D = separation distance
E = applied voltage

(a) Distribution of positive and negative ionic winds

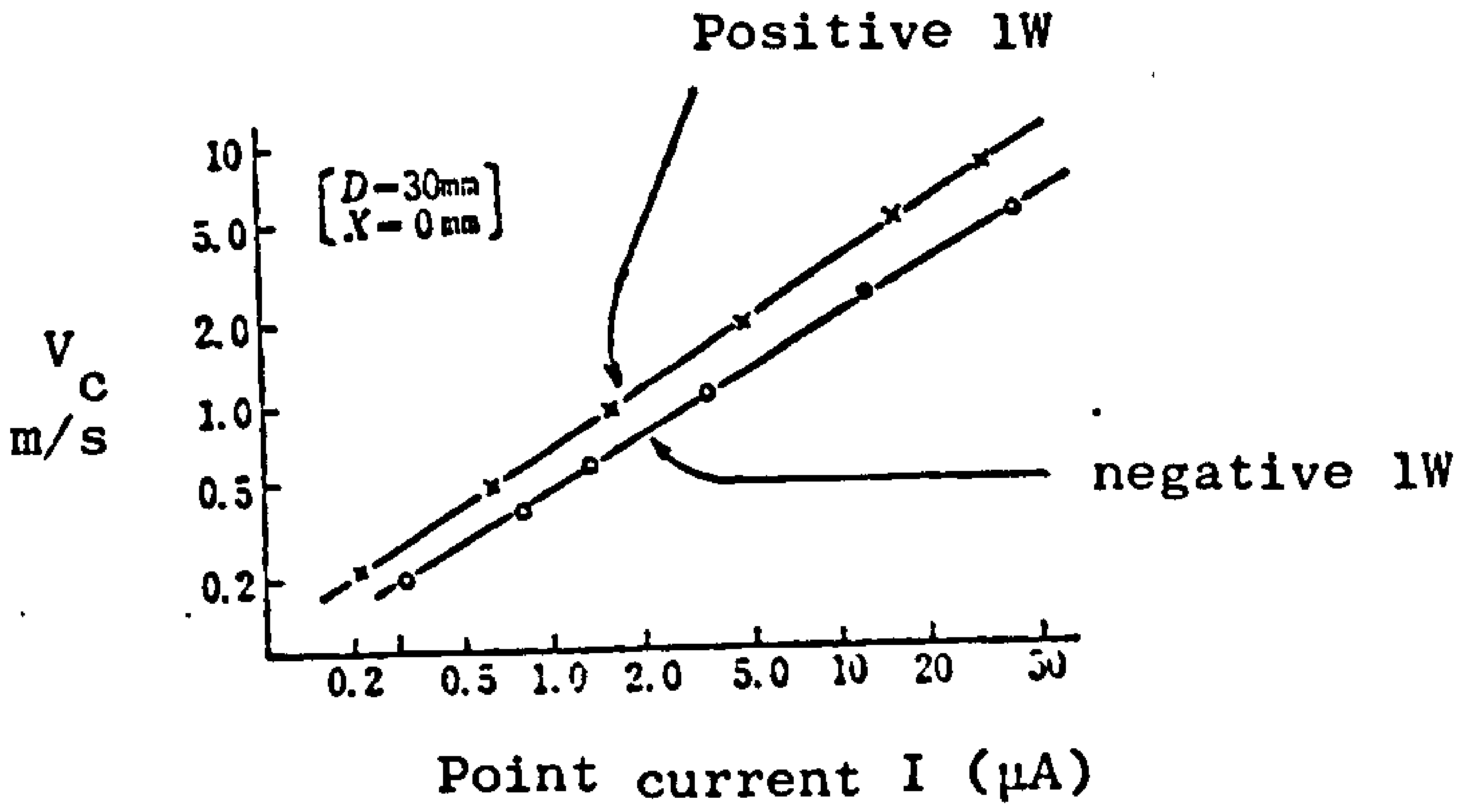

(b) Magnitude of ionic winds at corona point with different point currents

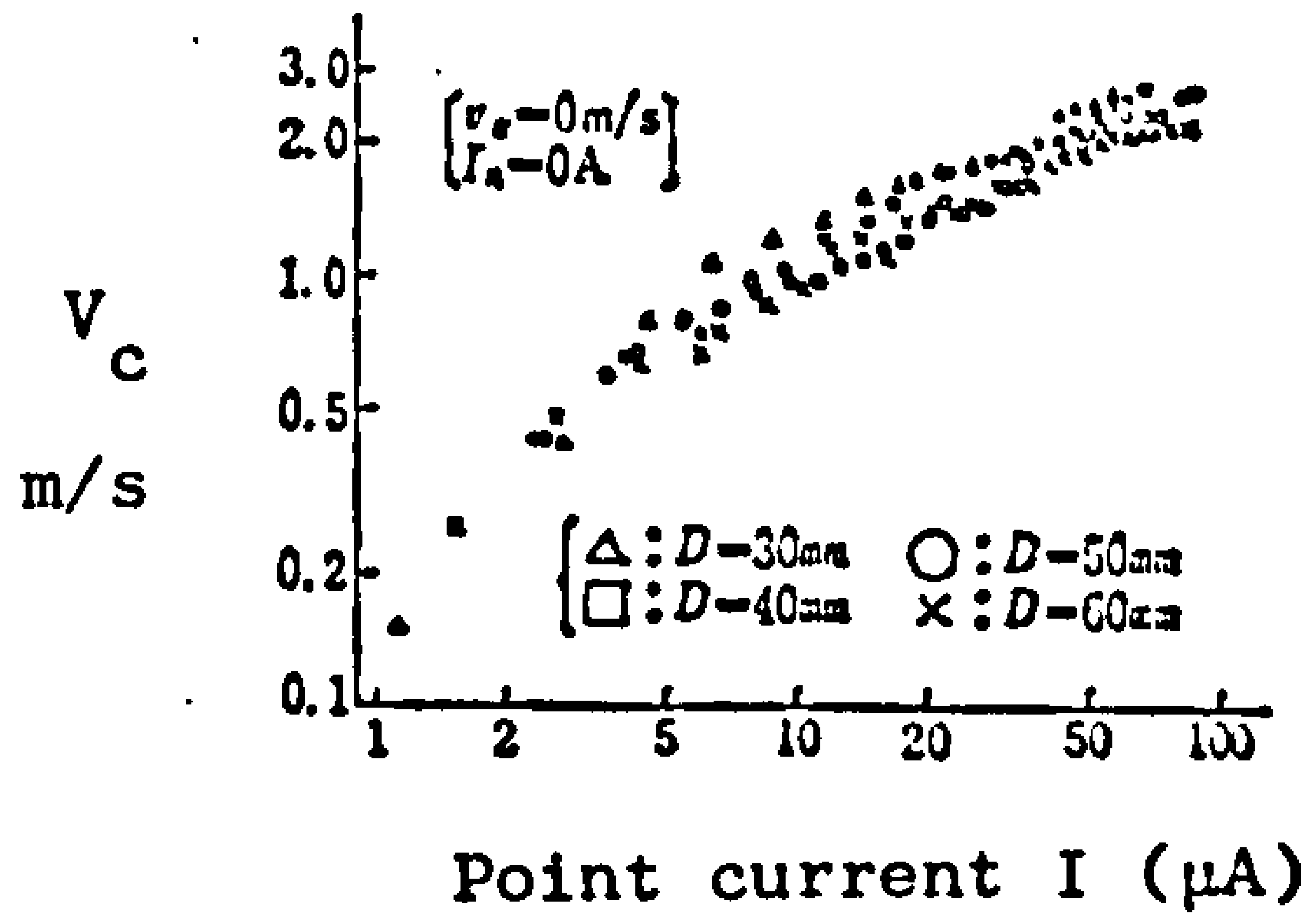

(c) Variation of ionic winds with separation distance

Figure 5.2 Ionic wind distribution

(figures reproduced from Reference (57))

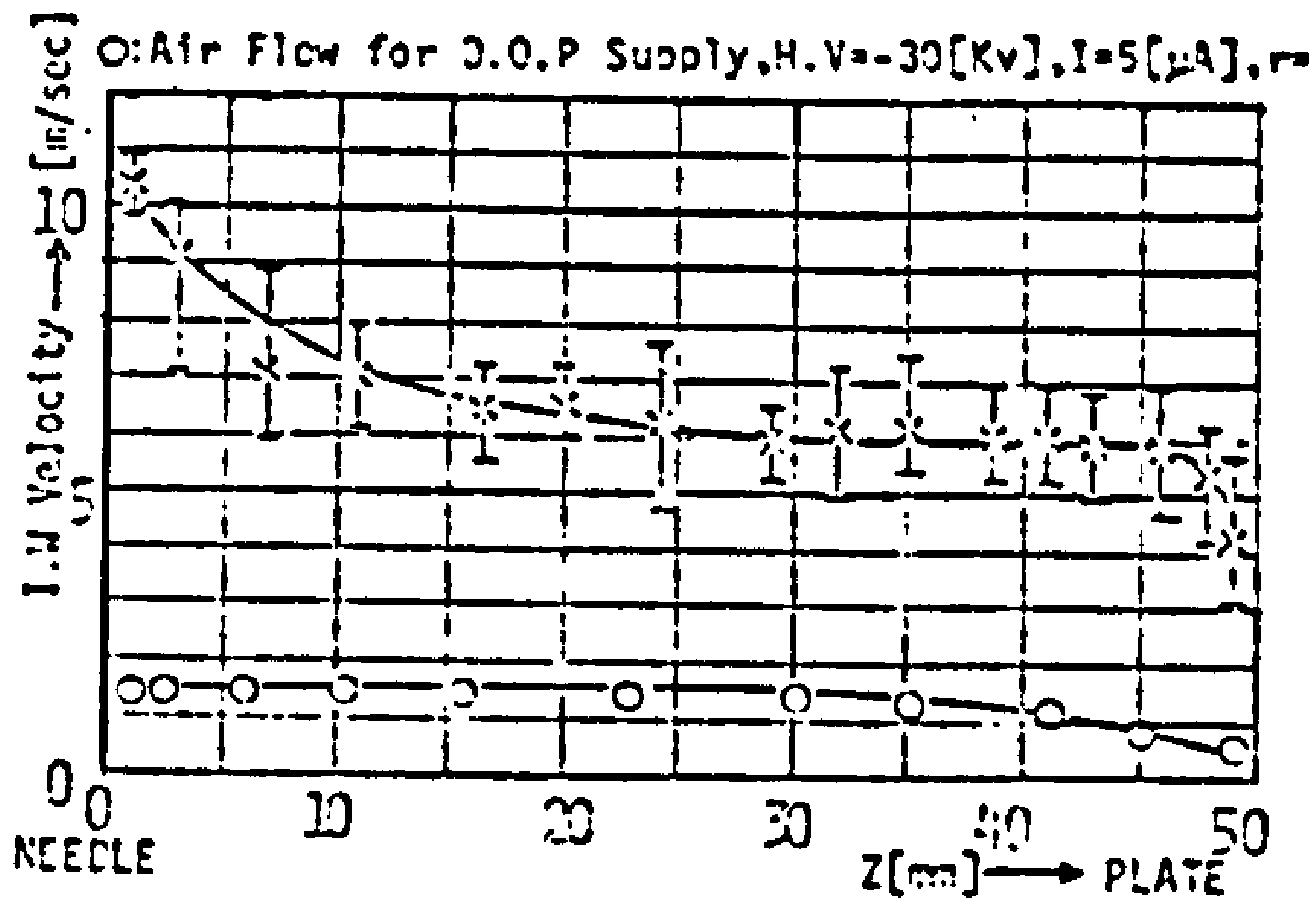

Figure 5.3 Negative ionic wind distribution (58)

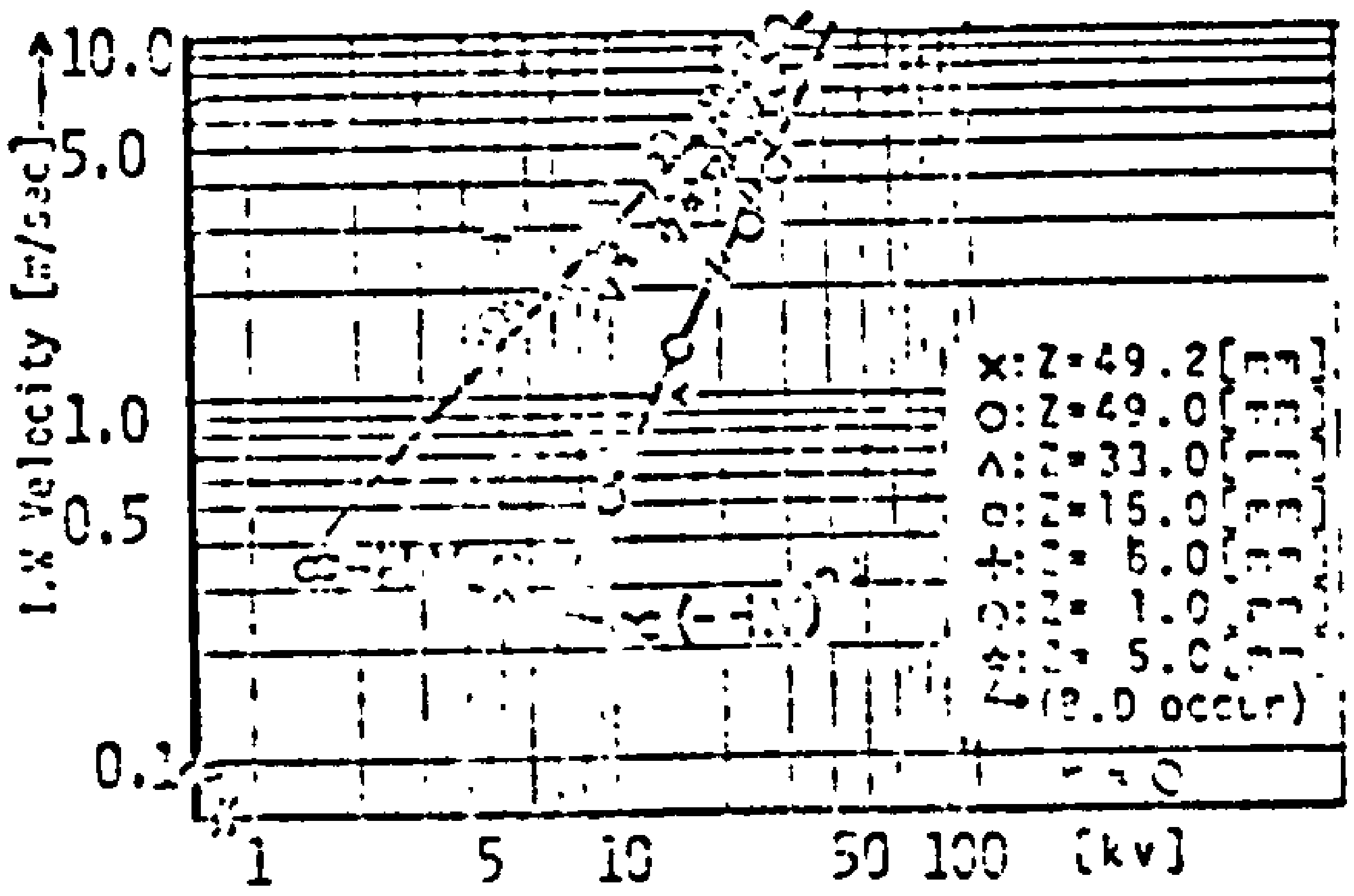

Figure 5.4 Negative ionic wind distribution (58)

the electric wind velocity could be important in the transport of fine particles of several microns in electrostatic precipitation. Figure 5.3 shows the wind velocity distribution for negative corona with an electrode separation of 5 cms. The maximum velocity of 10m/s occurred in the vicinity of the needle tip and for the most part the value was between 6-7 m/s . Near the electrode a relatively high value of 4m/s was measured. Figure 5.4 illustrates the dependence of the velocity on V the voltage. Near the electrode the velocity was proportional to V^2 whilst further away it was proportional to V. With the occurrence of back ionisation, magnitude of 7-10 m/s . near the object surface was observed.

To date Adachi et al (34) presented the most detailed calculation of ionic wind velocity. Briefly described here is the theoretical treatment which involves solving Navier-Stoke's equation with inclusion of the Coulombic force for two dimension. The Coulomb force density is defined as,

$$F = \rho E \qquad (5.2)$$

where F has the dimension of force per unit volume. The distribution of field E is obtained from solving Poisson's equation using a Relaxation method. With the inclusion of equation (5.2), Navier-Stoke's equation is ,

$$\frac{\delta u}{\delta t} + \frac{\delta u^2}{\delta r} + \frac{u^2}{r} + \frac{\delta uw}{\delta z}$$

$$= -\frac{1}{\rho_a}\left\{\frac{\delta p}{\delta r} - F_r\right\} + \gamma\left\{\frac{\delta^2 u}{\delta r^2} + \frac{\delta}{\delta r}\left(\frac{r}{u}\right) + \frac{\delta^2 u}{\delta z^2}\right\}$$

$$\frac{\delta w}{\delta t} + \frac{\delta uw}{\delta r} + \frac{uw}{r} + \frac{\delta w^2}{\delta z}$$

$$= -\frac{1}{\rho_a}\left\{\frac{\delta p}{\delta z} - F_z\right\} + \gamma\left\{\frac{\delta^2 w}{\delta r^2} + \frac{1}{r}\frac{\delta w}{\delta r} + \frac{\delta^2 w}{\delta z^2}\right\}$$

(5.3)

where u, w = velocities in (r, z) respectively

ρ_a = air density

p = pressure

γ = kinematic viscosity

Also the Continuity equation is described by,

$$\frac{\delta u}{\delta r} + \frac{u}{r} + \frac{\delta w}{\delta z} = 0 \qquad (5.4)$$

Using a Eulerian cell method, a set of difference equations are generated by combining equations (5.3) and (5.4). Coupled with the difference equations, a special numerical technique, "delta - p " method is used to consider the pressure difference at each step to calculate the wind velocity distribution. The experimentally measured value of wind velocity at the needle tip was used as the boundary condition. Figure 5.5 shows the comparison of calculated values and experimental data obtained using Schlieren method and laser Doppler anemometer.

The main arguement against the use of laser Doppler technique is the measured velocities of the submicron particles required to produce the 'Doppler shift effect' may be exaggerated. The particles are charged and consequently are subjected to the electrostatic field forces as described in Chapter 4. Calculation of the migration velocity w (equation (4.30)) shows that for a 0.3 μm DOP (dioctylphthalate) particle in a field of 6.0×10^5 v/m ($\epsilon = 8.5$), w has a value of 0.04 m/s. For 0.3 μm particle diffusion charging is the more important mechanism and the charge acquired is several times that due to ion bombardment charging process (59). Therefore the magnitude of w may be considerably higher. Provided the ionic wind velocity is significantly higher than about 1 m/s the laser Doppler data may accurately represent the ionic wind velocity.

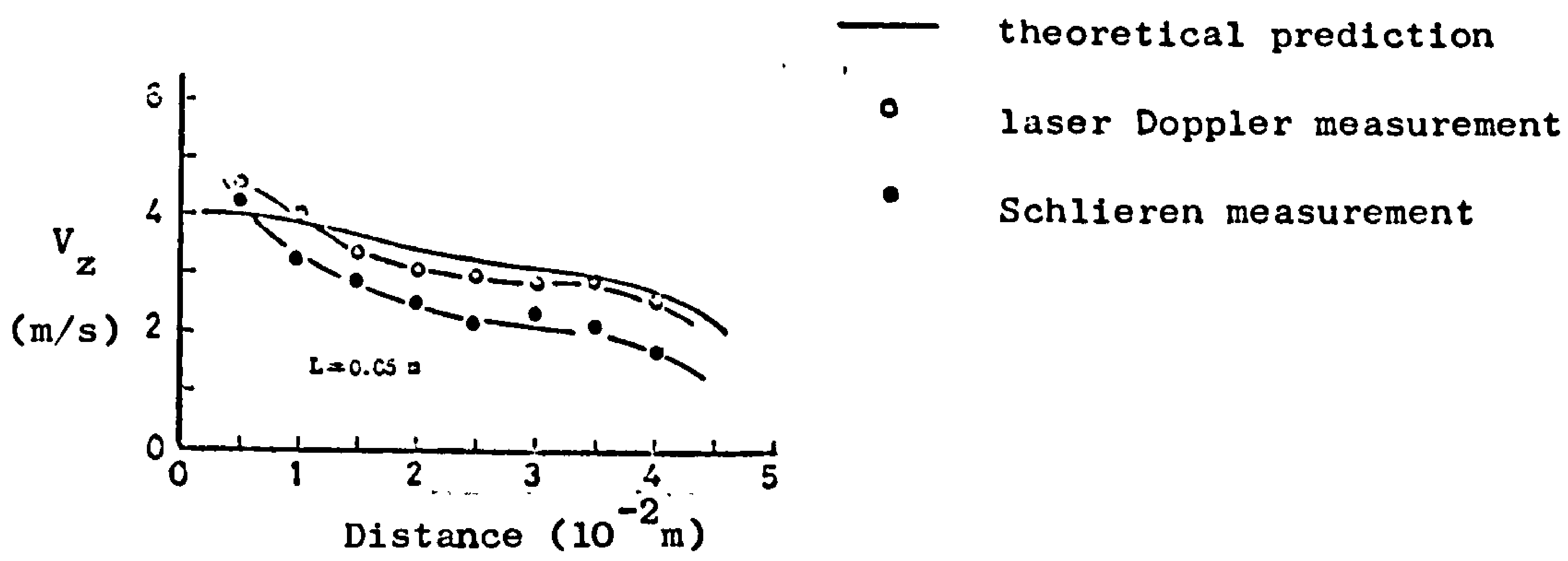

(a) for applied voltage $V = -2.0 \times 10^4$ V

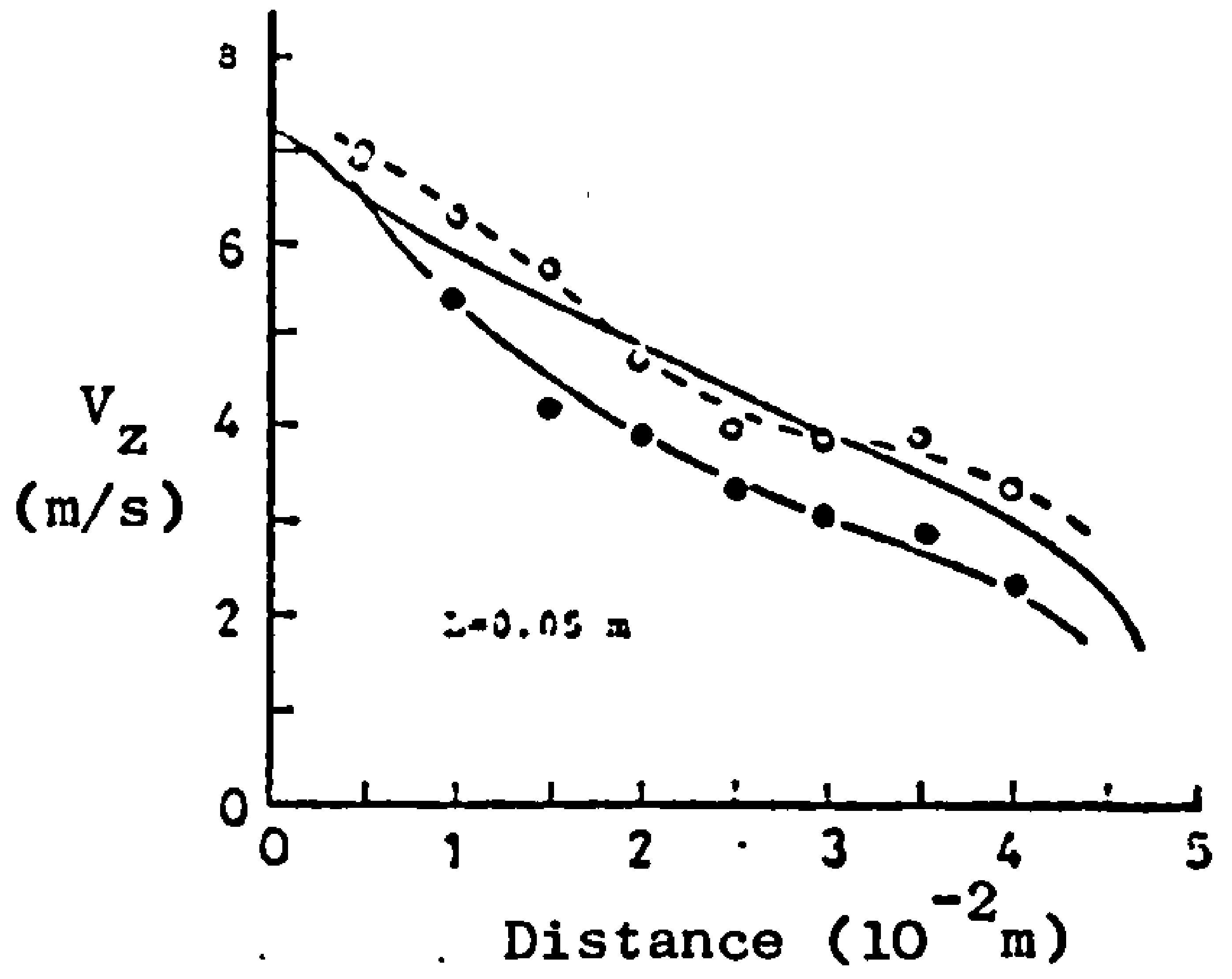

(b) for applied voltage $V = -3.0 \times 10^4$V

Figure 5.5. Comparison of theoretical prediction and experimental data for ionic wind velocity distribution along the axis (34)

Figure 5.5 shows that generally there is a difference of about 1 m/s between the results of laser Doppler method and Schlieren method. This can be attributed to the influence of the applied field forces. Under typical EPS conditions, the ionic wind velocity measured was about 1 m/s (55). Although the laser Doppler technique was employed, the particle charging was minimised by introducing a screen to effectively remove the ions. However, the screen would distort the original electric field and could also lead to secondary corona wind generation. Therefore although the laser Doppler anemometry is a very accurate technique, the Schlieren method appears to be a more suitable method because of its non-electrical interference.

Robinson (60) in the study of electrostatic blower proposed an approximate theory which is discussed in the next section. The ionic wind velocity was found to be a linear function of the voltage and this is consistent with the result shown in Figure 5.3. The velocity was also found to be proportional to the square root of the current. With an electrode separation of about 4 cms a maximum value of 4 m/s. was measured (maximum applied voltage of 60 kv and maximum current of 600 μ A). The potential of the blower was found to be very limited with a very low electrokinetic efficiency of about 1%. There was good agreement between the experimental and theoretical values. The theory, very similar to Stuetzer's (52,53) although appeared oversimplified when compared with Adachi's (34) sophisticated approach was found to be widely applicable to a variety of geometries.

5.3 THEORY OF CORONA WIND

The Coulombic force density of equation (5.2) represents the electrical force exerting on a unit volume of charged air. The force per unit volume has to be balanced by an ion drag pressure gradient of equal amount, resulting in

$$\nabla p = \rho E \qquad (5.5)$$

The total ionic velocity V_t consists of two components, viz the velocity of the charge movement with ion mobility of μ and the electric wind velocity V_c.

$$V_t = V_c + \mu E \qquad (5.6)$$

Equation (4.24) which describes the current density j is modified to,

$$j = \rho V_t = \rho (V_c + \mu E) \qquad (5.7)$$

Combining equations (5.5) and (5.7) leads to,

$$\nabla p = (j - \rho V_c)/\mu \qquad (5.8)$$

ρV_c represents the passage of current due to the mechanical wind generated by ion movement.

In gases, ρV_c can be neglected although in liquids, ρV_c is comparable to j. To emphasise the point, for air μE assumes a value of 22 m/s when $E = 10^5$ v/m and $\mu = 2.2 \times 10^{-4}$ m^2/v/s and μE for liquid is significantly less since μ is of the order of 10^{-7} m^2/v/s. Therefore the neglection of V_c term in equation (5.7) is justified.

Therefore,

$$\nabla p \approx \frac{j}{\mu} \qquad (5.9)$$

If r is the distance from the corona point,

$$\frac{dp}{dr} = \frac{j}{\mu} \qquad (5.10)$$

Thus,

$$p = \int_{r_c}^{r} \frac{j}{\mu} \, dr \qquad (5.11)$$

where r_c is the coordinate of the discharge point.

$$p = \frac{j}{\mu}\Big[\, r \,\Big]_{r_c}^{r} \qquad (5.12)$$

Without the simplifying assumption of neglecting the V_c term, Stuetzer's(53) derivation gives,

$$p = \frac{\varepsilon}{2}\left[\frac{2\,j\,r_d}{\varepsilon\,\mu} - 2\,\frac{V_c}{\mu}\left\{\left[\frac{2\,j\,r_d}{\varepsilon\,\mu} + \left(E_o + \frac{V_c}{\mu}\right)^2\right]^{\frac{1}{2}} - \left(E_o + \frac{V_c}{\mu}\right)\right\}\right] \qquad (5.13)$$

where r_d = collecting electrode distance

E_o = discharge electrode field

Equation (5.13) reduces to equation (5.12) when $V_c = o$ and $r = r_d$ with $r_c = o$.

The aerodynamic back pressure with air velocity V due to the electrical pressure is,

$$p = L\,\rho_a\,V^2/2 \qquad (5.14)$$

where L = loss factor

ρ_a = air density

Combining equations (5.11) and (5.14) yields,

$$V_c = \left[\frac{2}{L\rho_a\,\mu}\int_{r_c}^{r} j\,dr\right]^{\frac{1}{2}} \qquad (5.15)$$

Equation (5.15) is Robinson's equation and defines the relationship between the corona wind velocity and the current density.

Using equation (5.15), an equation for corona wind velocity and the field strength is derived as follows. With Poisson's equation,

$$\nabla . E = \frac{\rho}{\varepsilon} \qquad (5.16)$$

and equation (5.7),

$$j = \varepsilon \ \nabla . E \ (V_c + \mu E) \qquad (5.17)$$

Again neglecting V_c the equation becomes,

$$j = \varepsilon \ \mu E \ \nabla . E \qquad (5.18)$$

Substituting equation (5.18) into equation (5.15),

$$V_c = \left[\frac{2\varepsilon}{L \rho_a} \int E \ \frac{dE}{dr} \ . \ dr \right]^{\frac{1}{2}} \qquad (5.19)$$

Integration of equation (5.19) yields,

$$V_c = \left[\frac{\varepsilon}{L \rho_a} \left(E_r^2 - E_d^2 \right) \right]^{\frac{1}{2}} \qquad (5.20)$$

At the collecting surface, assuming a perfect sink situation $E_d = 0$ and equation (5.20) becomes

$$V_c = \left(\frac{\varepsilon}{L\rho_a} \right)^{\frac{1}{2}} E_r \qquad (5.21)$$

This is the same expression as equation (5.1) with a loss coefficient of unity and it represents the maximum corona wind velocity in a system when $E_r = E_o$, i.e. the corona point field.

For the present work $E_o = 3 \times 10^5$ v/m with a resultant V_c of 0.81 m/s in the corona region. Although the calculated value is not experimentally verified, the low magnitude is evident by two observations,

(i) There was no significant difference in the velocities of emerging charged and uncharged particles near the corona region in the experimental particle trajectories. Otherwise a high ionic wind velocity would undoubtedly enhance the velocity of emerging charged particles.

(ii) Professor Kinnersley (51) in 1952 stated " you may feel the fire .... (a point) discharges blow on your hand as a cool wind". By utilising the sensation of feel, the relative magnitude of the "cool wind" and an air jet with known emerging jet velocity could be crudely compared. This experiment eliminated the possibility of occurrence of high ionic wind velocity.

Equation (5.21) is used in this work to estimate the wind velocity and the sphere of influence is confined to the same boundaries as the other electrical forces present.

5.4 CONCLUSION

Although the ionic wind phenomenon has been known for a long while, there is a distinct lack of literature on the subject. Without entailing complex computational analysis Robinson's (60) simplified theory was found to be widely applicable to a variety of simple geometries. The approach of Adachi (34) should be pursued since it gives a more detail analysis of the ionic wind distribution. Published experimental data showed that the velocity could be considerable under certain experimental conditions and its importance as regards to influencing the performance of the process must be examined. In EPS the velocity is typically about 1 m/s and its affect on the particle trajectories is assessed in Chapter 7.

CHAPTER 6

Experimental Investigation of Particle Trajectories

6.1 Introduction

In the experimental study of particle trajectories in the EPS process, one must bear in mind the several constraints in the choice of the experimental technique and the design of the experimental system:

(i) The technique must afford high resolution of the particle trajectories in both time and space.

(ii) For the comparison with calculated particle trajectories, the quantities required are positional variation with time and particle velocities.

(iii) The introduction of measurement probe must be avoided as both the electrostatic field and air flow must remain undisturbed. Also in the high voltage environment, unprotected sensitive measurement probe may suffer damages because of possibility of corona discharges especially if the instrument contains sharp edges.

A survey of the literature showed that there are two particle tracking techniques viz. laser Doppler anemometer and photography conforming to the conditions listed above. A brief review of other local particle velocity measurement techniques is given by Birchenough (97). Although the laser Doppler system is capable of producing a continuous and instantaneous accurate particle velocity display, the photographic method is preferred in this study because:

(i) The complete 'history' of the flight of a particle can be recorded unlike the laser technique where information is derived only for a focussed spot at any instant. Consequently with the laser Doppler method many measurements are required at various locations to assemble the particle velocity distribution.

(ii) With the laser Doppler system, information of the two velocity components can only be obtained at great expense since two signal processing units are required.

However the photographic technique suffers from some drawbacks notably

(i) dilute suspension has to be used

(ii) due to the optical resolution of the photographic system currently employed, only particles greater than 40 μm can be successfully tracked.

The advantages and disadvantages of the photography method are listed in Table 6.1

Table 6.1 Advantages and disadvantages of photography for particle velocity measurement

Advantages	Disadvantages
relatively cheap equipment cost	use of dilute suspension
two component velocity measurement	size range of particles limited
complete history of particle flight	
no need to determine individual position for measurement	

6.2 Chronophotography

The use of photography as a technique of fluid velocity measurement by tracer particle tracking and a direct measurement technique of particle velocity is reviewed by Somerscales (95). The practical details and the quantitative aspects of accuracy of the various methods were discussed. Broadly there are three categories and they are photography with interrupted illumination or chronophotography which is adopted in the present study, multiple frame movie and streak-point image photography. The principle of operation of chronophotography is as follows. When the field of view of the fluid containing suspended particles is subjected to interrupted illumination, depending upon their position, successive images are recorded on a photographic plate. The velocities of the particles can be calculated from the distance travelled by the particles and the time interval between consecutive bursts of illumination. The angle of flight can also be measured directly from the enlarged photographs. Measurement techniques based on this principle have been used in various particle trajectory studies by Abuaf and Gutfinger (24, 83), Chigier (96), Tyler and Salt (98), Finlay and Welsh (99), Dombrowski and Tyler (100), Gubenskii and Fuchs (101, 102), Briffa and Dombrowski (103), Chandok and Pei (104) and Kane et al (105).

The intermittent illumination can be obtained by two methods. A source of regularly flashing light, like a stroboscope may be used to virtually 'freeze' the motion of the particle. Using this method Tyler and Salt (98) studied the trajectories of spheres being accelerated from rest behind a shock wave in a shock tube. Alternatively the interruption can be obtained either by regulated shielding of the beam from a continuous light source or by interrupting the view of the camera. This is achieved by using a sectored wheel which rotates across the incident light beam or across the line of sight of the camera. Abuaf and Gutfinger (24, 83) using a light 'chopper' studied the entrainment of solid particles in a turbulent air jet. A high power stroboscope was used for the present experimental investigation.

6.3 Experimental Design

6.3.1 General set up

A flow diagram of the apparatus for trajectory measurements is as shown in Figure 6.1 and Figure 6.2 is a photograph of the experimental rig. The set up consisted basically of:

(i) spray booth

(ii) the illumination and observation system

(iii) the powder spraying and powder charging system

6.3.2 The spray booth

The design of the spray booth which housed the test section was primarily governed by several factors with the first two the most important:

(i) the area of the field of view

(ii) the depth of field of the photographic system

(iii) the anticipated range of particle velocities

(iv) the photographic system

(v) the particle size

In EPS system, the spray gun/object separation is generally of the order of 0.3 m and in various investigations the separation was between 0.1 - 0.3 m (e.g. references 8, 24, 74). The compatibility with the theoretical analysis in two dimension would require the smallest achievable depth of field with the photographic system. A series of experiments were conducted to determine the optimay of the size of the spray booth and the area of the test section taking all the factors listed above into consideration. The results were:

size of spray booth - 0.72m x 0.72m x 0.72m

area of visual field - 0.22m x 0.22m

field of view/cameral distance - 0.36 m

Silica gel drying column

Rotameter

Manometer

Stroboscope power unit

Filtration unit

Electrode

Mirror

Discharge lamp

Vibratory spoon particle feeder

Water jet pump

Power supply for spray gun

Microammeter

Spray booth

Cooling fan for discharge lamp

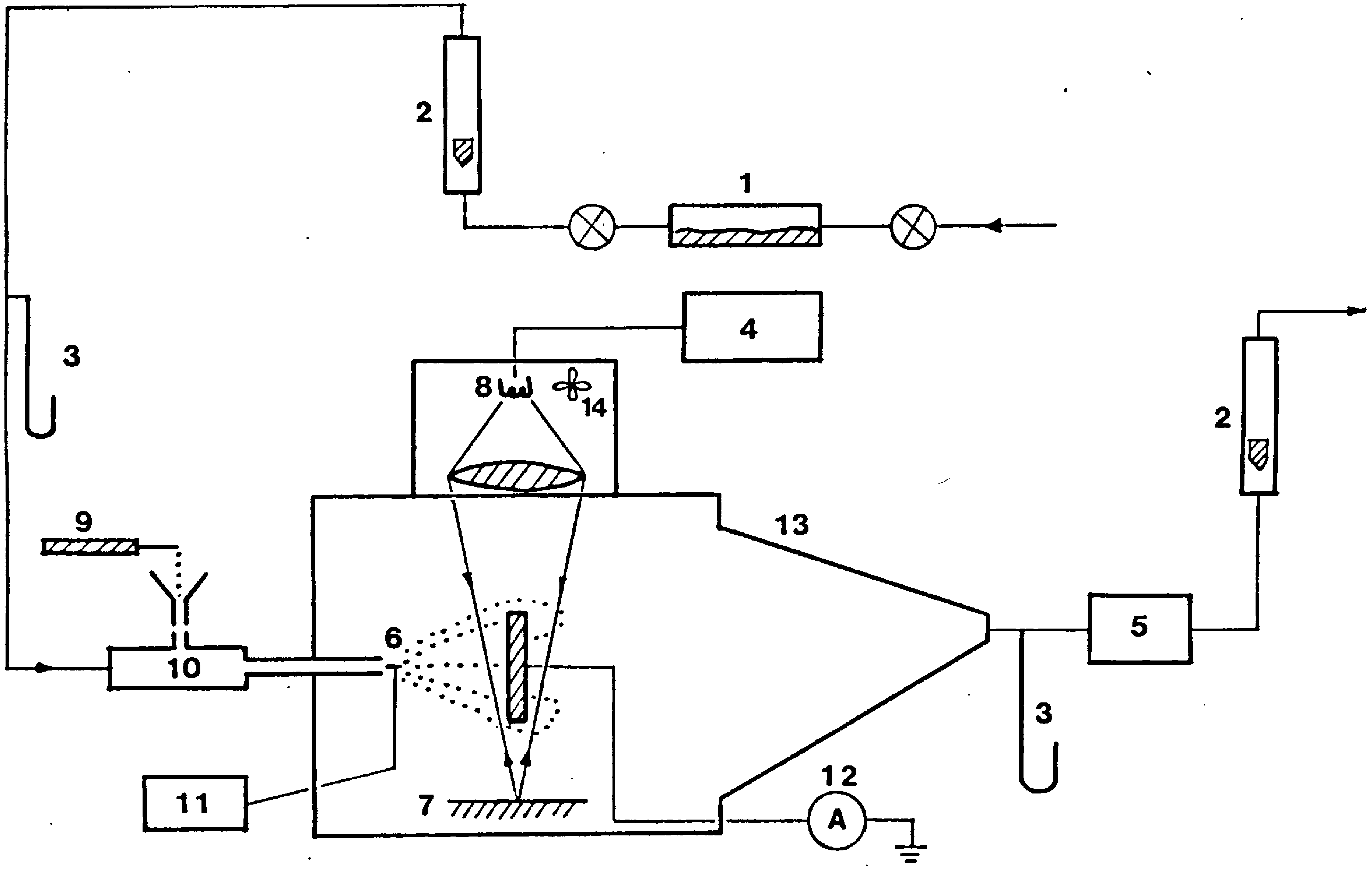

Figure 6.1 Schematic of experimental set-up

With the anticipated particle velocities, the area of view was considered to yield sufficient number of trajectory points for analysis. Also the position of the camera was far enough away from the test section to prevent the interference with the high voltage field. The determination of the depth of field is described in the next section.

The spray booth as shown in Figure 6.2 was constructed with wood with four glass windows to facilitate three dimensional particle tracking if required and for flexibility of the placement of the illumination system. The conical section was designed to permit smooth exit of the secondary air flow. To prevent stray light reflection from the walls reaching the observation system, the spray booth was appropriately lined with black velvet cloth or painted with black matt paint.

The objects to be coated were stainless steel plates of 5.3cm x 5.3cm with the dimension determined so as to conform to the conical geometry for the experimental separation distance. The target was held by an adjustable table mounted on an optical bench. The object position could be finely manipulated in all three directions with an accuracy of ± 2mm. In the design of the adjustable table every precaution was taken to insulate the metallic parts with polythene tubing, perspex and PTFE sheets. Also the object was held as far away as possible from the main part of the holder to minimise the field distortion. All sharp edges were covered thinly with silicone rubber to prevent the formation of corona points. Generally for safety purposes, where appropriate the experimental parts in the spray booth were constructed of non conducting material. Otherwise the parts were carefully earthed.

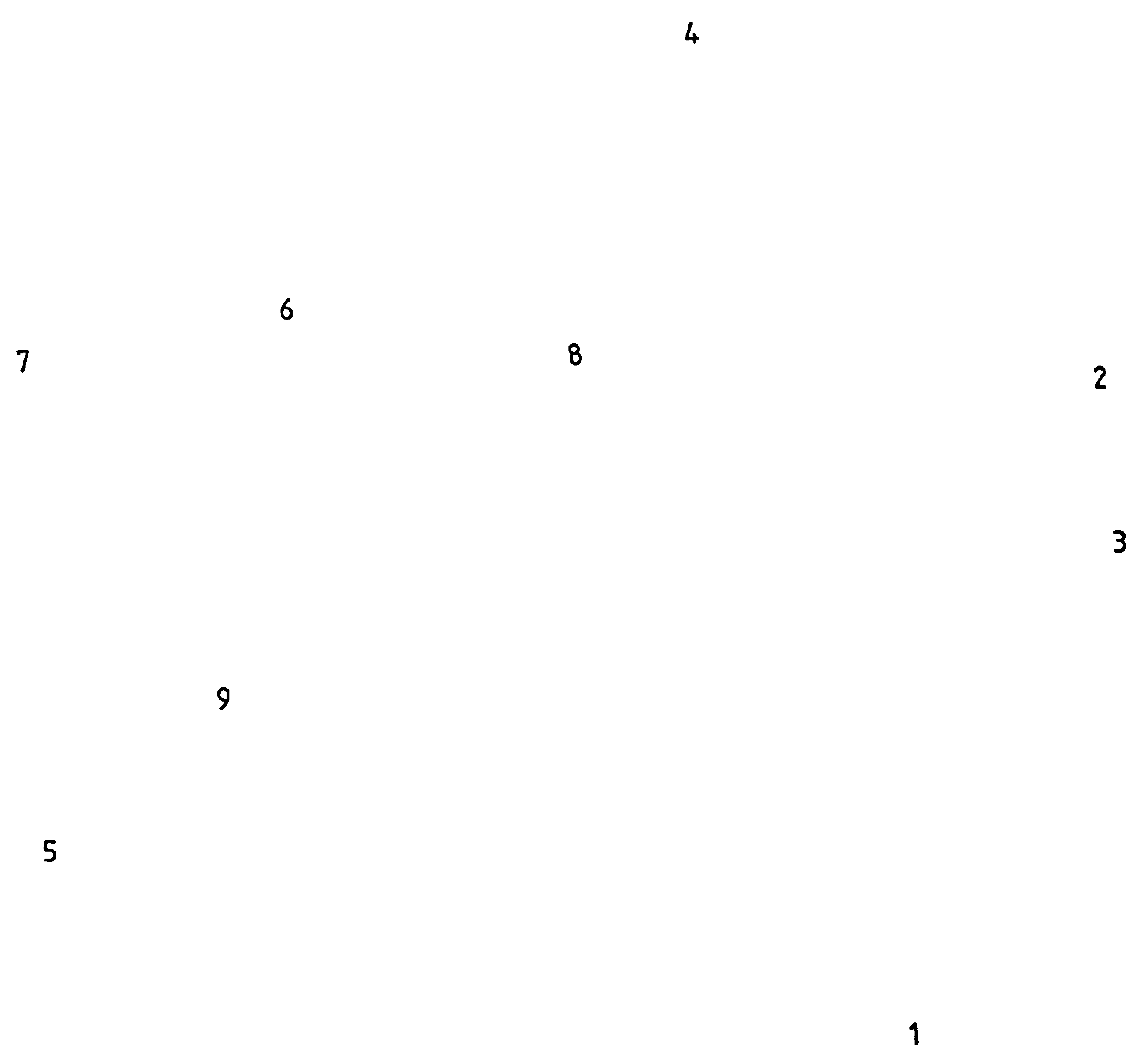

FIG. 6·2 EXPERIMENTAL RIG.

1 Stroboscope cabinet.
2 Spray booth.
3 Graticule / positional location grid.
4 Discharge lamp housing.
5 High voltage generator for the spray gun.
6 Particle feeding unit.
7 Manometer.
8 Electrode assembly.
9 Microammeter.

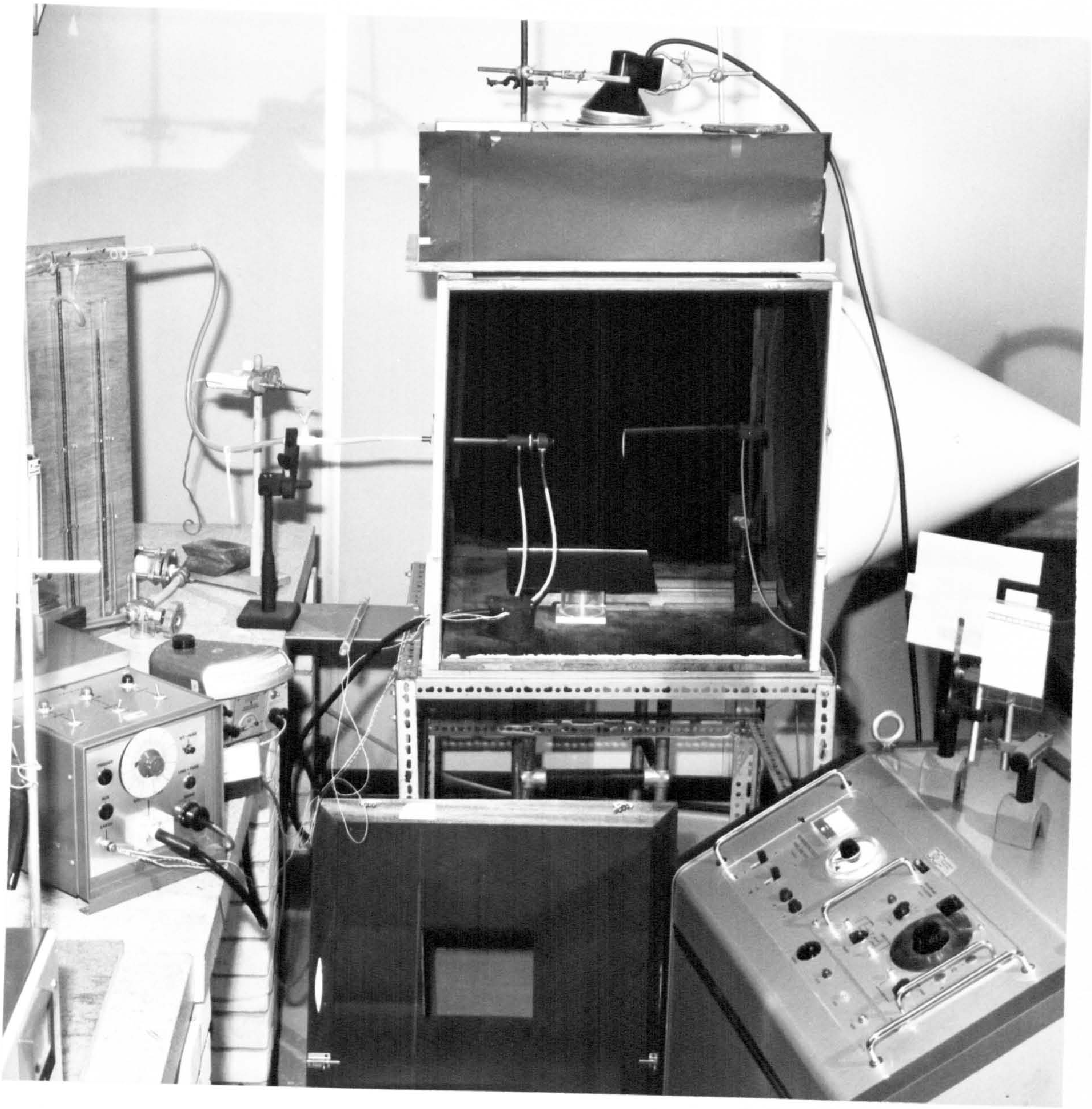

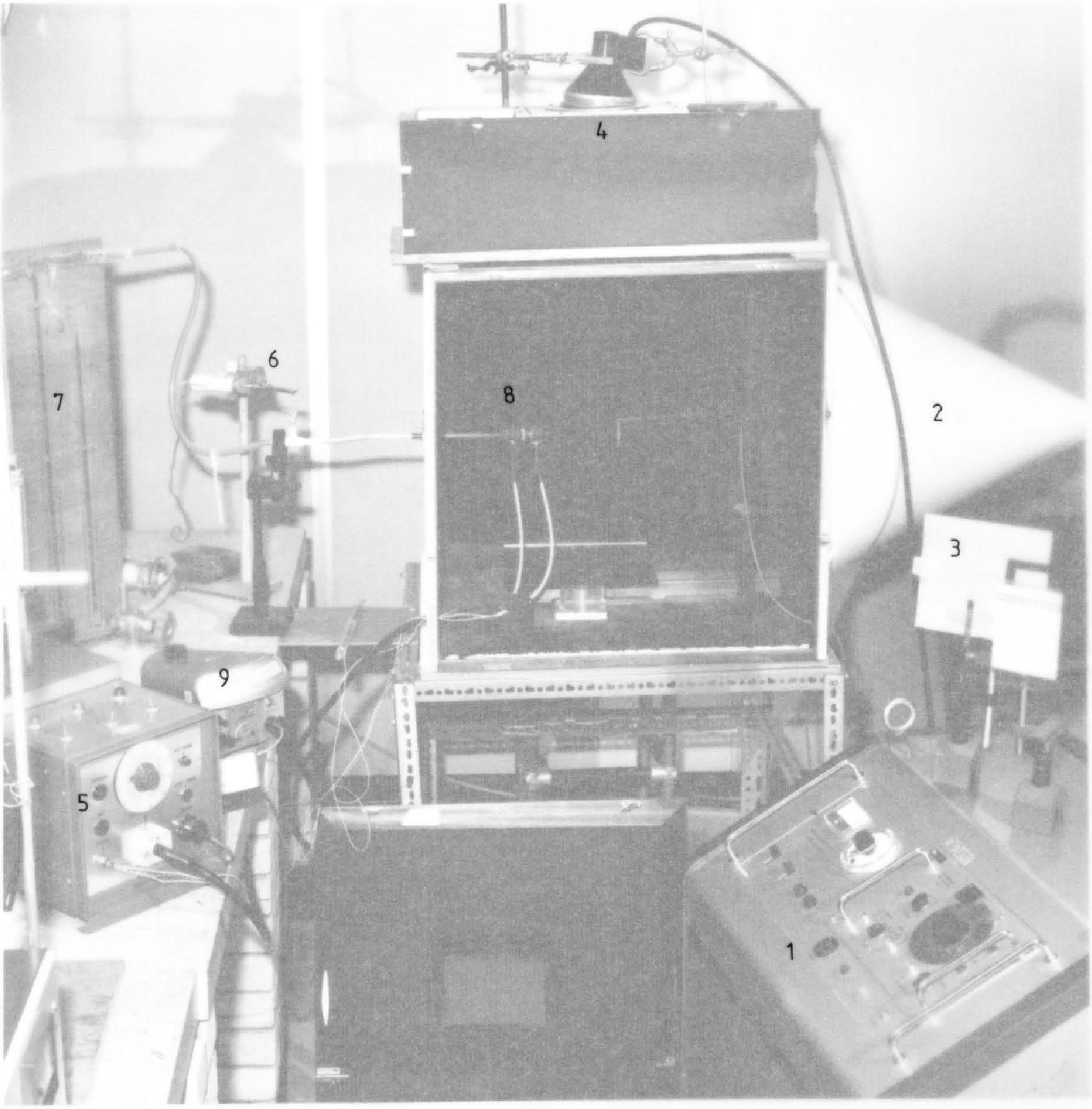

FIG. 6·2 EXPERIMENTAL RIG.

1 Stroboscope cabinet.
2 Spray booth.
3 Graticule / positional location grid.
4 Discharge lamp housing.
5 High voltage generator for the spray gun.
6 Particle feeding unit.
7 Manometer.
8 Electrode assembly.
9 Microammeter.

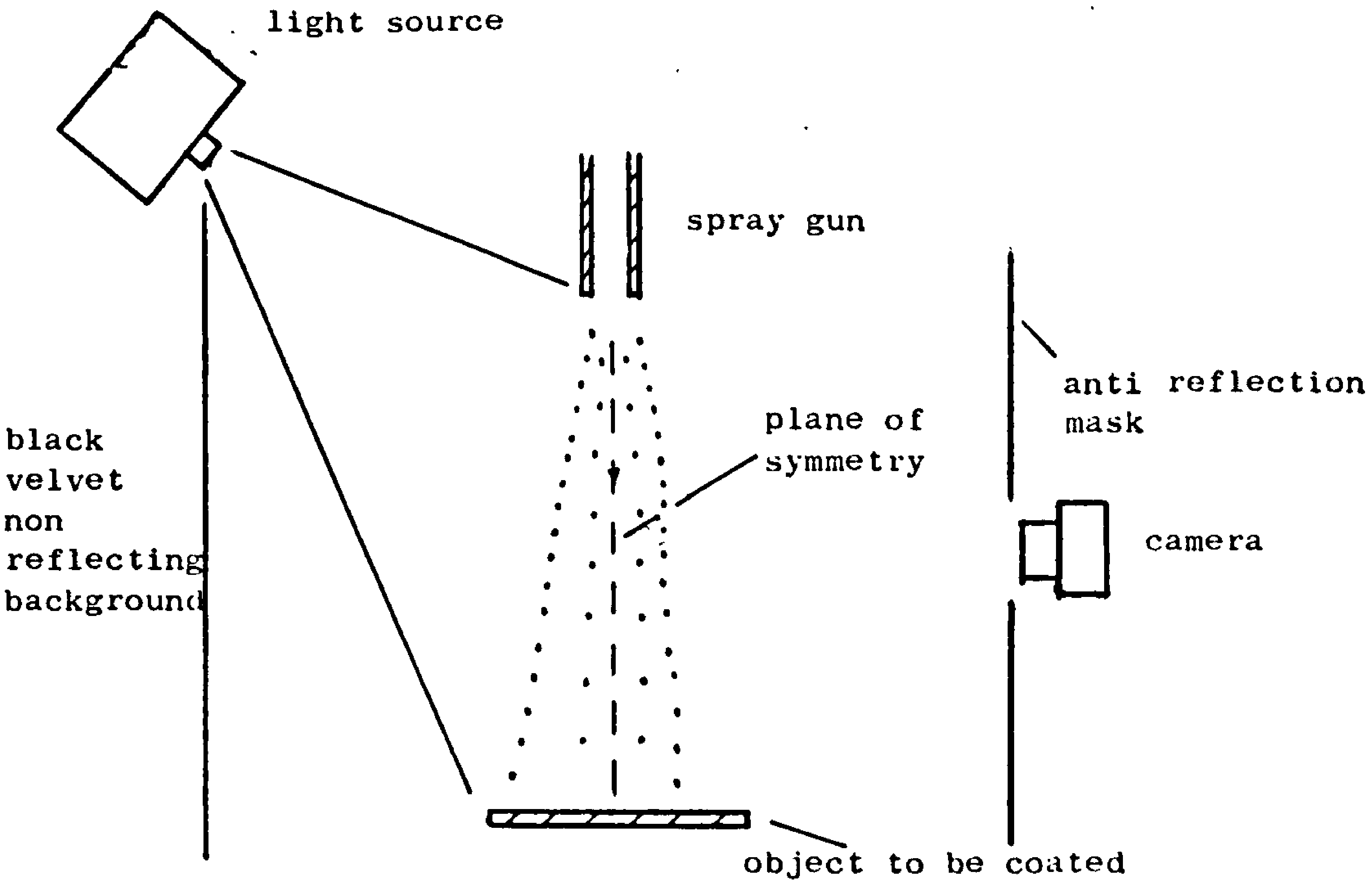

Figure 6.3 General arrangement for chronophotography

Compressed air after passing through a clean air filter and a drying column containing silica gel, flowed through a rotameter and was issued as a free jet. The rotameter was calibrated using a gas meter and a calibration graph enabled direct reading of the air exit velocity. The velocity was also checked using a hot wire anemometer. The nozzle exit velocities were between 6.80 - 10.60 m/s.

6.3.3 The photographic and illumination system

A schematic layout of the photographic and illumination system is as shown in Figure 6.3.

(a) The light source

The interrupted illumination was provided by a high power high speed short duration stroboscope (ERNEST TURNER model HSS/4/K-3). A high voltage power pack of output supplies energy through a suitable charging and smoothing system to a storage capacitor which is discharged through a special form of Xenon filled lamp controlled by a hydrogen thyratron switch. The flash repetition rate can be controlled by an internal three range oscillator, calibrated for between 400 and 16000 flashes/sec. Two alternative energy storage capacitors of .05 mfd and .025 mfd are provided giving flash energies of approximately 2 Joules and 1 Joule respectively. The flash duration is about 2.5μs.

The flashing rate of 400 - 600 flashes/sec was found to be adequate for this trajectory study. The internal oscillator is a multivibrator of high stability with an initial calibration of better than 0.1%. It was recalibrated using a digital counter and was found to give a maximum error of 0.6%. The precise flashing rate for the experiments was set with the digital counter. To obtain a maximum illumination over the particle trajectories a projector lens was used for focussing the light on the experimental region. The lens/mirror arrangement used is as shown in Figure 6.1.

The running time should always be kept to the minimum to avoid overheating and so obtain the maximum life from the discharge lamp. Under normal conditions the maximum number of consecutive flashes should not exceed 2000 at 2 Joules or 4000 at 1 Joule, and the maximum period of continuous operation should not exceed

$$\frac{4000}{\text{Joules x repetition rate}} \quad \text{sec.}$$

The number of consecutive flashes and running time may be extended by a further 50% with some reduction in the life of both the discharge lamp and the thyratron. A period of at least one minute should be given between runs to allow the flash discharge tube to cool. A small fan was installed in the lamp housing as shown in Figure 6.1 to help the cooling process. For the trajectory studies, a flashing duration of 0.5 second was sufficient. A complete detailed description of the stroboscope assembly and its operation is given in the instruction manual (117).

(b) Photographic system

The choice of the photographic equipment was governed by its depth of field at the plane of focus. Two conflicting factors have to be considered:

(i) For two dimensional study, the smallest achievable depth of field is desirable. Also if the depth of field is not sufficiently reduced many 'in focus' trajectories would be recorded making analysis difficult.

(ii) A very small depth of field will allow only a few particles, if any, to be in focus at any instant and therefore a large number of photographs are required. Therefore with the use of the conical electrode where the flow is more divergent the number of photographs needed would be even higher.

Many experiments were conducted with different camera-lens combinations and object-camera distances to produce a system with an acceptable depth of field which also afforded a high resolution of the particle trajectories. Initially particles of 180-210 μm were used and with refinement of the experimental design., trajectories for particles of 45-53 μm could be recorded.

The variables examined were different combinations of camera and lenses, neutral density filters, film types and flashing rates. A Yashica TL Electro X camera, equipped with a 35 mm f/2.8 Zeiss Flektogen lens with a 2 x teleconvertor was used for the initial

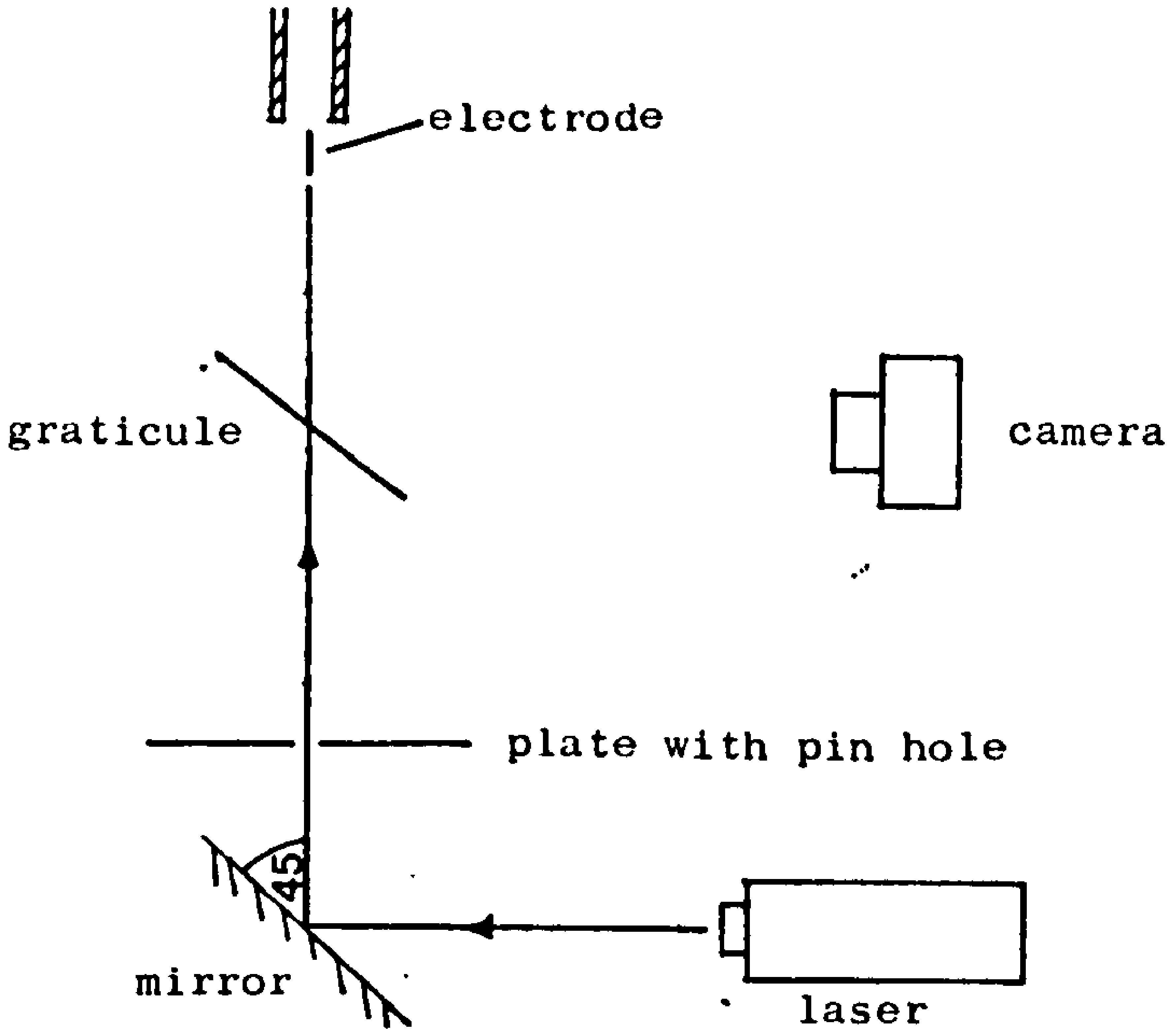

Figure 6.4 Experiment for location of plane of symmetry and determination of depth of field

photographic work. The experiments progressed later with a Nikon FD2 camera with a 35 mm f/2.0 Nikkor lens and a 2 x teleconvertor. PAN F film (ASA 50) was used and the film was overdeveloped in MICROPHEN. PAN F was chosen for its fine grain structure for good defination and the overdevelopment was to improve the contrast. A bolting arrangement was designed for the heavy duty tripod so that the camera would be slotted into its original position after film reloading to avoid any readjustment.

Figure 6.4 shows the experimental set up for the determination of the depth of field and the location of the plane of symmetry of the jet system. A Spectrophysics 10 mW He - Ne laser was used to align the object with a pin hole at its centre and the tip of the electrode. The camera was focussed precisely onto a graticule mounted at the located axial plane. The depth of field was 1 - 1.5 cm and was determined by photographing a graticule used for calibration. The depth of field of a lens D is given by (96),

$$D = 2\ (M + 1)\ c\lambda /\ M^2 \qquad (6.1)$$

where M = magnification

c = circle of confusion (focal length/1000)

λ = the f number of lens

The calculated values are D = 1.1 cm for the Nikon system and D = 1.6 cm for the Yashica system. These values agree well with the experimental results.

6.3.4. Feed material and particle feeder

A commercially available epoxy powder as shown in Figure 6.5 was used for this study. Separation into close size fractions was done by hand sieving with the following sieve fractions prepared : 105 - 125 µm, 75 - 90 µm and 45 - 53 µm. For the experimental set up, determined by the spraying distance and the depth of field prerequisites, the sieve size of 45 - 53 µm was found to be the bottom limit to yield acceptable photographic records of trajectories for analysis. Satisfactory trajectories for smaller particle (42, 100) could be obtained if there is a reduction in the field of view.

The particle feeder as shown in Figure 6.1 consisted of a vibratory spoon feeder and an Edwards water jet pump (PLASTIC MODEL 01-C047-02-000). The arrangement was such that only a few particles could be dropped and sucked into the air stream at any instant and the vibratory spoon feeder could maintain a steady flow of particles for entrainment. The number of particles emerging could further be restricted by the pin and ball valve assembly of the ejector.

6.3.5 The powder charging system

(a) Power generator

The power generator which provided the source of high tension

Figure 6.5 Epoxy particles

was part of an Aerostyle electrostatic powder coating system, capable of a maximum output of 80 - 90 Kv at 50 µA. The polarity of the output was negative. Using ten resistances of 10 GΩ connected in series the voltage supply was calibrated to an accuracy of ± 2 Kv. The one safety feature of the power generating system is the use of Piezo - Ceramic materials in the rf transformer stage whereby the collapse of the high tension output occurs in the event of a short circuit.

(b) The electrode design

In a conventional electrostatic powder spray gun as shown in Figure 3.1, the electrode serves two purposes:

(i) to provide a source of ions for powder charging and

(ii) to provide the field for directing the charged powder to the object to be coated. The most important factor in the design of the electrode system is to try to achieve saturation charge by maximising the residence time in the charging region. Two other systems which use the space charge deposition method are by tribocharging (9) and by the electrogasdynamic method (118, 119). Triboelectric charging method does not employ an electrode and the charge transfer takes place when different materials are rubbed against one another. Electrogasdynamic (EGD) gun as shown in Figure 6.5 utilises a low applied voltage within a spray gun to charge the particles and the induced space charge field causes precipitation on the target. The principle of operation is as follows: two internal electrodes (a corona electrode and a grounded electrode) with a potential difference between them are placed inside the gun. Whilst the particles are charged when passing through the space between the electrodes, the ions generated by the corona electrode are stripped by the positive electrode which also prevents the applied field emerging from the gun.

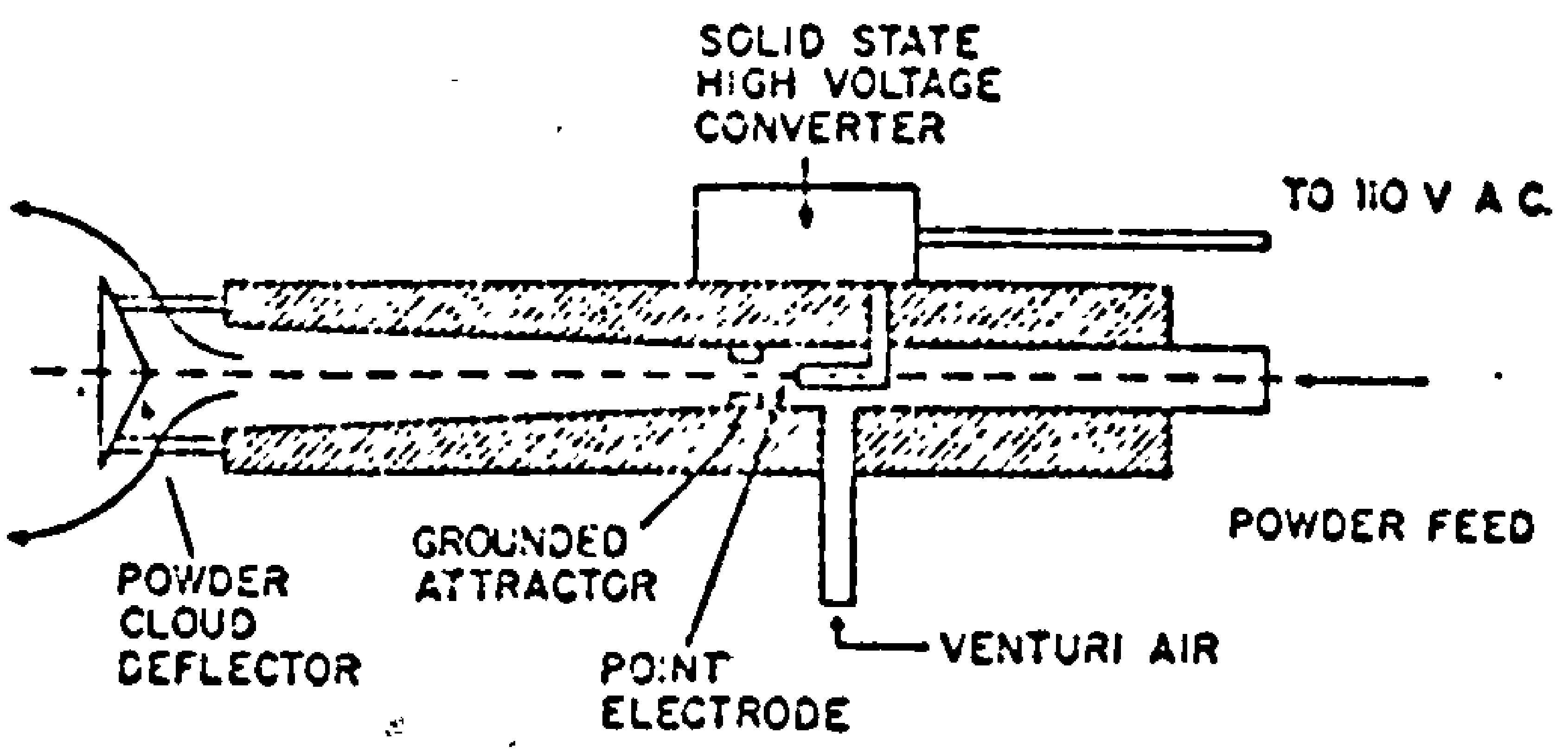

Figure 6.5 An electrogasdynamic gun (35)

The EGD coating method is claimed to be more efficient than the conventional spraying technique in several ways including higher deposition efficiency, higher particle charge, more uniform coating and also overcoming the Faraday cage effect. It is doubtful however if better charging of particles can be achieved with the EGD gun since with a shorter separation of the electrodes the charging time is much less than a conventional spray gun. Due to the proximity of the two electrodes, the problem of charged powder accumulation on the passive electrode is encountered. To overcome this an air source is normally used to keep the surface clean with the undesirable effect of increasing the particle velocity and hence reducing further the residence time. As discussed in Chapter 3, in the conventional spray gun, the attachment of the electrode at the end of the powder cloud deflector may cause inefficient charging because of inadequate mixing of the particles and the ions at the corona region where the field is highest. An electrode system was therefore designed to overcome these problems.

An electrode system as shown in Figure 6.6 comprising of two passive electrodes and a corona electrode was employed for the

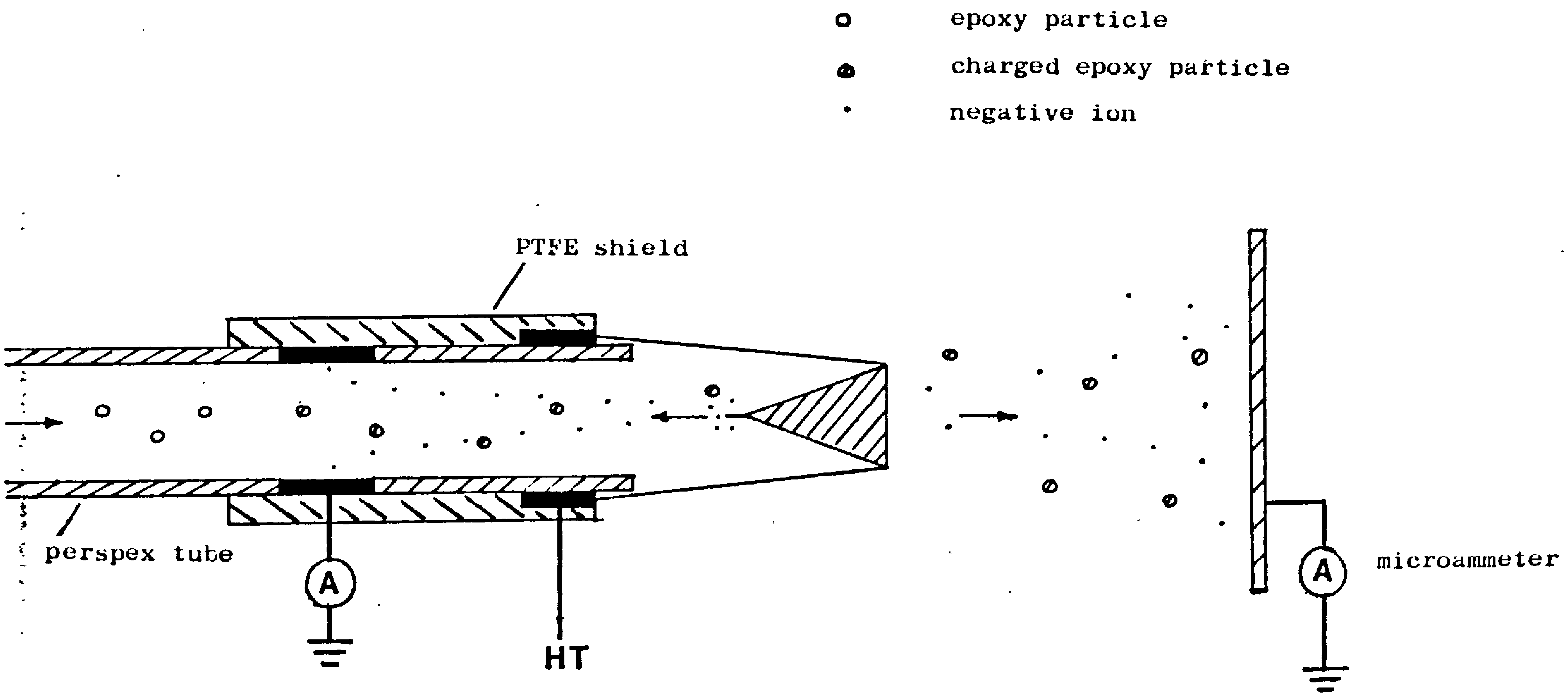

Figure 6.6 Electrode system for trajectory study

trajectory experiments. It utilises the 'counter stream' principle and the mode of operation is as follows. Particles moving towards the nozzle exit after passing the internal earthed ring electrode are charged by ions streaming from the corona electrode. The charging is further enhanced when passing through the corona region. The residence time in an ionic atmosphere is therefore improved substantially with this electrode system. Also the attachment of the corona electrode at the tip of the deflector would allow good mixing of ions and particles. The configuration of the conical electrode is as shown in Figure 6.6 with a needle (1 mm) protruding from the end of a cone (20°, 2.1 mm) made of brass. The point electrode was a short needle of 3 mm and the objects to be coated were square stainless steel plates.

Various experiments were conducted to optimise the separation of the corona electrode and the earthed ring electrode to achieve stable operation and to prevent charged particle deposition.. The optimum distance was found to be 4 cms with a measured current of the ring electrode of 0.3 µA and there was little fluctuation. A reduction of the gap would cause sparkover resulting in fluctuating current measurement with a maximum of 2 µA was obtained.

With the use of a dilute suspension it was difficult to evaluate the contribution made by the presence of the extra passive ring electrode. However during the experiments good deposition was obtained with no deposition of particles on the ring electrode. A similar electrode system was used by Sibbett (5) in experiments with powder delivery rate of about 4 gms/sec and good deposition was obtained.

6.4 Experimental procedure

Using a travelling microscope and the laser-mirror arrangement shown in Figure 6.4 the object and the electrode were aligned to conform with the conical arrangement requirement. After the location of the axial plane a graticule was mounted and the camera was focussed precisely on the graticule. With a negative of the graticule, small variations in the magnification due to the optical distortions in the system or uneven film shrinkage could be detected enabling compensation for these errors to be made.. Throughout the trajectory experiment, compensation for these errors was found unnecessary. Prior to any experimentation, the power supply was switched on in darkness to observe the occurrence of any corona point. The corona points were eliminated either with the application of silicone rubber or by smoothening of the sharp edges.

The trajectory experiments were conducted for,

(i) three particle size ranges

(ii) two air exit velocities

For each exit velocity experiments were performed for with and without applied voltage and using the point and conical electrodes. The applied voltage was set at 60 Kv. Generally the range of experimental conditions used corresponded to typical coating conditions. Also the experiments were designed in such a way as to show clearly the effect of the electric field on the trajectories of the particles.

The stroboscope was synchronised to flash when the vibratory spoon feeder was activated and the camera shutter opened. Stroboscope flashing of 0.5 sec duration was found to be sufficient.

6.5 Trajectory measurement

For tracing of the particle trajectories the negatives obtained were projected on to a wall using an Elmo slide projector with a good quality enlarging lens. The magnification of the experimental area was 2.5 times. The nozzle and the object were drawn together with the trajectories to determine the spatial relationship and the origin of the coordinate system. With the positional measurement result using the travelling microscope this would allow any error due to optical distortion to be rectified. Several negatives could be superimposed to produce an overall trajectory picture for a set of known experimental conditions. For analysis only complete trajectories in focus were considered. The theoretically predicted trajectories were then superimposed for comparison. The experimental particle velocity destribution was determined using the VANGUARD (P.C.D. Ltd. type ZAE 1/B) - digital X-Y data reader. Using a slide wire potentiometer device, the coordinates of a particle could be located accurately and the result was output on a teletype connected to the reader.

6.6. Results

The results are presented and discussed in Chapter 7. Examples of experimental particle trajectories are shown in Figures 6.7 - 6.12. Figure 6.7 shows trajectories of two uncharged particles (150 - 180 µm, U_o = 10.6 m/s) and demonstrates the usefulness of the photographic technique for accurate description of particle flights. Figure 6.8 shows a denser jet of charged particles (75 - 90 µm, U_o = 10.6 m/s) with good deposition. Using particles of similar size range and for the same air velocity Figures 6.9 - 6.12 show the outcome using two different electrodes and experimentation with and without the presence of an applied field. The use of a conical electrode with a secondary function as a particle cloud deflector is amply demonstrated by Figures 6.11 - 6.12 showing the more divergent spray pattern. An interesting observation of results of Figures 6.8, 6.10, 6.12 is that near the earthed substrate, there is particle acceleration due to increasing field intensity. This supports Corbett's (10) experimental measurement of field enhancement near the object. Throughout the experiments there was good deposition (results typified by Figures 6.8, 6.10, and 6.12) which suggested that good particle charging was achieved using the electrode system described previously.

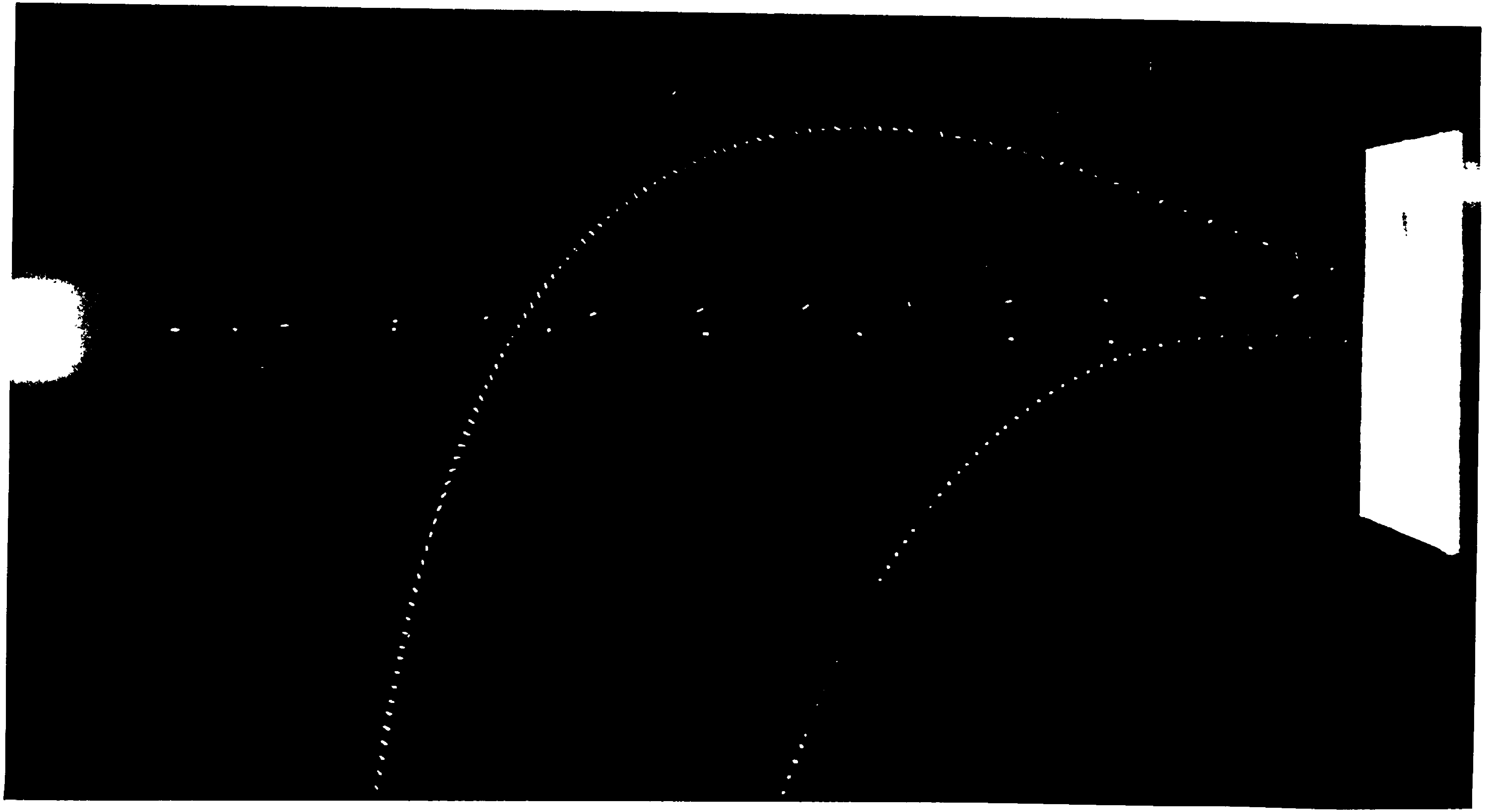

FIG. 6 7 TRAJECTORIES OF 150-180 µm UNCHARGED EPOXY PARTICLES ($U_0 = 10 \cdot 6$ m/s, 0 Kv)

TRAJECTORIES OF A DENSE JET OF CHARGED PARTICLES (U_o = 10·60 m/s, 75-90 μm, Kv)

FIG. 6·9 TRAJECTORIES OF 75-90μm PARTICLES USING A POINT ELECTRODE (0 Kv, U_0 = 10·60 m/s)

FIG. 6·10 TRAJECTORIES OF 75-90 μm PARTICLES USING A POINT ELECTRODE (60 Kv, $U_0 = 10{\cdot}60$ m/s)

FIG. 6·11 TRAJECTORIES OF 75-90µm PARTICLES USING A CONICAL ELECTRODE (0 Kv, $U_o = 10{\cdot}60$ m/s)

FIG. 6·12 TRAJECTORIES OF 75-90 μm PARTICLES USING A CONICAL ELECTRODE (60 Kv, U_o = 10·60 m/s)

CHAPTER 7

Comparison of experimental and theoretical trajectories - Results and Discussion.

The results of comparison of experimental data and the corresponding predicted values are presented by Figures 7.1 - 7.39 with a summary of the figures given in Table 7.1. The results are presented in three groups:

(i) Figures 7.1 - 7.23 show the direct comparison of experimental and theoretical pathlines for the three particle size ranges (45 - 53µm, 75 - 90 µm, 105 - 125 µm) using two different electrodes. The trajectories were recorded using two exit air velocities (9.15 m/s, 10.60 m/s) and also for with and without the presence of an electric field. For the results with field, comparison was also made with computed trajectories obtained under identical conditions but without field.

(ii) The experimental particle velocity profiles for the 105 - 125 µm particles are plotted in Figures 7.24 - 7.31.

(iii) In Figures 7.32 - 7.39 results of comparison of experimental particle velocities and predicted values for some particle trajectories of the 105 - 125 µm particles are shown.

The third group of result includes only those of 105 - 125 µm particles mainly just to emphasise the shortcoming of the prediction program and also since some 150 trajectories were examined it was not possible to include all the data. Furthermore as will be discussed later the discrepancy between comparison becomes more severe with decreasing particle size because particles begin to 'drift'.

The configuration of the experimental set up is as shown in Figure 7.40. For ease of result processing a magnification factor (2.45 x - 2.6 x) was included in the computer program to produce particle trajectories scaled to the same magnitude as the traced trajectories obtained using the slide projector.

Table 7.1 Summary of Results

Description	Figure number	Particle Size (μm)	Electrode Type	Magnification factor
Comparison between experimental and theoretical trajectories	7.1 - 7.4	105-125	Point	2.6
	7.5 - 7.8		Conical	
	7.9 - 7.12	75-90	Point	2.6
	7.13 - 7.16		Conical	
	7.17 - 7.20	45-53	Point	2.45
	7.21 - 7.23		Conical	2.6
Experimental particle velocity distribution	7.24 - 7.27	105-125	Point	
	7.28 - 7.31		Conical	
Comparison between experimental and calculated particle velocities	7.32 - 7.37	105-125	Point	
	7.38 - 7.39		Conical	

7.1 Discussion of experimental results

7.1.1. General Discussion

The photographic technique has successfully proved to be an effective charged particle trajectory tracking method giving accurate quantitative data produced with moderate labour. Examination of Figures 6.7 - 6.12 unfolds much interesting information like particle acceleration, particle drift, wrap-round, particle's own motion during flight and other features, information that would otherwise be difficult to assemble without extensive experimental effort.

As expected the presence of the electric field resulted in less disengagement of particles from the air jet and achieved a more uniform

FIG. 7·1 COMPARISON BETWEEN EXPERIMENTAL AND THEORETICAL TRAJECTORIES

FIG. 7·2 (1) COMPARISON BETWEEN EXPERIMENTAL AND THEORETICAL TRAJECTORIES

FIG. 7·2 (2) COMPARISON BETWEEN EXPERIMENTAL AND THEORETICAL TRAJECTORIES

FIG. 7·3 COMPARISON BETWEEN EXPERIMENTAL AND THEORETICAL TRAJECTORIES

FIG. 7·4 (1) COMPARISON BETWEEN EXPERIMENTAL AND THEORETICAL TRAJECTORIES

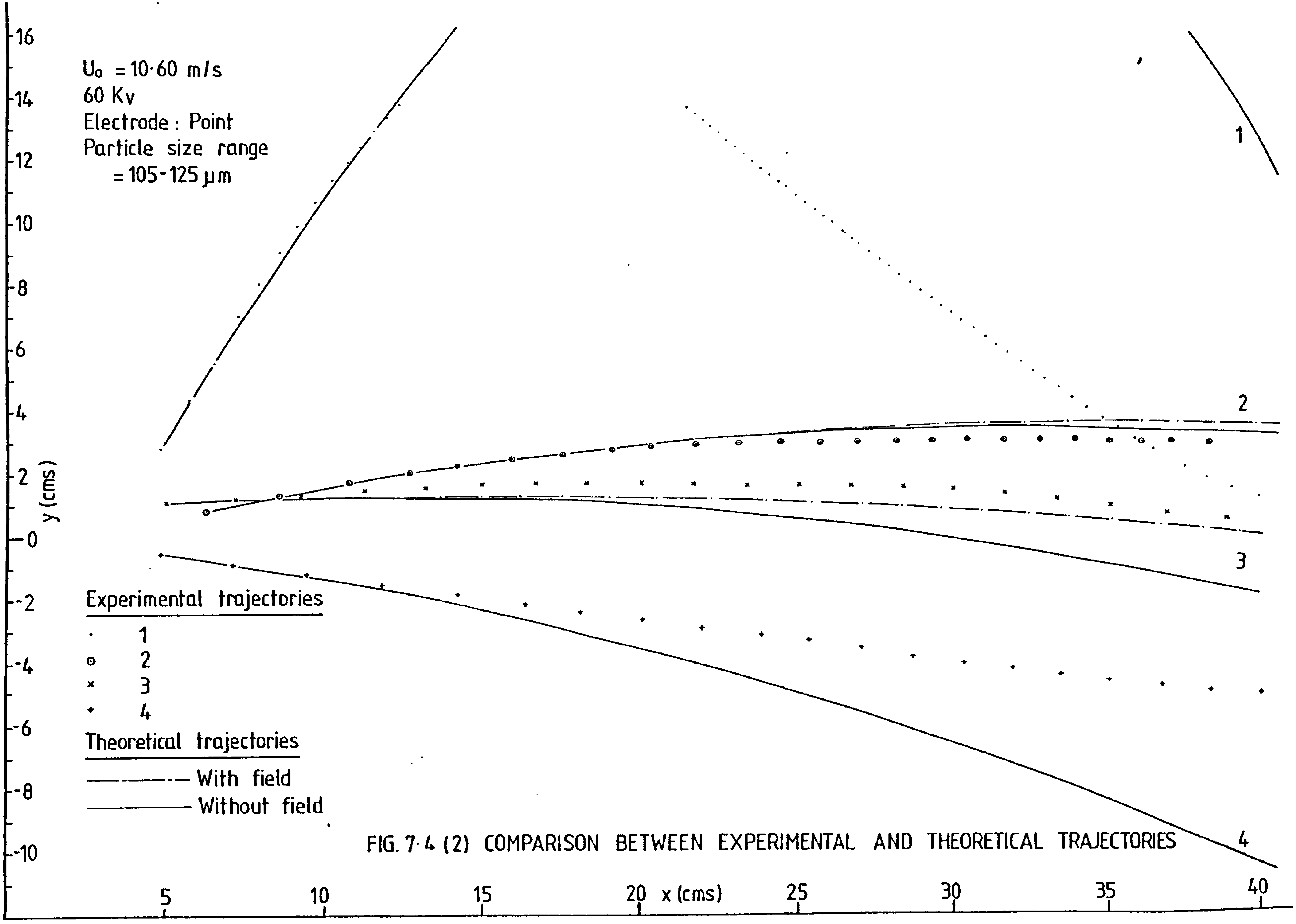

FIG. 7·4 (2) COMPARISON BETWEEN EXPERIMENTAL AND THEORETICAL TRAJECTORIES

FIG. 7·5 COMPARISON BETWEEN EXPERIMENTAL AND THEORETICAL TRAJECTORIES

FIG. 7·6 (1) COMPARISON BETWEEN EXPERIMENTAL AND THEORETICAL TRAJECTORIES

FIG. 7·6 COMPARISON BETWEEN EXPERIMENTAL (2) AND THEORETICAL TRAJECTORIES

FIG. 7·7 COMPARISON BETWEEN EXPERIMENTAL AND THEORETICAL TRAJECTORIES

FIG. 7·8(i) COMPARISON BETWEEN EXPERIMENTAL AND THEORETICAL TRAJECTORIES

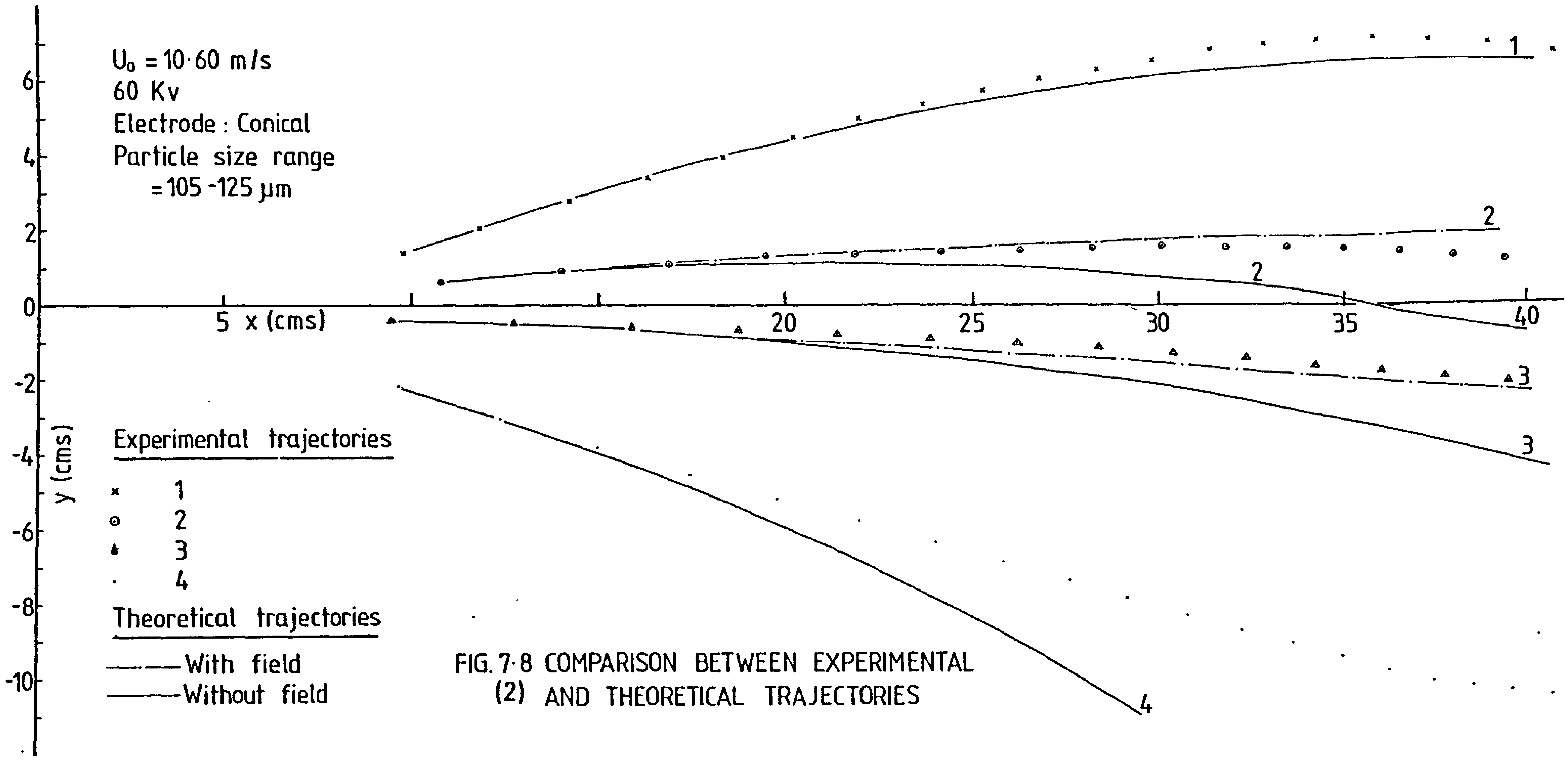

FIG. 7·8 COMPARISON BETWEEN EXPERIMENTAL (2) AND THEORETICAL TRAJECTORIES

FIG. 7·9 COMPARISON BETWEEN EXPERIMENTAL AND THEORETICAL TRAJECTORIES

FIG. 7·10 (1) COMPARISON BETWEEN EXPERIMENTAL AND THEORETICAL TRAJECTORIES

FIG. 7·10 (2) COMPARISON BETWEEN EXPERIMENTAL AND THEORETICAL TRAJECTORIES

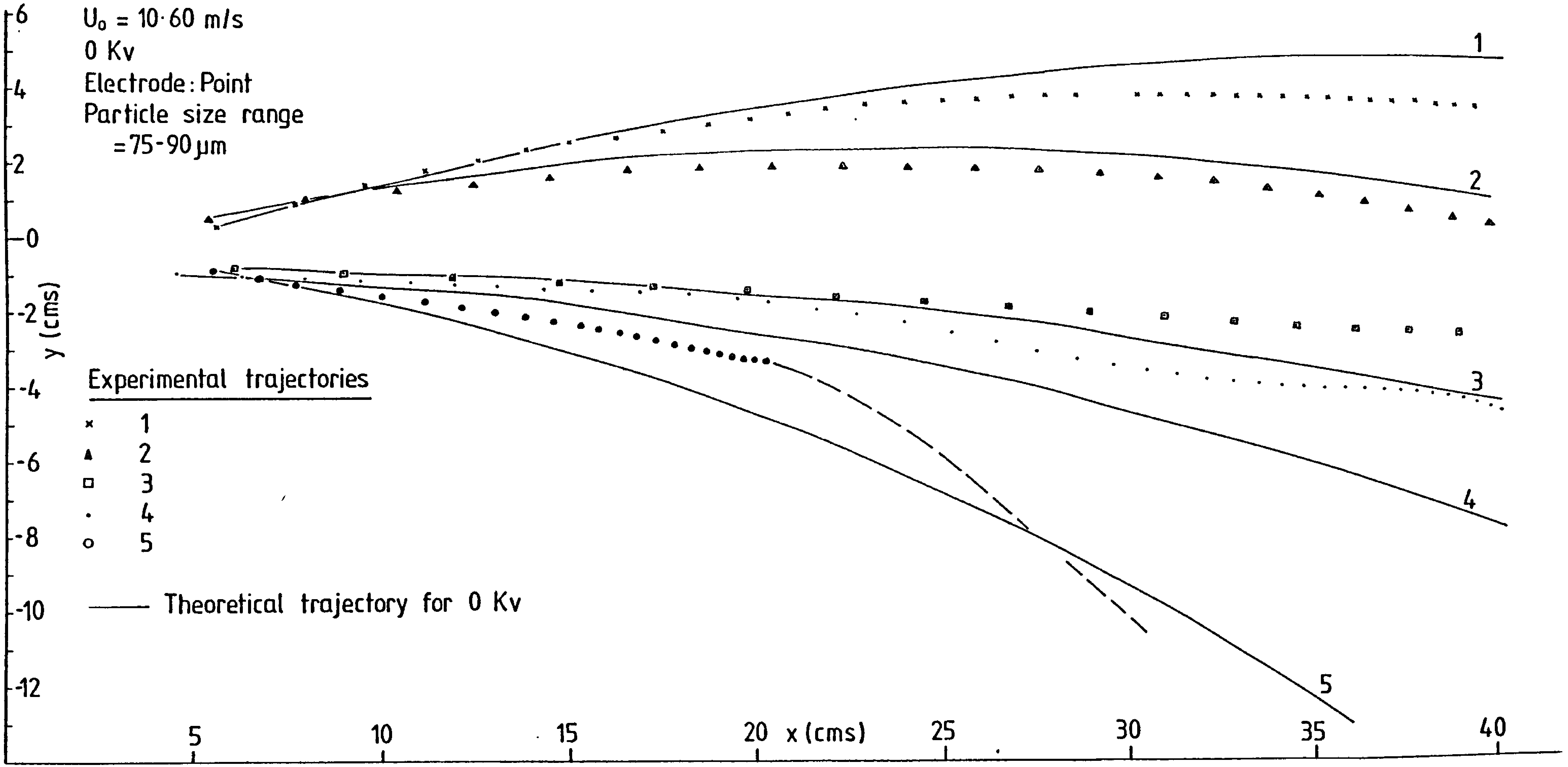

FIG. 7·11 COMPARISON BETWEEN EXPERIMENTAL AND THEORETICAL TRAJECTORIES

FIG. 7·12 (1) COMPARISON BETWEEN EXPERIMENTAL AND THEORETICAL TRAJECTORIES

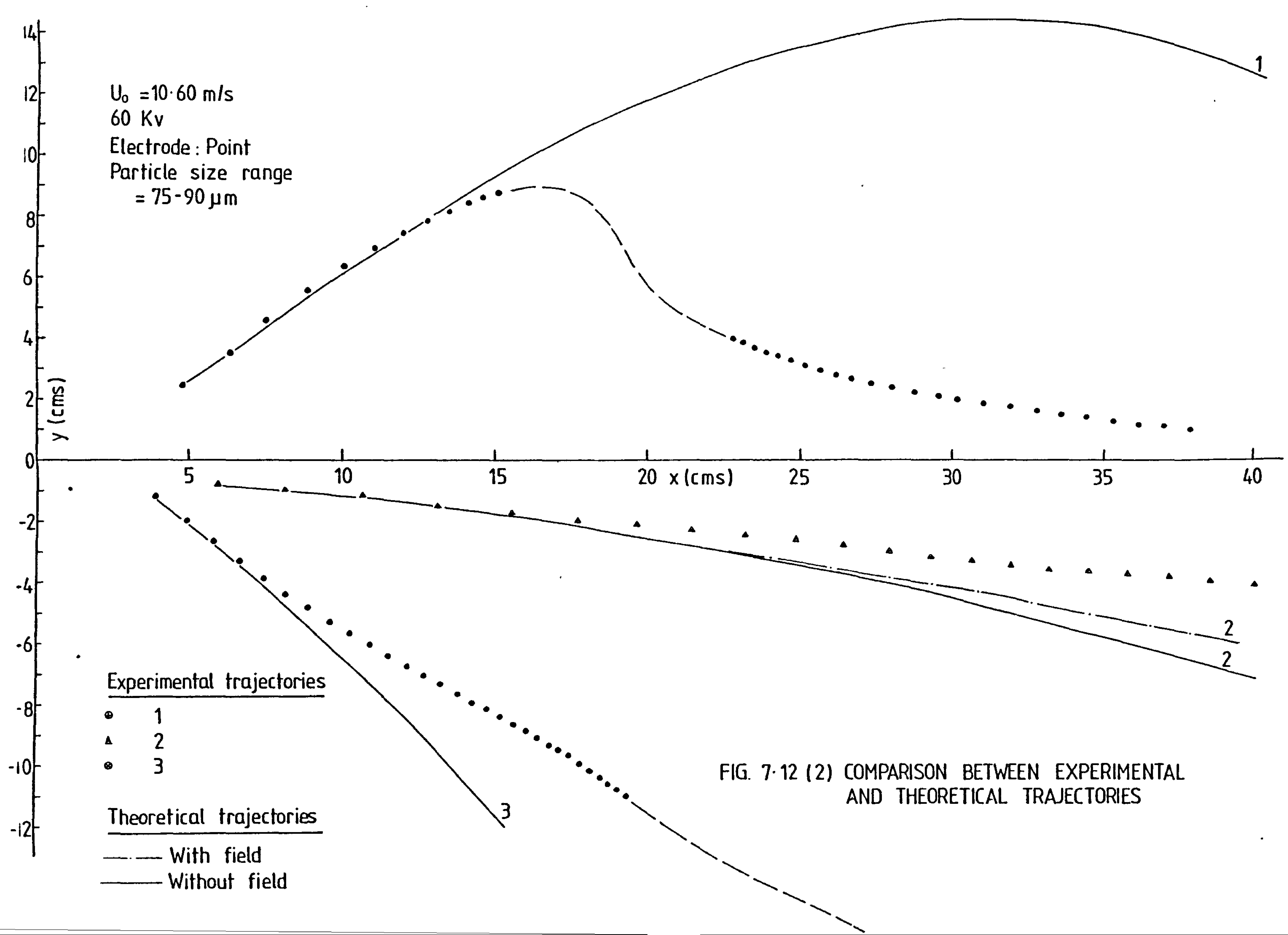

FIG. 7·12 (2) COMPARISON BETWEEN EXPERIMENTAL AND THEORETICAL TRAJECTORIES

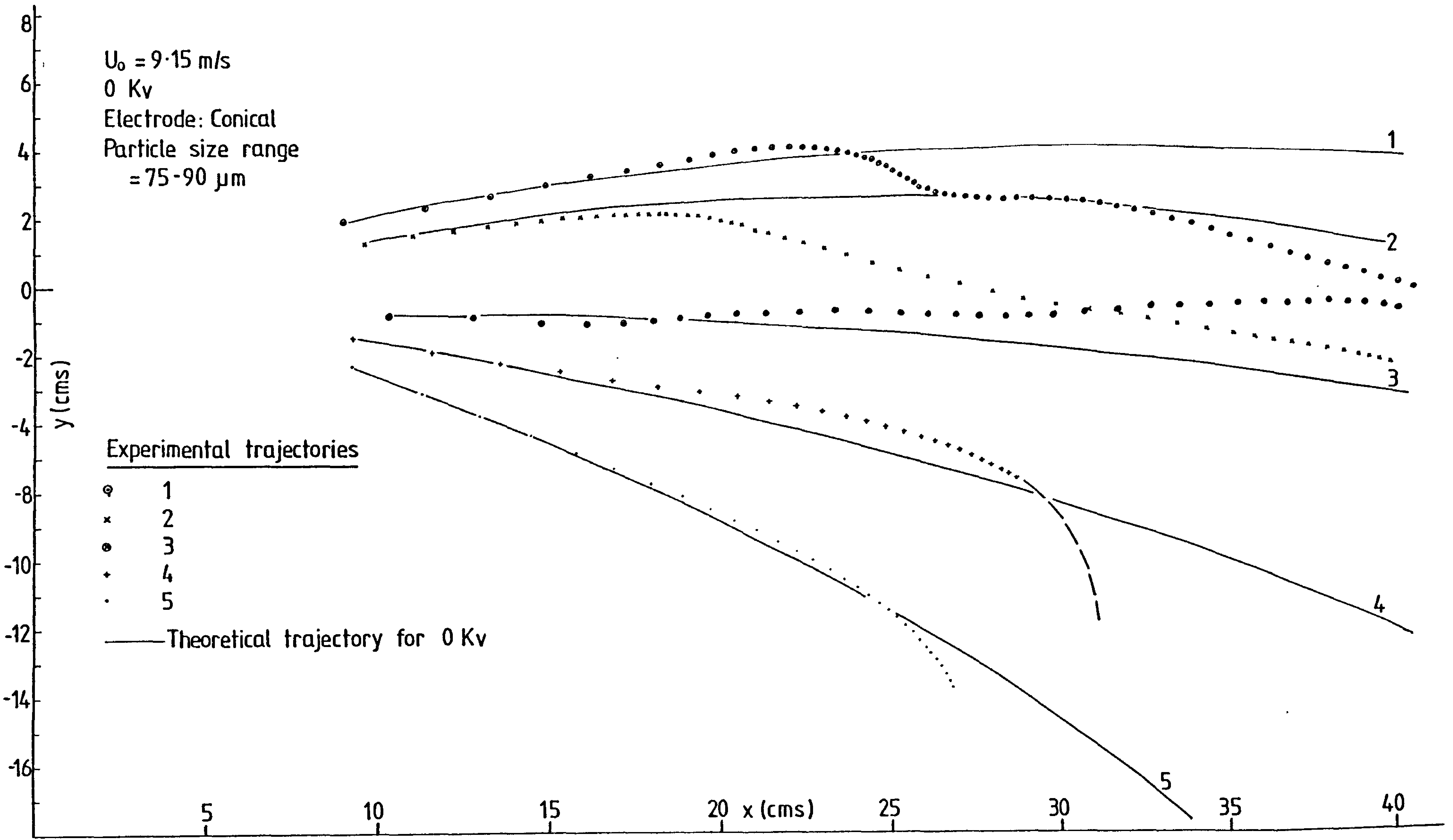

FIG. 7·13 COMPARISON BETWEEN EXPERIMENTAL AND THEORETICAL TRAJECTORIES

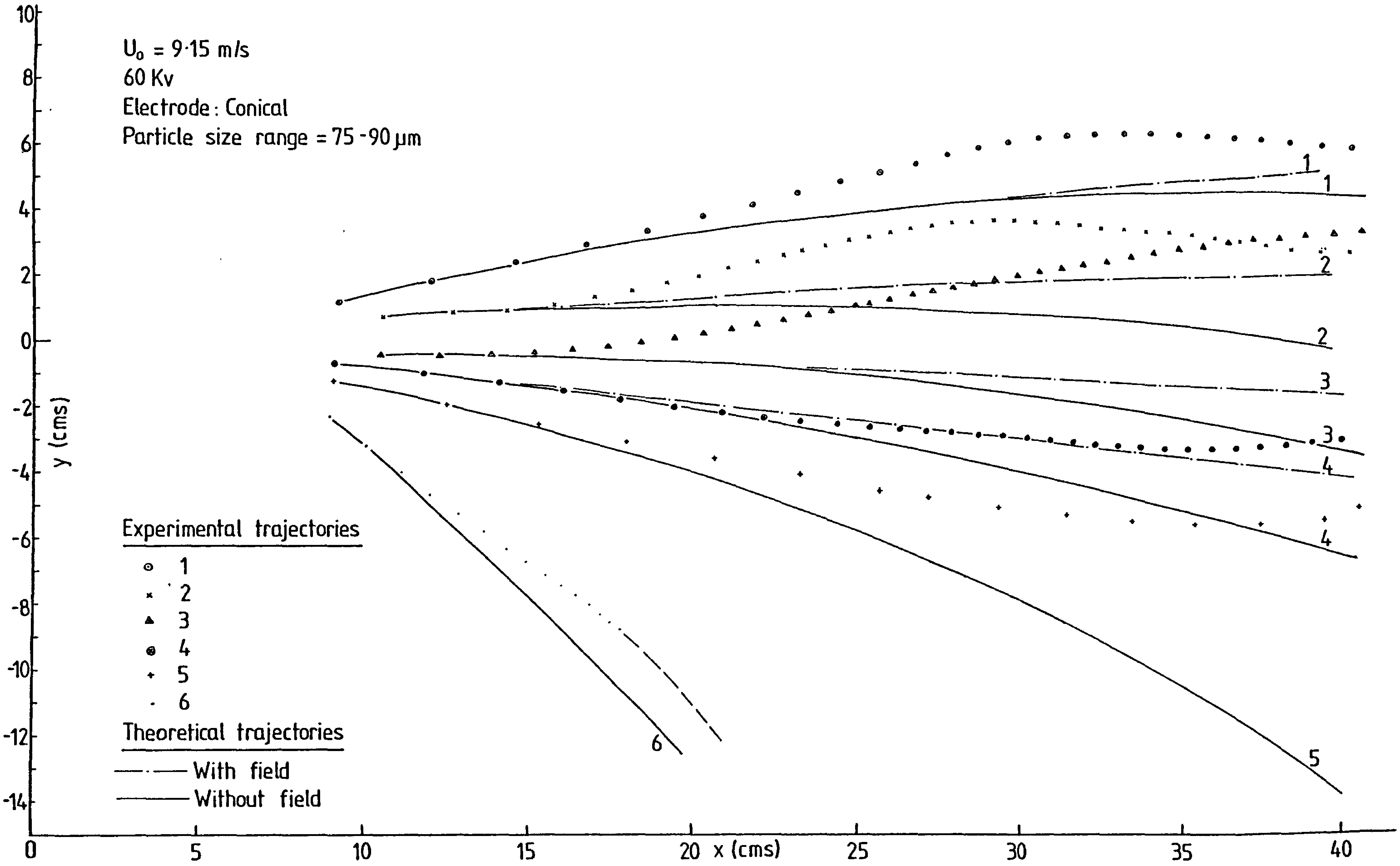

FIG. 7·14 COMPARISON BETWEEN EXPERIMENTAL AND THEORETICAL TRAJECTORIES

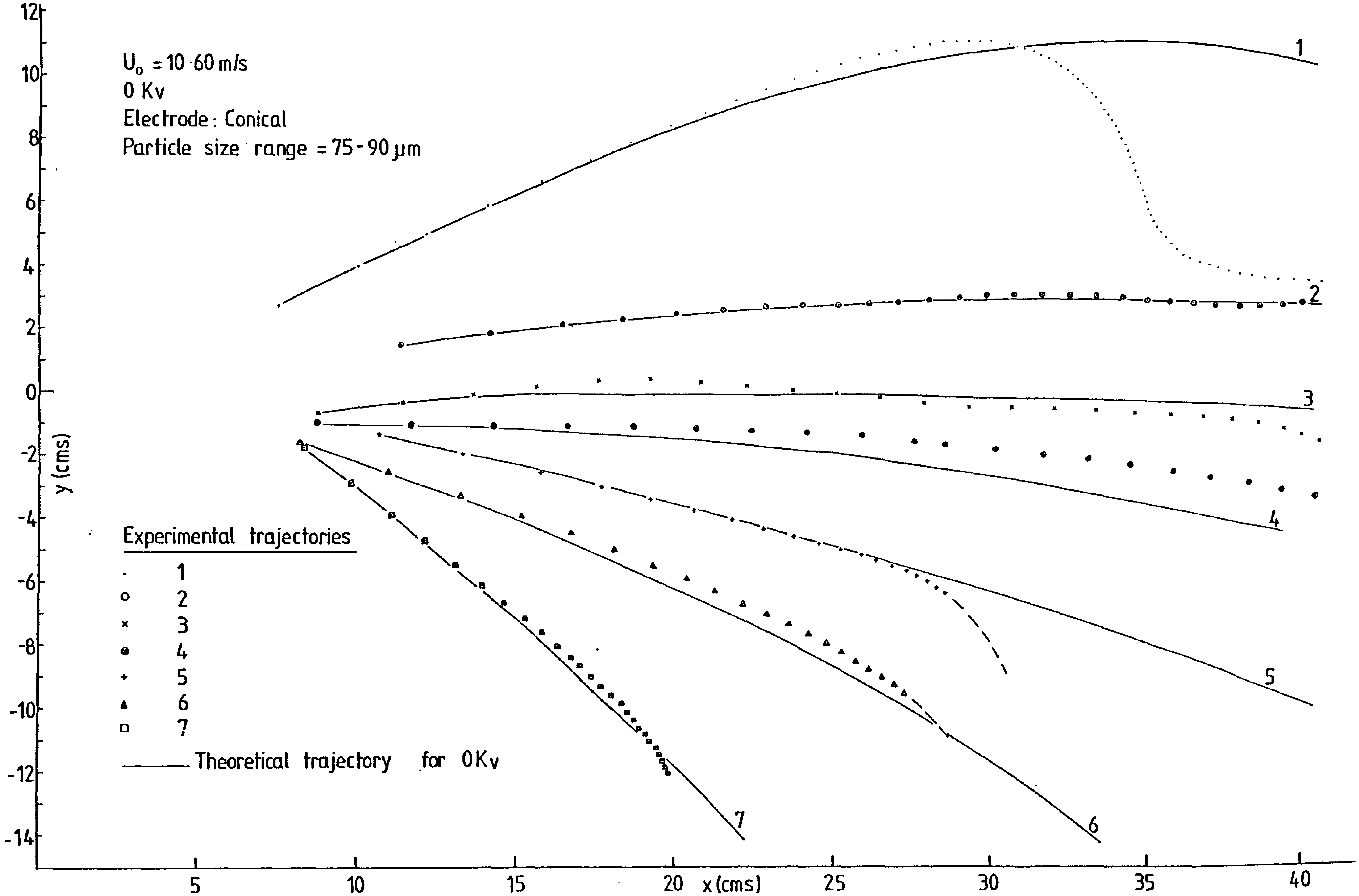

FIG. 7·15 COMPARISON BETWEEN EXPERIMENTAL AND THEORETICAL TRAJECTORIES

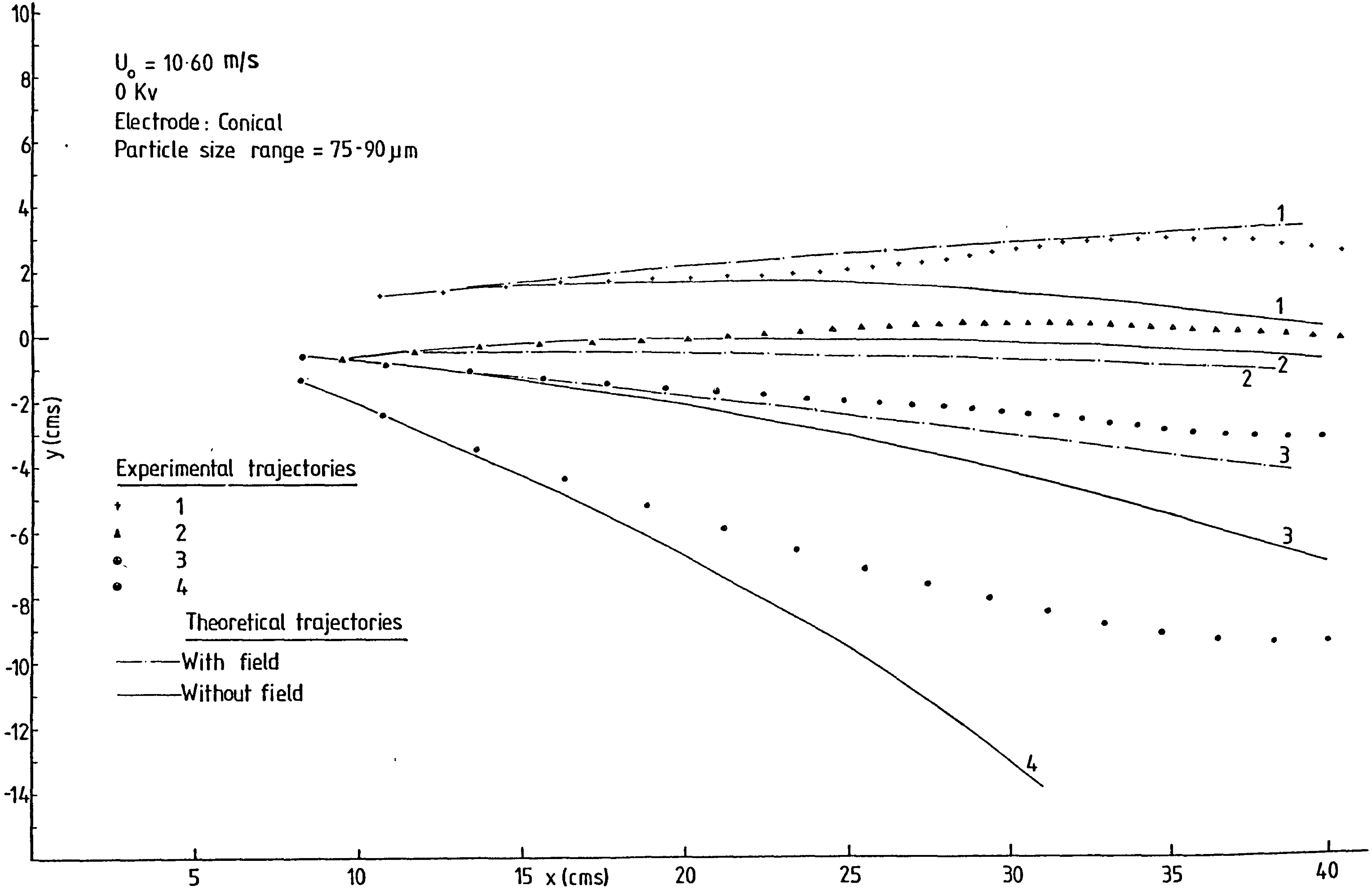

FIG. 7·16 (1) COMPARISON BETWEEN EXPERIMENTAL AND THEORETICAL TRAJECTORIES.

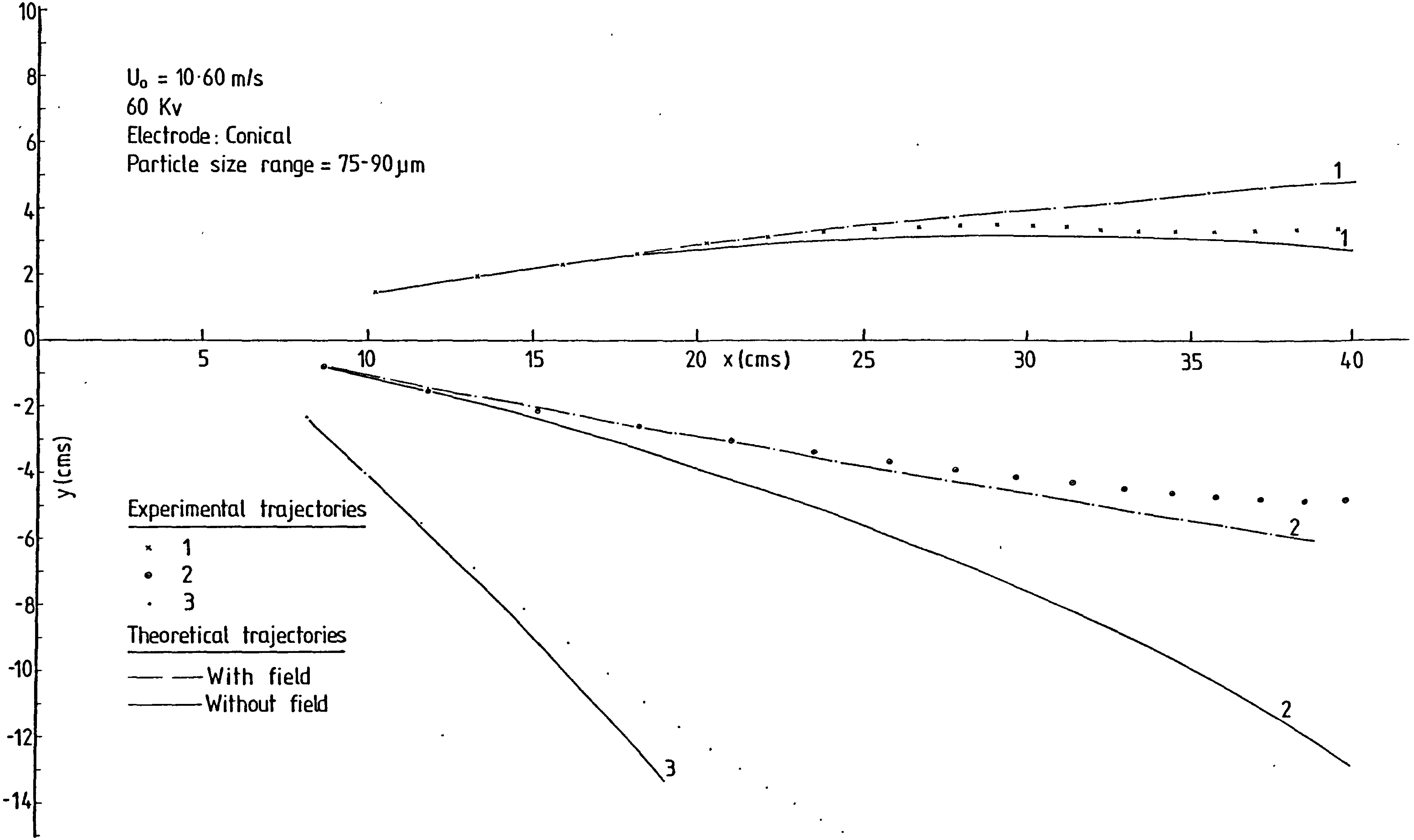

FIG. 7·16 (2) COMPARISON BETWEEN EXPERIMENTAL AND THEORETICAL TRAJECTORIES

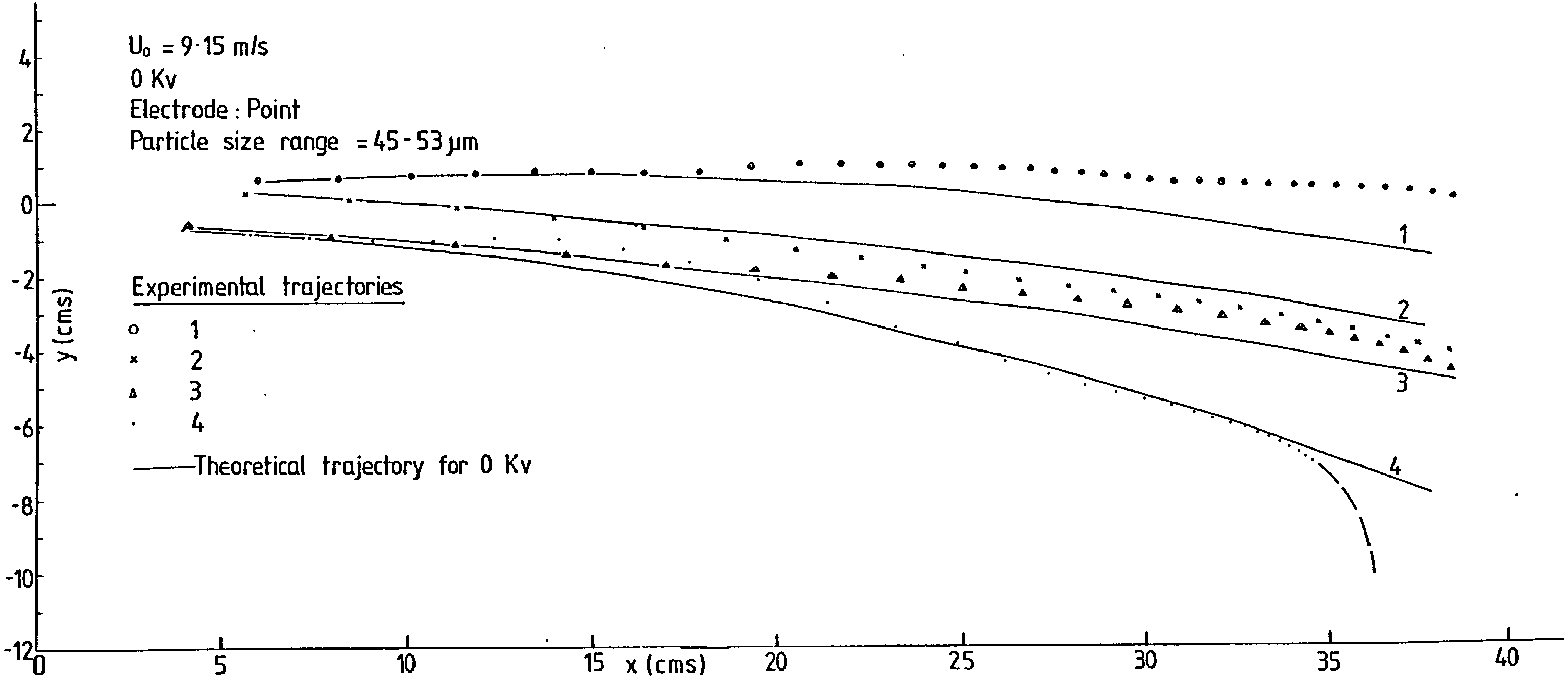

FIG. 7·17 (1) COMPARISON BETWEEN EXPERIMENTAL AND THEORETICAL TRAJECTORIES

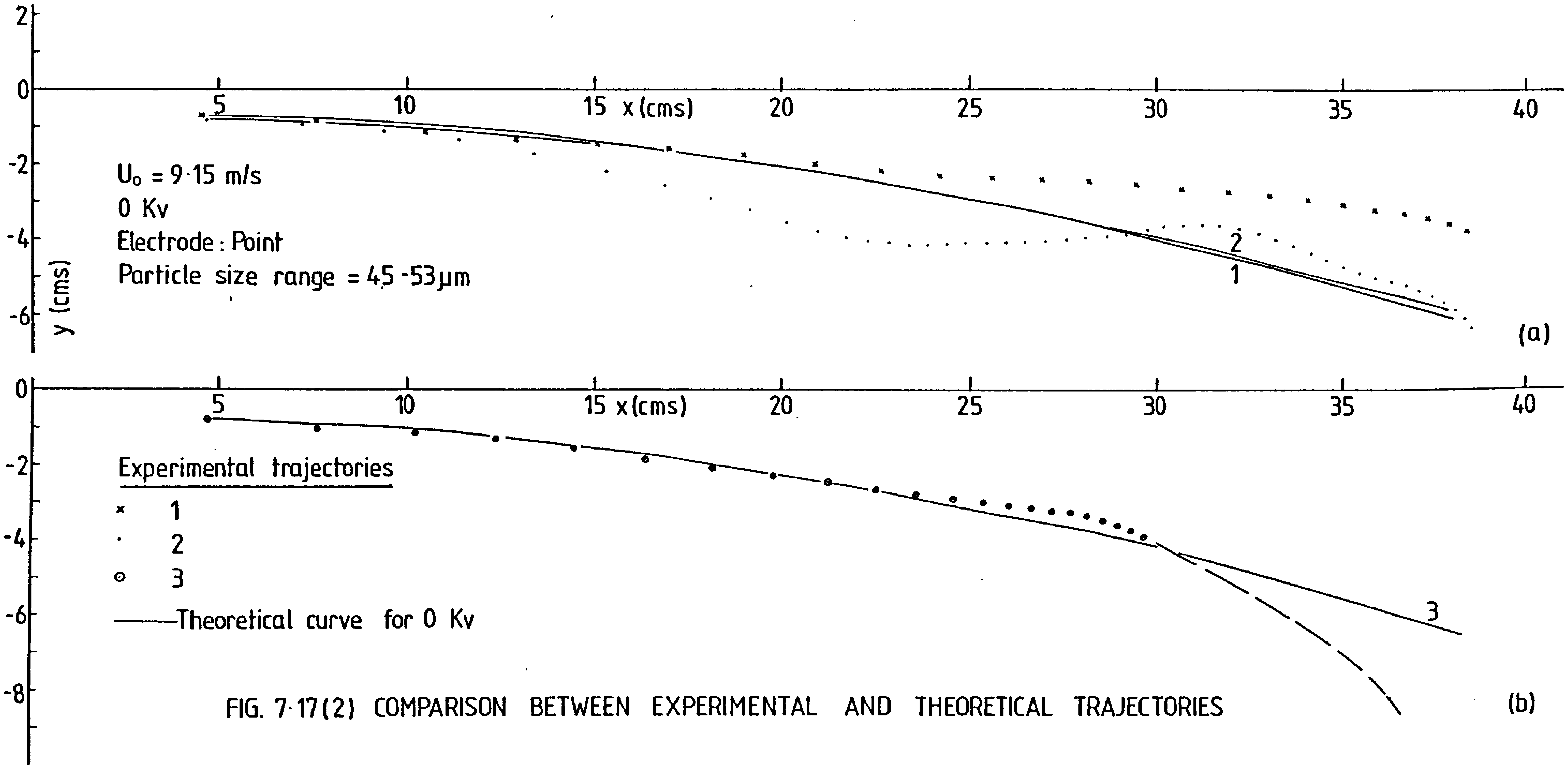

FIG. 7·17(2) COMPARISON BETWEEN EXPERIMENTAL AND THEORETICAL TRAJECTORIES

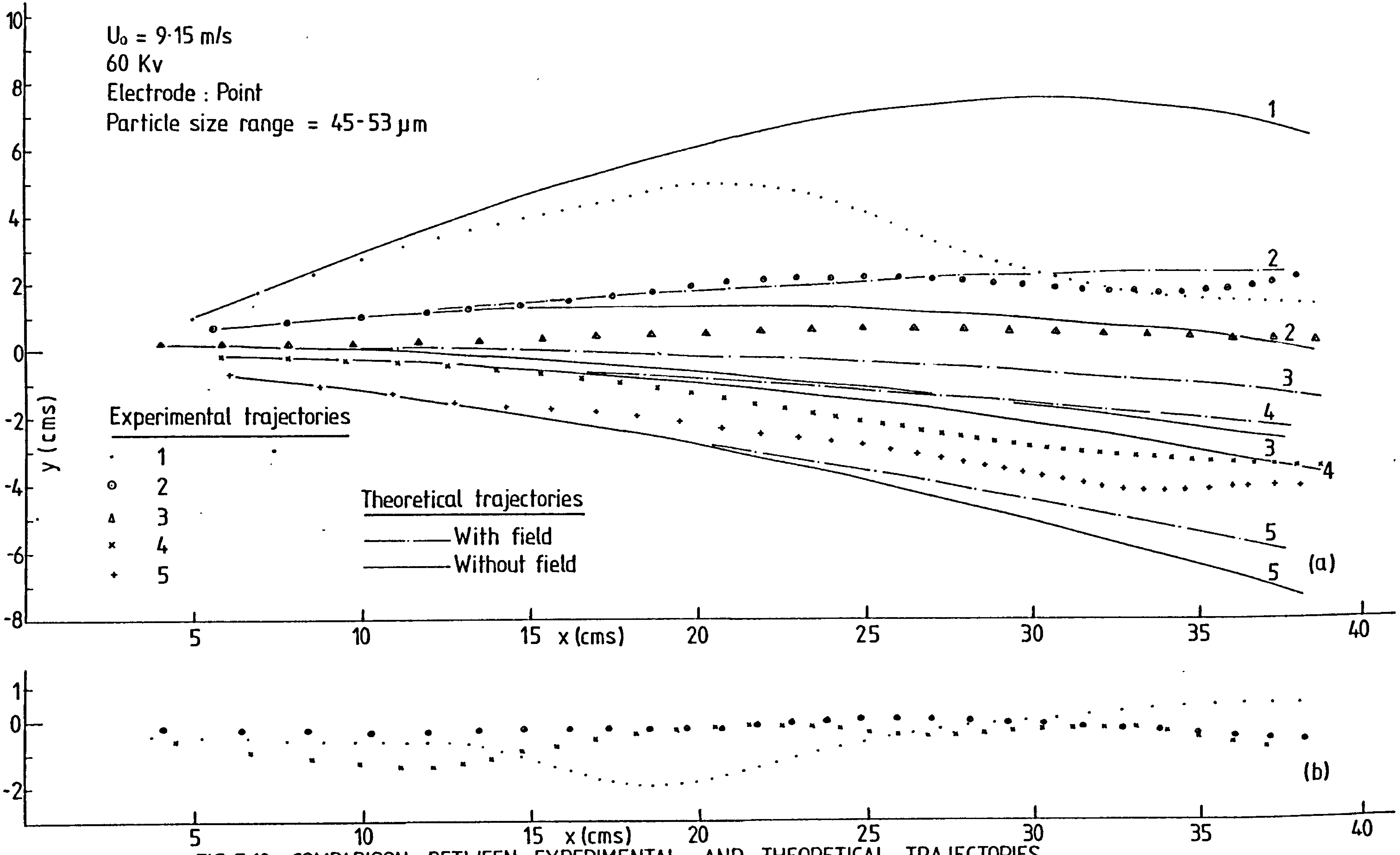

FIG. 7·18 COMPARISON BETWEEN EXPERIMENTAL AND THEORETICAL TRAJECTORIES

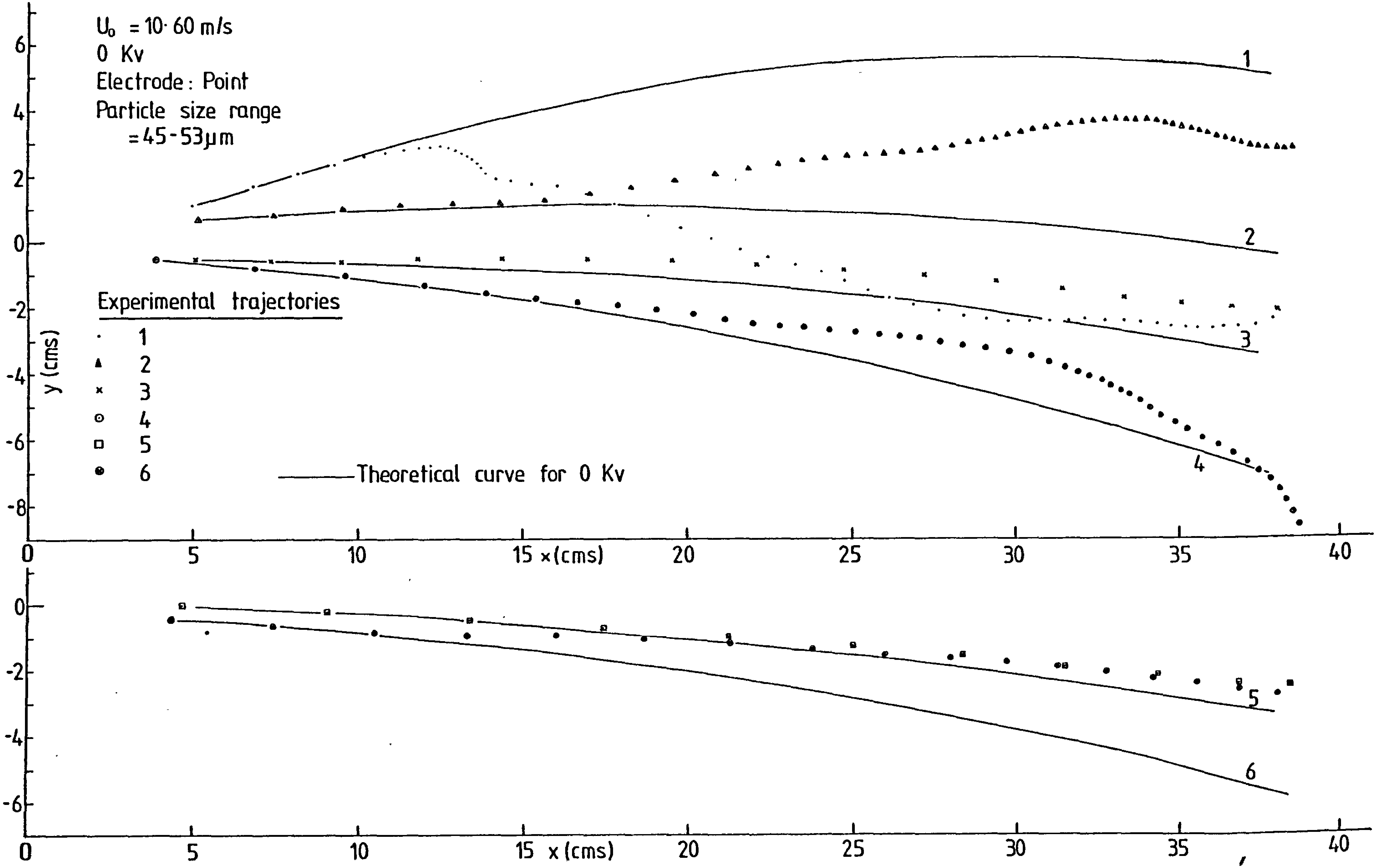

FIG. 7·19 COMPARISON BETWEEN EXPERIMENTAL AND THEORETICAL TRAJECTORIES

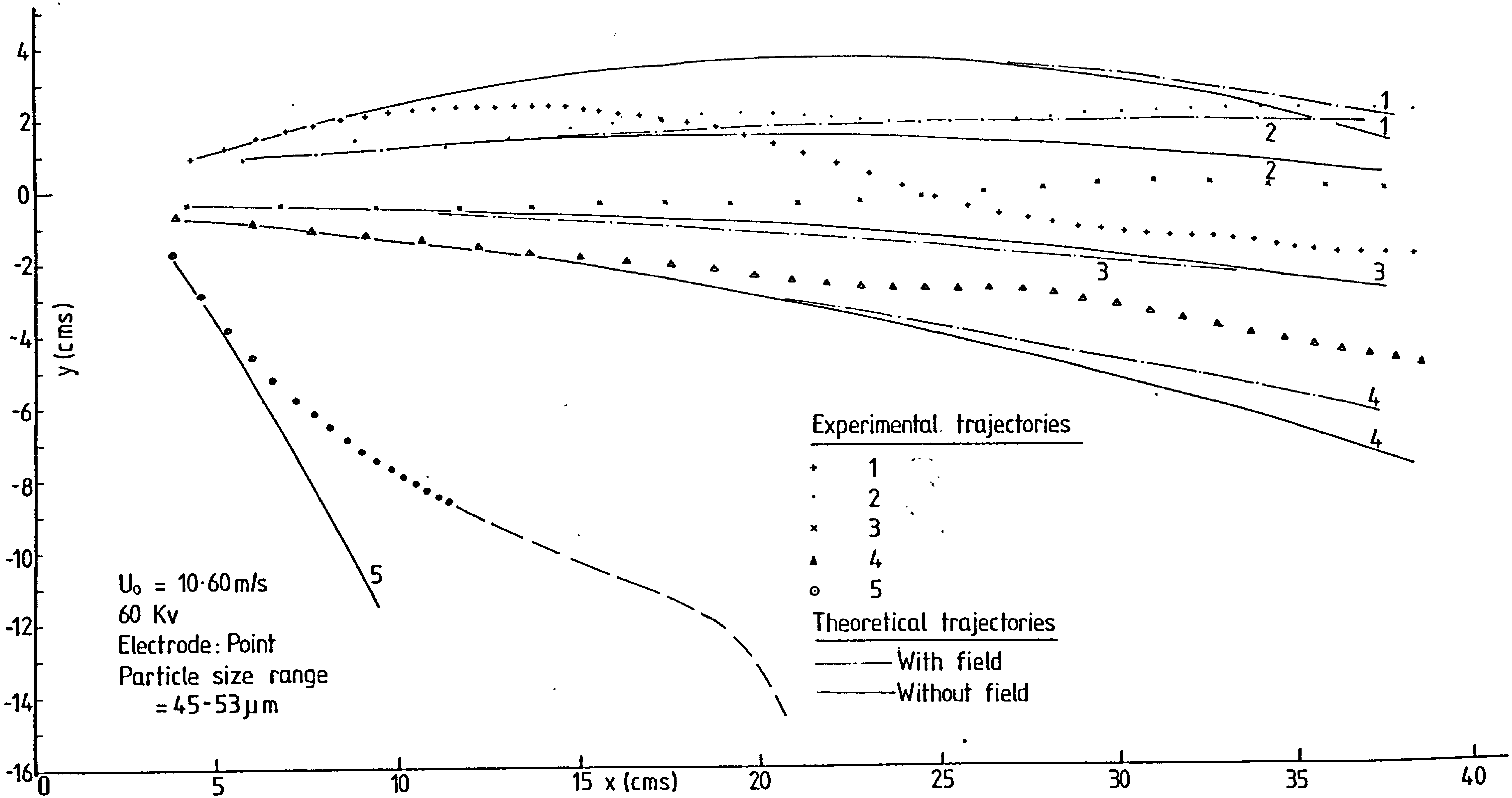

FIG. 7·20 (1) COMPARISON BETWEEN EXPERIMENTAL AND THEORETICAL TRAJECTORIES

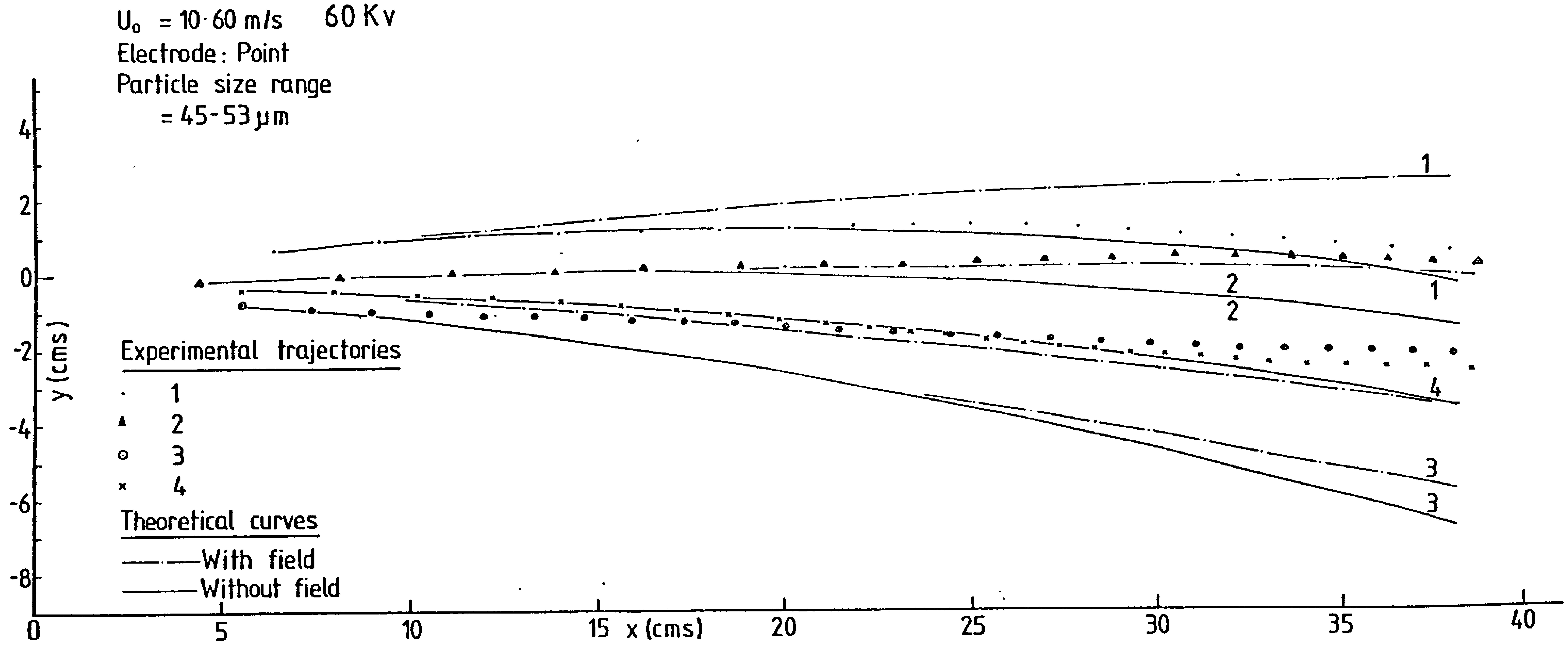

FIG. 7·20 (2) COMPARISON BETWEEN EXPERIMENTAL AND THEORETICAL TRAJECTORIES

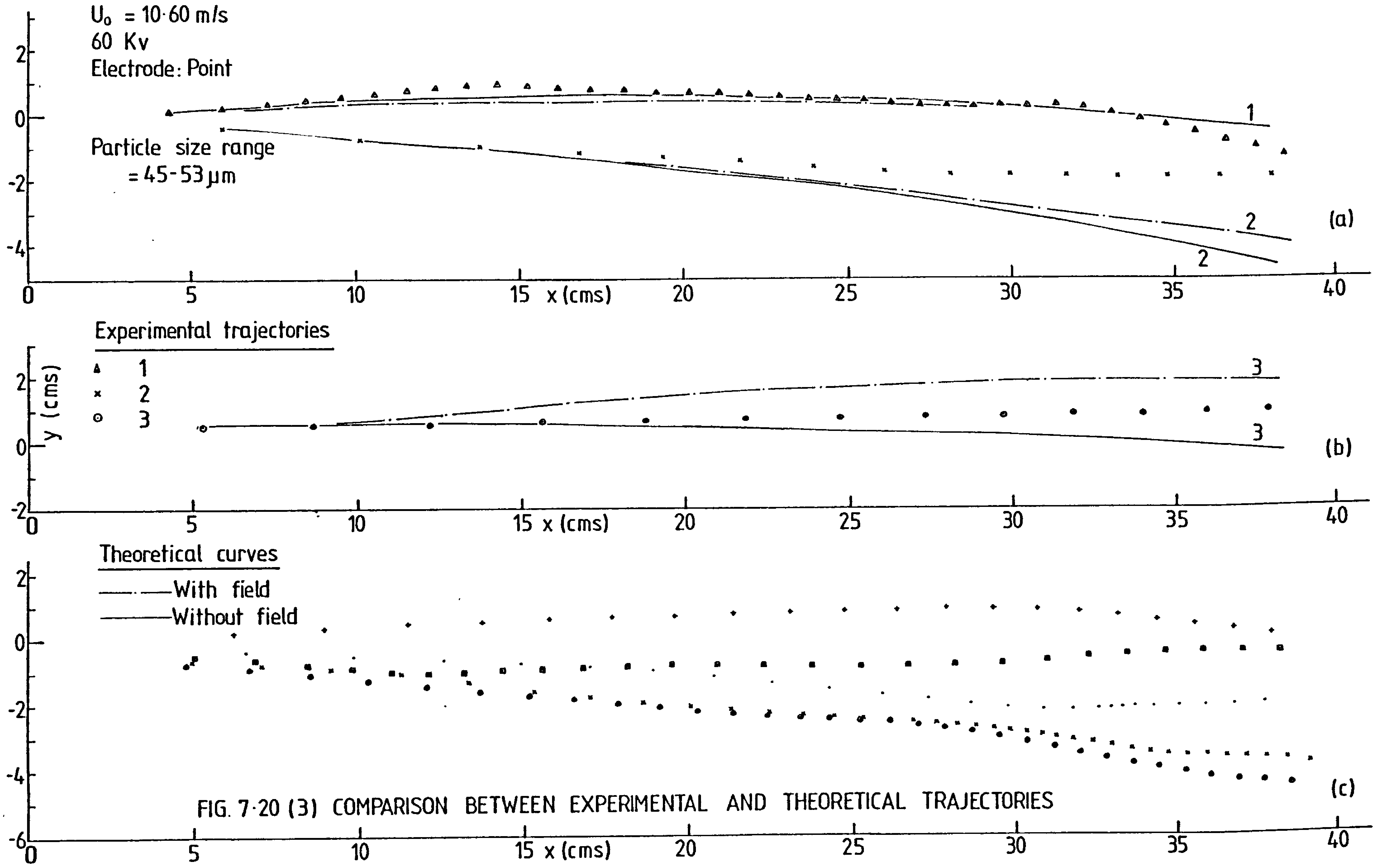

FIG. 7·20 (3) COMPARISON BETWEEN EXPERIMENTAL AND THEORETICAL TRAJECTORIES

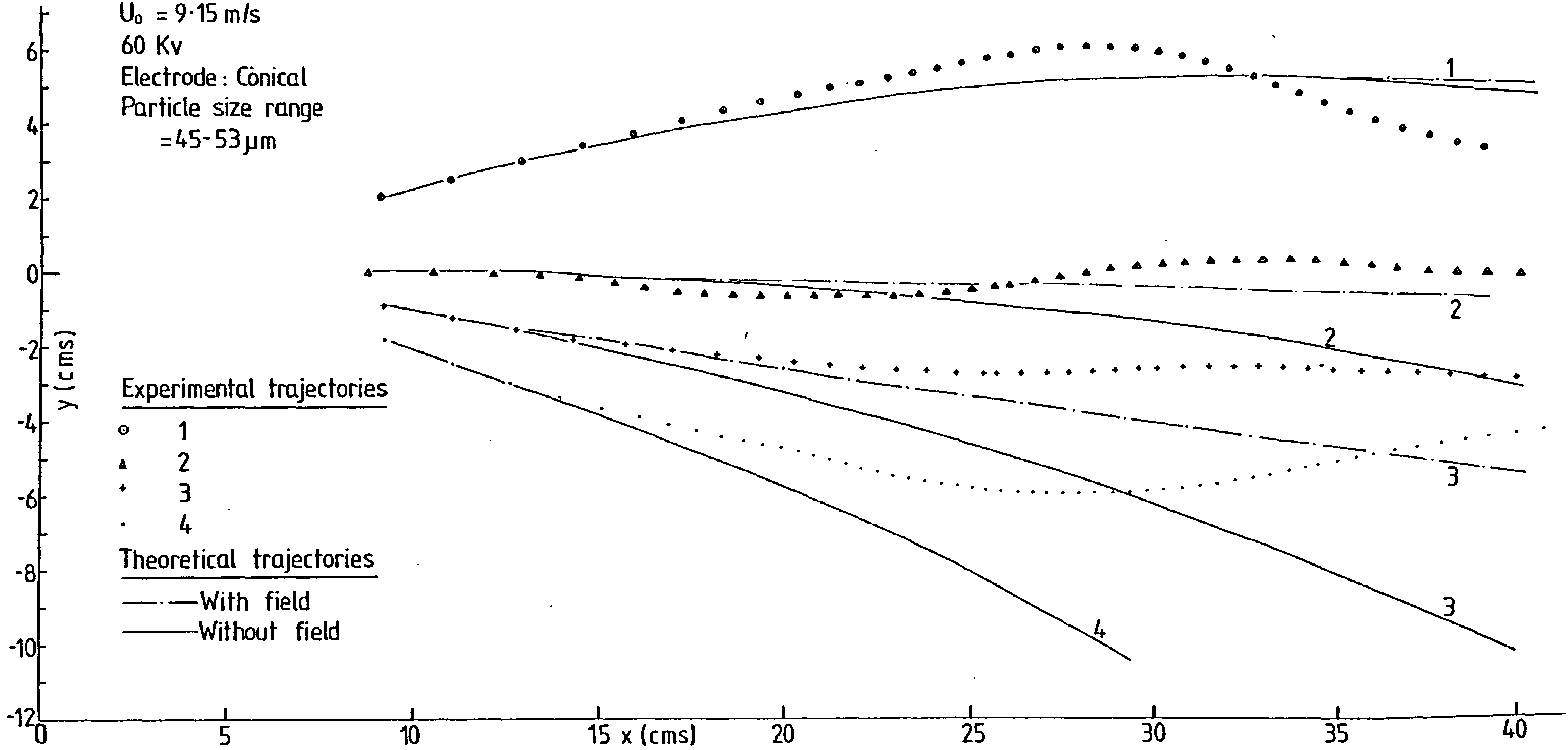

FIG. 7·21 COMPARISON BETWEEN EXPERIMENTAL AND THEORETICAL TRAJECTORIES

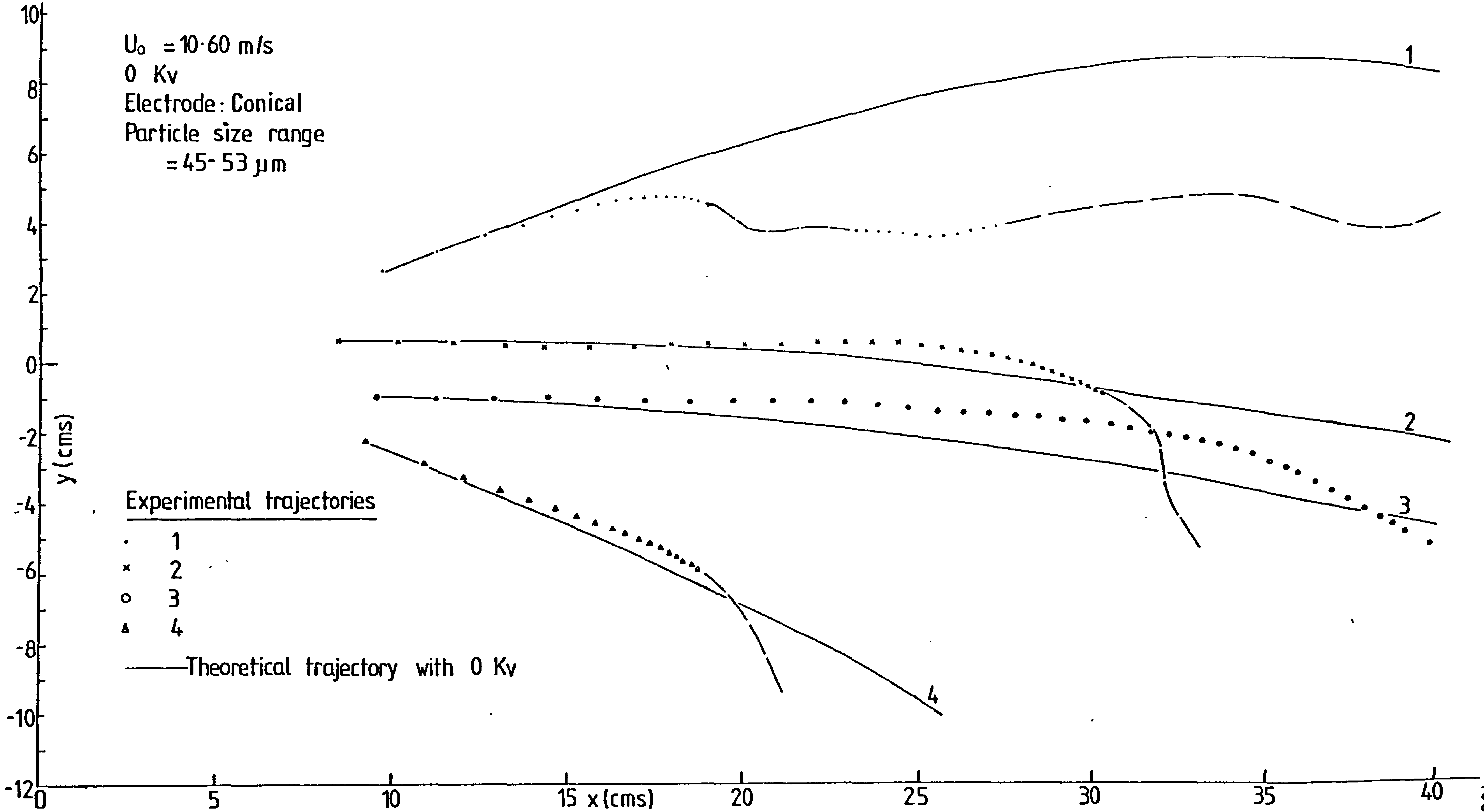

FIG. 7·22 COMPARISON BETWEEN EXPERIMENTAL AND THEORETICAL TRAJECTORIES

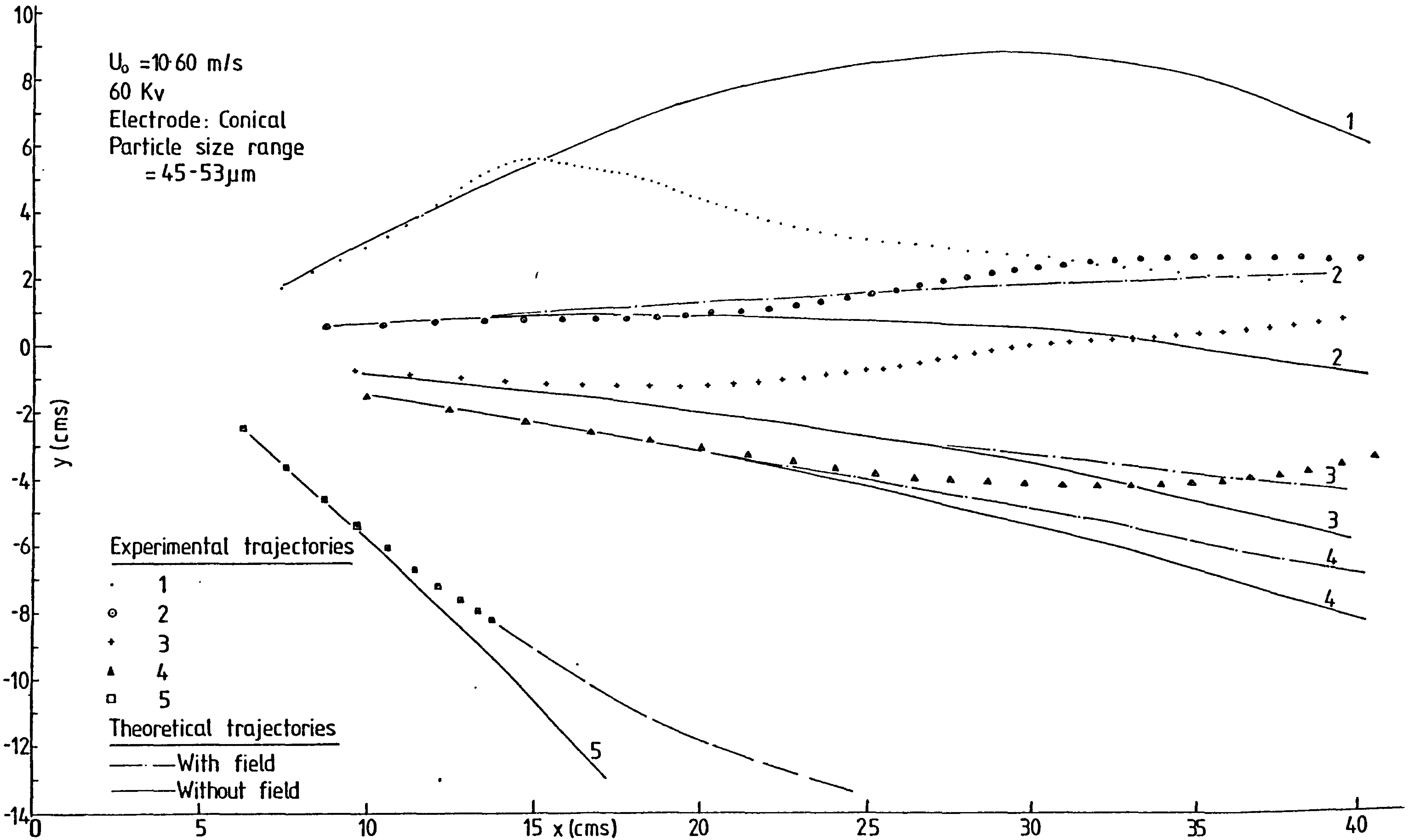

FIG. 7·23 (1) COMPARISON BETWEEN EXPERIMENTAL AND THEORETICAL TRAJECTORIES

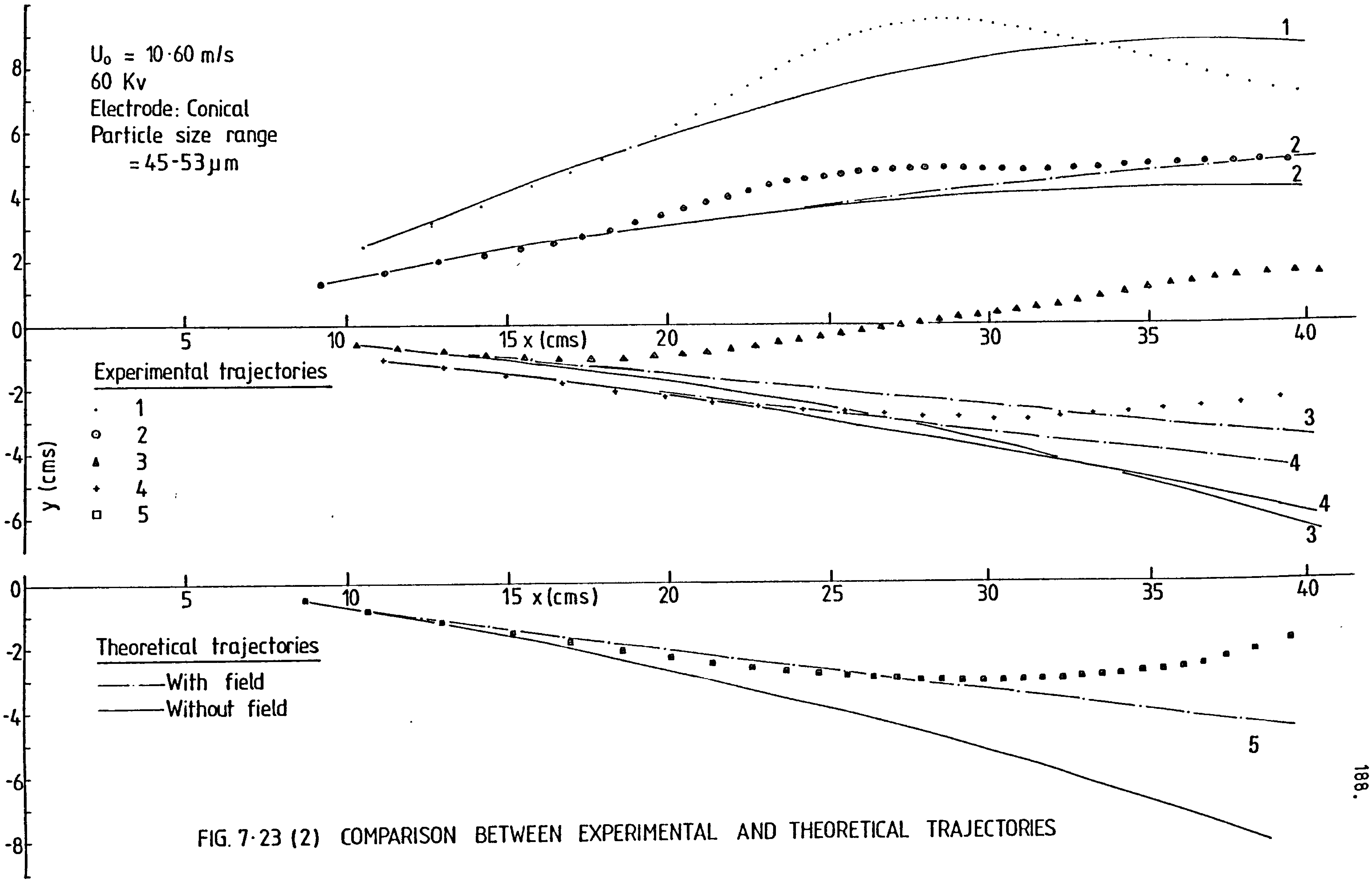

FIG. 7·23 (2) COMPARISON BETWEEN EXPERIMENTAL AND THEORETICAL TRAJECTORIES

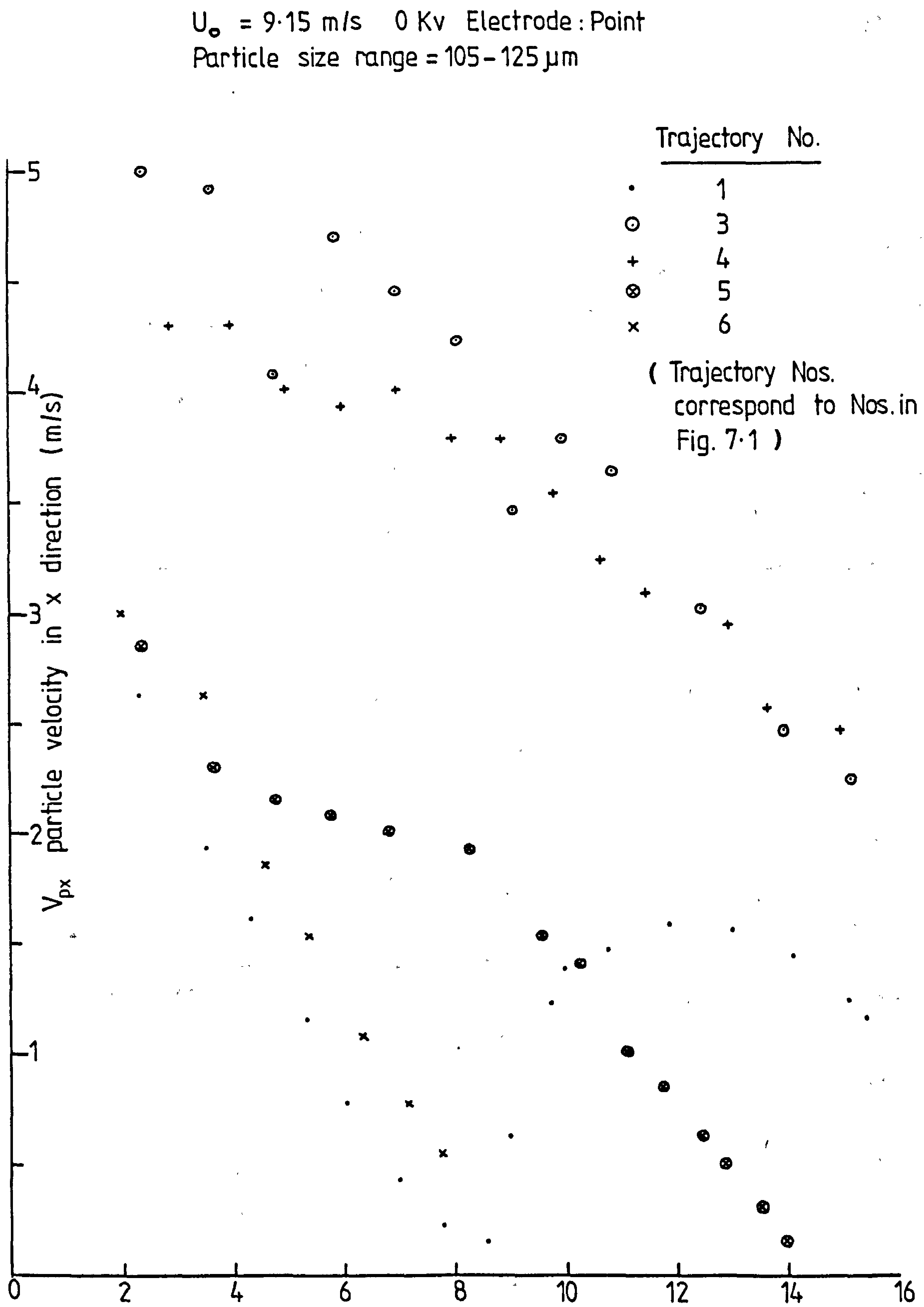
U_o = 9·15 m/s   0 Kv   Electrode : Point
Particle size range = 105 – 125 μm

FIG. 7·24 EXPERIMENTAL PARTICLE VELOCITY DISTRIBUTION (0 Kv)

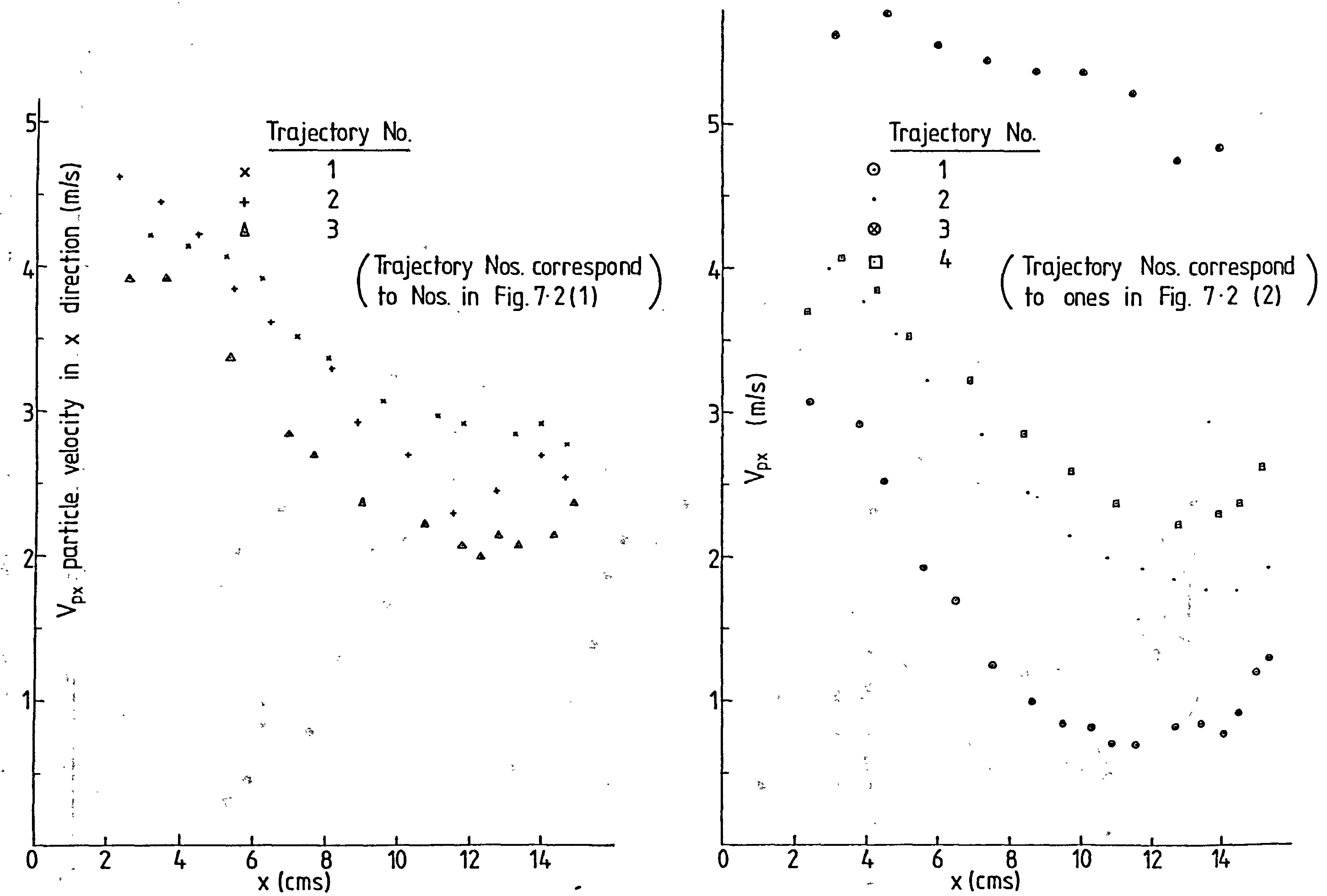

FIG. 7·25 EXPERIMENTAL PARTICAL VELOCITY DISTRIBUTION (60 Kv)

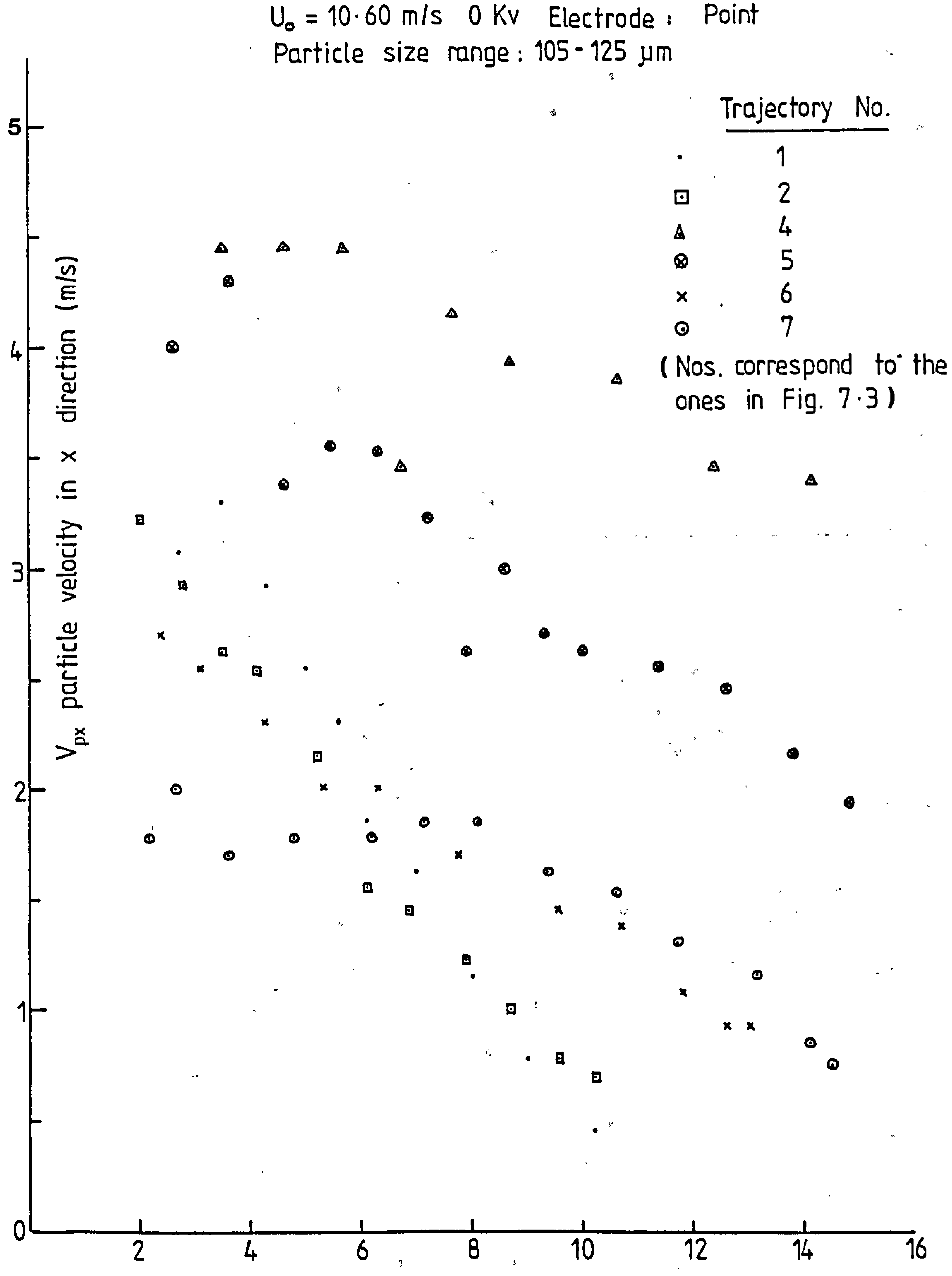

FIG. 7· 26 EXPERIMENTAL PARTICLE VELOCITY DISTRIBUTION (0 Kv)

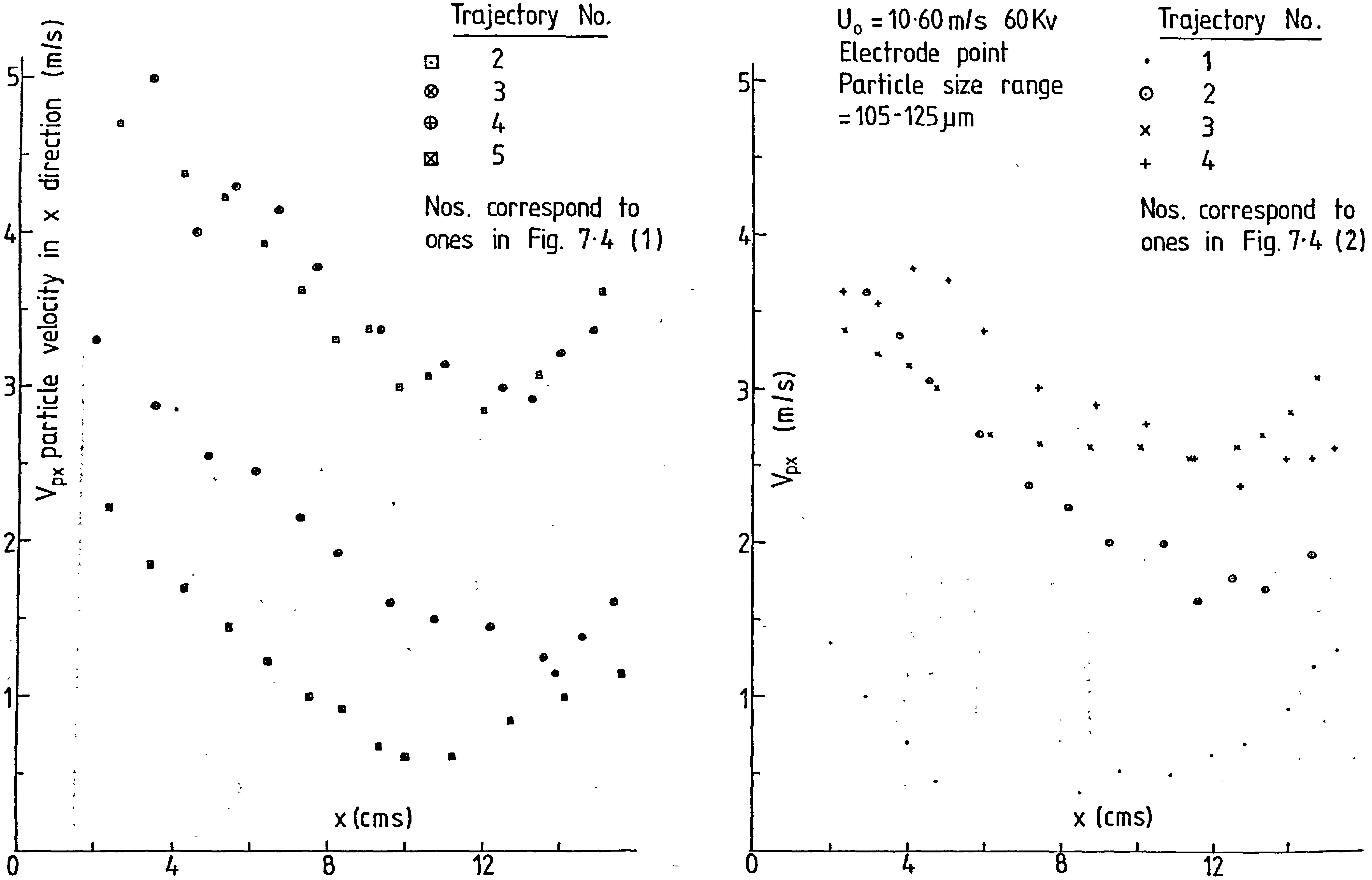

FIG. 7·27 EXPERIMENTAL PARTICLE VELOCITY DISTRIBUTION (60 Kv)

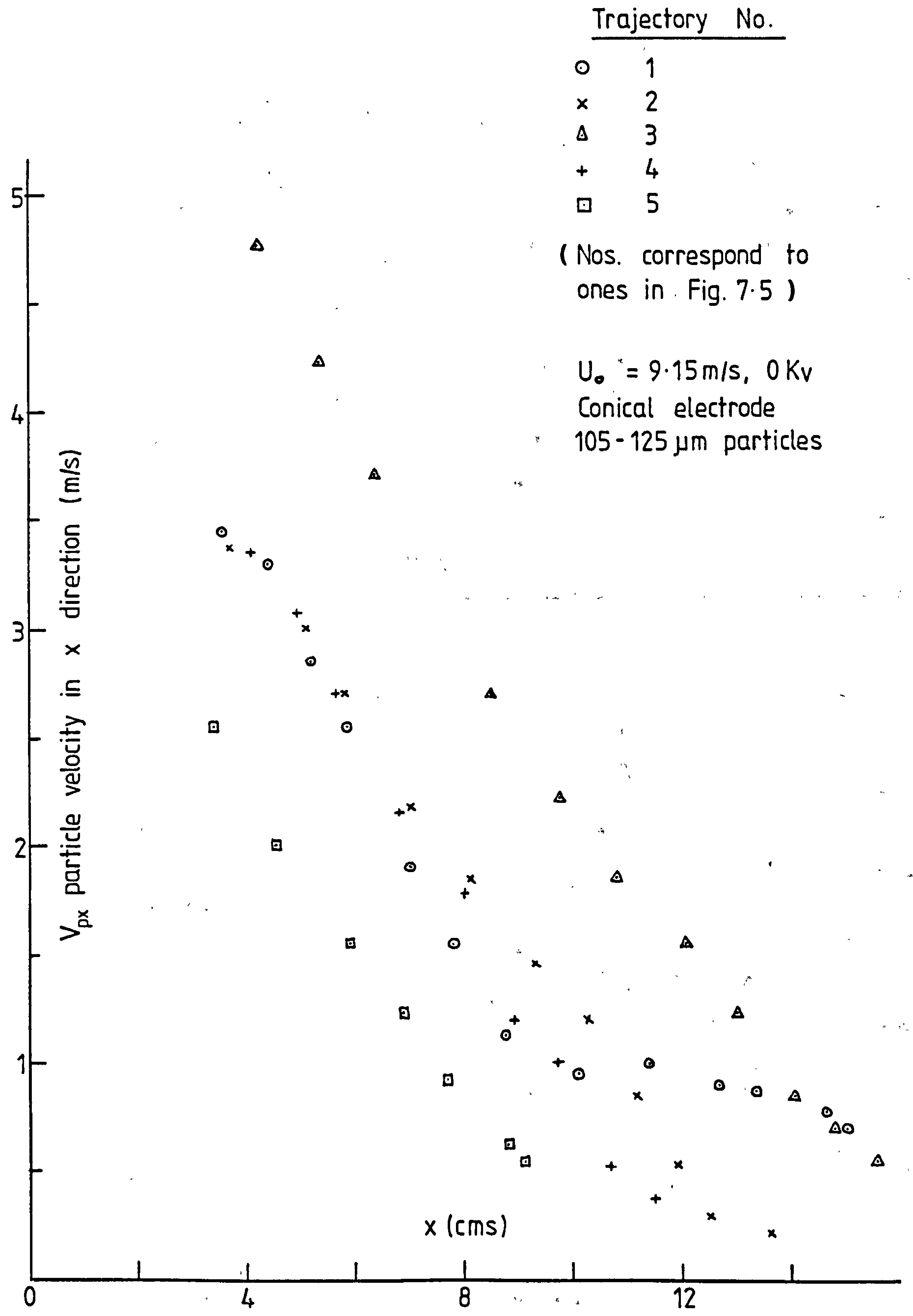

FIG. 7· 28 EXPERIMENTAL PARTICLE VELOCITY DISTRIBUTION (0 Kv)

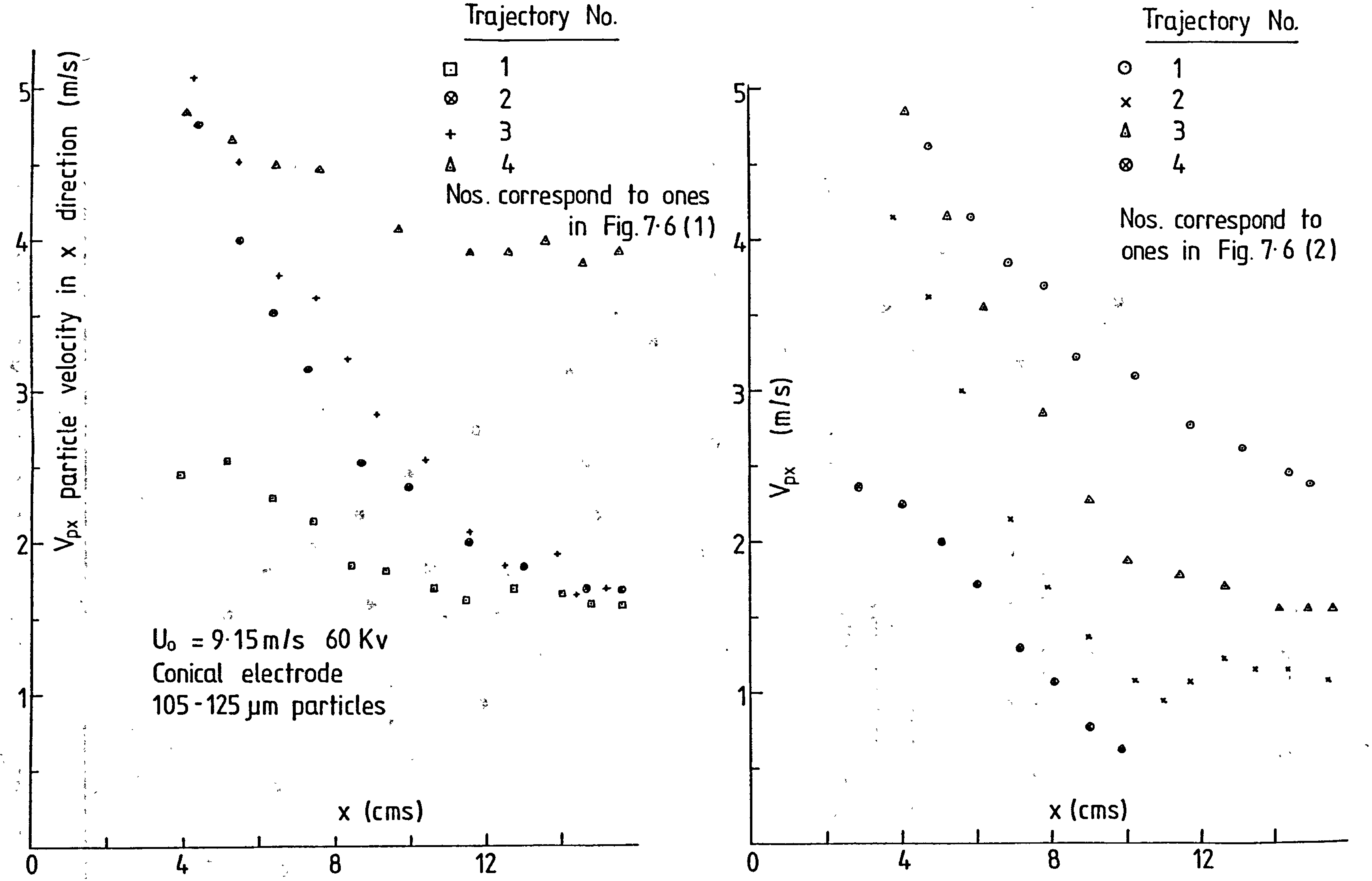

FIG. 7·29 EXPERIMENTAL PARTICLE VELOCITY DISTRIBUTION (60 Kv)

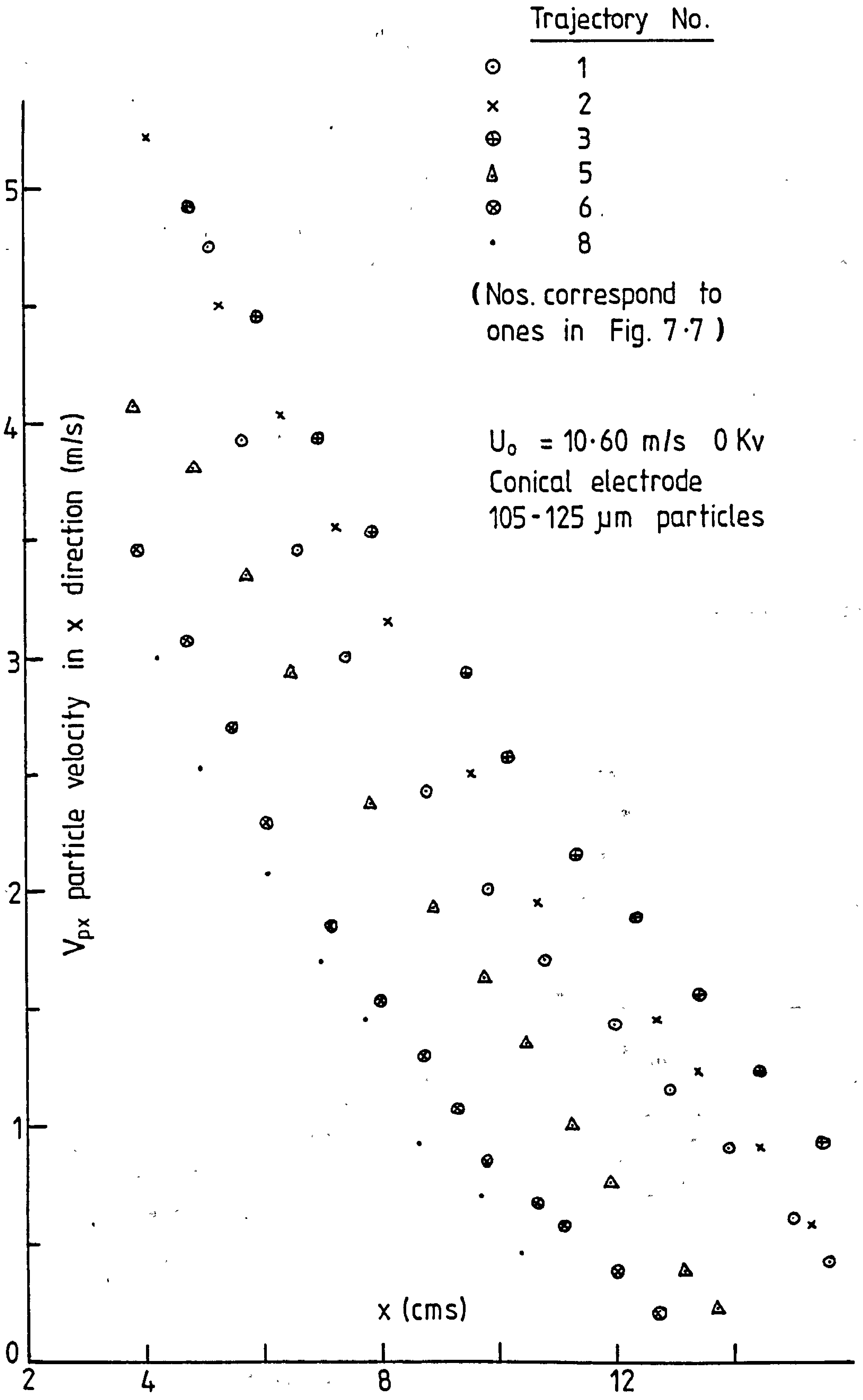

FIG. 7·30 EXPERIMENTAL PARTICLE VELOCITY DISTRIBUTION (0 Kv)

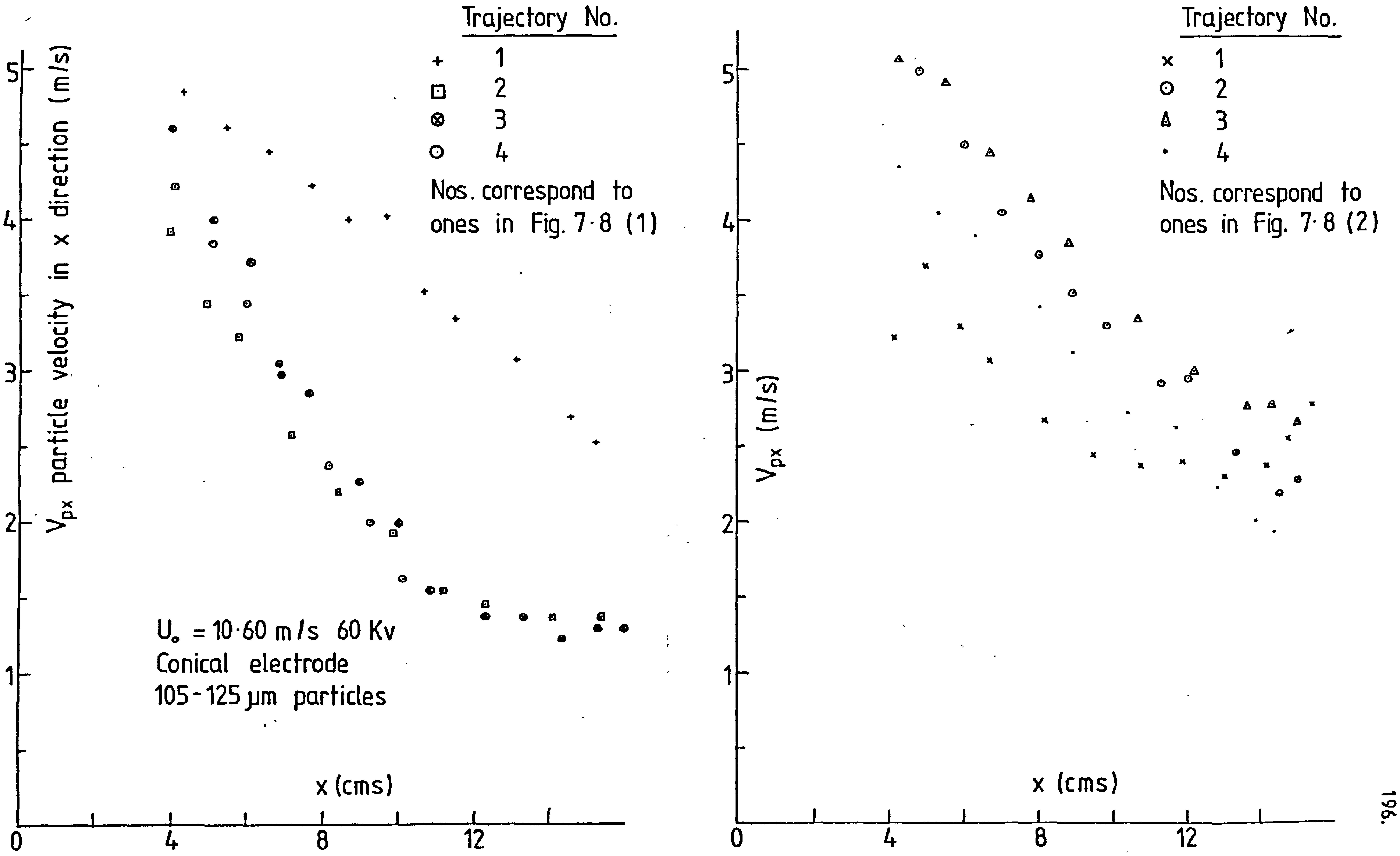

FIG. 7·31 EXPERIMENTAL PARTICLE VELOCITY DISTRIBUTION (60 Kv)

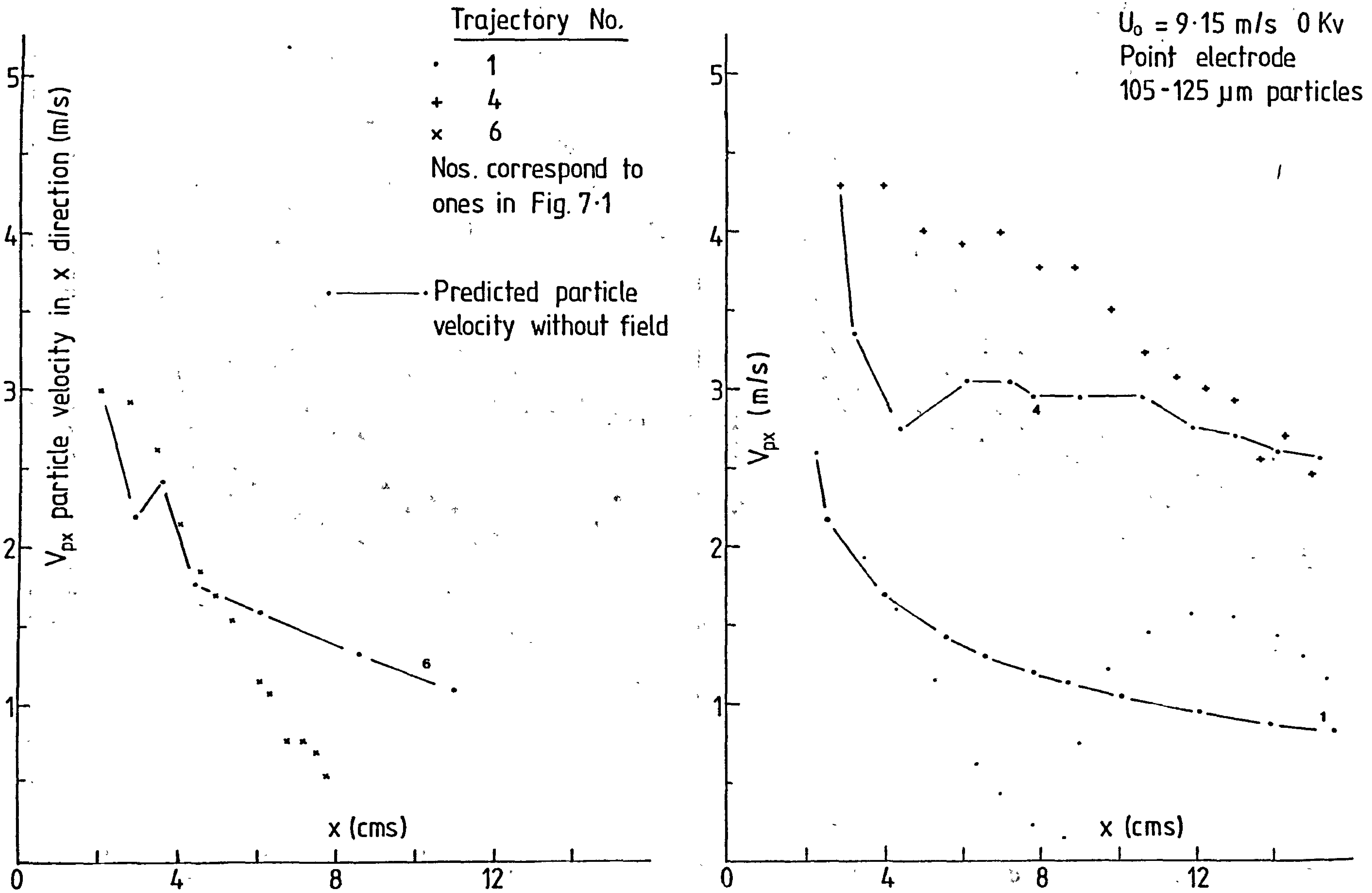

FIG. 7· 32 COMPARISON BETWEEN EXPERIMENTAL AND CALCULATED PARTICLE VELOCITIES

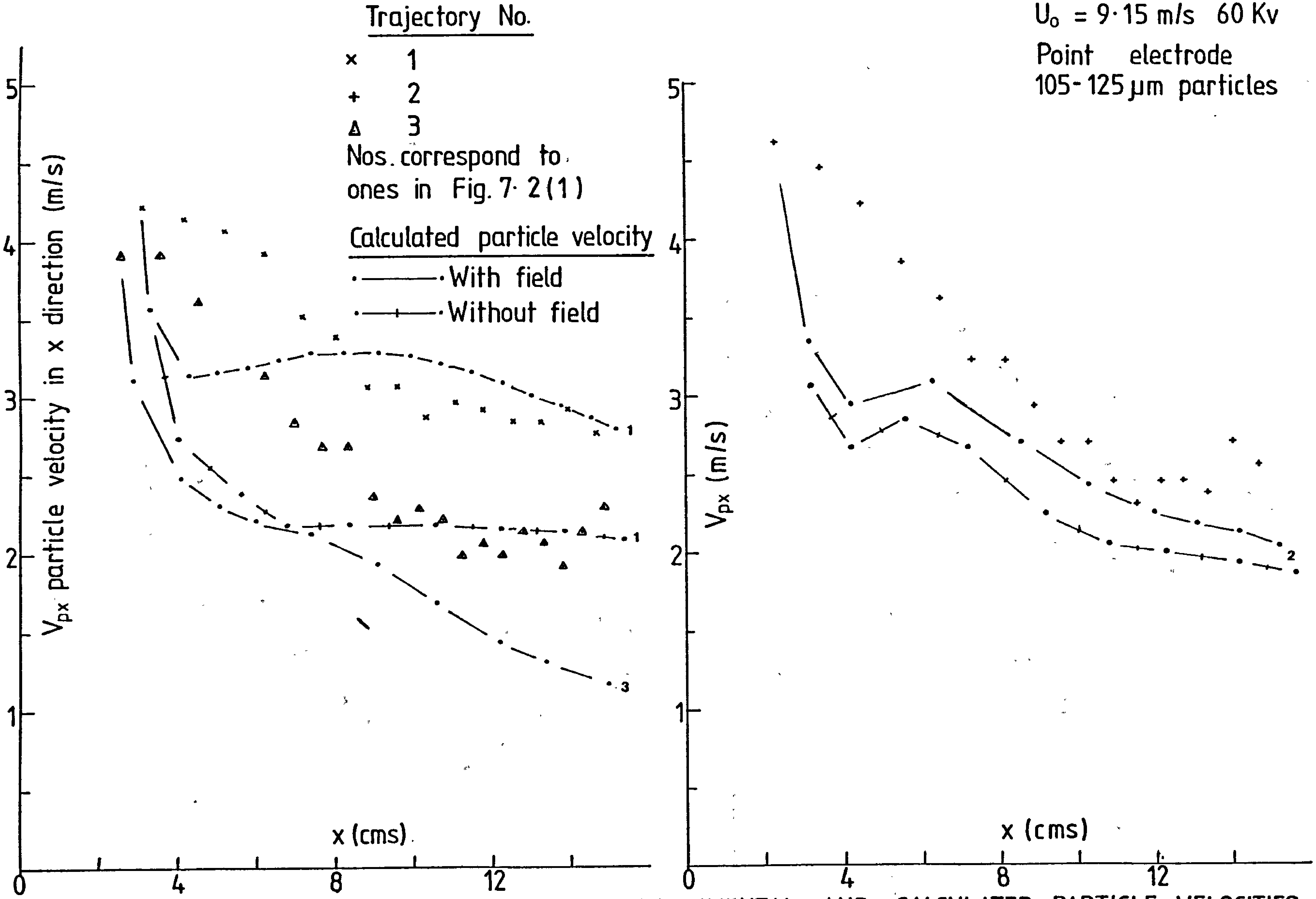

FIG. 7·33 COMPARISON BETWEEN EXPERIMENTAL AND CALCULATED PARTICLE VELOCITIES

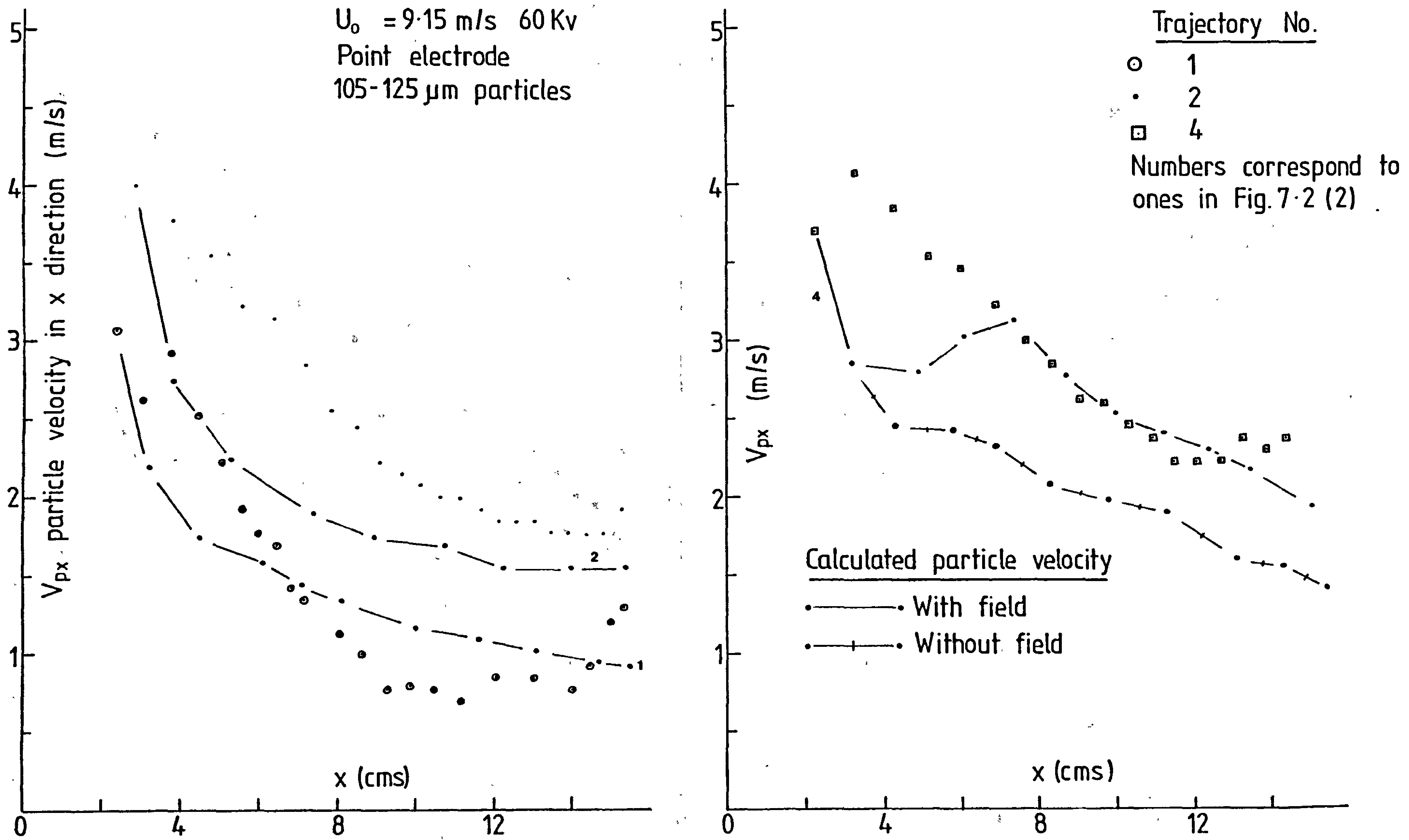

FIG. 7·34 COMPARISON BETWEEN EXPERIMENTAL AND CALCULATED PARTICLE VELOCITIES

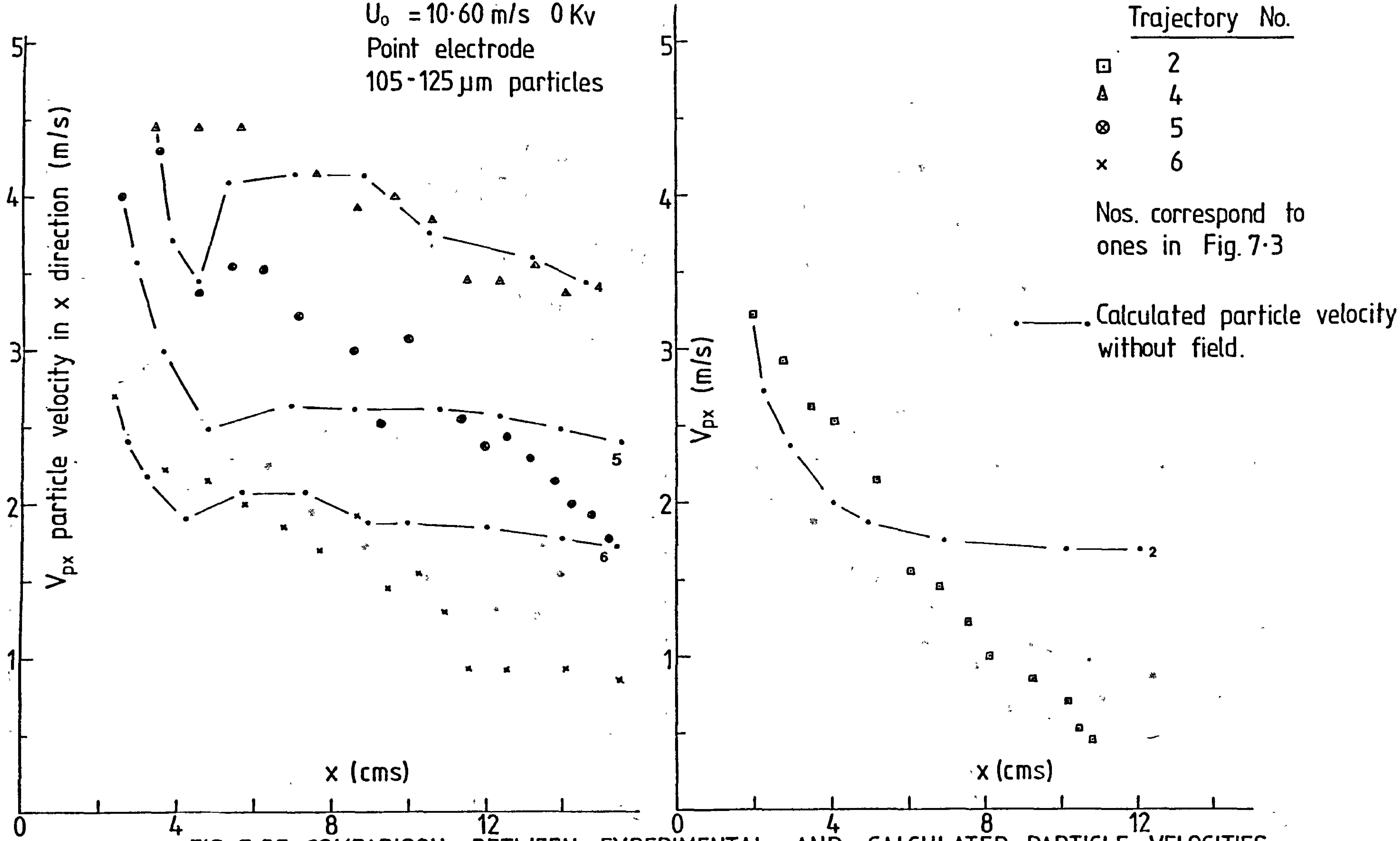

FIG. 7·35 COMPARISON BETWEEN EXPERIMENTAL AND CALCULATED PARTICLE VELOCITIES

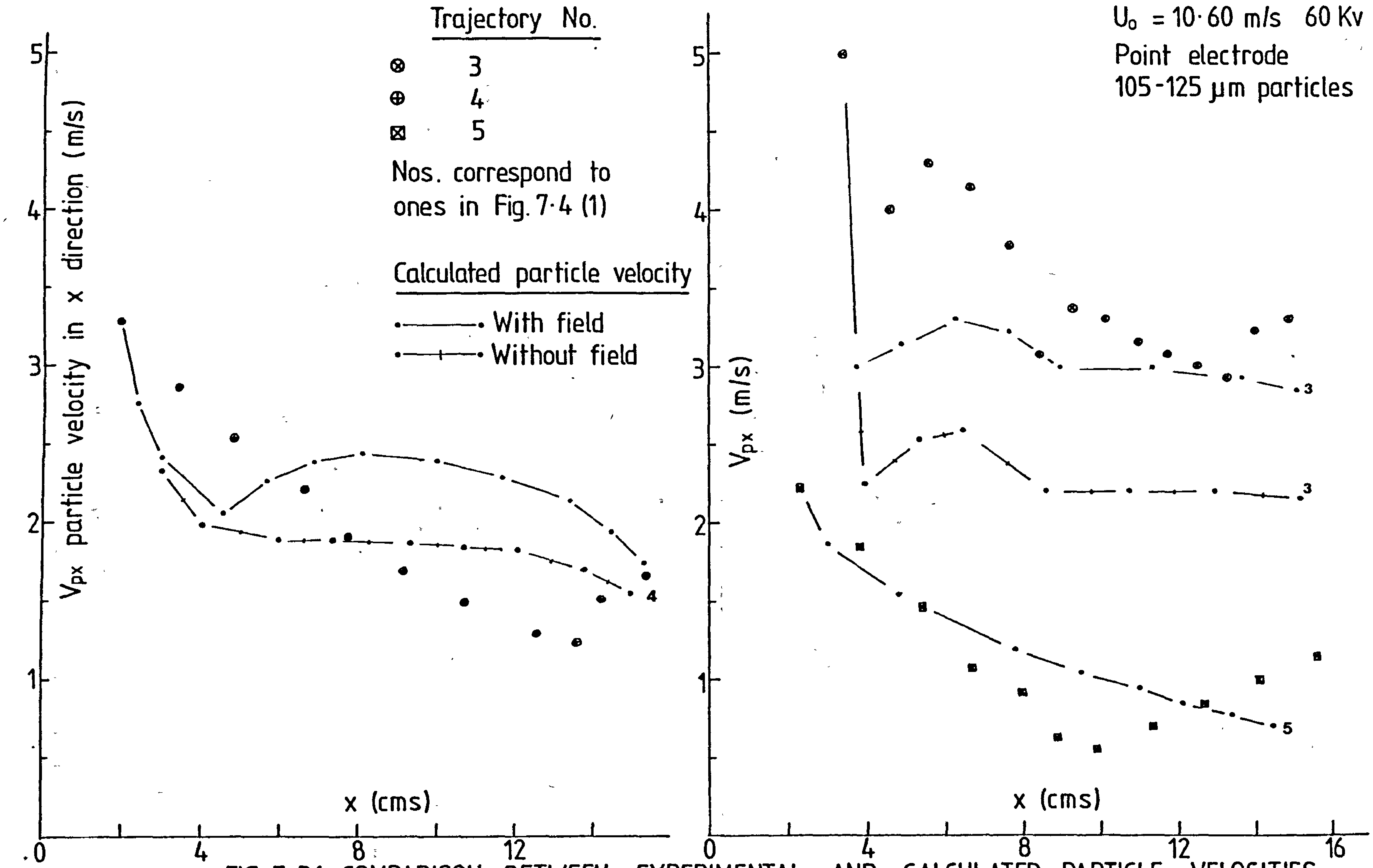

FIG. 7·36 COMPARISON BETWEEN EXPERIMENTAL AND CALCULATED PARTICLE VELOCITIES

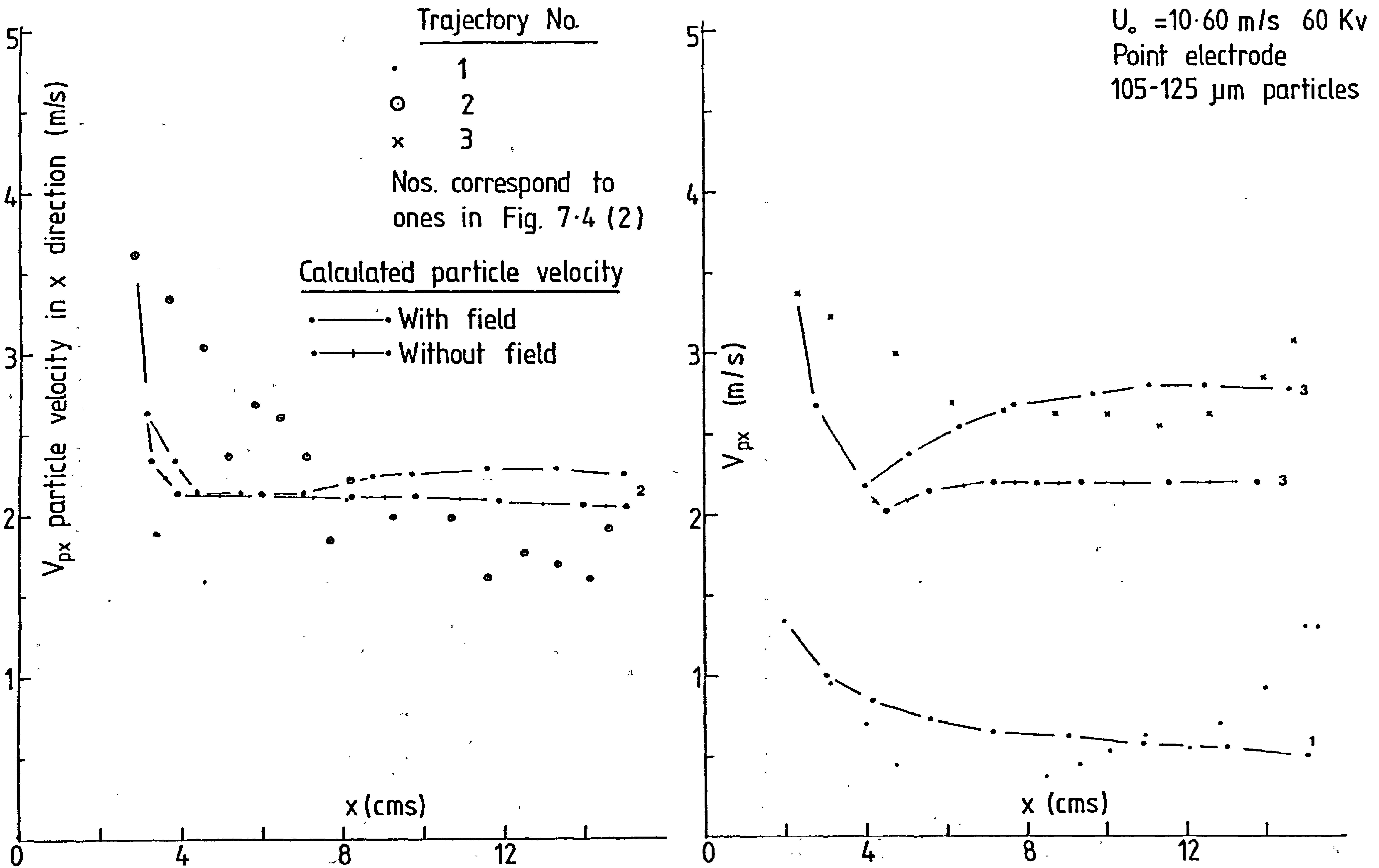

FIG. 7·37 COMPARISON BETWEEN EXPERIMENTAL AND CALCULATED PARTICLE VELOCITIES

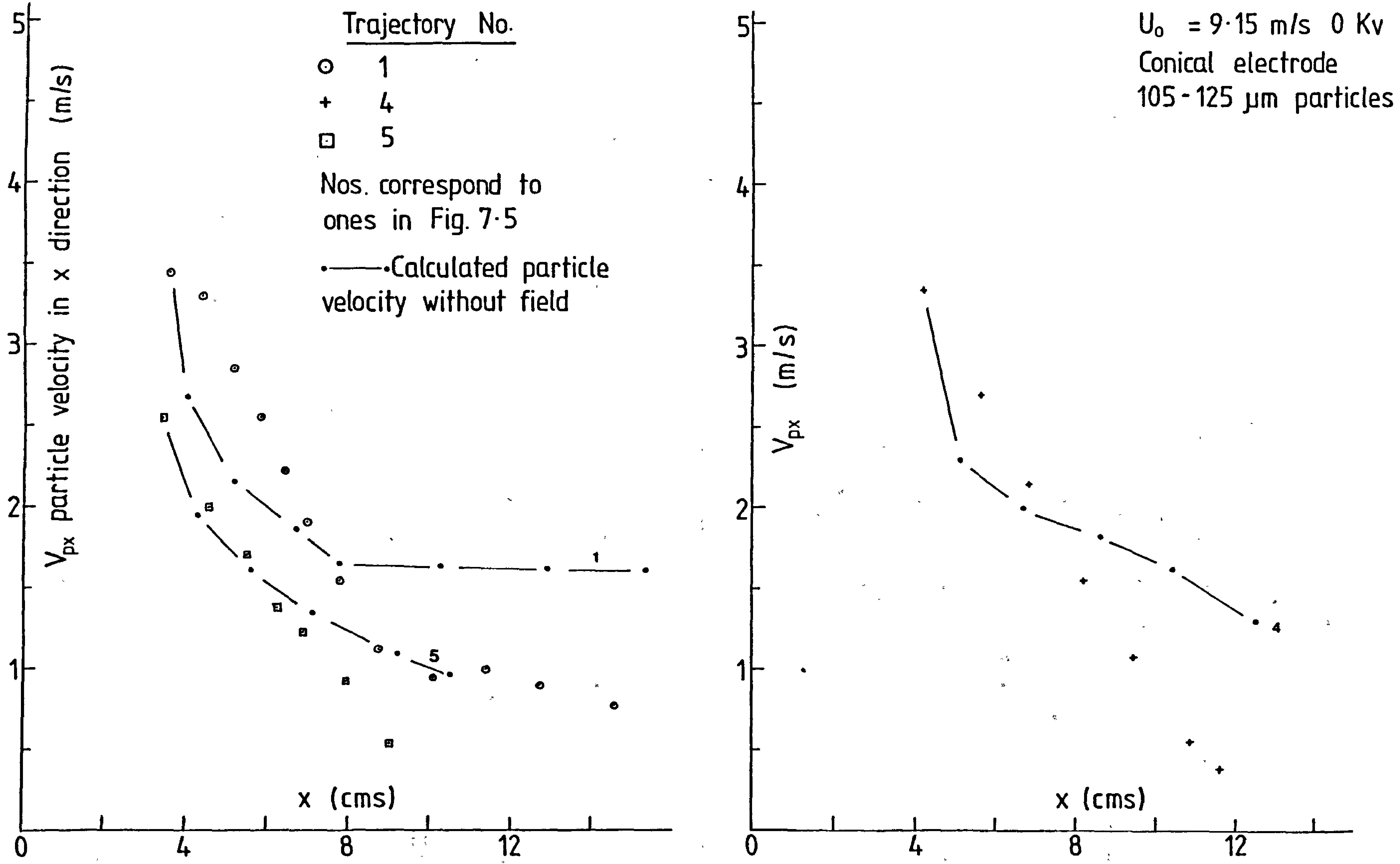

FIG. 7·38 COMPARISON BETWEEN EXPERIMENTAL AND CALCULATED PARTICLE VELOCITIES

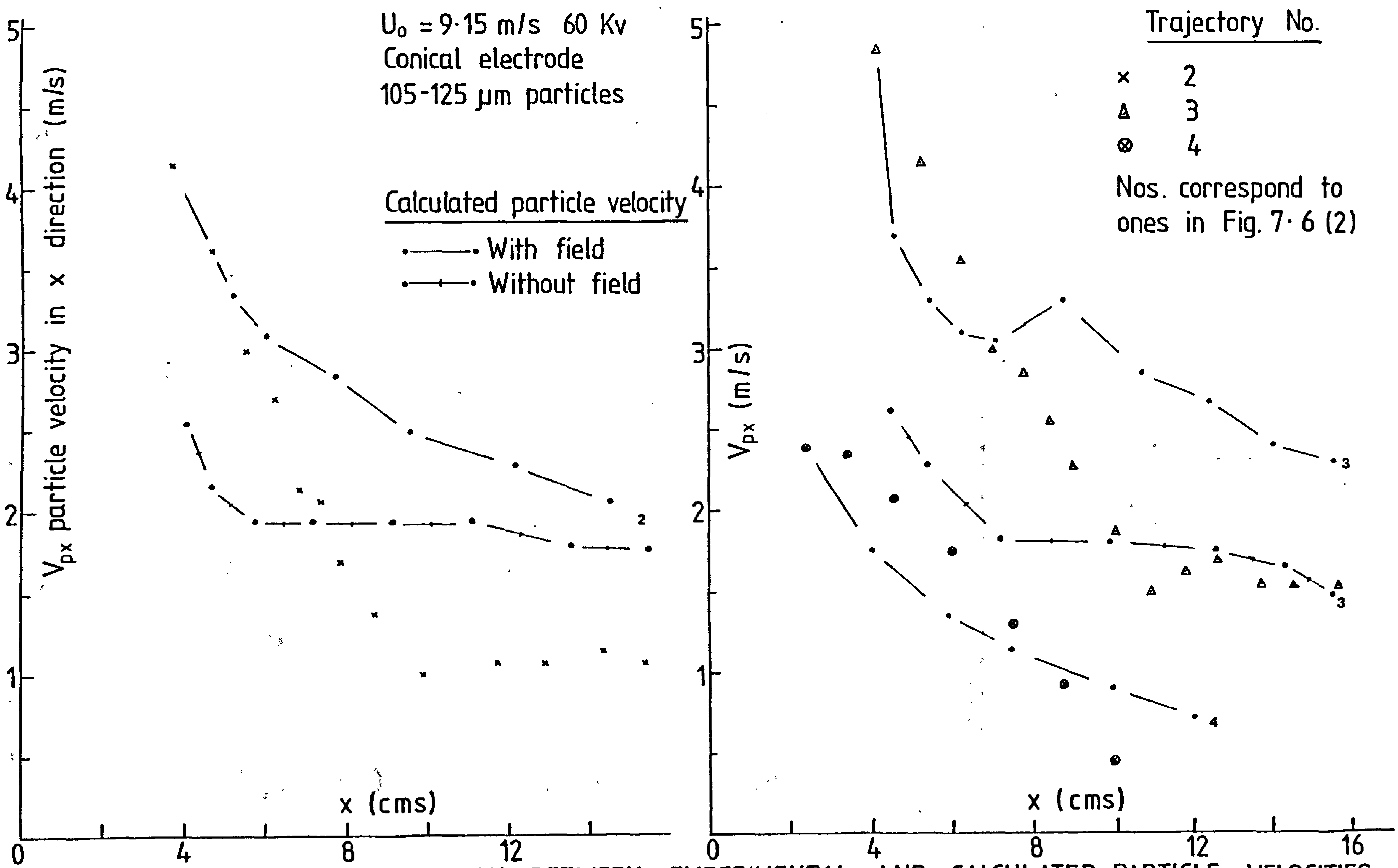

FIG. 7·39 COMPARISON BETWEEN EXPERIMENTAL AND CALCULATED PARTICLE VELOCITIES

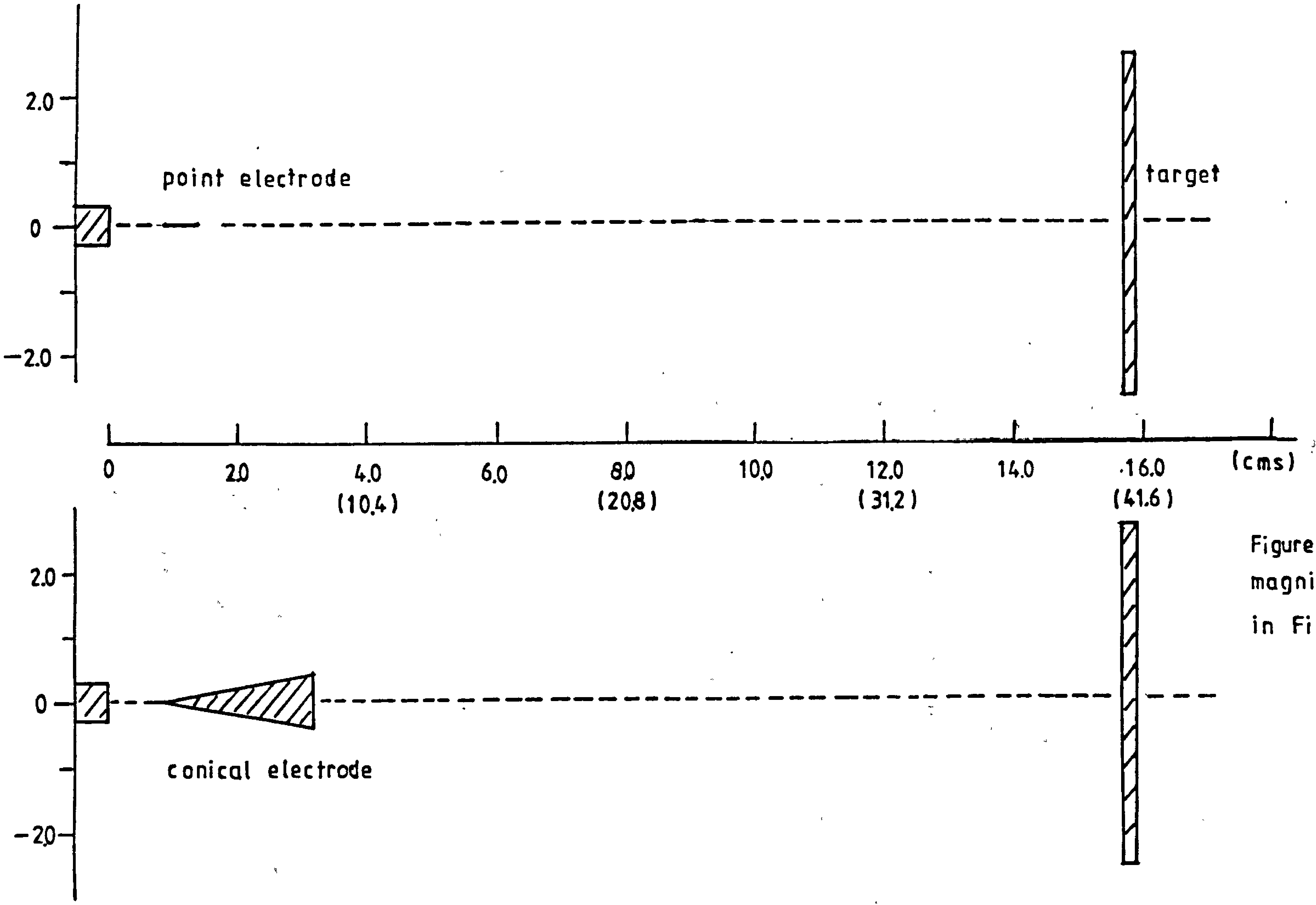

Figures in brackets are
magnified scales used
in Figures 7.1 — 7.23

Figure 7.40 Electrode configuration

flow of particles. The gravitational effect became less pronounced with decreasing particle size and with the use of conical electrode the spray pattern became more divergent. Throughout the experiments very good deposition was achieved indicating effective charging of the particles.

For particles emerging below the centreline, except for wide angle of emergence generally the field was sufficiently strong to overcome the gravitational effect as illustrated by the following three trajectories of 105 - 125 μm particles. The angle of emergence is defined as the angle subtended by the initial part of the trajectory with the horizontal centreline. As shown in Figure 7.6 (2) trajectory 4 emerging with an angle of - 30° succumbed to the gravitational force whilst trajectory 4 of Figure 7.8 (2) with an emergence angle of - 18° was deposited at the back of the object (not shown in figure). Trajectory 4 of Figure 7.8 (1) with an intermediate value of -26° showed an attempt by the field to 'lift' and attract the particle. Generally the result showed that if the exit angle did not exceed - 20° deposition would occur. For charged particles emerging above the axis deposition was good even for particles emerging with high positive angle of emergence since re-entrainment in the air jet was possible as illustrated by trajectories 1 of Figures 7.2(2) and 7.4 (2).

Figures 7.41-7.43 show the resultant deposition on the front and back of the object after each experiment. One interesting feature is the use of the conical electrode resulted in better coverage of the back of the plate and the edge of the front. The distribution became more uniform with the smaller particles.

7.1.2. Particle velocities.

The particle exit velocities of the recorded trajectories were generally between 3 - 5 m/s, representing 30-50% that of the exit air velocity. Surprisingly there was no significant difference between the particle velocities for the three size ranges although higher values for the smaller particles

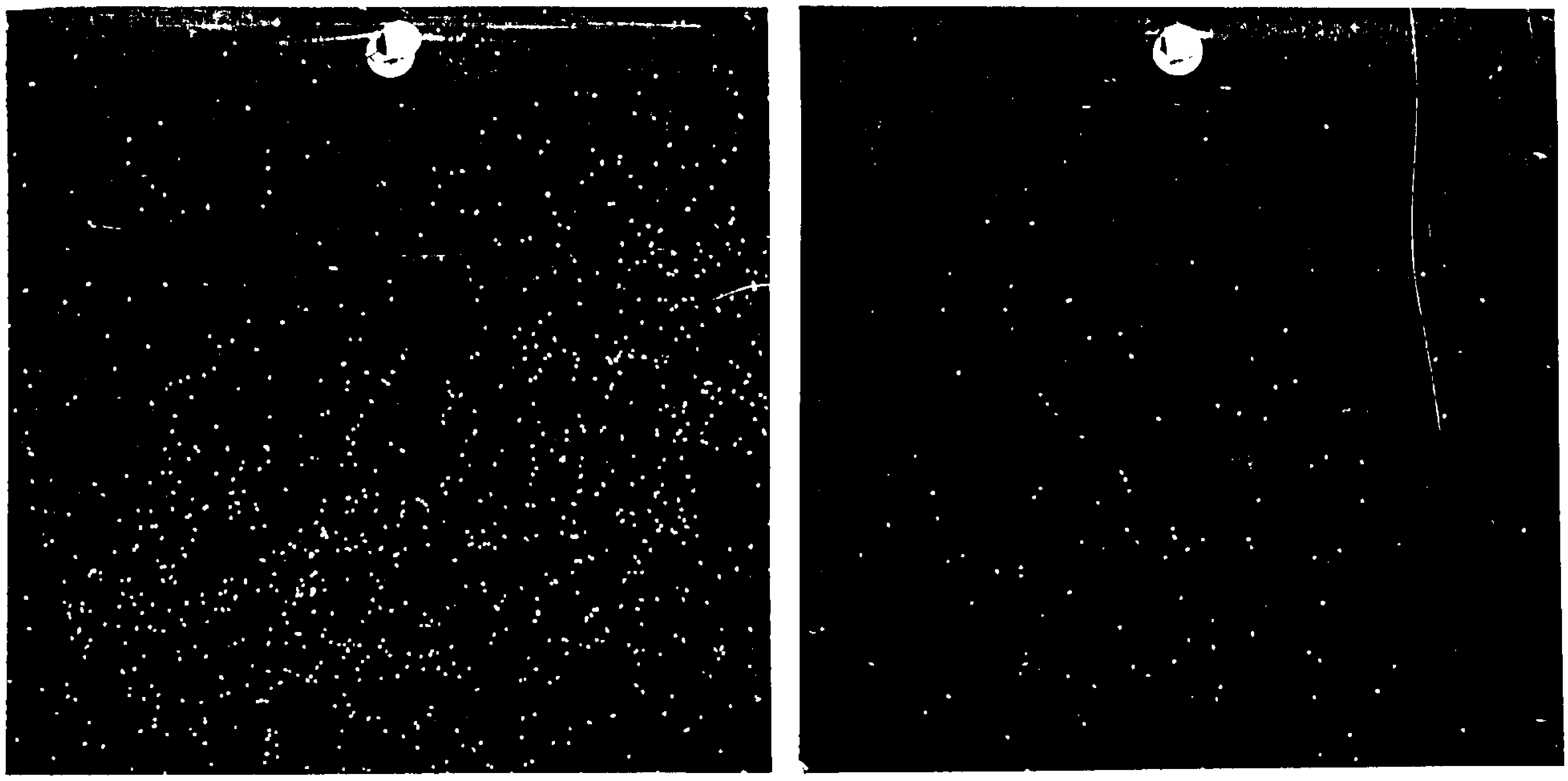

(a) Front of object (b) Back of object

Use of POINT electrode

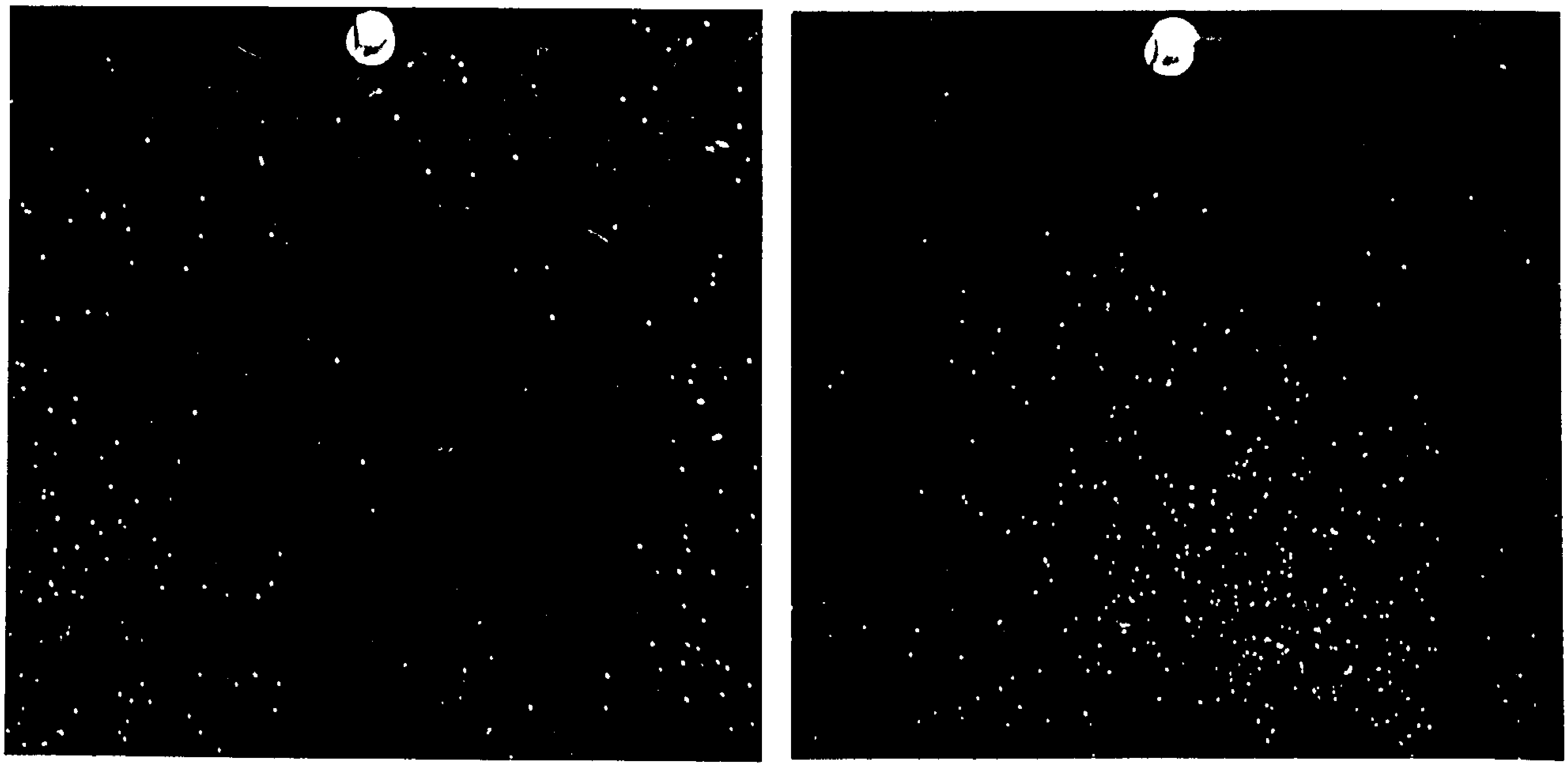

(c) Front of object (d) Back of object

Use of CONICLE electrode

FIG. 7·41. PARTICLE DEPOSITION USING POINT AND CONICLE ELECTRODES (105 - 125 μm)

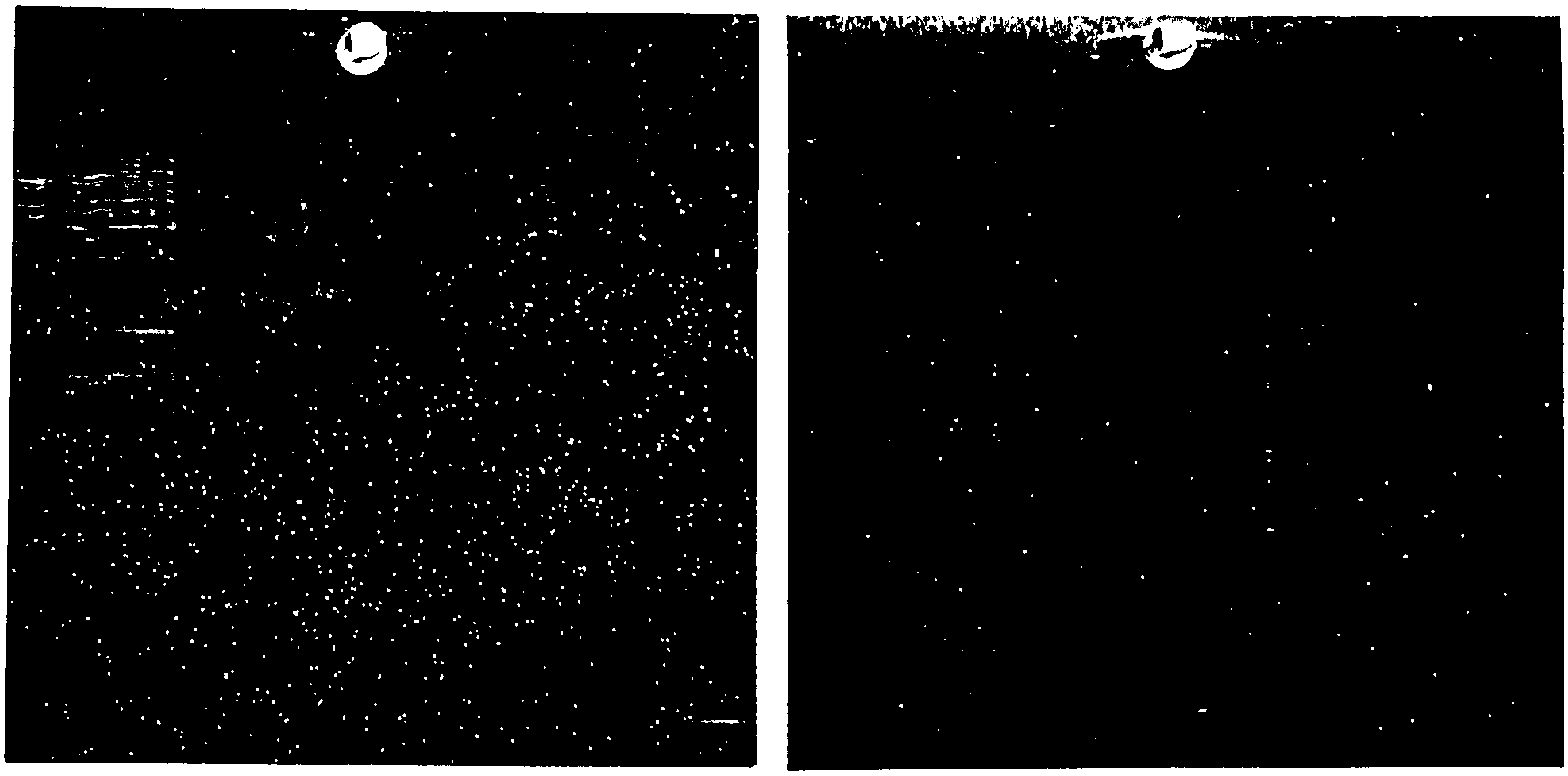

(a) Front of object (b) Back of object

Use of POINT electrode

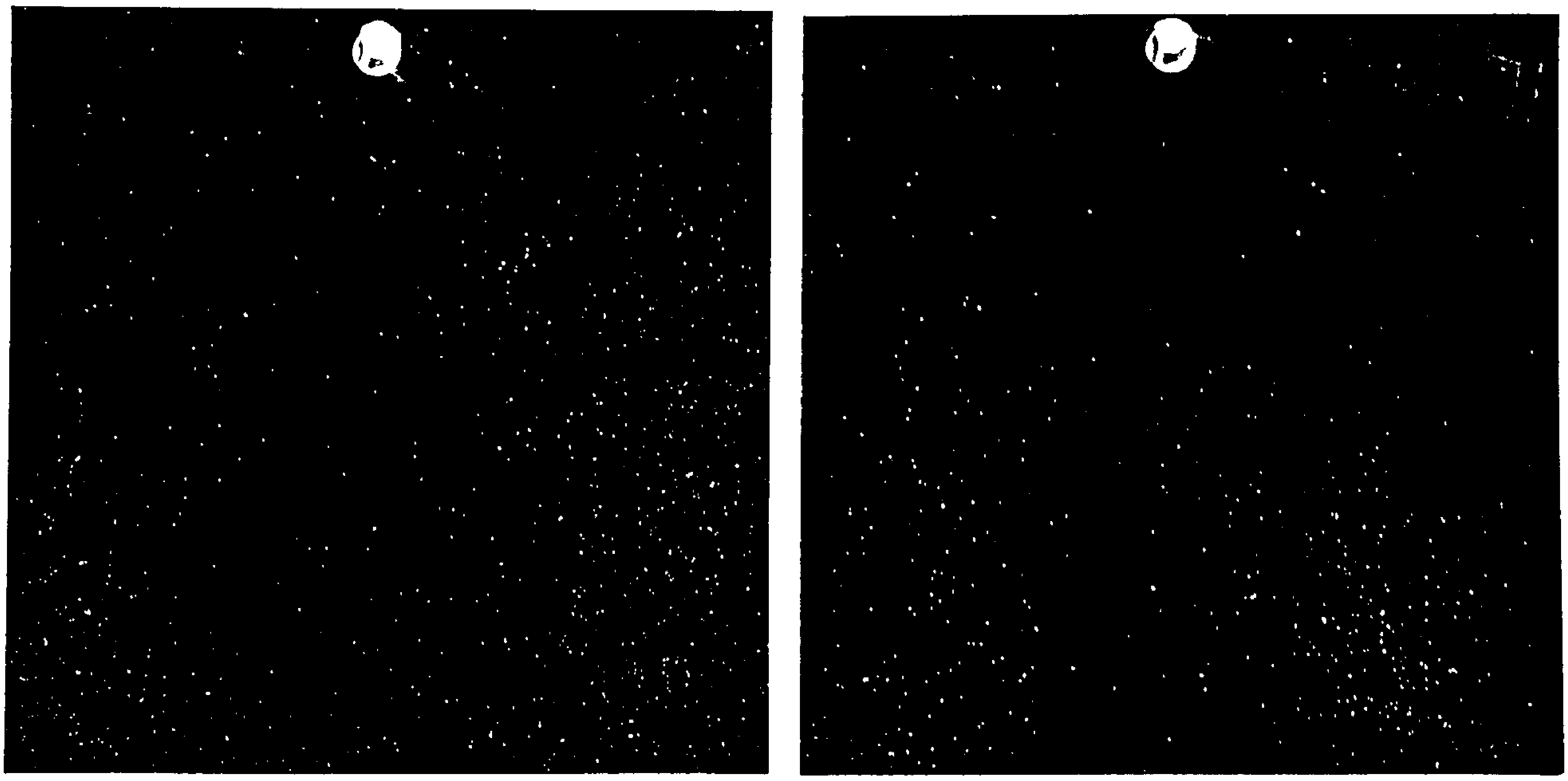

(c) Front of object (d) Back of object

Use of CONICAL electrode

FIG. 7·42. PARTICLE DEPOSITION USING POINT AND CONICAL ELECTRODES (75 - 90 μm)

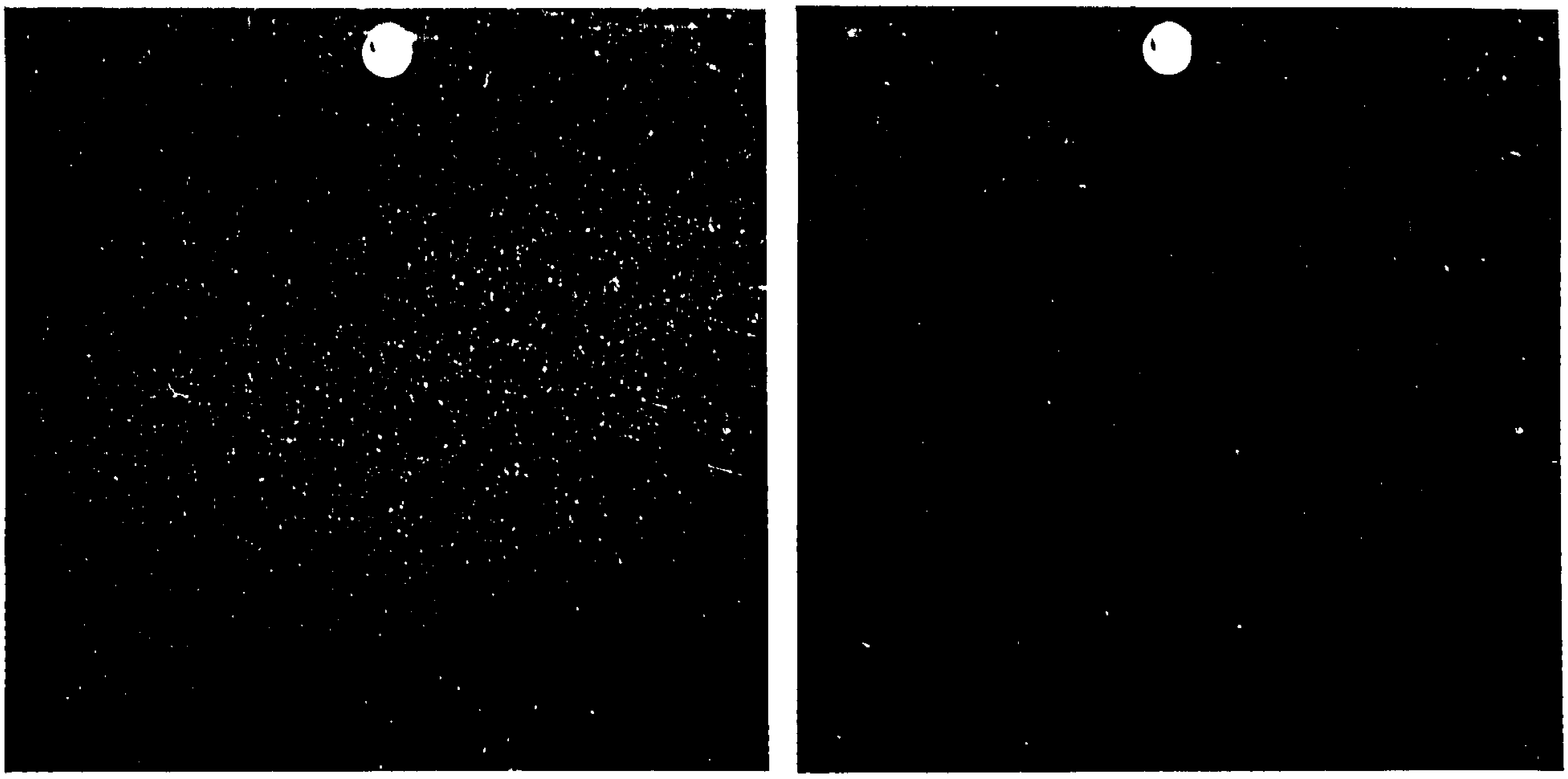

(a) Front of object

(b) Back of object

Use of POINT electrode

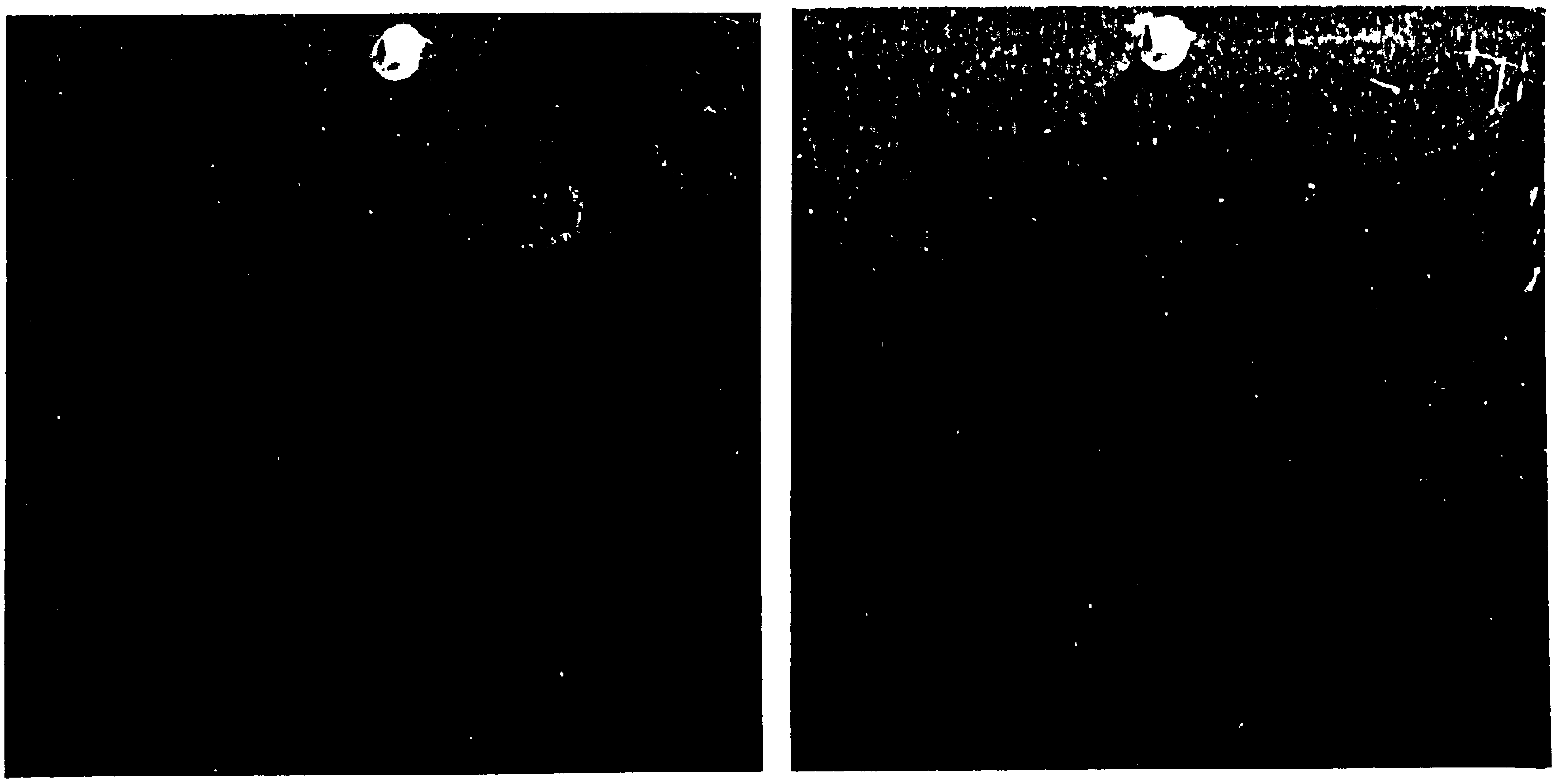

(c) Front of object

(d) Back of object

Use of CONICAL electrode

FIG. 7 43 PARTICLE DEPOSITION USING POINT AND CONICAL ELECTRODES (45 - 53 μm) were anticipated. The slip between the air and particle velocities obviously must be attributed to the loss of momentum due to collision with the tube wall. Using this photographic technique, the accuracy of particle velocity determination was estimated to be ± 0.08 m/s.

The choice of the magnitude of air velocity to demonstrate the effect of the electric field is well exemplified by the results using 105 - 125 µm particle when the conical electrode was employed (Figures 7.5 - 7.8). The effect of using two air velocities however was not clearly demonstrated by the results. Although desirable, it was not possible to reduce the air exit velocity further because the lower value of 9.15 m/s was found to be the minimum value capable of ensuring a smooth constant delivery of particles during the experiments. The main constraint was due to the internal structure of the particle feeder which comprised several constrictions restricting smooth particle flow. To overcome this problem would require the redesigning of the particle feeder system.

The experimental particle velocity distributions of Figures 7.24 - 7.31 for the 105 - 125 µm particles show the higher values resulted with the presence of electrostatic field especially when the conical electrode was used. The charged particles generally emerged with higher velocities embracing a velocity component contributed by the high voltage field. Though the field effect was apparent it was not possible to quantify precisely the velocity component due to the field effect when compared with the data obtained without field because particle trajectories were emerging with different velocities from different positions. The contribution of the electrostatic field was better shown by the result using the conical electrode. While without field invariably the particle velocity decayed rapidly the ones with field showed a slower decay and later attained constancy near the substrate. The electric field component near the object was generally between 1 - 2 m/s.

While it is difficult to determine the exact velocity component due to the electrical forces at various positions it can be concluded that the air flow from the spraying device is responsible for conveying the particles to the object with increasing electrical field forces domination near the object. Using laser Doppler anemometry system for particle velocity determination and with a gun-target distance of 25 cm, at a distance of 12 cm from gun Singh (122) concluded that the electrostatic forces contributed an additional component of 1 m/s at an applied voltage of 60 Kv. The velocity also increased linearly with increasing applied voltage. The laser technique is particularly useful in this aspect for assessing the electrostatic field contribution at a particular point in the spraying system.

For the 105 - 125 μm particles when using the point electrode, nearly all the recorded trajectories showed acceleration near the substrate [illegible]

[illegible]. The same trend however was not consistently shown by the smaller particles and also when using the conical electrode. The one plausible explanation is as stated in equation (4.35) the charge increases as the square of the particle radius and therefore with the same field intensity the electrical force exertion for a bigger particle is greater than for a small one. The particle velocity distribution for the smaller particles showed that the resultant electrical force was only sufficient to maintain the particle momentum and not to cause an acceleration. With the use of the concial electrode, the result implied that the field enhancement effect was exhibited to a lesser degree than the point electrode. There is no field measurement data available for this configuration and further experimental study of field intensity distribution would be useful.

7.1.3. Effect of particle size.

During the experiments it became apparent that with decreasing particle size the particles begin to 'dance' about. This meandering motion is well illustrated by several trajectories in Figures 7.17 - 7.23 for the 45 - 53 µm particles. Whilst for the larger particles of 105-125 µm range the particle inertia maintained an unwavering path, the 75 - 90 µm particles showed some tendency to drift, examples of which can be seen in Figure 6.12 and other trajectories in Figures 7.9 - 7.16. This drifting in powder coating process was first reported by Singh (108) spraying with epoxy powder of between 2 - 70 µm. With the presence of the electric field the diffusiveness seemed to have been restrained because of the imposition of electrical forces on the charged particles. The drifting of particles is fundamentally induced by turbulence of the fluid and the turbulent diffusivity of particles in two phase flow has recently been investigated by several people (85, 76, 91, 124). The presence of an electrode in an air jet would greatly enhance the fluid turbulence and would consequently lead to an increase in diffusivity for the small particles.

7.1.4 Edge effects

With an applied voltage many particles with wide angle of emergence have resulted in deposition (eg. trajectory 5 of Figure 7.4 (1)). All these particles were outside the sphere of influence of the electrical forces confined to the conical geometry defined in Chapter 4. These particles always preferably deposited around the edges of the plate. Calculation of the particle image force showed that it was too insignificant to overcome the gravitational effect and to maintain the particle course. This is solely an electrostatic effect since uncharged particles with similar position of emergence would result in disengagement from the jet. This suggested the presence of some form of electrical field other than the ones analysed.

One possible explanation of this extra field is that due to the edge effect of the object. It has been confirmed by Ting (120) that edge effects are always present on non-spherical substrates and would result in some degree of field enhancement because of the non-uniform field around the edges. For a flat plate, not unexpectedly the edge effects would result in different powder behaviour around the edges. This is further complicated that in the presence of a high voltage field a sharp edge or point would go into corona resulting in further field distortion. During the experiments every attempt was made to minimise the edge effect by smoothening the edges of the plate and also by application of thin coating of silicone rubber. This edge effect is an area requiring further investigation particularly the degree of enhancement and also its directional effect.

7.1.5. Effect of booth air flow .

Several experiments were conducted with the filtration system switched on which effectively introduced a uniform flow of air of about 0.3 m/s in the test section. Not unexpectedly this air flow did not make any noticeable difference in the particle velocity distribution or trajectories for the particle size ranges concerned.

7.2 Theoretical prediction

The prediction program has included many simple models and concepts and the scheme generally produced reasonable agreement with the experimental data. The calculation showed effectively the spreading of charged particles in the two phase jet under the influence of a high voltage field and overcoming the gravitational effect. Agreement is good in the vicinity of the centreline but away from it there is marked deviation between the experimental and theoretical comparison. This discrepancy generally becomes more severe with increasing value of angle of emergence with the experimental particle velocity data showing a faster decay that the theoretical value. It was assumed that the y direction variation in various components (eg. air and particle velocities) was small compared with the x direction variation and consequently the comparison was confined only to the x components. The trajectory comparison has shown that this assumption is generally valid for the near centreline data.

There were very few trajectory studies of two phase flow where there was direct comparison of experimental pathlines and calculated ones and Abuaf et al (24, 83) presented the only trajectory study relevant to the powder coating process. In their study excellent agreement was obtained because the experiments involved simpler geometry without the presence of an electrode in the jet stream. Also bigger particles of 250 - 417 µm were used where the inertial effect would be predominant and only particle trajectories that appeared to emerge from a common point source were chosen for comparison. Many of the findings in this study are in good agreement with the results of Abuaf et al.

Comparison of the theoretical and experimental particle velocity distributions of Figures 7.32 - 7.39 showed that generally the level of magnitude was correctly predicted. The calculation showed satisfactorily the dominance of electrostatic forces near the object with a maximum predicted value of the particle velocity component due to field effect of 1 m/s.

In the following sections the main discrepancies of comparison and shortcomings of the prediction procedure are discussed and with possible improvement suggested. The deviations between theory and experimental values may be attributed to uncertainties in evaluation of various factors like drag coefficient,particle size/shape and the modelling deficiencies in the description of air flow and electrostatic field intensity.

7.2.1. Drag Coefficient

The drag coefficient calculated for the trajectory prediction was based on an equation applicable to only spherical particles. The off centreline experimental data showed consistently significantly higher drag coefficient values than the calculated ones, clearly indicating the inadequacy of equation (2.7) to deal with non-spherical particles. The epoxy particles used in this study are angular as shown in Figure 6.5. One good illustration is trajectory 1 of Figure 7.4 (2) where no air flow would be encountered by the particle. The rapid decay of particle velocity shown experimentally was generally under predicted. The drag coefficient would further be affected by tumbling and rotation motion of the particle exhibited by the trajectories in Figure 6.7.

Although a fundamental parameter in particle motion studies there is a distinct lack of information on drag coefficient evaluation taking into account several important aspects eg. shape effect, rotation, roughness and others. Torobin and Gauvin (15) presented an extensive series of results examining the various complicating effects which rotation and shape would impose on the motion and drag of single particle entrained in a fluid. Generally for spheres rotation appeared to hardly affect the drag coefficient but was found to influence the linearity of the motion and there was no available information on non-spherical particles. The effect of shape is more complex as there is confusion as regards to the best method of characterising the shape of a particle. Experimental results of comparison of drag coefficients for various shapes using spheres, coal, anthracite, sandstone, Pyrites and shale particles for a range of Reynolds number showed much higher values for the non spherical particles. Typically for $10 < Re < 10000$, drag coefficients of 1.5 - 0.35 for spherical particles were obtained compared with values of 3.6 - 1.8 for the other particles. The accuracy of prediction can only be as accurate as the description of the mathematical models for field simulation and drag coefficient. Therefore undoubtedly considerable improvement in prediction can be made with more accurate evaluation of drag coefficient for non-spherical particles. This precise information for the present moment can only be obtained with experimental measurement of the drag coefficient of epoxy particles for a range of Reynolds number.

7.2.2. The air flow description of region behind the electrode.

In Chapter 3 it was pointed out that in most jet flow studies reported, the main emphasis has been centred on the fully developed region whereas the initial region has not commanded the same attention (73, 121). The presence of a small electrode in the initial region resulted in the shift of the virtual source of the jet and the existence of a region of rising velocity before the fully developed flow section. This was verified with hot wire anemometer measurement. In the prediction scheme a very simple approach was adopted describing the velocity distribution with an expression derived from the experimental measurement of the centreline velocities. As emphasised earlier the turbulent process would be greatly enhanced by the presence of electrode and the turbulence was only crudely represented by the Prandtl mixing length concept. Another assumption was made for this small region that the y component air velocity was unvarying and unimportant. This region behind the electrode not surprisingly provided the major source of discrepancy in the trajectory calculation.

This deficiency is well shown by the particle velocity distribution of Figures 7.32 - 7.39 where an initial sudden particle deceleration was predicted and a recovery was staged further downstream. Some experimental particle trajectories did show this deceleration though not consistently and certainly not to the magnitude predicted. Further downstream the velocities compared reasonably. Since at the initial region the aerodynamic force is the predominant force for the particle transport, subsequent improvement in trajectory calculation is possible if more accurate air velocity prediction can be obtained. As indicated by the pathlines comparison the predicted ones invariably fell below the experimental ones mainly due to the excess loss of particle momentum predicted after particle emergence from the spraying device.

The present approach is over simplified and a better understanding of the flow behaviour of this region with the presence of an electrode is only possible with a thorough experimental survey of the mean velocity profile and the associated turbulent quantities. From these measurements it is then possible to develop some satisfactory empirical models for air velocity prediction.

7.2.3. Prediction of trajectories for small particles.

As described earlier, with reduction in particle size, particle would be strongly influenced by the turbulence process and began to drift. This diffusion phenomenon was not anticipated and its unaccountability led to poor prediction of the pathlines. Nonetheless prediction results of Figures 7.17 - 7.23 show that for majority of the trajectories the eventual position of deposition was satisfactorily predicted despite using the very simple flow models. The calculation improved with the application of the high voltage field. To date there is generally a lack of studies of particle diffusion in a turbulent jet (eg. 85, 76) and much further work is required to understand this fluid/particle interaction process better. The turbulent flow field is represented by a sequence of eddies and the particle interaction with these eddies would be difficult to model. It is doubtful with the current knowledge of fluid/particle interaction whether it is possible to predict accurately this drifting movement exhibited by the small particles. Whatever improvement can be made would require sophisticated modelling beyond the scope of this work.

7.2.4. The Potential flow solution

Using the potential source flow model and the potential flow past a vertical plate model resulted in very high particle velocity prediction, very often of two to three times the order of magnitude using the jet flow solution. Result in Chapter 3 showed that the air velocity distribution was overpredicted and the decay away from the source and centreline of jet was too insignificant. This gross overestimation was transmitted in the particle velocity results. Hence the dimensionless Electrical number and Stokes number of Chapter 4 could not be suitably used to characterise the electrical and inertial effects.

7.2.5. Corona wind effect.

The corona wind as described simply by equation (5.21) was also included in the program and subsequent calculation compared to the one excluding corona wind effect showed insignificant change of pathline and charged particle velocity. Experimental evidence in various particle velocity measurement studies in powder coating process (116, 123) suggested that the velocity component contributed by corona wind effect was negligible especially near the substrate.

7.2.6 Space charge effect

As discussed in Chapter 4 with an estimated charge density of 10^{-5} C/m^{3}, using the space charge density criterion as guideline, equation (4.21) was chosen for field intensity calculation. From the results of comparison of data using the point electrode it seems that equation (4.16) with space charge consideration perhaps would be the appropriate expression to demonstrate qualitatively the field enhancement effect near the object causing particle acceleration. For the conical electrode geometry the use of equation (4.21) resulted in slight overestimation of the particle velocity and further deviation would incur if equation (4.16) was used.

7.3 Summary and conclusions

For the comparison between the experimental and theoretical calculation of particle trajectories the following important conclusions can be made:

(i) Both theoretical and experimental analysis have shown that the aerodynamic force due to the air flow from the spraying device was the predominant force responsible for the particle transport and the electrostatic forces became important near the substrate mainly due to the space charge effect.

(ii) With a reduction of particle size, the turbulent mechanism became important resulting in particle drifting. The present knowledge in turbulent particle diffusion modelling would not significantly improve the prediction. Overall the prediction of the final position of deposition was reasonable especially when the presence of the electrostatic field was considered.

(iii) Generally, despite the simplicity of models employed the calculated trajectories compared favourably with the experimental data. The degree of accuracy of prediction depended on the initial particle exit conditions. The deviation became significant away from the jet centreline. As for particle velocity prediction the magnitude was satisfactorily predicted.

(iv) Edge effect was postulated to play a significant role for particle deposition for particles outside the conical zone where the electrical forces were assumed to be operating. This required further experimental verification.

(v) Chronophotography has shown to be a good particle tracking technique giving vivid details of particle motion and several important aspects like particle drift, acceleration and wrap round - information that would be difficult to envisage using other techniques.

(vi) Two major sources of discrepancy were due to poor prediction of particle drag coefficient and the air flow field for the region between the electrode and the fully developed jet region.

(vii) The influence due to the secondary air flow from the filtration system on particle trajectories was minimal for the size ranges considered. Theoretically it was shown that the corona wind effect was unimportant as a particle transport mechanism.

CHAPTER 8

General Discussion and Summary

8.1. Objective of investigation

The electrostatic powder coating process has been widely used during the last few years in the metal finishing industry. Despite its many obvious advantages, it is generally believed that the process will be economically more attractive if the deposition efficiency can be significantly improved. Various studies have shown that during the spraying process the deposition efficiency would progressively deteriorate and would eventually result in back ionisation where there would be a continual rejection of charged powder sprayed on the surface. Although the concept of the process is simple, it is a time dependent operation embracing complicated interactions between several electrostatic and aerodynamic forces. The first step towards improving the deposition efficiency therefore is to improve understanding of the fundamental mechanisms.

A survey of the literature showed that while some aspects of powder coating process were extensively investigated and well understood, e.g. back ionisation phenomenon and effect of powder resistivity other areas received relatively little attention, e.g. air flow distribution from a spray gun. Certain important variables had been examined but the results were inconclusive, e.g. corona wind effect and field measurement of a dense cloud of charged particles. There is also a lack of published information on fundamental particulate properties notably the effect of shape irregularity on the charging mechanism and the drag coefficient of particles. Most studies on deposition efficiency adopted a direct approach whereby a varying parameter was chosen to examine its influence while constancy for other operating variables was maintained. With so many interacting forces involved an extensive experimental programme would be required to examine the individual contribution. Furthermore the time of spraying would be a critical factor.

This study adopted an indirect approach whereby the trajectories of particles were studied. The theoretical analysis involved performing a balance of the forces involved and calculating the variation of particle velocity and position due to the exertion of the resultant force. It is conceivably a more difficult method as it requires formulating various mathematical expressions to model the forces. However it has a notable feature of possibility of incorporating all the varying parameters associated with the spraying process in one prediction package and enabling the study of their interactions. The objectives in this study are twofold:

(i) to demonstrate the feasibility of using the computer facility to study this two phase process and to obtain good qualitative agreement with the experimental data.

(ii) to identify the relative importance of the aerodynamic and electrostatic forces involved. The literature has indicated that most studies so far have been experimental in nature with a distinct lack of theoretical treatment and theory should be developed to simulate the phenomena and where possible verified by experiments.

The present investigation is restricted to using dilute suspension and the theory is applicable to the initial coating process. With further improvement the trajectory technique will be a potentially useful tool for studying the process. The state of art of the various other aspects associated with the coating process that would be required for further development of the program (eg.concentration effect and charge density distribution) was included in the literature review. Further development will also require the introduction of time dependent quantities (eg. field variation of deposited layer and ionic current distribution) and good prediction will be possible if the physical mechanism of these quantities can be accurately modelled. With the inclusion of these variables described, the deposition efficiency can be predicted. With such a prediction scheme, the advantages are many. The influence of the various operational parameters on the deposition efficiency can be demonstrated (eg. spray size, spray distance and applied voltage). Also it is possible to get indication of means of improving deposition, eg. introduction of further electrostatic or air flow fields for focussing in the spray booth.

The result of this investigation showed that trajectories of particles were reasonably accurately predicted using simple models to describe the various force fields. Future improvement of the program would only be possible with extensive research on several aspects of the coating process.

8.2. Overall scheme of investigation

The overall plan of investigation is as follows:

(i) Identify the electrostatic and aerodynamic forces involved.

(ii) Trajectory calculation -

(a) Perform a force balance and define the boundaries of operation of these forces.

(b) Obtain mathematical expressions to describe these forces and where possible experimentally verify the theories or compare with published experimental data.

(iii) Design an experiment to record the particle trajectories.

(iv) Comparison of experimental and calculated particle trajectories and particle velocities.

8.3 Summary of results of investigation

8.3.1. Study of aerodynamic forces.

The air flow field in the spray booth is the resultant of two air flows - one due to the extraction system and the other due to the air flow from the spraying device. The component due to the filtration system was insignificant and for the particle size ranges considered the experimental trajectories were unaffected. Two solutions were used to describe the air flow from the spray gun - Tollmien's turbulent jet theory and a potential flow solution. Experimentally the air velocity distribution was determined using hot wire anemometry system to verify the accuracy of the models. Good agreement was obtained using Tollmien's solution but the potential flow solution which represented an ideal flow situation led to overestimation. The effect of a deflector was simulated using a conical electrode and with a virtual origin determined experimentally reasonable agreement was obtained. Two electrodes - a point and a cone were used. The calculated air velocities and width of jet were found to be overestimated with the presence of electrodes. Unfortunately the measurement of turbulent quantities especially the turbulent intensity was neglected and the information would have been useful in the particle trajectory analysis. The development of other jets due to a direct jet impingement on a plate was found to have insignificant effects.

For the region between the electrode and the fully developed jet region, the air velocity was found to be significantly less than that of the air jet. This has an important implication that due to bad mixing of powder particles and ions and a reduction in charging time in this region of high field intensity the particles may not be efficiently charged. For the present study the design of the electrode system was modified to include an internal electrode. This assembly essentially prolonged the particle charging time. In the powder coating process, the size of the diffuser and the exit air velocity will determine the flow pattern in this region and can make a significant difference in the coating performance. The air velocity distribution for this domain was approximated by an expression derived from experimental data of centreline air velocity. This was a major source of discrepancy for the trajectory comparison.

As for modelling the effect of particle concentration in the spray, the indication from literature is that it can still be described by turbulent jet solution with modified virtual origin and spreading coefficient derived experimentally.

8.3.2. The Electrical forces.

For the evaluation of the field intensity and potential, a simple model for point - plane electrode geometry was derived taking into consideration the space charge effect. To test the validity of the theory, Corbett's data for ionic cloud field distribution was used for comparison. The results compared favourably and the bahaviour of the experimental curves was well predicted. The theory is also applicable for the conical electrode system but there is no experimental data available for this geometry for comparison. An expression to calculate the particle image force was also derived.

This space charge effect was known to be responsible for the suppression of field strength at the corona region and enhancement near the object. The field enhancement was confirmed by Corbett's experimental data and also the charged particle acceleration of the present study. Calculation showed that with decreasing magnitude of space charge density, its effect on the applied field became less significant. A criterion was therefore established to assess the importance of space charge effect.

Method of evaluation of ionic and charged particulate components of the charge density was suggested. The literature indicated that further progress of dense charged particulate cloud study will only be possible with development of suitable instrumentation.

8.3.3. The corona wind effect.

Several recent studies have shown that under certain experimental conditions the corona wind contribution can be considerable. The literature however is scarce and inconclusive. For the current analysis Robinson's theory (60) was extended and a simplified expression was used in the computer program to calculate the contribution of corona wind velocity. The calculation showed a maximum value of about 1 m/s and the recent experimental investigations in EPS indicated that the magnitude was of similar order. Further research in this field is desirable to examine the effects of electrode geometry and electrode separation on the magnitude of this ionic wind.

8.3.4. Experimental design

A photographic technique using intermittent illumination was chosen as the particle tracking technique. The technique yields accurate quantitative data of positional variation and particle velocities with moderate effort. The notable feature is the capability of this method to record the complete history of particle flight from the gun to the target. Also the results revealed some interesting information like particle acceleration, particle drift, wrap round and the rotatory motion of the particles. However it suffers the main drawback of only able to deal with dilute suspension. With an area of field of view of 22 cm x 22 cm due to the optical resolution of the photographic system the minimum size limit yielding acceptable photographic records was about 50 µm. To obtain efficient particle charging, an electrode system was designed to include an internal electrode and utilised the 'countercurrent stream' principle.

8.3.5. Computer program and result of comparison of trajectories

For the prediction of particle trajectories, a computational procedure based on Runge - Kutta integration technique was used. This approach required initially the setting up of a force balance of the various aerodynamic and electrostatic forces involved with the 'boundaries' of influence of these forces clearly defined. With the involvement of several interacting forces assumptions had to be made to simplify the prediction scheme.

The theoretical trajectories overall compared favourably with the experimental results despite the simplicity of the calculation procedure. The results demonstrated the effect of superimposing electrical forces on a jet of charged particles emerging from a spray gun. The magnitude of particle velocity distribution was generally correctly predicted.

The accuracy of the prediction depended on the initial particle exit conditions with better agreement for particles emerging near the jet centreline. Air flow from the spraying device was found to be the dominant particle transport mechanism with the electrostatic force becoming more important near the substrate. The main weaknesses of the calculation procedure were identified and the two major sources of discrepancy in comparison were due to poor description of

(i) particle drag coefficient

(ii) air flow model for the intermediate region between the electrode and the fully developed jet.

With the reduction in particle size, the flow turbulence mechanism became important resulting in particle drift. It is doubtful with the current knowledge of turbulent particle diffusion modelling if this meandering motion can be satisfactorily predicted. Theoretically it was shown that the contribution from corona wind and booth air flow could be discounted. For particles emerging away from the centreline edge effect was postulated to play a significant role in deposition but this would require verification.

8.4. Recommendations for further work.

In order to improve and extend the calculation method, several areas have been identified that would require further investigation.

(a) Measurement in charged particulate cloud

There are three problems that will require experimental studies:

- The effect of concentration of charged particles on the applied field.
- The space charge density distribution of charged particulate cloud.
- The edge effect.

With the experimental data the applicability of the theory derived in Chapter 4 to charged particulate cloud can be examined.

The ballistic probe devised by Corbett (10) was found to be unsuitable measurement system in mixed ion and particulate cloud due to probe - particle interaction. Therefore there was no experimental data available for comparison with the equations derived. There is certainly the need for further development of an instrument for charged particulate cloud measurement. Corbett suggested the development of a low speed rotary ballistic probe could be the answer. The examination of the field distribution behind the object would be useful to study the wrap round deposition.

(b) Examination of air velocity distribution.

The inaccuracy of air flow description for the region between electrode and the fully developed jet region was found to contribute the major source of error in the prediction. The air velocity distribution for this region would require detailed analysis so that a suitable model may be formulated. The investigation should incorporate the measurement of turbulence quantities. It would be useful to survey the turbulence intensity further downstream to substantiate the experimental measurement presented in this study. The experimental programme should include using an industrial spray gun and also the use of other electrode geometries.

The velocity distribution in a dense two phase jet should be pursued to study the concentration effect. The laser Doppler anemometer is more suitable for this purpose since the hot wire technique suffers from calibration changes in a two phase jet.

(c) Particle drag coefficient

The off centreline data showed that a higher degree of drag was experienced by the particles as compared to predicted values assuming sphericity of particles. The shape factor is undoubtedly responsible for the difference but the phenomenon is still not clearly understood. For the present purpose it would be beneficial to measure the drag coefficients of the particles for a range of Reynolds numbers. To achieve a high degree of accuracy the computer should be fed the correct experimental drag values for the relevant Reynolds number during the integration.

(d) Study of field due to growing deposited layer

With the growth of the deposited layer during coating the layer electric field and potential would vary until the onset of back ionisation with the attainment of a limiting coating thickness. This time dependence behaviour therefore has to be incorporated in the program to fully describe the process. The results from various studies on this topic have been summarised in Section 4.8 and initially Makin's (49) approach may be adopted. Experimentally particles can be sprayed at regular intervals and in between dilute suspension can be sprayed to study the effect of growth of deposited layer on trajectories.

(e) Miscellaneous

There are several areas that have been examined but the results are inconclusive and require further extensive theoretical and experimental investigations:

- the particle charging of non-spherical particles
- the corona wind effect
- the turbulent particle diffusion process

8.5 Concluding remarks.

This thesis in attempting to describe the trajectories of charged particles in an air jet and electrostatic field for electrostatic powder spraying process has had reasonable success. The theoretical model suffers from the lack of understanding of some important physical parameters. - eg. aerodynamic drag of non spherical particles, corona wind, small particle diffusion and equilibrium charging for non spherical particles but despite this the model predicted trajectories remarkably well. The prediction program could be used in its present state to develop a better understanding of the interactions in a spray booth. To do better will require much detailed research into areas which have much wider significance and application that just electrostatic powder spraying and even then, the predictions may not be significantly improved. This thesis has achieved its objective and a useable mathematical model has been produced which will predict particle trajectories at the initial stages of the coating process. This model can and should be used in further studies.

REFERENCES

1 LEVINSON,S.B.
'Electrocoat powder coat radiate' Which and why?
J. Paint Technol., 44 (1972), 38-56.

2 GEMMER,D.E.
General aspects on electrostatic powder spraying and fluidised bed technique.
Powder Coatings 1970, The 2nd International Conference on Plastic Powder Coatings, 1970, London.

3 HARRIS,S.J.
The technology of powder coatings.
Portallis Press, London, 1976.

4 BRIGHT,A.W. CORBETT,R.P.
Electrostatic powder coating in industry - a survey of recent advances and future developments.
Conf. of Electrical Machines Forming and Coating 1975.

5 SIBBETT,R.A.
The effects of powder characterisation on film properties.
Report May 1977, Co-ordinated Powder Research Programme, Southampton University/Loughborough University.

6 ABRAMOVICH,G.N.
The theory of turbulent jets.
The M.I.T. Press, Cambridge, Mass., 1963.

7 MILLER,E.P. TAFT,D.D.
Fundamental of powder coating
SME, Dearborn, Michigan, 1974.

8 HARDY,G.F.
Role of critical coating thickness in electrostatic powder deposition.
J. Paint Technol., 46 (1974), 73-82.

9 BRIGHT,A.W. BASSETT,J.
Plant and equipment for the application of powder coatings.
Particle Workshop 1975, Electrostatic Powder Coating, Chem. Eng. Dept., Loughborough University, England.

10 CORBETT,R.P.
A study of the eletric fields and deposition processes relevant to electrostatic powder coating.
Ph.D. Thesis, Southampton University, 1972.

11 LESCHONSKI,K.
Calculation of particle trajectories and their application in the design and operation of classifiers.
Particle Workshop 1971, Chem. Eng. Dept., Loughborough University, England.

12 GAUVIN,W.H. KATTA,S. KNELMAN,F.H.
Drop trajectory predictions and their importance in the design of spray dryers.
Int. J. Multiphase Flow, 1 (1975), 793-816.

13 YEH,H.C.
A fundamental study of aerosol filtration by fibrous filters.
Ph.D. Thesis, University of Minnesota, 1972.

14 STENHOUSE,J.I.T.
Mechanism of fibrous filtration.
Ph.D. Thesis, Loughborough University, 1973.

15 TOROBIN,L.B. GAUVIN,W.H.
Fundamental aspects of solids-gas flow. Part IV. The effect of particle rotation, roughness and shape.
Can. J. Chem. Eng., 38 (1960), 142-153.

16 CROWE,C.J. SHARMA,M.P. STOCK,D.E.
The PSI - CELL model for gas droplet flows.
Journal of Fluid Engineering, Trans. ASME, 99 (1977), 325-332.

17 BOOTHROYD,R.G.
Flowing gas-solids suspensions.
Chapman and Hall Ltd., London, 1971.

18 MASUDA,S. MATSUMOTO,Y.
Motion of a microcharge particle within electrohydrodynamic field.
Electrical Engineering in Japan, 94 (1974), 20-26.

19 WHITE,H.J.
Industrial electrostatic precipitation.
Addison-Wesley, Reading, Mass., 1963.

20 KRAMER,H.J. JOHNSTON,H.F.
Collection of aerosol particles in presence of electrostatic fields.
Ind. Eng. Chem., 47 (1955), 2426-2434.

21 ZEBEL,G.
A simple model for the calculation of particle trajectories approaching nuclepore filter pores with allowance for electrical forces.
Aerosol Science, 5 (1974), 473-482.

22 NIELSON,K.A. HILL,J.C.
Collection of inertialess particles on spheres with electrical forces.
Ind. Eng. Chem., Fundam., 15 (1976), 149-157.

23 NIELSON,K.A. HILL,J.C.
Capture of particles on spheres by inertia and electrical forces.
Ind. Eng. Chem., Fundam., 15 (1976), 157-163.

24 ABUAF,N. GUTFINGER,C.
Trajectories of charged solid particles in an air jet under the influence of an electrostatic field.
Int. J. Multiphase Flow, 1 (1974), 513-523.

25 SOO,S.L.
Fluid dynamics of multiphase systems.
Blaisdell Publ. Co., Waltham, Mass., 1967.

26 JAMES,M.L. SMITH,G.M. WOLFORD,J.C.
Applied numerical methods for digital computation with FORTRAN.
International Textbook Company, Scranton, Pennsylvania, 1967.

27 McCORMICK,J.M. SALVADORI,M.G.
Numerical methods in FORTRAN.
Prentice-Hall, New Jersey,1964.

28 ANON
GINO F user Manual, Issue 2,
Computer Aided Design Centre, Cambridge, 1976.

29 KORF,Chr.
Powder coating - a report on materials, testing, plant and application.
R.H. Chandler Ltd., Braintree, Essex, 1976.

30 SAVAGE,D.R.
Electrostatic powder application spray enclosure.
Prod. Finish, 2nd Quarter (1976) 12-15.

31 BRIGHT,A.W.
Recent advances in electrostatic powder coating.
Conf. Powder Coating, London, 1967.

32 SILVESTER,P.
Modern electromagnetic fields.
Prentice-Hall, New Jersey, 1968.

33 WEBER,E.
Electromagnetic fields, theory and applications (4th Ed.).
John Wiley and Sons, New York, 1960.

34 ADACHI,T. MASUDA,S AKUTSU,K.
Velocity distribution of negative ionic wind in corona space between needle and plate electrodes.
Trans. Inst. Electrical Engrs. Japan, 52A (1977), 259-266.

35 WU,S.
Electrostatic Charging and deposition of powder coatings.
Polym.-Plast. Technol. Eng., 7 (1976), 119-220.

36 OGLESBY,S. NICHOLS,G.B.
A manual of electrostatic precipitation technology.
Southern Research Inst., Birmingham, Alabama, 1970.

37 GOOCH,J.P. McDONALD,J.R. OGLESBY,S.
A mathematical model of electrostatic precipitation.
Southern Research Int., Birmingham, Alabama, 1975.

38 PAUTHENIER,M.M. MOREAU-HANOT,M.
Le charge des particules spheriques dans un champ ionise.
J. Phys. Radium, 3 (1932), 590-613.

39 YU,C.P.
Precipitation of unipolarly charged particles in cylindrical and spherical vessels.
J. Aerosol Sci., 8 (1977), 237-241.

40 FAITH,L.E. BUSTANY,S.N. HANSON,D.N. WILKE,C.R.
Particle precipitation by space charge in tubular flow.
I & EC Fundamentals, 6 (1967), 519-526.

41 CHEEVER,G.D.
Electrostatic charge acceptance and decay of powder coating particles.
J. Appl. Polym. Sci., 19 (1975), 147-163.

42 SMITH,P.L. PENNEY,G.W.
The charging of nonspherical particles in a corona discharge.
AIEE Transactions, 80 (1961), 340-346.

43 BAUCH,H.
On the formation of laminae in the electrostatic application of plastic powders.
Plaste U. Kautschuk, 21 (1974), 853-859.

44 ZABEL,L.W. ESTCOURT,A.R.
The measurement of charge response of powders exposed to ion bombardment.
J. Appl. Polym. Sci., 13 (1969), 1909-1919.

45 CROSS,J.A.
Adhesion of electrostatic powder coatings.
Inst. Phys. Conf. Ser. No. 27 (1975), 202-214.

46 SPILLER,L.L.
Measurement of charging and discharging characteristics of powdered polymers.
Conf. American Chem. Soc. Div. of Org. Coatings & Plastics, Washington, 31 (2), 582-595 (1971).

47 GOLOVOY,A. COLVIN,A.D.
Charge decay from electrostatically charged powders.
J. Paint Technol., 47 (1975), 65-70.

48 CROSS,J. BASSETT,J.D.
Observations during electrostatic deposition of high resistivity powders.
Trans. Inst. Metal. Fin., 52 (1974), 112-113.

49 MAKIN,B. CORBETT,R.P. BRIGHT,A.W.
Electrodeposition of particle layers in liquids and gases.
I.E.E. Conf. Pub., 61 (1970), 119-126.

50 GOLOVOY,A.
Growth of film thickness in electrostatic spraying of powder coatings.
J. Paint Technol., 45 (1973), 74-79.

51 ROBINSON,M.
A history of the electric wind.
Am. J. Phys., 30 (1962), 366-372.

52 STUETZER,O.M.
Ion drag pressure generation.
J. Appl. Phys., 30 (1959), 984-994.

53 STUETZER,O.M.
Ion drag pumps.
J. Appl. Phys., 31 (1960), 136-146.

54 SINGH,S. O'NEILL,B.C. BRIGHT,A.W.
A parametric study of electrostatic powder coating.
J. Electrostatics, 4 (1978), 325-334.

55 SINGH,S.
Private communication.
Applied Electrostatics Group, Electrical Engineering Dept.
Southampton University.

56 ADACHI,T.
Ionic wind in the electrostatic precipitator-experimental treatment by the Schlieren method.
Trans. I.E.E. Japan, 93B (1973), 273-280.

57 ADACHI,T.
Ionic wind in the electrostatic precipitator.
J. Res. Assoc. Powder Tech., Japan, 12 (1975), 146-153.

58 MASUDA,S. AKUTSU,K. AIHARA,K.
Study on electric wind inside an electrostatic precipitator.
Proc. of 1977 Annual Meeting of Institute of Electrical Eng., Japan, No. 1028.

59 LOWE,H.J. LUCAS,D.H.
The physics of electrostatic precipitation.
Brit. J. Appl. Phys., 4 (1953), S40-S47.

60 ROBINSON,M.
Movement of air in the electric wind of the corona discharge.
Trans. AIEE., 80 (1961), 143-150.

61 SAVAGE,D.R.
The application of dry powder coating materials.
Metal Fin., 72 (1974), 44-54.

62 HINZE,J.O.
Turbulence (2nd Ed.).
McGraw-Hill, New York, 1975.

63 RAJARATNAM,N.
Turbulent jets.
Elsevier, Amsterdam, 1976.

64 MANDI,I.K. PLETCHER,R.H.
Prediction of turbulent jets in co-flowing and quiescent ambients.
ASME Journal of Fluids Engineering, 97 (1975), 558-567.

65 LAUNDER,B.E. MORSE,A. RODI,W. SPALDING,D.B.
Prediction of free shear flows- a comparison of the performance of six turbulence models.
Proc. of the Langley Working Conference on Free Turbulent Shear Flows, N.A.S.A. SP-321, Vol. 1, 1972, pg. 361-422.

66 LAUNDER,B.E. MORSE,A.
Numerical prediction of axisymmetric free shear flows with a second order Reynolds stress closure.
Proc. Symp. on Turbulent Shear Flows, Penn. State Univ. U.S.A. 1977.

67 TOLLMIEN,W.
Calculation of turbulent expansion processes.
ZAMM, 6 (1926), 468-478.

68 POREH,M. CERMAK,J.E.
Flow characteristics of a circular submerged jet impinging normally on a smooth boundary.
Proc. 6th Mid.-Western Conf. on Fluid Mechanics, University of Texas, 1959.

69 BOLDMAN,D.R. BRINICH,P.F.
Mean velocity, turbulence intensity and scale in a subsonic turbulent jet impinging normal to a large flow plate.
NASA TP 1037, 1977.

70 BELTAOS,S. RAJARATNAM,N.
Impinging circular turbulent jets.
Proc. A.S.C.E., J. Hydraul. Div., 100 (1974), 1313-1328.

71 GUTMARK,E. WOLFSHTEIN,M. WYGNANSKI,I.
The plane turbulent impinging jet.
J. Fluid Mech., 88 (1978), 737-756.

72 SCHLICHTING,H.
Boundary layer theory (6th Ed.).
McGraw-Hill, New York, 1968.

73 BOGUSLAWSKI,L. POPIEL,C.O.
Flow structure of the free round turbulent jet in the initial region.
J. Fluid Mech., 90 (1979), 531-539.

74 CROW,S.C. CHAMPAGNE,F.H.
Orderly structure in jet turbulence.
J. Fluid Mech., 48 (1971), 547-591.

75 LAU,C.J.
The vortex-street structure of turbulent jets. Part I.
J. Fluid Mech., 67 (1975), 299-337.

76 SHINICHI,Y. NAOTO,Y. YASUO,H. TOMOSADA,J.
Particle turbulent diffusion in a dust laden round jet.
A.I.Ch.E.J., 24 (1978), 509-519.

77 STRIBLEY,J.
Review of current electrostatic powder coating techniques and future lines of development.
Powder Coatings 1970, The 2nd International Conference on Plastic Powder Coatings, London, 1970.

78 WINTER,P.
Powder coating- a review.
Metal Finishing J., 20 (1974), 234-235.

79 COWLEY,M.
Transfer efficiency: the primary criterion of powder plant design.
Product Finishing, 28 (1975), 22-24.

80 POPPER,J. ABUAF,N. HETSRONI,S.
Velocity measurement in a two phase turbulent jet.
Int. J. Multiphase Flow, 1 (1974), 715-726.

81 GOLDSCHMIDT,V.W. ESKINAZI,S.
Two phase turbulent flow in a plane jet.
Trans. ASME, J. Appl. Mech., 33 (1966), 735-747.

82 HETSRONI,G. SOKOLOV,M.
Distribution of mass, velocity and intensity of turbulence in a two phase turbulent jet.
Trans. ASME, J. Appl. Mech., 38 (1971), 315-327.

83 ABUAF,N. GUTFINGER,C.
Entrainment of solid particles in a turbulent air jet - a preliminary study.
Israel J. Tech., 9 (1971), 389-395.

84 McCOMB,W.D. SALIH,S.M.
Comparison of some theoretical concentration profiles for solid particles in a turbulent jet with the results of measurements using a laser-Doppler anemometer.
J. Aerosol Sci., 9 (1978), 299-313.

85 DAVIDSON,G.A. McCOMB,W.D.
Turbulent diffusion in an aerosol jet.
J. Aerosol Sci., 6 (1975), 227-247.

86 LAATS,M.K.
Experimental study of the dynamics of an air dust jet.
Inzhenermo-Fizicheskii Zhurnal, 10 (1966), 11-15.

87 LAATS,M.K. FRISHMAN,F.A.
Assumptions used in calculating the two phase jet.
Izv. An SSSR, Mekhanika Zhiskosti i Gaza, 5 (1970), 186-191.

88 LAATS,M.K. FRISHMAN,F.A.
Scattering of an inert admixture of different grain size in a two phase axisymmetric jet.
Heat Transfer Soviet Res., 2 (1970), 7-11.

89 MELVILLE,W.K. BRAY,K.N.C.
The two phase turbulent jet.
Int. J. Heat Mass Transfer, 22 (1979), 279-287.

90 DANON,H. WOLFSHTEIN,M. HETSRONI,G.
Numerical calculations of two phase turbulent round jet.
Int. J. Multiphase Flow, 3 (1977), 223-234.

91 MELVILLE,W.K. BRAY,K.N.C.
A model of the two phase turbulent jet.
Int. J. Heat Mass Transfer, 22 (1979), 647-656.

92 MILNE-THOMSON,L.M.
Theoretical hydrodynamics (5th Ed.),
MacMillan Press Ltd., London, 1976.

93 ROBERTSON,J.M.
Hydrodynamics in theory and application.
Prentice Hall, New Jersey, 1965.

94 DOMMASCH,D.O.
Principles of aerodynamics
Pitman Publishing Corporation, N.Y., 1953.

95 SOMERSCALES, E.F.C.
Fluid velocity measurement by particle tracking in Flow - Its Measurement and Control in Science and Industry, Vol. 1.
Instrument Society of America, 1974.

96 CHIGIER, N.A.
Velocity measurement of particles in sprays in Flow - Its Measurement and Control in Science and Industry, Vol. 1.
Instrument Society of America, 1974.

97 BIRCHENOUGH, A. MASON, J.S.
Local particle velocity measurements with a laser anemometer in an upward flowing gas-solid suspension.
Powder Technol., 14 (1976), 139-152.

98 TYLER, A.L. SALT, D.L.
Periodic discontinuities in the acceleration of spheres in free flight.
Trans. ASME, J. Fluid Engineering, 100 (1978), 17-21.

99 FINLAY, I.C. WELSH, N.
National Engineering Laboratory (England).
Report No. 331, 1967.

100 DOMBROWSKI, N. TYLEY, L.R.
High speed photography of fast moving particles.
The Journal of Photographic Science, 15 (1967), 40-44.

101 GUBENSKII, V.A. FUCHS, N.A.
Determination of the size and charge of individual particles in electrostatic spraying of paints.
Lakokrasoch. Materialy, 4 (1965), 50-57.

102 GUBENSKII, V.A.
Experimental investigation of the electrostatic spraying of paints.
Lakokrasoch. Materialy, 1 (1966), 28-33.

103 BRIFFA, F.E. DOMBROWSKI, N.
Entrainment of air into a liquid spray.
A.I.Ch.E.J., 12 (1966), 708-717.

104 CHANDOK,S.S. PEI,D.C.T.
Particle dynamics in solids-gas flow in a vertical pipe.
Pneumotransport Conf. Churchill College, Cambridge, 1971.

105 KANE,R.S. WEINBAUM,S. PFEFFER,R.
Characteristics of dilute gas-solids suspensions in drag reducing flow.
Pneumotransport Conf. Univ. of Surrey, Guildford, 1973.

106 LEVER,R.C.
A new development in deposition efficiency and colour change of electrostatically applied powders.
Product Finishing, 2 (1978), 29-33.

107 PETER,E.
Efficient colour changes.
The 4th North American Conference on Powder Coating, Toronto, Canada, 1976.

108 SINGH,S. HUGHES,J.F.
Annual report 1978.
Co-ordinated Powder Research Programme, Southampton University/ Loughborough University, England.

109 GOLOVOY,A.
Deposition efficiency in electrostatic spraying of powder coating.
J. Paint Technol., 45 (1973), 42-48.

110 GOLOVOY,A.
Particle deposition in electrostatic spraying of powder coatings.
J. Paint Technol., 45 (1973), 69-73.

111 Heberlein,V.I.K.
Wirkungsgrad bei Pulverbeschichtungen.
Industri-Lackier-Betrieb, 39 (1971), 426-430.

112 MASUDA,S.
Electric curtain spray booth for powder coating.
Research on Electrostatic Precipitation and Applied Electrostatics, Annual Report (1976-1977), Masuda Laboratory, Dept. Of Elect. Engineering, University of Tokyo, Japan.

113 ANON
Design and installation of large paint booths for heavy equipment.
Powder Finishing World, Nov.-Dec. (1977) 9-10.

114 MASUDA,S.
A booth for electrostatic spray coating of work pieces with powder particles.
British Patent 1372928 (1972).

115 ALBERTSON,M.L. DAI,Y.B. JENSEN,R.A. ROUSE,H.
Diffusion of submerged jets.
Trans. ASCE, 115 (1950), 639-634.

116 SINGH,S.
Studies of EPC by lase Doppler anemometry.
Annual Report 1975.
Co-ordinated Powder Research Programme,
Southampton University/Loughborough University, England.

117 ANON
Instruction book for high power high speed short duration stroboscope MODEL HSS/4/K-3.
Ernest Turner Electrical Instruments Ltd., High Wycombe, Bucks.

118 GOURDINE,M.C.
Electrogasdynamic powder coating tunnel.
SME Technical Paper FC73-521 (1973).

119 KNOTT,J.K.
Electrogasdynamic powder coating.
Technical report, Electropaint Ltd., Birmingham Road, Lichfield, Staffs, 1978.

120 TING,Y.C.
Back Ionization in Electrostatically Deposited Powder Layers.
M. Phil. Thesis, Southampton University, 1978.

121 ISLAM,S.M.N. TUCKER,H.J.
Flow in the initial region of axisymmetric turbulent jets.
ASME Journal of Fluids Engineering, 102 (1980), 85-91.

122 SINGH,S. BRIGHT,A.W.
Laser anemometry studies of powder deposition process.
3rd Int. Congr. on Static Electricity ,Grenoble, France, (1977).

123 SINGH,S.
Fundamentals of Electrostatic Powder Coating - Laser Anemometry
Progress Report, Sept. 1977.
Co-ordinated Powder Research Programme, Southampton University/
Loughborough University, England.

124 ALQUIER,M. GRUAT,J. VALENTIAN,F.
Influence of large eddies on the suspension of solid particles.
Int. J. Multiphase Flow, 5 (1979), 427-436.

Appendix 1

Included in this appendix are the listing of a program for single trajectory calculation, results of two calculations and an explanation of the symbols used. Several programs were used for calculation with variation of electrode geometry and for single or two trajectory calculation. The program used as an example in this section can easily be extended for two trajectory calculation. The various subroutines - AXISCA, AXIDRA, GRAMOV, GRALIN are graph plotting routines and are described in Reference 28.

Program symbols

FORTRAN symbol	Meaning	Equation of first mention
T	t	2.1
EPSI	ϵ	4.32
EPSIO	ϵ_o	4.1
VA	V_a	4.4
VIS	μ	2.5
GRAV	g	2.1
ROS, ROF	ρ_s ρ_f	2.1
PLA	d	Figure 2.3
ANGLE	θ	Figure 2.3
C	C	4.14
EO	E_o	4.19
D1, D2, D4	D1, D2, D4	Figure 2.3
DP	d_p	2.1
Z	Z = 0 or 1 specifying calculation without and with consideration of electrostatic forces	
DT	time interval for integration	

FORTRAN symbol	Meaning	Equation of first mention
SOURU	U_o	3.31
VIX, VIY	V_{ix}, V_{iy}	2.14
X (1), Y (1)	x, y	2.14
A	a	3.33
DJET	2 x R_o	3.65
CON	Constant for calculation of length of region between electrode and fully developed jet section	
P	S_o	3.65
SLOPE, CEPT	Gradient, intercept	3.66 - 3.67
CHARGE	q	4.32
FAPP	N_{app}	4.48
FI	N_I	4.50
VEL1, VEL2	U, V	2.3 - 2.4
XP	x coordinate from jet source	
Q	φ	3.20
A1 - A6, B1 - B6	components of jet equations	3.26 - 3.27
Z1	z	3.27
Z2	z'	3.26
CMEANU	u_m	3.33
EAPPX, EAPPY	E_{appx}, E_{appy}	4.48 - 4.49
APPX, APPY	F_{appx}, F_{appy}	4.45 - 4.46
EMAGEX	F_{ix}	4.50
FORCEX, FORCEY	ΣF_{ex}, ΣF_{ey}	2.8 - 2.9
REYN	Re	2.5
CDRAG	C_d	2.7
AK1 - AK4, BK1 - BK4	incremental components in Runge - Kutta integration method	
XMAG, YMAG	magnified x, y coordinates	
GAM	magnification factor for graph plotting	

```
JOB MLA002,CG,MLA3247
FORTRAN ,,;LIBRARY(ED,SUBGROUPGINO)
FDUMP $JAN/MLA3247JETC
****
DOC FORTRAN
      MASTER TOOTBOO
C     A PROGRAMME FOR MODELLING AN ELECTROSTATIC POWDER COATING PROCESS
C     JETPACK-------- USE OF CONICAL ELECTRODE
      DIMENSION X(1),Y(1)
      T=0.0
      EPSI=2.0
      EPSIO=8.85E-12
      VA=60000.0
      VIS=0.0000185
      GRAV=9.98
      ROS=1000.0
      ROF=1.2928
      PLA=0.0265
      ANGLE=0.17453
      C=0.02290
      EO=300000.0
      READ(1,10) D1,D2,D4
      READ (1,13) DP,Z,DT
      READ(1,15) SOURU
      READ(1,17) VIX,VIY
      READ(1,19) X(1),Y(1)
      READ(1,21) A,DJET,CON,P
      READ ( 1,40 ) SLOPE,CFPT
      READ (1,41) GAM
C    GAM IS  THE MAGNIFICATION FACTOR FOR GRAPH PLOTTING
```

```
 10 FORMAT(3E0.0)
 13 FORMAT(3E0.0)
 15 FORMAT(1E0.0)
 17 FORMAT(2E0.0)
 19 FORMAT(2E0.0)
 21 FORMAT(4E0.0)
 40 FORMAT ( 5E0.0 )
 41 FORMAT (1E0.0)
    COM=3.0*3.142*(EPSI/(EPSI+2.0))*EPSIO*EO
    CHARGE=COM*DP*DP
    FAPP=CHARGE*C*VA*(D1-D2)/(D1-D2-C)
    FI=CHARGE*CHARGE/(4*3.142*EPSIO)
    C2=DP*ROF/VIS
    C1=0.75*ROF/(ROS*DP)
    C4=3.142*DP**3.0*ROS/6.0
    WRITE(2,110) D1,D2,D4
    WRITE(2,112) DP,Z,DT
    WRITE(2,114) SOURU,VIX,VIY
    WRITE(2,24) FAPP,FI
    WRITE (2,30) A,DJET,CON,P
    WRITE (2,31) SLOPE,CEPT
110 FORMAT(1H ,4X,3HD1=,F7.5,3X,3HD2=,F7.5,3X,3HD4=,F7.5)
112 FORMAT(1H ,4X,3HDP=,E10.4,3X,2HZ=,F3.1,3X,3HDT=,F6.4)
114 FORMAT(1H ,4X,6HSOURU=,F7.5,3X,4HVIX=,F6.4.3X,4HVIY=,F6.4)
 24 FORMAT (1H ,4X,5HFAPP=,E10.6,6X,3HFI=,E12.6//)
 30 FORMAT (1H ;4X,2HA=,F7.5,3X,5HDJET=,F7.5;3X,
   14HCON=,F7.5,3X,2HP=,F7.5)
 31 FORMAT (1H ,4X,6HSLOPE=,F7.5.3X,5HCEPT=,F7.5)
    WRITE (2,25)
 25 FORMAT (1H ,4X,4HX(1),5X,3HVIX,8X,4HY(1);6X,3HVIY,6X,4HVEL17
```

```
     15X,6HFORCEX,5X,4HVEL2,6X,6HFORCEY,5X,1HT,9X,4HXMAG,6X,4HYMAG)
      CALL LP120
      CALL AXISCA (1,20,0.0,0.17,1)
      CALL AXISCA (1,20,-0.05,0.30,2)
      CALL AXIDRA (1,1,1)
      CALL AXIDRA (-1,-1,2)
      CALL GRAMOV ( 0.157,0.027)
      CALL GRALIN ( 0.157,-0,027)
C  CALCULATION OF VELOCITIES VEL1 AND VEL2
   50 XCORE=CON*DJET
      RJET=DJET/2.0
      IF ( X(1)-XCORE ) 100,150,150
C RISING VEL REGION
  100 VEL2=0.0
      IF ( ABS (Y(1)-RJET))  160,160,170
  160 VEL1=SLOPE*X(1)/DJET+CEPT
      GOTO 210
  170 VEL1=0.0
      GOTO 210
C  FULLY DEVELOPED JET REGION
  150 XP=X(1)+P
      IF ( ABS ( Y(1)).GE. 0.0265 ) GOTO 900
      IF ( ABS(Y(1)).LE. 0.0005 )  Y(1)=-0.0005
      Y1= ABS ( Y(1) )
      Q= Y1/(A*XP)
      A1=ALOG(Q+Q/2)
      A2=Q**1.5
      A3=Q**3.0
      A4=Q**4.5
      A5=Q**6.0
```

```
      A6=Q**7.5
      Z1=A1=0.27*A2=0.001*A3+0.00018*A4+0.000025*A5+0.000002*A6
      B1=2/Q
      B2=Q**0.5
      B3=Q**2.0
      B4=Q**3.5
      B5=Q**5.0
      B6=Q**7.5
      Z2=B1=0.4*B2-0.04*B3+0.00082*B4+0.00015*B5+0.000014*B6
      F1=EXP(Z1)
      F2=Z2*F1
      CMEANU=0.96*SOURU*RJET/(A*XP)
      VEL1=F2*CMEANU/Q
      VEL2= (F2-F1/Q)*A*CMEANU
      IF ( VEL1.LT.0.0 )VEL1=0.0
      IF ( VEL2.LT. 0.0 )  VEL2=0.0
      X(1)=XP-P
      GOTO 210
  900 VEL1=0.0
      VEL2=0.0
C  CALCULATION OF ELECTROSTATIC PARAMETERS FORCEX AND FORCEY
  210 IF (Z.EQ.0.0) GOTO 300
      IF ( X(1).LT.D2) GOTO 300
      IF ( ABS(Y(1)).GE.(TAN(ANGLE)*(X(1)-D2))) GOTO 240
      DIFF=X(1)-D2
      BOT=((DIFF*DIFF)+(Y(1)*Y(1)))**1.5
      EAPPX=DIFF/BOT
      EAPPY=Y(1)/BOT
      APPX=FAPP*EAPPX
      APPY=FAPP*EAPPY
```

```
      GOTO 250
  240 APPX=0
      APPY=0
  250 IF (ABS(Y(1)).GE.PLA) GOTO 260
      EIX=1.0/((D1-X(1))*(D1-X(1)))
      EMAGEX=EIX*FI
      GOTO 280
  260 EMAGEX=0
  280 FORCEX=APPX+EMAGEX
      FORCEY=APPY
      GOTO 320
  300 FORCEX=0
      FORCEY=0
C  DEFINITION OF TWO TRAJECTORY EQUATIONS
C  VIX=DX/DT , VIY=DY/DT
C  F(VIX)=DERIV OF VIX , F(VIY)=DERIV OF VIY
C  CALCULATION OF TRAJECTORY USING RUNGE KUTTA 4TH ORDER METHOD
  320 DIFF1=(VEL1-VIX)*(VEL1-VIX)
      DIFF2=(VEL2-VIY)*(VEL2-VIY)
      VREL=(DIFF1+DIFF2)**0.5
      REYN=C2*VREL
      CDRAG=(REYN/24.0)*(1.0+0.15*(REYN**0.667))
      C3=CDRAG*VREL*C1
      C5=FORCEX/C4
      AK1=DT*(C3*(VEL1-VIX)+C5)
      AK2=DT*(C3*(VEL1-VIX+AK1/2)+C5)
      AK3=DT*(C3*(VEL1-VIX+AK2/2)+C5)
      AK4=DT*(C3*(VEL1-VIX+AK3)+C5)
      C6=FORCEY/C4-GRAV
      BK1=DT*(C3*(VEL2-VIY)+C6)
```

```
      BK2=DT*(C3*(VEL2-VIY+BK1/2)+C6)
      BK3=DT*(C3*(VEL2-VIY+BK2/2)+C6)
      BK4=DT*(C3*(VEL2-VIY+BK3)+C6)
      XMAG=X(1)*GAM
      YMAG=Y(1)*GAM
      WRITE(2,3) X(1),VIX,Y(1),VIY,VEL1,FORCEX,VEL2,FORCEY,T,XMAG,YMAG
    3 FORMAT(1H ,11F10.6)
      CALL GRASYM (X(1),Y(1),1,4,1)
      X(1)=X(1)+DT*VIX+DT*(AK1+AK2+AK3)/6
      VIX=VIX+(AK1+2*AK2+2*AK3+AK4)/6
      Y(1)=Y(1)+DT*VIY+DT*(BK1+BK2+BK3)/6
      VIY=VIY+(BK1+2*BK2+2*BK3+BK4)/6
      T=T+DT
      IF (X(1).GE.D1) GOTO 350
      GOTO 50
  350 CALL DEVEND
      STOP
      END
      FINISH
```

(a) Single trajectory calculation

```
D1=0.15691    D2=0.00925    D4=0.01384
DP=0.1150E-03   Z=0.0    DT=0.0025
SOURU=9.15000   VIX=2.8690    VIY=-.2360
FAPP=-.513851E-10        FI=0.246210E-15


A=0.16500   DJET=0.00600   CON=7.10000    P=-.01600
SLOPE=0.11000   CEPT=-.10770
X(1)        VIX         Y(1)        VIY         VEL1        FORCEX      VEL2        FORCEY      T           XMAG        YMAG
0.019983    2.869000   -0.003230   -0.236000    0.000000    0.000000    0.000000    0.000000    0.000000    0.051948   -0.008398
0.026666    2.471378   -0.003815   -0.229734    0.000000    0.000000    0.000000    0.000000    0.002500    0.069332   -0.009913
0.032555    2.234580   -0.004592   -0.234029    0.000000    0.000000    0.000000    0.000000    0.005000    0.084638   -0.011420
0.037935    2.066680   -0.004936   -0.242321    0.000000    0.000000    0.000000    0.000000    0.007500    0.098624   -0.012968
0.042930    1.937644   -0.005607   -0.252912    2.738406    0.000000    0.149662    0.000000    0.010000    0.111642   -0.014577
0.047790    1.944757   -0.006266   -0.274597    2.490019    0.000000    0.143188    0.000000    0.012500    0.124260   -0.016291
0.052658    1.947429   -0.006980   -0.297361    2.249061    0.000000    0.131800    0.000000    0.015000    0.136910   -0.018149
0.057527    1.948246   -0.007754   -0.321184    2.029528    0.000000    0.119805    0.000000    0.017500    0.149571   -0.020159
0.062393    1.948402   -0.008587   -0.345310    1.834036    0.000000    0.108541    0.000000    0.020000    0.162235   -0.022325
0.067269    1.948160   -0.009480   -0.369329    1.661327    0.000000    0.098342    0.000000    0.022500    0.174899   -0.024648
0.072138    1.947504   -0.010435   -0.392920    1.508984    0.000000    0.089201    0.000000    0.025000    0.187559   -0.027125
0.077004    1.945392   -0.011444   -0.415821    1.374435    0.000000    0.081010    0.000000    0.027500    0.200210   -0.029754
0.081863    1.941919   -0.012511   -0.437824    1.255308    0.000000    0.073641    0.000000    0.030000    0.212844   -0.032528
0.086711    1.936415   -0.013631   -0.458775    1.149517    0.000000    0.066975    0.000000    0.032500    0.225448   -0.035442
0.091542    1.926514   -0.014805   -0.478571    1.055266    0.000000    0.060911    0.000000    0.035000    0.238009   -0.038488
0.096355    1.917978   -0.016023   -0.497162    0.971022    0.000000    0.055364    0.000000    0.037500    0.250511   -0.041659
0.101125    1.904708   -0.017287   -0.514344    0.895470    0.000000    0.050261    0.000000    0.040000    0.262934   -0.044947
0.105877    1.888733   -0.018594   -0.530750    0.827487    0.000000    0.045544    0.000000    0.042500    0.275263   -0.048344
0.110567    1.870188   -0.019940   -0.545647    0.766108    0.000000    0.041162    0.000000    0.045000    0.287480   -0.051843
0.115219    1.849191   -0.021322   -0.559723    0.710501    0.000000    0.037072    0.000000    0.047500    0.299569   -0.055436
0.119814    1.826511   -0.022733   -0.573076    0.659952    0.000000    0.033236    0.000000    0.050000    0.311514   -0.059119
0.124364    1.801546   -0.024186   -0.585416    0.613841    0.000000    0.029624    0.000000    0.052500    0.323305   -0.062884
0.128819    1.775299   -0.025664   -0.597050    0.571636    0.000000    0.026206    0.000000    0.055000    0.334930   -0.066726
0.133222    1.747369   -0.027170   -0.608080    0.000000    0.000000    0.000000    0.000000    0.057500    0.346381   -0.070643
0.137490    1.665370   -0.028687   -0.604713    0.000000    0.000000    0.000000    0.000000    0.060000    0.357476   -0.074585
0.141560    1.594455   -0.030195   -0.604632    0.000000    0.000000    0.000000    0.000000    0.062500    0.368072   -0.078516
0.145473    1.532421   -0.031713   -0.606540    0.000000    0.000000    0.000000    0.000000    0.065000    0.378236   -0.082453
0.149734    1.477388   -0.033233   -0.610 53    0.000000    0.000000    0.000000    0.000000    0.067500    0.388019   -0.086407
0.152672    1.428301   -0.034765   -0.615 21    0.000000    0.000000    0.000000    0.000000    0.070000    0.397462   -0.090389
0.156384    1.363 5    -0.03631    -0.621 84    0.000000    0.000000    0.000000    0.000000    0.072500    0.406599   -0.094407
```


20
18
16
14
12
10
8
6
4
2
0
-2
-4
-6
0
1
2
3
4
5
6
7
8
9
10
11
12
13
14
15
16
17
X10-2

(b) Double trajectory calculation

```
D1=0.15635    D2=0.00883    D3=0.13935    D4=0.03138
DP=0.1150E-03    Z=1.0    H=0.0025
SOURU=9.15000    SOURM=0.08750    VX=4.7420    VY=-.4090

B1=0.183492E-06       CHARGE=0.165485E-12
GRAV=  0.045261       STK=      13.712817
FAPP=  2.088804       FI=0.191072E-05

P=-.01500    CON=9.15000    DJET=0.00600    SLOPE=0.12000    CEPT=-.59660
 X(1)       VIX        Y(1)       VIY        VEL1       FORCEX     VEL2       FORCEY     T          XMAG       YMAG
0.034980  0.518251 -0.003210 -0.044099  0.103000  2.097506  0.000000 -0.257476  0.000000  0.090948 -0.008346
0.048021  0.620883 -0.004413 -0.060320  0.363823  0.937141  0.000000 -0.105525  0.863208  0.124855 -0.011474
0.062703  0.662374 -0.005855 -0.065717  0.326950  0.496582 -0.040131 -0.053971  1.726415  0.163029 -0.015224
0.077969  0.672206 -0.007409 -0.070088  0.187980  0.301653 -0.022118 -0.032326  2.589623  0.202719 -0.019263
0.093217  0.661068 -0.009032 -0.071773  0.121925  0.202498 -0.014079 -0.021673  3.452830  0.242364 -0.023483
0.108101  0.640529 -0.010679 -0.072215  0.086078  0.146301 -0.009873 -0.015738  4.316038  0.281064 -0.027765
0.122466  0.615629 -0.012328 -0.072011  0.064605  0.111620 -0.007411 -0.012109  5.179245  0.318411 -0.032053
0.136238  0.588821 -0.013969 -0.071448  0.050752  0.088762 -0.005848 -0.009731  6.042453  0.354220 -0.036319
0.149391  0.561410 -0.015594 -0.070679 -0.000331  0.072922 -0.099947 -0.008087  6.905660  0.388416 -0.040546

   NO ELECT FIELD

 XA(1)      VIXA       YA(1)      VIYA       VEL1       FORCEX     VEL2       FORCEY     T          XMAG       YMAG
0.034980  0.518251 -0.003210 -0.044699  0.103000  0.000000  0.000000  0.000000  0.000000  0.090948 -0.008346
0.046542  0.492917 -0.004231 -0.044512  0.354244  0.000000  0.000000  0.000000  0.863208  0.121010 -0.011002
0.057706  0.483237 -0.005251 -0.044529  0.407917  0.000000 -0.050157  0.000000  1.726415  0.150035 -0.013653
0.068707  0.478642 -0.006304 -0.047512  0.258433  0.000000 -0.030335  0.000000  2.589623  0.178638 -0.016391
0.079500  0.465207 -0.007409 -0.049103  0.179331  0.000000 -0.020600  0.000000  3.452830  0.206701 -0.019264
0.089940  0.447766 -0.008543 -0.050004  0.132885  0.000000 -0.015149  0.000000  4.316038  0.233845 -0.022212
0.099961  0.428556 -0.009693 -0.050517  0.103385  0.000000 -0.011795  0.000000  5.179245  0.259899 -0.025201
0.109535  0.408718 -0.010852 -0.050793  0.083485  0.000000 -0.009583  0.000000  6.042453  0.284791 -0.028214
0.118655  0.388876 -0.012015 -0.050919  0.069414  0.000000 -0.008046  0.000000  6.905660  0.308503 -0.031239
0.127325  0.369386 -0.013180 -0.050942  0.059082  0.000000 -0.006933  0.000000  7.768868  0.331046 -0.034268
0.135556  0.350455 -0.014345 -0.050897  0.051260  0.000000 -0.006099  0.000000  8.632075  0.352446 -0.037296
0.143362  0.332201 -0.015508 -0.050803 -0.000374  0.000000 -0.100077  0.000000  9.495283  0.372741 -0.040320
0.150727  0.311911 -0.016735 -0.056448 -0.000345  0.000000 -0.099912  0.000000 10.358491  0.391889 -0.043512
```


X10-1
0
2
4
6
8
10
12
14
16
18
20
22
24
26
28
30
32
34
36
38
40
42
44
46
48
50
52
54
56
58
60
35
30
25
20
15
10
5
0
-5
-10
-15
-20
-25
-30
-35
-40
-45
-50
-55
-60